DOWNHOLE WIRELINE MECHATRONICS AND DRILLSTRING VIBRATION DYNAMICS

A Thesis

by

OMAR MOHAMED ABDELZAHER

Submitted to the Office of Graduate and Professional Studies of
Texas A&M University
in partial fulfillment of the requirements for the degree of

MASTER OF SCIENCE

Chair of Committee,	Alan Palazzolo
Co-Chair of Committee,	Shehab Ahmed
Committee Member,	Won-jong Kim
Head of Department,	Andreas A. Polycarpou

August 2014

Major Subject: Mechanical Engineering

Copyright 2014 Omar Mohamed Abdelzaher

ABSTRACT

The work is divided into two parts: The First part discusses and documents simulation investigations on the interactive effect of the different conveyance accessories tools and their designs on the wireline cable tension force, and how it can influence the wireline cable performance especially in open hole logging operations with highly deviated and rugose zones. A computer simulation model was built to predict the cable tension force applied on conveyed wireline string so as to assess and analyze the effect of the different conveyance accessories, such as centralizers, bottom-nose tools, and wireline coating, on wireline penetration rates. A numerical computing approach was then utilized to represent and analyze the simulation studies output results in a friendly graphical form. Improving the wireline logging performance, especially in highly deviated rugose openhole wells, could increase the percentage of successful logging operations, reducing time, cost and improving data quality with the increased wellbore coverage. The second part discusses the possible violent drillstring vibrations encountered during drilling and its effect on the overall rate of penetration and sustainability. This entails a complete identification and modeling of the drillstring dynamics and the sources of vibrations excitation that include stick-slip, bit-bounce, and whirling with its two forward and backward types to better control its functional operation and improve its performance.

A Matlab numerical simulator model based on Finite-Element-Method of 3D-Timoshenko beam elements is developed for this purpose to predict and simulate the rotordynamic behavior of the bottom-hole-assembly (BHA) and the PDC-Drillbit cutting

dynamics. The model also includes the coupling between the torsional and bending vibrations of drillstrings with the nonlinear effects of drillstring/wellbore friction contacts. The work extends previous models of drillstring vibrations in the literature to include the destructive drillstring vibration backward whirling type with Pure rolling behavior and answers some crucial questions: the operation conditions that possibly causes backward whirl vibrations, possible stabilizers' configuration to reduce chance of backward whirl, best stabilizers locations in the BHA to minimize the sever vibration effects on the drillstring, and other arising questions.

DEDICATION

To Parents.

To Wife.

..and Baby Murad.

ACKNOWLEDGEMENTS

I would like to thank my committee chairs, Dr. Palazzolo and Dr. Ahmed for their limitless support and guidance throughout the course of this research. I would also like to thank Dr. Kim for serving on my committee, and giving his insights.

Thanks also go to my friends and colleagues and the department faculty and staff for making my time at Texas A&M University a great experience. I also want to extend my gratitude to the Qatar National Research Fund for funding this research and making this work possible.

Finally, thanks to my mother and father for their encouragement and to my wife Yaman for her patience, altruism, and love.

NOMENCLATURE

A	Cross section area
A_c	Contact area
a	Drillbit Radius
a_r	Radial acceleration
a_t	Translational acceleration
b	Roller-Cone Drillbit Factor
BHA	Bottom-Hole-Assembly
C	Damping Matrix
CG	Center of Gravity
C_T	BHA Torsional Damping-to-Ground
c_1, c_2	Axial Applied Load – ROP Relation Factors
d, d_n	Total Depth of Cut & Depth of Cut/Blade
D	Hysteresis damping coefficient
DP	Formation Differential Pressure
D_i	Inner Pipe Diameter
E	Modulus of elasticity
e	Mass Unbalance eccentricity
el	Elongation coefficient per KN per Km
FEM	Finite Element Model
F_e	mass unbalance centrifugal force

F_f	Friction force
F_i	Total impact forces
F_s	Sticking force
F_T	Wireline Cable tension force
F_r, F_t	Radial & Tangential BHA-Wellbore Contact Forces
F_n	Normal contact force
F_y, F_z	Lateral Forces Due to BHA Mass Unbalance in Y & Z Directions
J	BHA Inertia
K	Stiffness
K_b	Wellbore Contact Stiffness
k_c	Equivalent Rock Formation Stiffness
K_T	BHA Torsional Stiffness-to-ground
L	Length of wireline cable
L_c	Wireline contact length
l	Drillbit Wearflat Length
LWD	Logging While Drilling
M	Mass Matrix
m	Mass
MWD	Measurement While Drilling
NPT	Non-Productive-Time
n	Number of Blades
p	Formation pressure

PDC	Polycrystalline Diamond Compact
R	Rotor radius
r	Radial Displacement of BHA CG
R_c	Radial BHA-Wellbore Clearance
ROP	Rate of Penetration
s, s_0	Formation, Mean Formation Elevation
t	time
T_b	Formation friction torque
T_c, T_f	Cutting, Friction Components of TOB
T_d	Top Drive Torque
TOB	Torque on Bit
t_{pipe}	Pipe Thickness
t_n	Blade Time Delay
V_a	Axial element velocity
V_r	Radial element velocity
V_{rel}	Relative velocity
W	Element weight
W_c, W_f	Cutting, Friction Components of WOB
W_a	Axial component of element weight
W_n	Normal component of element weight
W_o	Axial Applied Load at the Top of the Drill Rig
WOB	Weight on Bit

x_d, y_d, z_d	BHA CG Displacements in X, Y & Z Directions
α	Inclination of WOB with Respect to BHA
ε	Rock Specific Intrinsic Energy
ζ	Drillbit-Formation Interaction Factor
φ	Angular Displacement
μ, μ_0	Drillbit-Formation Stribeck & Mean Contact Friction
μ_w	Wellbore-BHA Mean Contact Friction
υ	Poisson's Ratio
ρ	Material Density
σ	Rock Cutting Stress
Ω	Whirling velocity
ω	angular velocity
ω_d	Top Drive Spin Velocity
Γ	Precession frequency ration

TABLE OF CONTENTS

Page

LIST OF FIGURES

LIST OF TABLES

1. PART ONE: INTRODUCTION TO WIRELINE MECHATRONICS

1.1 Introduction and Problem Identification

During wireline logging there are some challenges that affect the performance of the downhole wireline-string especially when conveying in highly deviated wellbores with rugose openhole zones. These challenges can cause the wireline string to get what called 'get stuck'. 'Stuck wireline' can occur where a combination of wellbore geometry and changes in wellbore direction, together with the wireline bottom-hole assembly stiffness and arrangement of conveyance accessory tools such as centralizers and bottom noses, prevent the wireline string from passing through a section of the wellbore especially in the highly deviated rugose openhole zones. A second major cause that can make the wireline tool-string to get stuck is when the borehole pressure exceeds the formation pressure and a mud cake is formed around the wireline part forcing the wireline to stick to the formation in a condition called differential sticking. Failing to achieve 100% penetration and the tool string got stuck or hanged up somewhere in the borehole can result in costly delays that can directly affect the profit margin for both the operators and service companies that employ the tools. Loss in the measured cable-head tension force of the logged wireline is known to be the main indication of wireline overall logging performance inside the wellbore and whether if it's getting stuck.

A method to simulate and facilitate a visual investigation of the conveying behavior of a downhole wireline-tool assembly and predict numerically the resultant cablehead-tension could help in better understanding the underlying physics and hence identify the best wireline configuration for highest penetration rates in openhole wellbores.

Having a clearer sense of how different wireline conveyance tools affect the logging performance, could lead in a better realization of the best configuration the wireline should have to suite the different wellbore conditions (e.g. Vertical/inclined, cased/openhole, rugose or flat..etc). This may increase in accordance the percentage of the successful logging operations and hence reduce time, cost and improve data quality and increase wellbore coverage.

1.2 Background and Literature Review

In conventional wireline and slick-line operations, a tool string comprising different tools is lowered in a borehole from a wire or cable spooled from a drum located at the surface of the wellbore. It is often necessary to perform wireline or slick-line operations during for example completion, maintenance and servicing, installation and retrieval of downhole apparatus, intervention and well logging. Tool strings are often comprised of electrical devices that collect data from the wellbore such as temperature, salinity etc. of recovered fluids. In addition to deceinding the tool string, the wire cable acts also as a medium to transfer the electric power to the tools to carry out their functions in the wellbore, and sending the electric signals to convey the data gathered by downhole sensors back to the surface.

Tool strings usually operate better in vertical and near vertical wells, however when they are used in deviated wells problems may arise. Formation evaluation in high-deviation wells still encounters challenges because the logs behave differently in highly deviated wells than in vertical wells. As deviation increases to even moderate angles, the resulting frictional resistance between these heavy tools and the wellbore surface can make wireline access difficult or even impossible or as said to be stuck. The term of "Stuck wireline" is applied to situations when the movement of the wireline logging tool assembly is restricted due to downhole events or forces, where the wireline tool string is unable anymore to be lowered or pulled inside or outside the borehole. Stuck wireline causes can be broadly referred whether to 'wellbore geometry' or to 'Differential sticking'.

Differential sticking can occur if a portion of the wireline downhole assembly become embedded in the filter/mud cake (an impermeable film of fine solids) opposite a permeable zone (e.g. sand) and is held in place by the difference between hydrostatic and formation pressure, see Figure 1. The resultant force of the overbalance (differential pressure) acting on the contacted surface area of the wireline is the force that sticks the wireline against the wellbore [1]. This mechanism normally occurs:

1- at stationary or very slow moving wireline assembly (during wireline formation sampling)
2- When contact exists between the wireline string and wellbore formation
3- When an overbalance pressure is present
4- Across a permeable formation
5- In a thick filter/mud cake (high water loss/high solids content).

This mechanism can generate extremely large side forces, such that the logging tools cannot be pulled free unless the pressure seal can be broken in some manner.

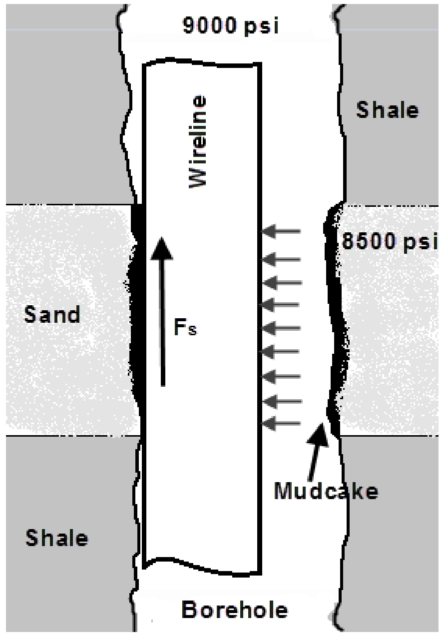

Figure 1 Wireline Sticking due to Differential Pressure

The sidewall forces increase by increasing the wellbore deviation, which results in a greater risk of differential sticking. The filter cake thickness is critical in differential sticking as the thicker it is the bigger the cross sectional area that the formation pressure acts on and hence a higher differential sticking force. Having a lower formation pressure than the wellbore pressure makes the mud filtrate invade the porous and permeable formation until the solids present in the mud clog enough pores to form a mud cake. The thickness of the mud cake depends on the mud properties and the porosity of the formation. The danger of differential sticking is usually in sand, where the formations have high porosity and permeability and therefore a thick mud cake tends to build up and hence the area of contact can be double by the thickening of the filter cake [2].

This mechanism can generate extremely large side forces, such that the logging tools cannot be pulled free unless the pressure seal can be broken in some manner. The force holding the wireline logging tools against the borehole wall can be calculated very quickly. The cablehead-tension force has to be higher than this force to prevent the wireline from being stuck in this location, or an extra pulling force should be applied to free up the wireline from this situation. The equation for determining the sticking force is:

$$F_S = \mu . DP . A_C \tag{1}$$

Where,

F_S: The sticking force (lbs)

DP: The pressure differential between the borehole and the formation (psi)

A_C: The area of contact between the wireline tool and the filter cake (in^2)

μ: The coefficient of friction between the wireline tool and the filtercake (-)

The effective area of contact is the chord length (L_c) of the imbedded portion of the wireline tool multiplied by the thickness of the mud cake (T_{mc}). The friction coefficient factor depends on the formation and the wireline tool material properties. Almost same techniques, for releasing and fishing the differential stuck wireline, are typically used as stuck drill pipe or collar [1, 3]. Other new techniques to reduce or prevent differential sticking are recently proposed [4, 5, and 6].

On the other hand, the second general reason of Wireline sticking due to 'wellbore geometry'; is attributed to bridges/ledges, borehole caving, severe doglegs, key-seating, casing shoe, or borehole washouts. Wireline logging operation in openhole wellbores can become even worse in highly deviated boreholes. Washout enlargement can be caused by excessive bit jet velocity, soft or unconsolidated formations, chemical attack and swelling or weakening of shale as it contacts fresh water. Generally speaking, washouts become more severe with time [7]. Another cause of hole rugosity that causes the geometrical irregularities is the Key-seating, which happens when the wireline cuts a groove into the borehole wall.

This can easily happens in deviated or directional wells where the wireline may exert considerable pressure at the contact point with the borehole, usually on the high side of the hole Key-seating can cause problems since the logging tool diameter is generally much bigger than the groove cut by the wireline [8], and thus can present a serious obstacle to normal ascent out of the hole.

Differential sticking and borehole geometry may raise the risk of the wireline getting stuck. This may cancel the benefits of acquiring log data and lose important well information and incurring the operation cost by running pipe-conveyed logging or some fishing operations. Figure 2 shows a visualization model, based on a caliper data, of a wellbore openhole section with associated rugosity.

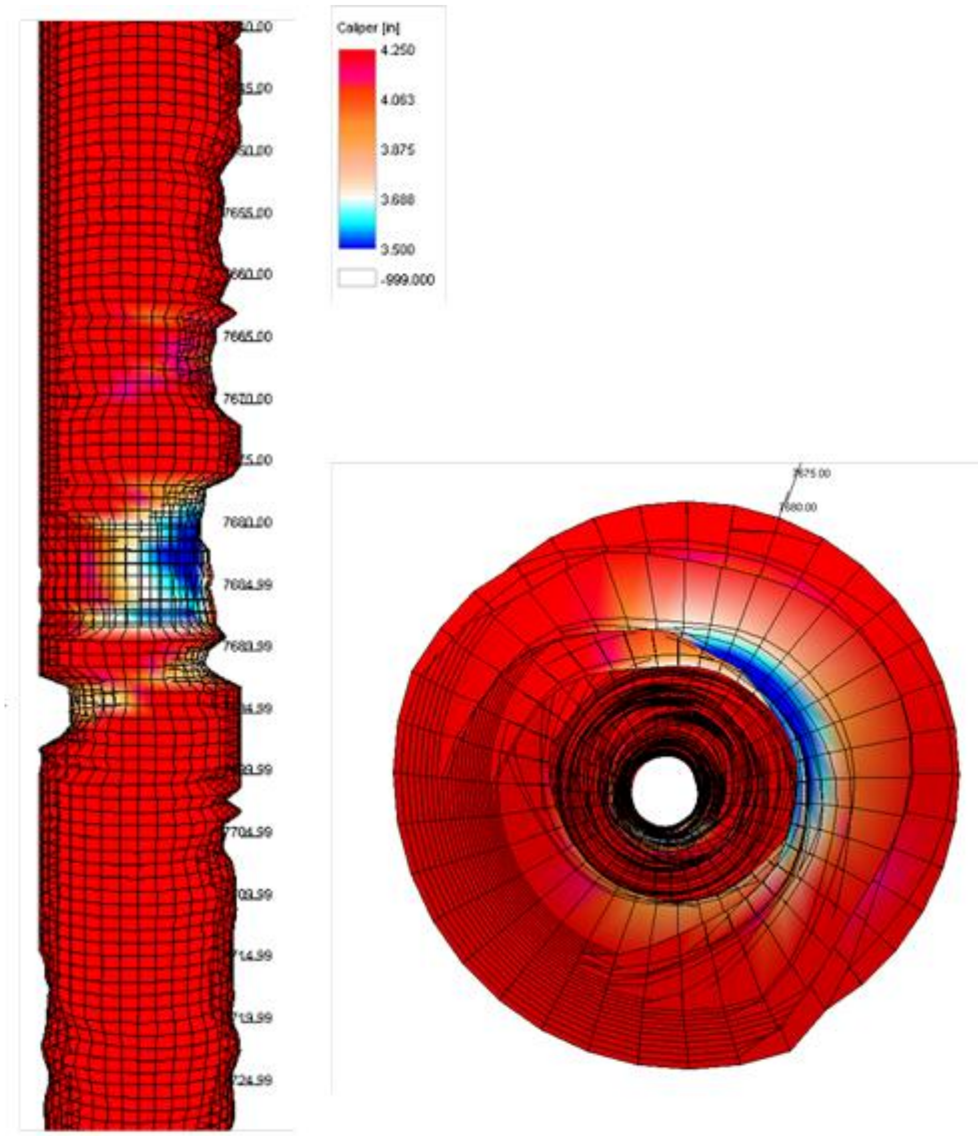

Figure 2 Wellbore with Associated Rugosity

One method that is being conventionally used to reduce the likelihood of differential sticking of wirelines during logging, especially in oilfield operations in deviated wells, is the use of wireline stand-offs (i.e. Centralizers). The wireline stand-off device ameliorates the effects of differential sticking and key-seating of the wireline by eliminating direct contact of the wireline tool or the logging cable with the borehole wall by lifting the tool string away from the side wall of the bore during the logging operation. This is typically achieved by clamping an array of stand-offs onto the outside of the wireline, resulting in lower contact area per unit length of openhole, lower applied pressure of the wireline against the borehole wall, and lower dragging resistance when conveying the wireline in or out the hole. The conventional stand-offs have fluted fins (straight blades) cut along their external body to allow easy movement through mud cake and other debris which usually build up at the borehole wall during drilling operations [9]. Low-friction Teflon stand-off conveyance accessory, typically used by Schlumberger, reduce the frictional drag forces acting on a tool string in a deviated well by effectively reducing the friction coefficient.

More efficient low-friction stand-off products derived from the Free-roller principle have been developed by oil & gas companies to mitigate differential sticking and increase the net pulling-down force while helping the tool string ride over borehole imperfections and debris. The roller stand-offs provide a rolling resistance, rather than sliding resistance, in the downhole environment, which reduces the effective friction coefficient. In addition, the contact area of the roller assembly with the borehole is reduced in comparison with that of the conventional stand-off, which in accordance reduces the differential sticking force and allow the tool string to roll out of the overbalanced permeable formation with minimum wireline over-pull [10, 11].

In addition to conventional stand-offs and other roller stand-off devices, new conveyance methods have been introduced in the oilfield industry attempting to use a more reliable conveyance tools that may help the tool string to achieve more wellbore penetration by giving the tool string's end an additional capability to assist the tools past the breakout zones. These breakouts can form ledges developed at the interface between layers of differing hardness [12], and hence may allow the logging tool to drop out of the path and then lodge into the formation and stop its travel throughout to downhole. These breakout ledges can be approximately described according to the image log of the wellbore as a series of cones spaced along the borehole. When these cones are close together they could support more and guide the logging tool down the hole. The nose of the tool may hence contact the ledges but the contact is at a minimum. In this case the logging tool will hardly fall out the path of the well. However, when these "cones" are spaced far enough apart the logging tool can translate and then impact the ledge. As a result and at the worst case this action can cause the logging tool to hang on the ledge. Therefore, and as an initial idea, a tool with a front rolling nose, low-friction nose surface, or with a free articulating nose could be a good basic solution to let the logging tool roll off the ledges and pass the breakouts with minimum resistance.

A "hole-finder" apparatus incorporating a locally flexible body adapted for attachment to the tool string was introduced commercially to the industry for the purpose to assist the tool string to past the ledges. As the tools string in navigated through the borehole, the flexible body provides local flexibility to lessen the likelihood of jamming the tool string while tripping down the borehole by providing a lateral force at the obstruction [13]. Experience has shown that it only provides a real benefit in deviated holes, as it closely follows the curves of the borehole and guides the tool down [14]. One drawback was recorded that the flexible rubber nose in certain conditions deflects in an improper manner that causes the rubber extension to deform downward instead of moving upward when hitting an acute ledge.

Another passive tool used for the same purpose has had better success with the use of a spherical Teflon bottom nose at the end of the stool string. The bottom nose tool has proven successful in deflecting off obstructions and practically improved the wireline penetration rates compared to the other passive methods conventionally used before.

Another nose-tool design based on the free-rolling concept has been recently commercially released and experimented in high deviated rugose openholes. A single front self-orienting wheel made of steel provides good stand-off from the wellbore's surface reducing the overall frictional drag. The big rolling self-orienting wheel ensures minimum loss of momentum while running in borehole by allowing complete flexibility for tool string integration and optimum positioning [15].

The use of these conveyance accessories can significantly reduce the frictional drag forces acting in a tool string in a deviated well by effectively reducing the momentum loss while negotiating the borehole irregularities and avoiding differential sticking trap. For various reasons some logging attempts, in some challenging wellbores, failed to achieve 100% penetration and the tool string got stuck or hanged up somewhere in the borehole. Insufficient downhole tools design may result in costly delays that can directly affect the profit margin for both the operators and service companies that use these tools.

The present research study employs a physics based computational approach to obtain a better understanding of the wireline logging and its behavior negotiating wellbore geometry, to obtain the highest reliability and operational efficiency, with regards to wireline penetration rate.

Efforts toward achieving the proposed goal involved simulation studies of wireline tool conveyance in a 3D solid wellbore model of 60^0 degrees from vertical inclined with high rugosity section represents a challenging case study.

A wireline model with different conveyance accessories tools were implemented in the wellbore simulator model. The wireline tool model was subjected to descend in the borehole under a constant velocity passing the breakouts interruption in the openhole wellbore model with experimentally measured boundary conditions and gravitational load.

A method to predict the drag forces involved in conveying the tool string into the deviated wellbore model has been presented in order to assess the different factors that directly contributes in the wireline penetration rates, as the cable tension force is the main obvious indication of the wireline behavior inside the wellbore.

Simulation studies results are presented in graphical form, and then discussion and conclusion are provided.

1.3 Objective and Significance

The main objective is focused towards understanding the underlying physics in logging operation, and investigating possible means of improving penetration mainly by studying the behavior of the wireline tool string conveyed inside the wellbore and analyzes the output results of the head tension force graph from the wellbore simulator. This will help identify the major influences on the head-tension force variation and its approximate contribution rate. Having a clearer sense of how different wireline conveyance tools affect the logging performance, could lead in a better realization of the best configuration the wireline should have to suite the different wellbore conditions (e.g. Vertical/inclined, cased/openhole, rugose or flat..etc).

Using conveyance accessories, or Low-friction coefficient wireline tools coating, can significantly reduce the frictional drag forces acting on a tool string in a deviated well by effectively reducing the momentum loss while negotiating the borehole irregularities and avoiding differential sticking trap.

2. DOWNHOLE SIMULATOR MODEL DESCRIPTION

Until recently, a method to accurately visualize the motion of the wireline string inside a wellbore and to clearly understand the behavior of the logging tools negotiating openhole irregularities was not possible. Usually when there is a loss in head tension force and the wireline is said to be get stuck, the operators up-hole use the output readings from the different gauges as well as they analyze the mud circulation formation and pump pressure to identify the cause of wireline stop. Not like differential sticking, which has specific symptoms and therefore a definite solution to prevent wireline from sticking, there are some other factors, or combination of mixed factors, that can hinder the wireline from complete penetration especially in high deviated openholes. These factors unfortunately cannot be accurately defined under the lack of vision inside the borehole.

The wellbore simulator helps to visualize and quantify what happens downhole to every part of the wireline string as the wireline is conveyed in the wellbore. Caliper data from real open-hole well was used to construct a 3D solid model of the wellbore openhole section in this wellbore simulator tool. After studying the rugosity of various real wellbores, a model for a representative 235 ft section long was constructed from a cloud of points in the simulator. A gauge hole section of another 150 ft flat bore section was added on top of this rugose section to help the tool build the needed momentum and allow for the numerical convergence needs of the simulations. This could also considered as a representative to the cased hole section of the borehole. Since the wellbore model should account the hole deviation and rugosity as an ideal case for better understanding the wireline behavior, the wellbore model was built inclined at 60^0 from the vertical, and a gauge hole of 8.5” with a maximum diameter of 24” were applied into the model. A wireline tool string was modelled and mated inside the wellbore computer model having the same weight per unit length and dimensions symmetrically as one of field wireline strings typically used in logging operations with 3-3/8” OD and 110 ft length.

The wellbore simulator also accounted the tool string shape and limberness (taking the material elasticity into consideration). The combination of tool limberness and borehole deviation contributes significantly to the inability of the wireline to penetrate. For example as shown in Fig.3; a sample of 100 feet of a 3-3/8” diameter tool string has approximately a 1 feet drop due to limberness when fixed from one end. The wireline string is connected to a bottom nose tool body via a 3° spherical knuckle joint, and at the end of this tool body is where any nose devices could be attached.

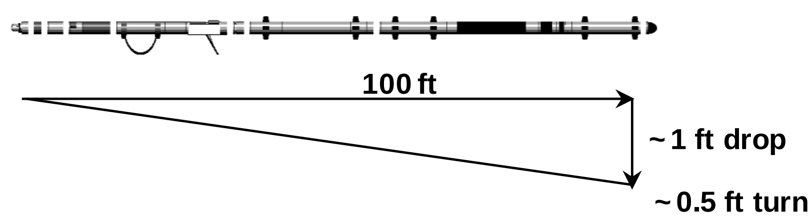

Figure 3 Illustration of Tool String Limberness

The 110 feet modelled wireline has a steel material with a total mass of 2020 lbs, and connected to a steel bottom nose tool with a total length of 20 feet having a total mass of 600 lbs, which is the maximum mass limit the wireline could handle in real life according to the wireline company specifications.

A model of a stand-off device with fluted straight Teflon blades was used to lift up the wireline assembly from the modelled wellbore internal walls so as to reduce friction and, in real life, to mitigate differential sticking. These stand-offs are typically modelled in the simulator having the same size and dimensions as the commercially used ones with the same material properties and same approximate coefficient of friction between the Teflon blade surface and the borehole internal profile (formation) which is 0.08, while a coefficient of friction between the wireline steel bodies and the openhole formation can be chosen to be of average 0.35, 0.4 dynamic and static respectively according to [16, 17]. The exact value depends on fluids in the well and roughness of the wellbore surface. An array of these Teflon centralizers (9 pieces) have been spaced equally and clamped onto the modelled wireline assembly to cover the openhole section being logged to.

After modelling the wireline components and assembling them together including the Teflon centralizers, the complete wireline assembly is inserted inside the inclined wellbore model. Gravity is then defined in the proper direction, and friction coefficients between the different components and the wellbore are defined. The complete wireline assembly is then driven through the wellbore at a constant descending velocity of 8000 ft/hr (133 fpm). This is the average maximum speed typically used and provided by a logging company to descend on the typically used wireline.

According to an actual logging data and as the wellbore begins to deviate, the friction resistance increase causing the wireline string to slow down and loss its forward momentum until it gets to a hold status for a while till it released again and begin moving after the applied force from the logging cable reaches a value that overcomes the static resistance friction force. This phenomenon is known as stick-slip which results in wireline intermittent motion rather than smooth continuous motion during logging operations. Depending on actual downhole conditions, the tool string may come to a hold at deviations as low as 40 degrees resulting in failure to reach target depth. This could be even worse in highly deviated openhole sections with severe irregularities that make the tool string stop in even shallower depths.

Accordingly, the wireline motion behavior inside the borehole and the measured cable head tension during the logging operation can be considered the best indication in representing the overall performance of the wireline tool string and its capability of achieving better penetration rates downhole. To simulate the wireline motion behavior inside the 3D borehole model, a model of the conveyance cable should be attached at the end of the wireline assembly where the cable head tension could be measured. A loss of the measured cable tension force therefore indicates that the wireline string begins to slow down and stop, however a continuous tension indicates that the wireline is conveying without problems towards downhole target zone.

Theoretically speaking, the conveyance cable wire should be modelled by having three equivalent stiffnesses:

- Bending stiffness; which represents the bending and buckling in cable.
- Linear stiffness; which represents the elongation and compression in cable.
- Torsional stiffness; which represents the resistance of cable twisting.

Hence, the conveyance cable could be modelled as a series of springs having stiffness, K, connected between lumped masses, M, whereas each lumped mass represents a knot that could move freely in the three dimensions equivalent to the real cable entity that moves according to the different forces applied (e.g. buckling, torsional, and tension). For sake of simplicity, and since we are not concerned about the behavior of the conveyance cable itself the presence of bending and torsional stiffness are ignored. Only the linear stiffness will be accounted in our simulation studies as it is the only direct contributor in logging tool performance study. Therefore, the conveyance cable model is modelled with only one spring component to be attached at the end of the wireline assembly. The stiffness value of the linear spring used should be estimated to be equivalent to the stiffness of the conveyance cable used in real logging operations. The linear stiffness, K, of the cable-model could be easily computed using the following formula:

$$K = E.A/L \quad \text{(N/m)} \tag{2}$$

Where,

E: Modulus of Elasticity of the cable

A: cross section area of the cable

L: length of the cable

As the logging cables are usually manufactured from different materials (armor, coating, conductor wires, fillings…etc.), it will be hard to directly calculate the overall modulus of elasticity to get the equivalent stiffness. However, the stiffness, K, is estimated from the elongation coefficient parameter described from the cable specifications, where:

$$K = F/el \quad \text{(N/m)} \tag{3}$$

Where,

F: is the applied force (1 kN)

el: elongation coefficient (per KN per Km)

K: linear stiffness (N/m)

The elongation coefficient estimation is based on a number of relationships and equations described in details according to reference [18]. Applying the elongation coefficient value of the cable type used in the upper equation, a certain value of K could hence be obtained. Substituting this obtained value of K, with the cable cross section area, A, and the 1 Km cable length in equation (2) we get the equivalent cable modulus of elasticity, E. Also According to the equation, the cable stiffness K will have different values as cable length, L, change. Therefore, by reaching more depths, the cable stiffness will decrease accordingly. Reaching extended logging depths the wireline will be subjected more to stop and lose more of its inertia due to impacts when logging in irregular openhole zones. Applying different cable stiffnesses corresponding to different logging depths will be taken into consideration in the presented simulation studies as the wireline behavior will definitely change.

As discussed previously, the efforts and the main objective in this paper study is focused towards understanding the underlying physics in logging operation, and investigating possible means of improving penetration mainly by studying the behavior of the wireline tool string conveyed inside the wellbore and analyze the output results of the head tension force graph from the wellbore simulator. This will help identify the major influences on the head-tension force variation and its approximate contribution rate. Having a clearer sense of how different wireline conveyance tools affect the logging performance, could lead in a better realization of the best configuration the wireline should have to suite the different wellbore conditions (e.g. Vertical/inclined, cased/openhole, rugose or flat...etc).

Understanding the underlying physics of the wireline logging, requires analyzing and understanding the different forces acts on the system. A computational simulator is developed for this purpose. Some wellbore parameters in the simulator were assumed constant or neglected in order to isolate and focus on the parameters that directly contribute on the wireline logging performance. The neglected parameters include pressure, temperature, fluid flow forces (fluid lift, fluid shear drag, and fluid form drag), cable weight, buoyancy force, mud & drill cuttings existence...etc. Thus; only mechanical forces will be present during wireline logging that is accounted while performing dynamic motion simulation. These mechanical forces can be simplified and classified under the following forces list:

- The wireline and tool string weight
- Friction force between wireline/tool string elements (steel tools and wireline steel segments, Teflon centralizers, and front nose) and the wellbore
- Tension force applied on the wireline resultant from the conveyance cable in order to maintain a constant wireline descending velocity
- Normal forces produced from externally impacts of the wellbore irregularities on the wireline steel tools and centralizers.

According to the Newton's laws of motion, the calculations are performed by summing the forces along the length of the wireline string at a specific depth in a well, starting from the downhole end of the wireline string and calculating the forces on each segment of the tool string, progressing up till the surface. The calculation is explained by using a simple wireline segment located in a straight, inclined section of a well without fluids or pressures as shown in Figure 4.

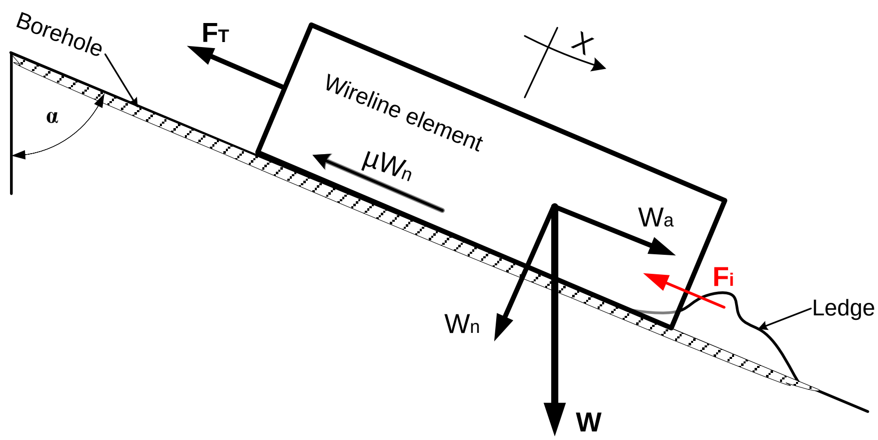

Figure 4 Wireline Mechanical Forces in an Inclined Section of Wellbore

The force-equilibrium analysis of the logging wireline element in a wellbore, assuming steady state conditions, shows the different mechanical forces applied on the wireline element during the logging operation. The element weight, W, is divided into two component forces. W_a is the force component in the axial direction along the axis of the wellbore, while, W_n, is the force component in the normal direction (normal to the axis of the wellbore). These forces components could be calculated using the following equations:

$$W_a = W.\cos\alpha \quad \text{(N)} \tag{4}$$

$$W_n = W.\sin\alpha \quad \text{(N)} \tag{5}$$

The friction force, F_f, is calculated by multiplying the normal weight component by the friction coefficient, μ.

$F_f = \mu . W_n$ (N) (6)

In our study, the friction coefficient, μ, will have two values depending on which wireline element is in contact with the wellbore wall, whether it is the Teflon centralizers or the steel tool segments. Also since the wellbore has an irregular profile, then the normal forces, W_n, due to the contact with the different wireline elements (whether the centralizers or the steel tools) will have different directions not necessarily perpendicular to the wellbore axis and therefore a variable friction force, F_f, will generated at each wireline increment. The friction coefficient force, F_f, sign depends on the wireline direction of motion whether it is RIH or POOH.

In addition to these body forces, there is impact force, F_i, which acts on the wireline nose due to impact with the wellbore ledges. These impact forces are applied discontinuously over a short time period on the wireline nose and may have high magnitudes due to the momentum change of the wireline which depends on its overall mass and velocity. This force only appears while conveying the wireline downhole in rugose openhole zones, and is widely believed to be the main cause of the loss of the wireline momentum, ultimately causing the wireline to stop. This view will be discussed and countered in the next section.

The impact forces, F_i, could be calculated according to the following formula according to [19]:

$F_i = K . \delta^n + D . \delta'$ (N) (7)

Where,

K: is the approximate stiffness between the part and the wellbore formation

δ: Relative penetration depth value of one geometry into another

n: A positive real variable that specifies the exponent of the force deformation characteristic.

δ': relative impact velocity at contact point

D: hysteresis damping coefficient

The first term of the impact force equation represents the elastic force, and the second term accounts for the energy dissipation. Summing the axial components of these forces applied on all wireline elements results in the equivalent tension force, F_T, applied on the conveyance cable, which will be shown later in the next section how it reflects the overall performance of the wireline during logging operation.

$$F_T = W_a - F_i \pm F_f \quad \text{(N)} \tag{8}$$

If there is a rotational motion resulted during the wireline logging, a different friction force component will be computed in the axial direction since the resultant velocity vector, V_T, of a rotational wireline element will generated from the sum of the axial element velocity, Va, and the rotation velocity, Vr, as shown in Figure 5. The actual friction force should be in the direction opposite to V_T, and hence should be break down into two components; one in the axial direction and the other in the rotational direction based on angle between V_T and Va, β.

$$F_f = \mu . W_n \cos\beta \quad \text{(N)} \tag{9}$$

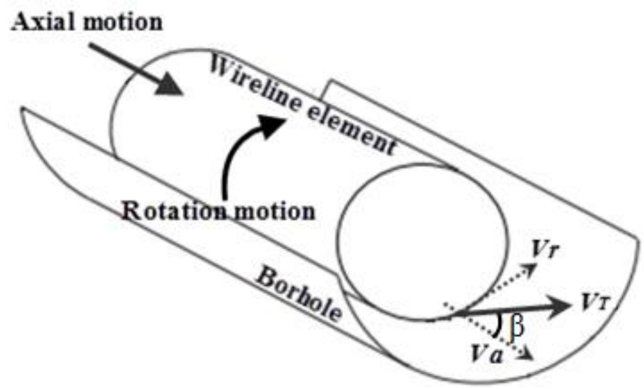

Figure 5 Wireline Element Axial and Rotational Motion

The overall performance of the conveyance wireline could be easily predicted and calculated for cased hole logging. Severe irregular profiles in highly deviated wells add considerable complexity to system logging in openhole boreholes and complicate, in accordance, the performance prediction and calculation of different forces acting on the wireline tools. Choosing the right wireline conveyance tools in terms of type and design, according to the intended wellbore condition, will be kind of venture.

As the cable tension force is the main indicator of the wireline behavior inside a wellbore. A computer simulator capability was developed for that purpose to predict and estimate the cable forces applied on the wireline strings conveyed in highly deviated wellbores with rugose openhole sections. This was done to assess different design factors that may directly contribute in the wireline penetration rates and performance.

The wellbore simulator was developed using the COSMOS-Motion computer software tool which is for simulating mechanism motions [20]. The wellbore simulator using COSMOS-Motion employs simulation engine, ADAMS/Solver, to solve the equation of motion of the modelled wireline assembly being conveyed inside the static wellbore, and calculates the position, velocity, acceleration, and reaction forces acting on each element in the wireline tool string assembly. The wellbore simulator utilizes a multiple inputs to calculate the total downhole forces acting on each individual wireline element to predict the measured cablehead tension reading acting on the tested wireline. The wellbore simulator requires several inputs, such as:

- Good 3D structural resolution of the tested wellbore model.
- Accurate data for the tested wireline tool-string assembly (size, dimensions, materials, weight per length).
- Accurate friction coefficient values between wireline assembly elements and wellbore formation.
- Accurate mechanical properties (e.g. elasticity and density) of the wireline assembly elements (steel parts, Teflon parts...etc.), as well as the wellbore model.
- Accounting limberness and flexibility of the wireline parts in the simulator model.
- Applying gravity.
- Good contacts and joints definition between the interacted parts.
- Accurate contact properties defined between the collide parts (contact stiffness, exponent, max. damping coefficient, max. penetration values).

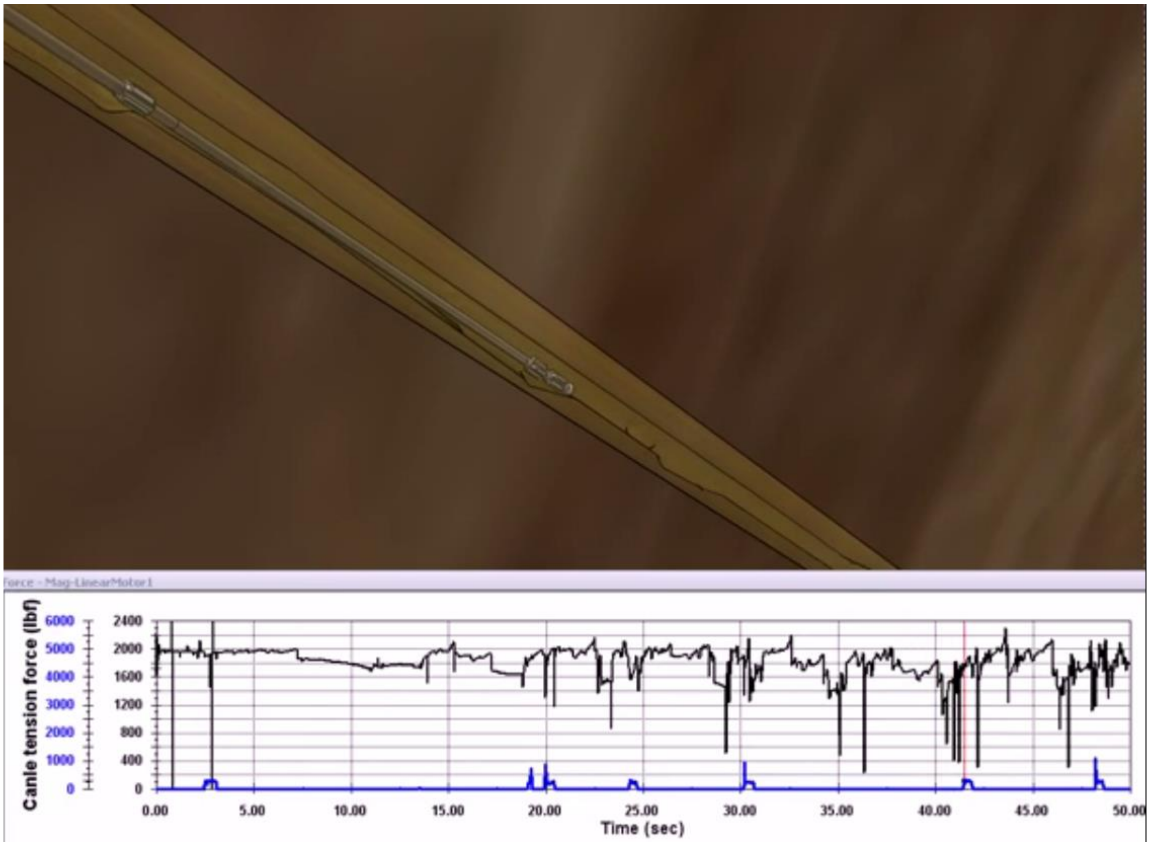

Figure 6 Simulator Snapshot Indicating the Measured Cable Tension Force

Figure 6 shows a snapshot from the simulator built in Solidworks/COSMOS-motion showing the wireline-string logged inside the wellbore model with irregularities, and indicating the wireline measured cable tension force (Black plot), as well as the measured impact forces on the bottom nose (Blue plot).

2.1 Simulation Studies

The wireline assembly model is composed of a set of steel tools having a 3-3/8" OD resulting in a combined tool string length of 110 ft and 2020 lbs of tool weight connected to an additional 20 ft bottom-nose steel tool with a 600 lbs total mass. The simulator calculates the output cablehead tension force by solving the equation of motion of each wireline element in X, Y, and Z coordinates as the wireline descends. The generated cablehead tension output curve from the simulator represents the resultant cumulative drag forces along the length of the wireline for a given depth. This can be compared with measured wireline forces at the surface. The simulation ran until the tool assembly successfully reaches the bottom of the hole, after which results are then obtained and studied. Figure 7 shows a sample of actual cablehead-tension force versus descent depth data obtained from a successful 3-3/8" wireline tool-string run in a calcium carbonate openhole wellbore in the Arabian Gulf area.

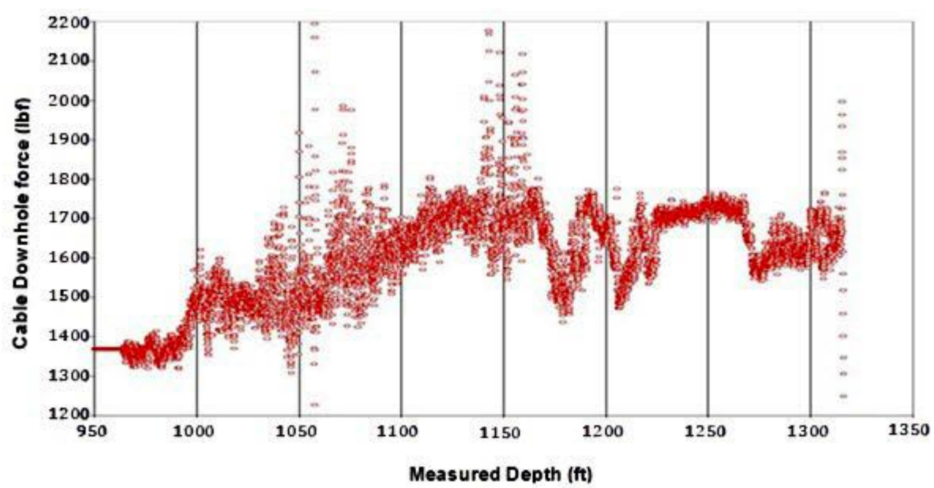

Figure 7 Sample Actual Wireline Cablehead-Tension Data versus Logging Depth

The fluctuating of the cablehead-tension force reading, represented in the plot's dips and peaks, reflects the encountered different resistance forces of due to the openhole borehole nature. Similar outputs will be produced by the simulator tool under the different studies. These simulation studies can be listed as follows:

1. Effect of Differential Sticking
2. Effect of Standoffs Design
3. Effect of Wireline Low-Friction Coating
4. Effect of Passive Bottom-Hole Nose Design

3. DOWNHOLE SIMULATOR RESULTS AND DISCUSSIONS

Various configurations were simulated with the wireline tool string assembly – wellbore traversal code to better understand the wireline behavior, and to identify the best wireline configuration for highest penetration rates in openhole wellbores with highly deviated and rugose sections. These simulation studies also revealed the contribution of each wireline component on the overall wireline performance.

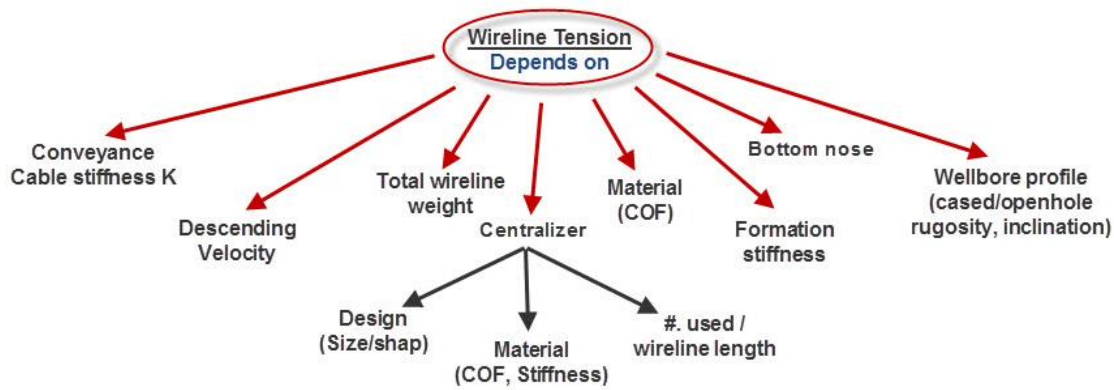

Figure 8 Factors Affect Wireline Cablehead Tension Reading

Figure 8 summarizes the different factors that might affect the wireline cable tension reading during the logging operation. (Excluding factors like: Temperature, pressure, mud weight, fluid drag force). These factors have a contribution in the resultant mechanical forces that acts on the wireline assembly body and hence affects the cablehead tension force reading Series of designed simulation studies were configured to achieve the targeted objective. The effects of the following variables on wireline performance were studied:

1. Centralizer Designs

2. Wireline Low-Friction Coefficient Coating

3. Passive Bottom-Hole Nose Design Concepts

The wireline model assembly used in all simulation studies has as prescribed a 3-3/8” OD with a total length of 130 ft steel parts and weighs about 2700 lbs (including the 20ft/600lbs bottom steel tool). The wireline tool string used in simulations is in size, dimensions, and weight as one of field wireline strings typically used in logging operations. Different stand-off designs and bottom-hole noses are used in some simulation studies. A cable-like model with varying stiffness feature is attached to the wireline tool-string upper end. The inclination of the 235ft wellbore model is fixed in all simulation studies to be 60 degrees relative to vertical. The extended upper 150ft flat section of the wellbore model is used to facilitate the validation of the simulation results with the calculated results before running in the irregular section. The applied friction coefficient of any steel parts with the wellbore formation was 0.35 dynamic, and 0.4 static. The friction coefficient between any Teflon model parts and the wellbore formation is selected to be 0.05 dynamic, and 0.08 static. An actuator with a constant descending linear velocity of 8000 fph (133 fpm) is applied on the upper end of the cable-like model in all studies. A total Simulation time of 145 seconds is fixed in all studies.

3.1 Effect of Differential Sticking on Wireline Performance

As a reference guide, the wireline assembly model was first logged in the wellbore simulator without stand-offs or any conveyance accessories attached to its body. This aided in isolating the parameters under investigation from affecting the cablehead tension force readings, and hence to provide a benchmark for comparing results for models which included the effects. This also considered to be the worst case where the bared wireline tool-string will have a direct contact with the borehole formation with the steel's high coefficient of friction of 0.4/0.35 static and dynamic respectively. The best case considered when if the whole wireline body is coated by a low-friction material having a COF of 0.08/0.1 dynamic and static respectively without attaching any centralizers or special noses that could affect the head-tension with drops due to impact forces. Figure 9 shows the simulation results of the cablehead-tension force of the bared wireline tool when decent at depth equivalent to 5000 ft (logging Cable stiffness K=4.8 N/mm).

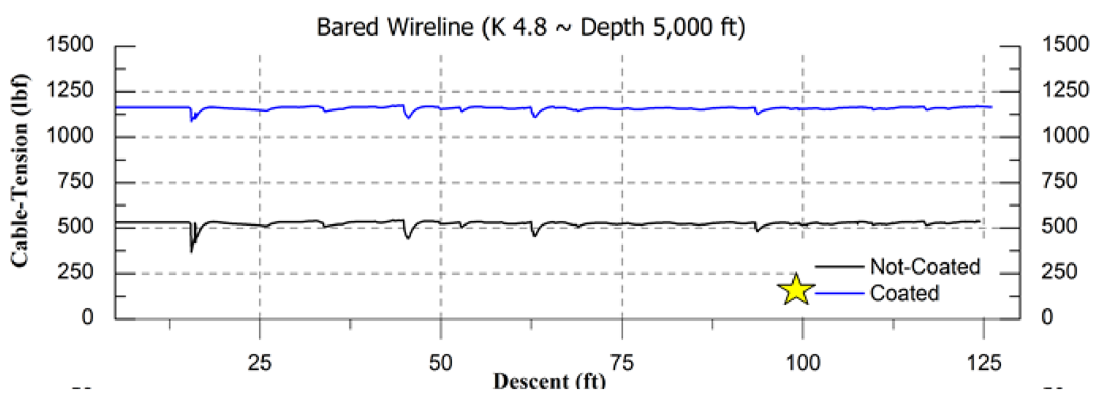

Figure 9 Simulator Cablehead Tension of Bared Wireline (Coated Vs. Not-Coated)

The cablehead-tension force readings show values identical to the hand calculated ones according to the body force analysis. According to the simulation resultant plot, the following points could be concluded:

- It is obvious that the coated wireline has a better performance with a higher cable-tension force plot than the bared steel wireline with higher COF.

- The small notches (dips) in the curve reading are due to the wireline nose impacts during logging, since there are no centralizers or any other accessories attached to the wireline body having a projection area or protrusions.
- The Blue curve (Coated wireline) shows better penetration rate than the Black curve (Not-coated one) at the same simulation time period.
- The wireline assembly that will have the best conveyance accessories arrangement (e.g. centralizers, bottom noses, coating material) will considered to have the best configuration, when its cablehead-tension curve is more flattened and have higher average cablehead-tension force reading.

Although the results seem to be good especially with the coated wireline assembly with its flattened cablehead-tension force curve, however this configuration is practically prevented due to the differential sticking concerns. As prescribed previously the resultant sticking force due to differential pressure could be massive. Referring to equation (1), the friction coefficient factor depends on the formation and the wireline tool surface. It can vary from 0.2 and 0.5. As realization how huge the sticking force the wireline might face, consider the friction coefficient to have a value of 0.4 in case of uncoated steel wireline tool, and 0.1 in case of coated wireline.

For simplification purpose, consider the mudcake thickness is (8mm) which makes (1/4) of the wireline tool circumference will be embedded in the mud cake as the tool cross-section dashed lines shows in Figure 10.

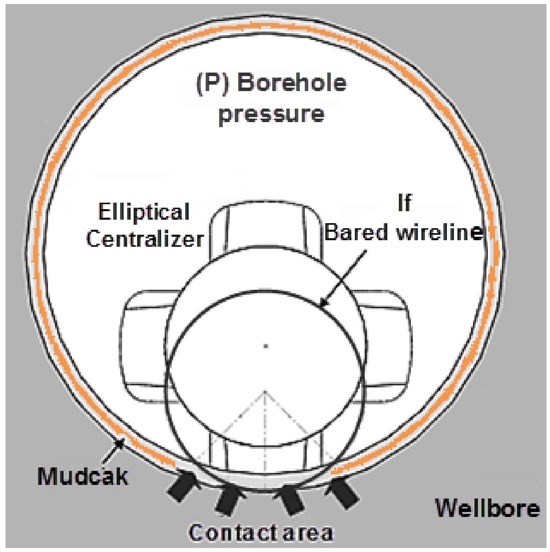

Figure 10 Mudcake Contact Area with Tool and Centralizer

As in our simulations we use a 3-3/8th OD wireline tool string, the sticking force could be therefore calculated in terms of the differential pressure (DP) and the subjected wireline contact length (L_C) as follows:

$$F_S(uncoated) = 0.4.\pi.3.375".\frac{1}{4}.(L_C.DP) = 1.06(L_C.DP) \quad (10)$$

$$F_S(coated) = 0.1.\pi.3.375".\frac{1}{4}.(L_C.DP) = 0.265(L_C.DP) \quad (11)$$

Figures 11 & 12 show the estimated sticking force in (lbs) of uncoated & coated wireline tool assembly under different differential pressures and contact lengths with the mud cake. Apparently the resultant differential sticking force is HUGE whether the tool is coated or uncoated. By referring to Figure 8 for the simulated cablehead tension forces for bared wireline tool assembly (having no centralizers), almost any condition of DP or L_C will definitely make the wireline string to get stuck. Increased contact area can significantly increase the differential sticking force.

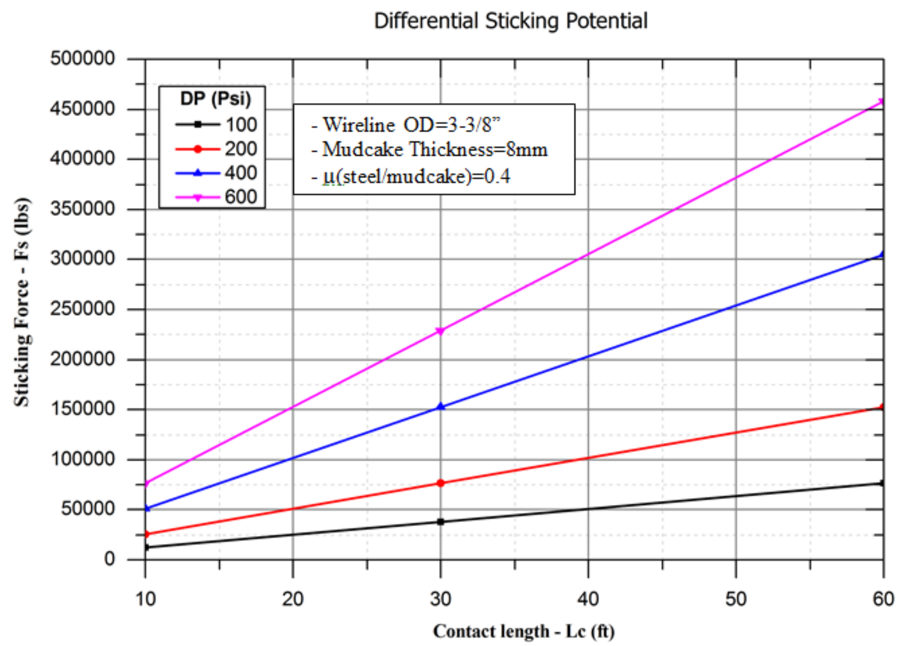

Figure 11 Sticking Force of Uncoated Steel Wireline Tool Assembly

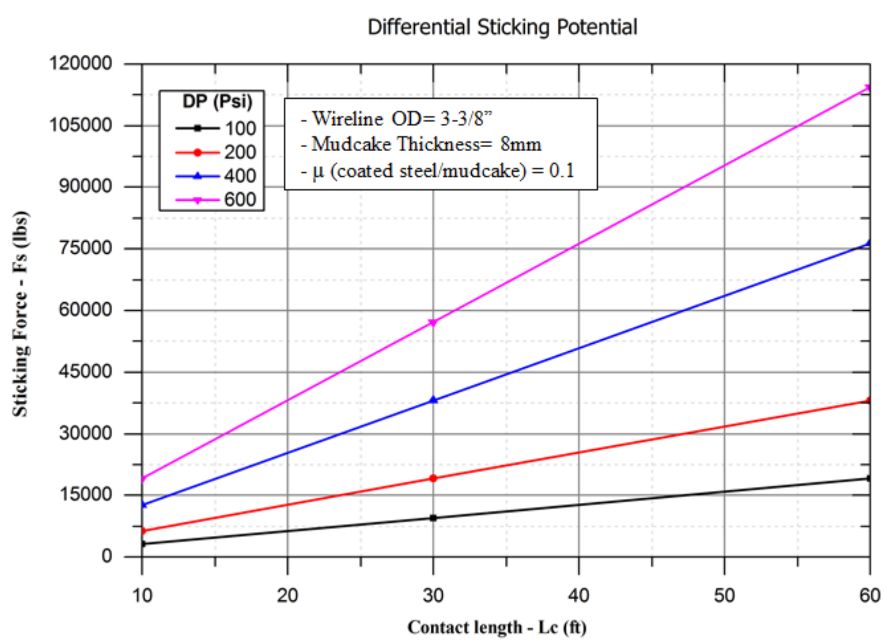

Figure 12 Sticking Force of Coated Steel Wireline Tool Assembly

On the other hand and by using centralizers, to left the wireline tool off from the borehole formation and the built-up mudcake in permeable zones, the generated sticking force in this case is dramatically reduced whether the centralizers are having a low-coefficient of friction or not as the contact area comparatively is very small. Figure 10 and Figure 13 show how the contact area between the Mudcake & the Centralizer is very limited comparing when using a bared wireline tool embedded in the same mudcake thickness (8mm). Figure 10 shows how using a fluted centralizers reduces the overall contact area as the circumference contact is reduced. Figure 13 shows how the contact length is reduced as well, according to the centralizer's length instead of having the full length of the mudcake contacted by the bared wireline's length.

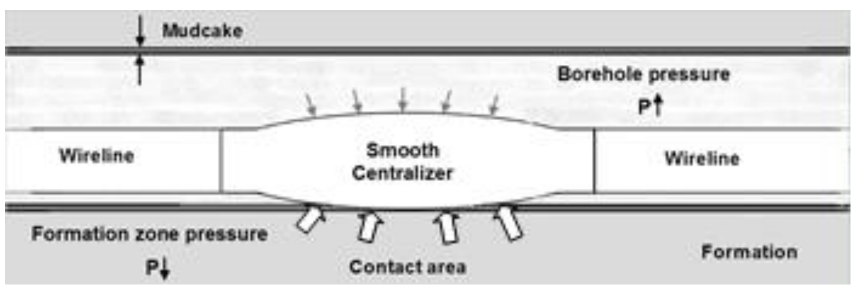

Figure 13 Mudcake Contact Area with Centralizer

Figures 14 & 15 show the resultant sticking force of steel & Teflon 0.75" centralizers respectively. The results shows that the sticking force using centralizers could varies between tens and a maximum of several hundred sticking force depending on how many centralizers will be contact simultaneously with the mudcake zone and the mudcake thickness, comparing to tens-to-hundreds of thousands of differential sticking force when using a bared wireline tool in contact.

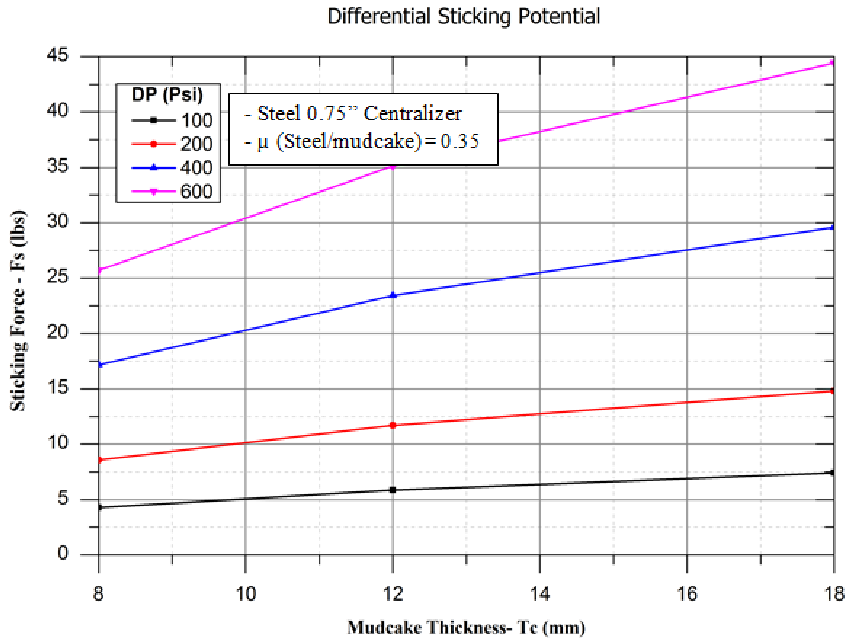

Figure 14 Sticking Force of Steel 0.75" Centralizer

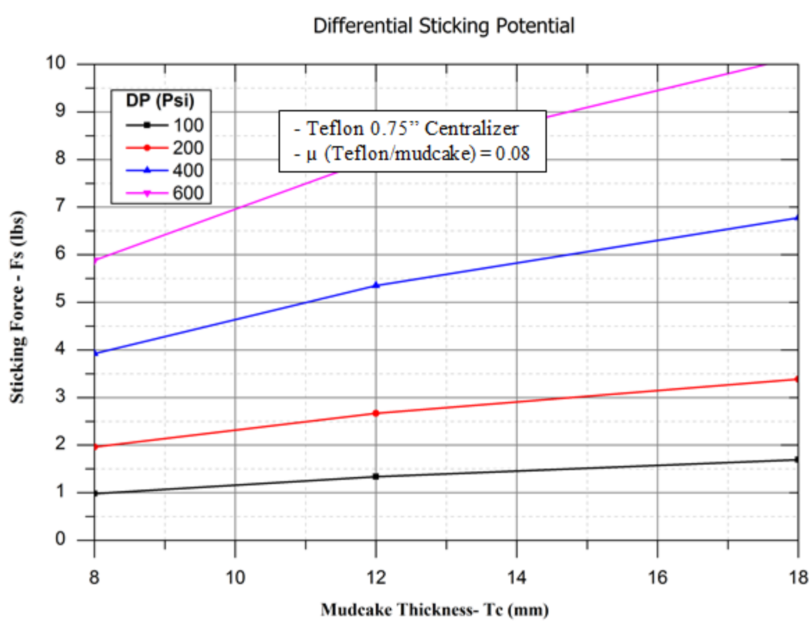

Figure 15 Sticking Force of Teflon 0.75" Centralizer

As a conclusion; centralizers are required in openhole logging especially when there is a chance of mud cake presence in the borehole.

3.2 Effect of Standoff (centralizer) Design on Wireline Performance

Centralizers are used to mitigate the effect of differential sticking by lifting the wireline assembly from the borehole wall. Wireline logging involves a risk of sticking, in either of two ways. Either the wireline tool will stick and the logging cable in the hole remains free, or the wireline tool remains free while the logging cable itself get stuck above to the wellbore wall [21]. Another purpose for the centralizers is to ensure that the tool string is in centralized position especially in highly deviated wells.

Figure 16 Reduced Contact Area Teflon Centralizers

Certain centralizers designs widely used in oil field offer the opportunity to reduce mechanical friction drag in high angle wells and therefore increase the wireline average cablehead-tension force. For example, roller centralizers provide typical friction factor reductions of between 50% and 70% in cased wells [9]. Use of materials such as Teflon integrated with solid centralizers and also some other composites have shown noticeable reduction in casing running drag. However, their performance in openhole is less certain especially in openholes with severe rugosity. Their shape and size, whether of the roller centralizers or the solid fluted ones, plays an important role in their effectiveness. In order to understand the effectiveness of such devices, it is important to study different designs and shapes of and their effect on the main performance metric: cablehead-tension force. Figure 16 shows two different centralizers' shape design used in our simulations studies, one with conventional straight fluted blades, and other with elliptical smooth fluted profile.

The aim of this study is to test the effect of the centralizers design in terms of standoff distance and profile shape on the cablehead tension force reading. Four low-friction Teflon centralizer designs (COF=0.08/0.05 static & dynamic respectively) have been investigated first in the wellbore simulator:

1. Conventional Shape Centralizer with 1.5" Stand-off Distance
2. Conventional Shape Centralizer with 0.75" Stand-off Distance
3. Smooth Shape Profile Centralizer with 1.5" Stand-off Distance
4. Smooth Shape Profile Centralizer with 0.75" Stand-off Distance

Simulation runs were performed using the same prescribed wireline assembly model. The simulation runs were repeated under different logging depths to be sure that the same behavior trend will be obtained for the different centralizer's designs. Figures 17 to 19 show the simulation results obtained of the four Teflon centralizers' designs under different logging depths.

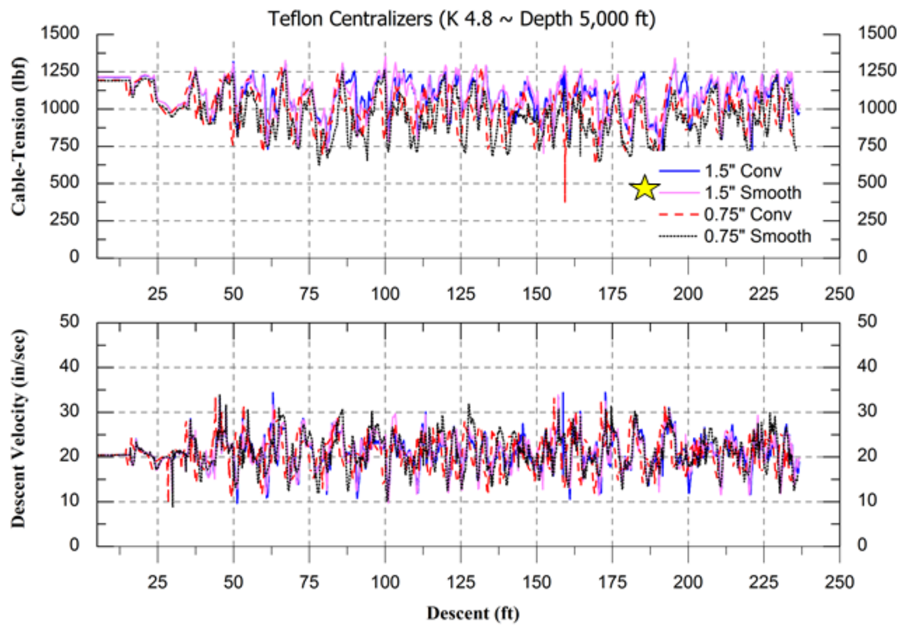

Figure 17 Teflon Centralizers Designs @ 5,000 ft Depth

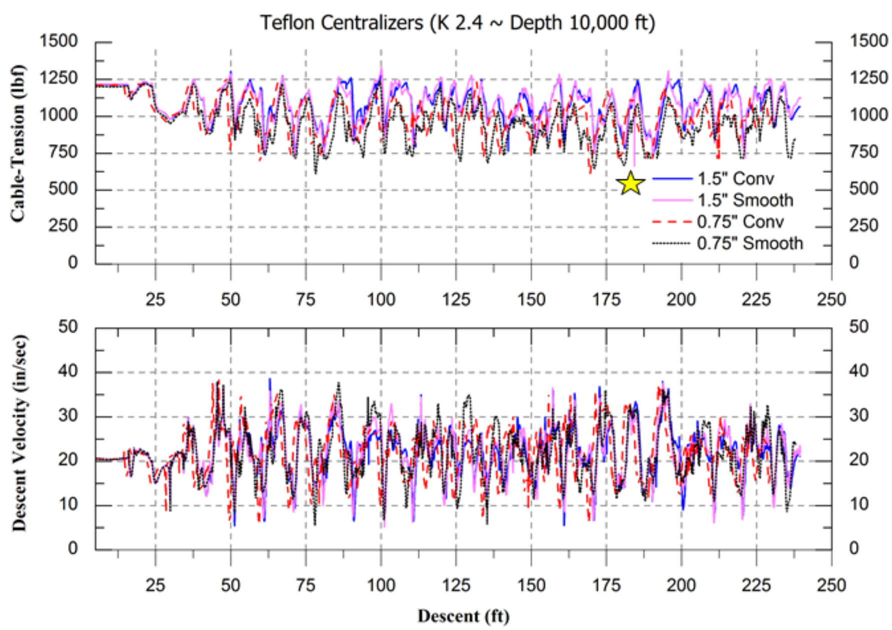

Figure 18 Teflon Centralizers Designs @ 10,000 ft Depth

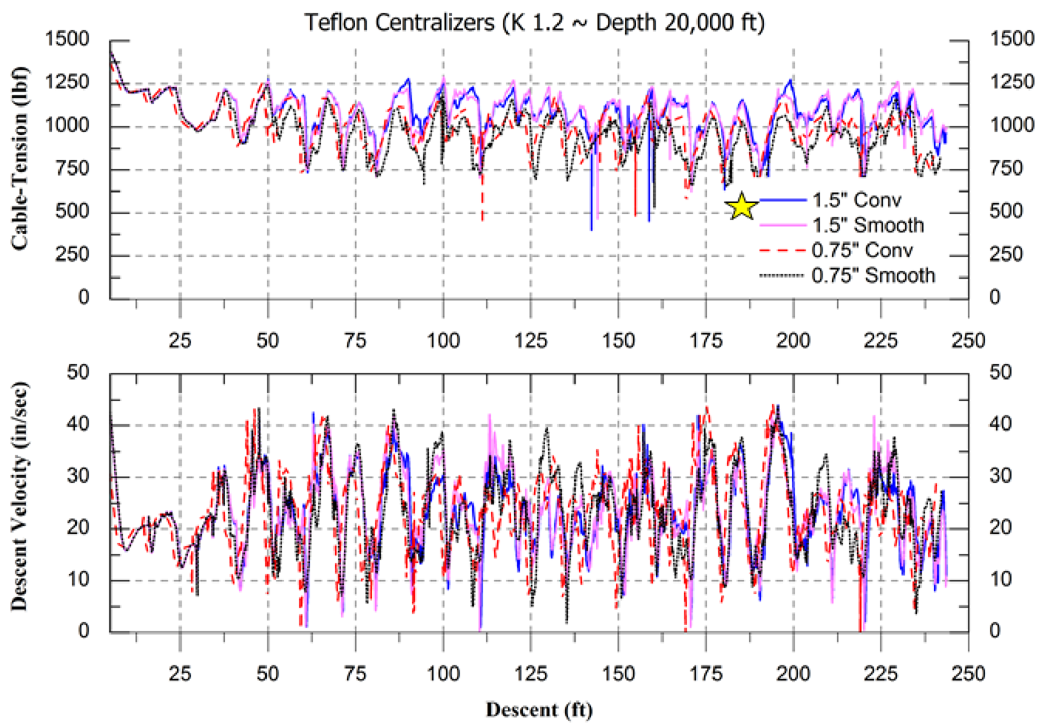

Figure 19 Teflon Centralizers Designs @ 20,000 ft Depth

By analyzing the output results, the following behavior points could be concluded:

- The plots show a significant improve in the wireline string overall performance indicated by the rise of the average cablehead tension readings from 550 lbf (in case of bared steel wireline) to about 1000 lbf when using low friction centralizers onto the wireline string (compare Figure 9 with Figure 17). The percentage of improvement depends on the friction coefficient value of the installed centralizers.
- The upper cablehead-tension limit, and the most optimum reading is considered when the wireline is conveyed and logged inside a flat/-or cased wellbore, where the wireline will always be left on the Teflon centralizers with its low-COF. This

upper limit appears in the first 10 ft of the simulation results having a value of 1250 lbf when the wireline is still in the flat section of the wellbore model.

- The multiple dips, in the cablehead-tension curves and the wireline velocity curves, appeared as the wireline is being logged in the openhole rugose zone. These dips are mainly due to centralizers impacts, between ledges and stand-offs' projection, not the nose impacts (compare Figure 9 with Figure 17).
- These impact forces work against the wireline dragging force until the applied force on the conveyance cable builds up and overcomes the resistive force, resulting in a recovery in wireline descent velocity and cable tension force.
- Generally the three graphs show that the shape factor in the centralizer design does not have a significant contribution on the wireline performance, since the difference between the projections areas subjected to impacts of the two centralizers' shape are very small. From the graphs, the plots of the 1.5" conventional centralizer & the 1.5" smooth one are almost identical, just as the 0.75" conventional & smooth centralizers.
- The stand-off distance factor in centralizer design, on the other hand, appears to have more contribution on the cablehead tension reading. In case of logging in openhole zones, the 1.5" standoff centralizers have higher average tension readings than the 0.75" centralizers. The plots shows an average overall cable-tension drop in the 1.5" centralizers of 150 lbf (i.e. 1250-1100=150 lbf), while for the 0.75" centralizers the overall drop reached (1250-900=350 lbf). That could be explained that by using centralizers with small standoff distance (0.75"), more area of the

wireline body will be subjected in contact and friction with the borehole wall, unlike when using bigger standoffs (1.5”) where the wireline will be more lifted and hence less likely to contact while logging.

- Increasing logging depths (or decreasing cable stiffness K), result in more fluctuations in the cable-tension force and wireline velocity plots. By comparing the three figures (Figure 17 to Figure 19), we will see higher intense of fluctuations with maximum dips values at higher logging depths (or with lower cable stiffness values). For example in the K=1.2 N/mm ~ 20,000 ft depth (Figure 19), there is more dips values lower than 600 lbf compared to at K=4.8 N/mm~5,000 ft depth (Figure 17). Also in Figure 18, the velocities are reaching more to the zero value than in Figure 17 which didn’t exceed the 10 in/sec value. That explains why when reaching higher logging depths the wireline is subjected more to stop and lose of its momentum due to impacts when logging in rugose openhole zones. Also, stiffer conveyance cables are more recommended than cables with low stiffnesses.

As a final conclusion from the previous simulation results, the centralizer shape factor doesn’t have an obvious contribution on the wireline cablehead-tension performance as the results show the mean cablehead-tension force value and the Minimum cablehead-tension force value of the Conventional shape Teflon centralizer versus the smooth elliptical shape of Teflon centralizers when comparing at same stand-off distance, see Figure 27 (Blue section). However, and from the differential sticking prospect, using centralizers with smoother profiles (e.g. elliptical) could help in eliminating differential sticking as the area of contact with mudcake will be minimum comparing to the conventional straight fluted centralizers or spring centralizers. As previously illustrated, even the very small contact area (AC) could result in high sticking force when multiplied by the pressure differential (PD). Roller steel centralizers is much likely to give better results when conveying in borehole since rolling resistance is lower than dragging resistance (as in the conventional centralizers case), where the contact will be only in a point. In addition, dragging will subject the centralizers' surface to wear.

Higher stand-off distance, in case of low-friction or roller centralizers, contributes directly to a better wireline logging performance in openhole rugose zones. Refer to the summary simulation results in Figure 27 and compare the mean force values and the minimum tension force values of the obtained simulation results of the Teflon centralizers study in the 'Blue section' using the 1.5" and 0.75" as stand-off distances.

The maximum allowable external diameter of the centralizer used is generally governed by the borehole minimum internal diameter, and fishing tools constraints. While the minimum stand-off distance is governed by the minimum allowable distance that could prevents differential sticking caused by wellbore overbalance pressure and mud cake thickness. The spacing between the centralizers depends on the nature for the particular borehole being logged. The higher the borehole severity, the shorter spacing is recommended between installed wireline centralizers.

The previous section discussed the effect using low-friction centralizers, and how the different design factors contributed to the overall wireline performance. As the shape factor appears to not have a direct contribution on the cable-tension force, Figure 20 shows the simulation results of wireline having steel centralizers (COF=0.4/0.35 static & dynamic respectively) with different stand-offs.

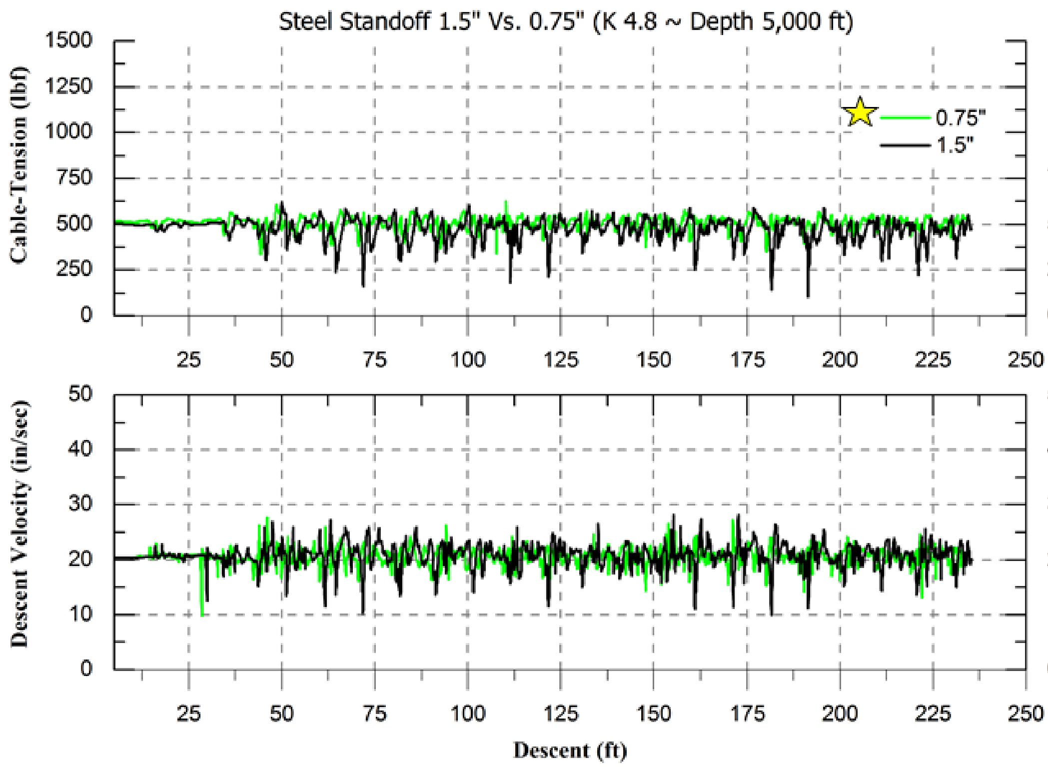

Figure 20 Uncoated Wireline with Steel Centralizers having Different Standoffs

The results in Figure 20 compared to the bared uncoated wireline plot in Figure 9 shows generally a worse overall wireline performance by using steel centralizers. The effect of centralizers impacts, represented in the plot dips, could lead the wireline string to lose inertia and stop especially when using higher stand-offs. The results could be even worse at higher depths and using logging cables with low stiffness as it appears in the obtained simulation results in Figure 21 where a wireline tool having a 1.5” steel centralizers were logged at depth of 20,000 ft. The plot revealed a coincide trend between dropping in the cablehead-tension force readings and the deceleration descending of the wireline tool. From the graph the wireline is appeared to be halted at location 181 descent feet until the applied force is build up, and the wireline recovers its inertia.

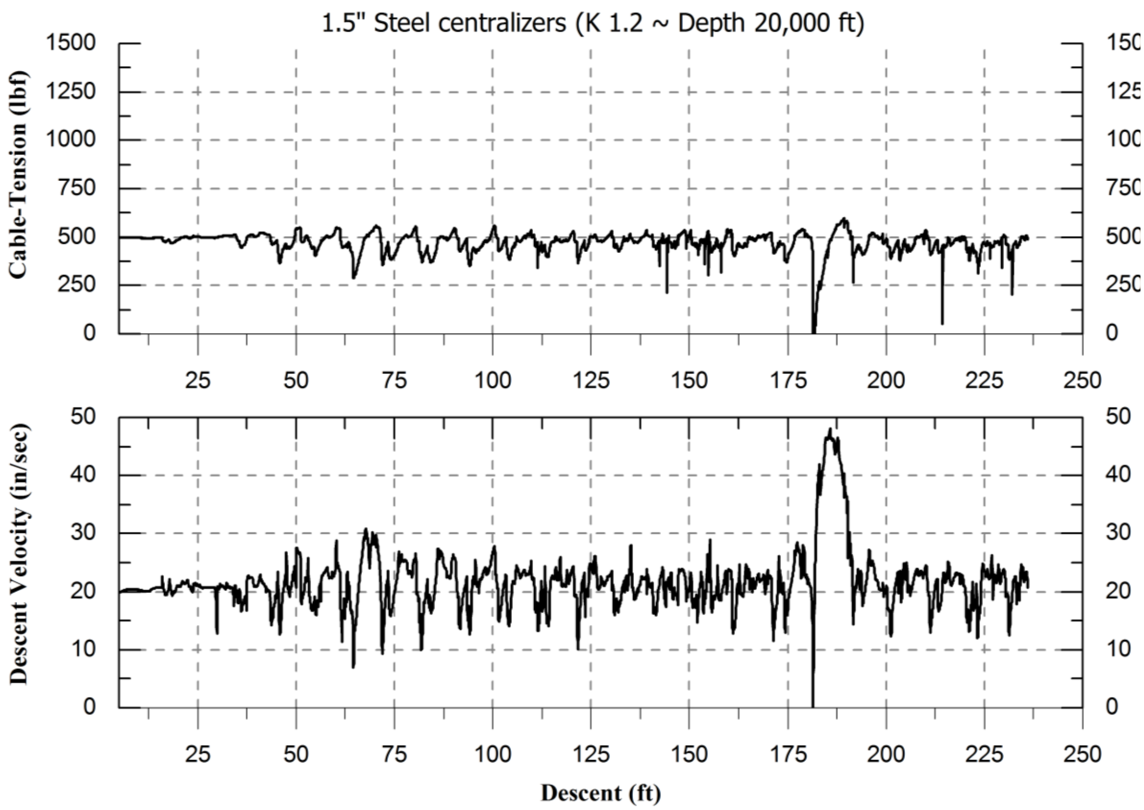

Figure 21 1.5” Steel Centralizer at High Depths

This study is summarized in Figure 27 in the ‘Steel centralizers’ violet section, where using a steel centralizers leads to a worse overall wireline performance compared to the rest of wireline configurations.

3.3 Effect of Wireline Low-Friction Coating on Wireline Performance

As friction is the enemy of conveyance, this study tests the effect of using low-friction coating material with wireline having Teflon centralizers and steel centralizers. The wireline is considered to be coated with a material having COF of 0.08/0.1 dynamic and static respectively. In this case, lower standoff centralizers are recommended, to have the minimal affect due to impacts since the wireline is already coated and no need to lift highly the wireline to prevent contact. Figure 22 shows the simulation results obtained when 0.75” steel and Teflon centralizers are used with the coated wireline.

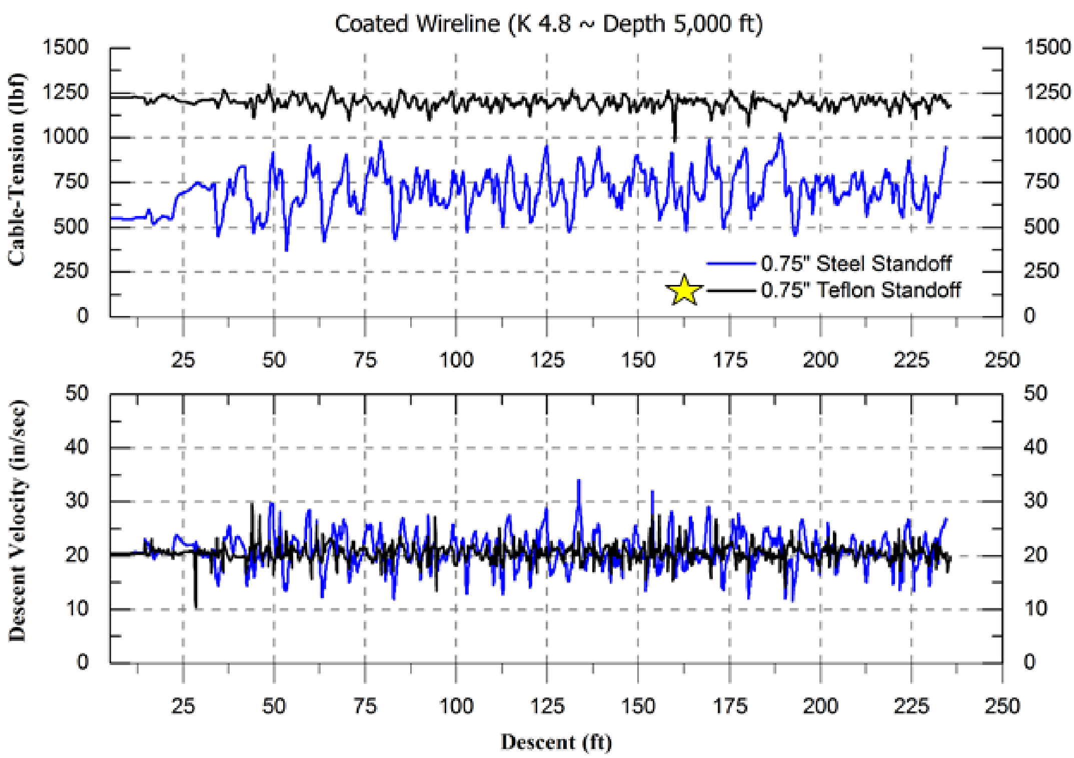

Figure 22 Steel Vs. Teflon Centralizers with Coated Wireline

By analyzing the plots, the following points could be concluded:

- Using low-friction (Teflon) small centralizers with coated wireline body leads to the optimum configuration of the wireline when logging in rugose openhole inclined wellbores. The low friction coefficient centralizers significantly decreased the cablehead tension dips due to impacts when comparing it to the steel centralizers. However, this is considered to be the most expensive configuration of a wireline.
- The velocity readings also coincide with the cablehead tension force behavior. A more flattened cable-tension readings result in a more continuous smooth descend velocity plot.
- By comparing the cablehead-tension plot of the steel centralizer with a coated wireline in Figure 22 (blue curve) by the plot of the Steel/Uncoated wireline having low-friction centralizers in Figure 20 (green curve), we will conclude that it is more efficient to use low-friction centralizers with uncoated wireline steel assembly.

Accordingly, the results proved the added improvement on the wireline performance when using a low-friction coating on the wireline tools. The percentage of improvement depends on how efficient and wear resistant the coating is.

In oil field industry downhole tools are typically consist of metallic parts that are often moving and chafing against the borehole wall and passing through mud/hydrocarbon fluids in extreme harsh environment of temperatures and pressures which may also contains chemically aggressive materials, and as a result corrosion occurs. For a solution, an inert coating materials are recently been used for reducing wear and corrosion, and hence improving the downhole tool’s operating life. A further advantage can be added to the applied wear/corrosion resistance coating to improve the overall performance of the wireline logging string by using coating materials that have a low-friction coefficient. Several papers [22, 23] and patents [24, 25] were recently issued discussing different suggested low-friction coating materials for downhole applications that may be applied, and proven to have positive effects. Examples suggested, using Hardide-T Nano structure material [22], and another one by using Tungsten Disulphide as a coating material [24]. These materials shown to provide friction factors of the order of 0.1 or less as typically applied in this simulation study. Using Low-friction coating on logging tools could also prevent tool sticking when pulling the wireline out of the hole, especially when reaching extended depths.

In addition to the conventional stand-offs and centralizers and using low-friction coating materials, Downhole bottom noses are also believed to have a contribution on improving the penetration rates of the conveyed tools. Different designs of low-friction bottom noses were recently used to reduce the frictional drag forces and enables deeper descents of conventional wireline in deviated wells. The following section will discuss different passive bottom nose designs practically used in logging operations by oil-field companies, and whether they are effective or not.

3.4 Effect of Passive Bottom-Hole Nose Design on Wireline Performance

The aim of this study is to compare two different bottom-hole passive noses, been recently commercially used in logging operations, versus the No-Nose/hemisphere wireline tool end. The first passive nose design (Teflon-Ball nose) is based on the low-friction concept in conveying the wireline downhole, while the other nose design (Self-

Orienting Front-wheel nose) is based on the free-rolling concept in conveying the wireline downhole as shown in Figure 23. The design is to ensure complete flexibility for tool string integration and optimum positioning by having an extra degree of freedom represented in the swivel feature.

Figure 23 Wireline Bottom Noses

In addition, this study should show to which extent the bottom-hole nose contributes in improving the wireline penetration performance. First, a simulation run is conducted to evaluate the effect of the nose size on the cablehead-tension. A followed simulation run is conducted to compare the three passive nose designs of a Teflon-Ball & Front-Wheel having a same size. All simulation runs were conducted at same equivalent depth of 5,000 ft (K=4.86 N/mm) using the same wireline logging tool assembly having a 1.5” Teflon centralizers. Figure 24 shows the output results of Teflon-Ball bottom nose design in three different sizes 5, 6, and 7 inches.

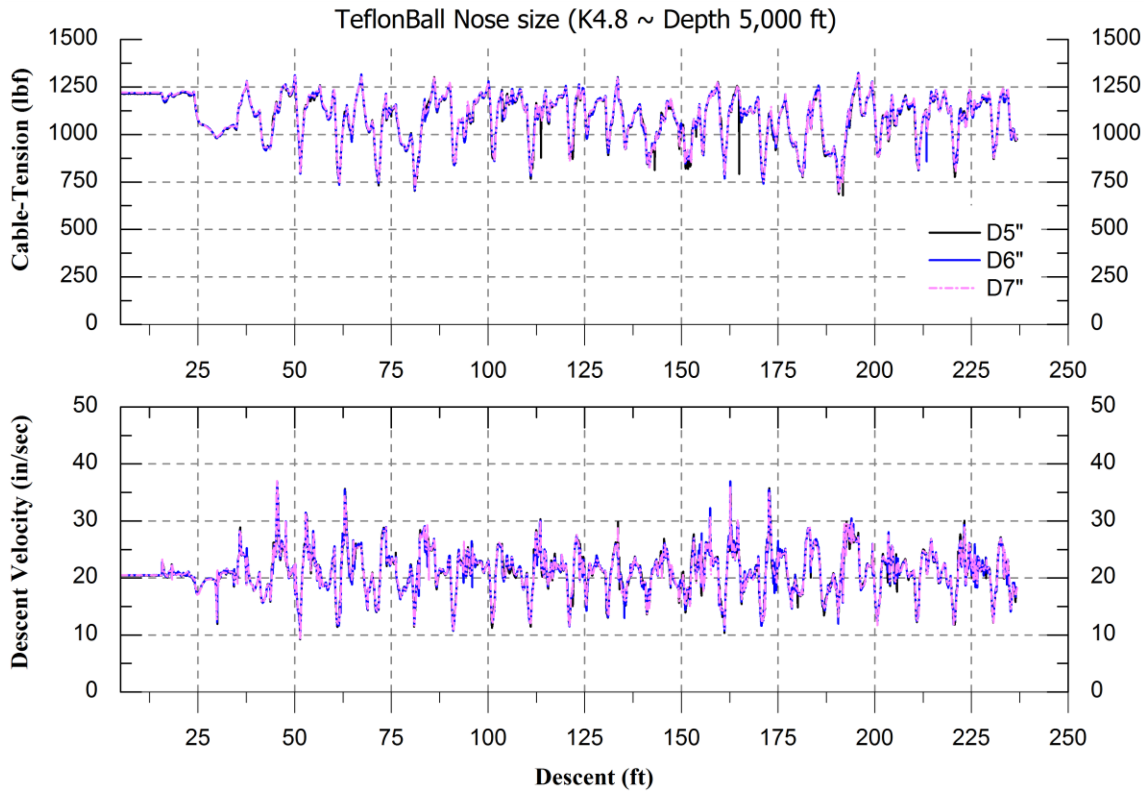

Figure 24 Teflon-Ball Bottom Nose with Different Sizes

The results show that the size of the bottom nose does not really have a significant effect on the conveying performance. The three plots are almost identical on each other. The fraction square inch of the projection areas differences between the three sizes subjected to impacts does not really have considerable effect on the overall performance comparing to the impacts on the centralizers. Note that the 3-3/8" wireline is lifted on centralizers with a 1.5" standoff making the overall external diameter equals to 6-3/8". That means the 5" & the 6" Teflon-Ball nose sizes are normally not touching the borehole ground (except during impacts), while the 7" Teflon-Ball nose is normally having contact with the borehole.

Figure 27 in the 'Cyan' Section summarizes the simulation output results of the different Teflon ball sizes and shows how the three mean tension-force readings are almost the same as well as their minimum tension force values.

Now, three different nose designs were compared (Teflon-Ball, self-orienting front-wheel, and hemisphere nose) in the wellbore simulator. The Teflon-Ball nose and the Front-wheel nose were chosen to have the same size of 6". Figure 25 shows the obtained simulation results of the cablehead-tension as well as the wireline descending velocity.

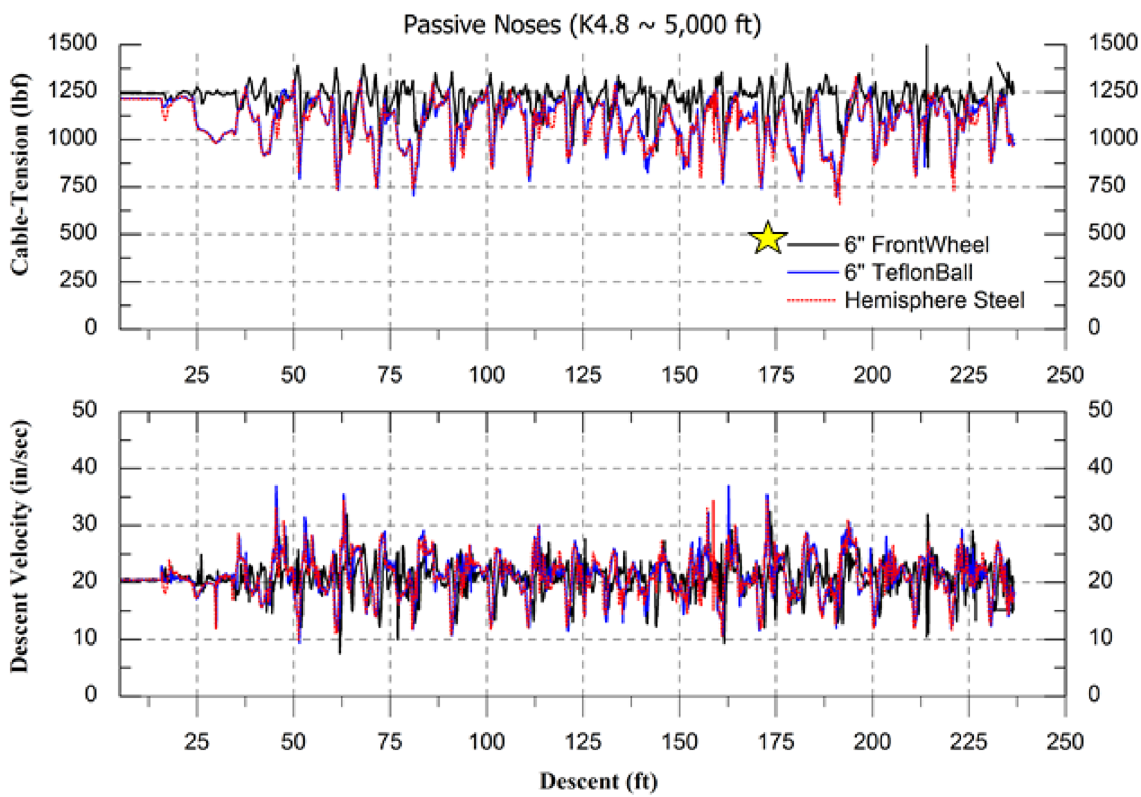

Figure 25 Different Bottom-Hole Noses Comparison

By analyzing the output results of the three bottom nose designs as well as observing their behavior in the simulator, the following points could be concluded:

- It is remarked by visual observation, that the Teflon bottom nose and the front-wheel bottom nose have better navigation behavior with ledges than the hemisphere steel nose.
- The cablehead-Tension readings show that the self-orienting Front-wheel concept has a more positive influence on the wireline overall performance than the other two nose designs. The maximum tension dip recorded in the Front-Wheel nose is about 900 (lbf) compared to 700 (lbf) in the Teflon-Ball & hemisphere noses' case. In conclusion, the self-orienting Front-wheel Nose shows a better navigation to the borehole roughness and ledges, and hence better penetration performance could be achieved. The results can be easily concluded as it appears in the simulations output results summary in Figure 26 in the 'Orange' section. This gives more credit to the free rolling self-orienting concept over the low-friction dragging concept. However, using a rolling wheel in openhole environment in presence of cuttings and other debris is still questionable.
- By visually inspecting the simulation runs at the head-tension major dips positions, it has been observed that these dips occur when a multiple centralizer engages with different ledges simultaneously, see Figure 26. Therefore, that confirms that the nose alone does not have the major contribution on the penetration performance. The centralizers do have an obvious effect.

Different bottom nose passive designs were used recently in logging operations especially in the high deviated wells with openhole sections as a trial to prevent the logging tool from stopping by a ledge and losing its momentum. Therefore, different nose concepts based on free-rolling or low-friction dragging has been commercially released and successfully experimented in deviated wellbores. More passive nose devices with extra degree of freedoms are being developed to give the wireline tool-string the flexibility to convey past ledges, washouts, and contractions which may be present in irregular boreholes with highly deviated angles [26, 27]. These nose devices may include swivel, articulated, roller parts to act as a “hole-finder” when negotiating the borehole irregularities. This makes the wireline string experience less resistance forces when navigating the wellbore and hence higher cable-tension force will be achieved as concluded from equation (8). More active downhole tools (Tractors) are being developed to improve penetration especially in extended horizontal wells. These devices are usually powered and controlled that invests friction in order to push the wireline tool-strings out to the end of the wellbore [28- 30].

4. DOWNHOLE SIMULATOR SUMMARY AND CONCLUSION

This work has identified and analyzed some challenges that affect the performance of the downhole wireline-string especially when conveying in highly deviated wellbores with rugose openhole zones. These challenges can cause the wireline string to get what called ‘get stuck’. ‘Stuck wireline’ can occur where a combination of wellbore geometry and changes in wellbore direction, together with the wireline bottom-hole assembly stiffness and arrangement of conveyance accessory tools such as centralizers and bottom noses, prevent the wireline string from passing through a section of the wellbore especially in the highly deviated rugose openhole zones. Figure 26 shows two centralizers are hitting wellbore ledges simultaneously that causes a drop in cable-head tension reading that might reach zero or get ‘stuck’. A major cause also can make the wireline tool-string to get stuck, is when the borehole pressure exceeds the formation pressure and a mud cake is formed around the wireline part forcing the wireline to stick to the formation in a condition called differential sticking.

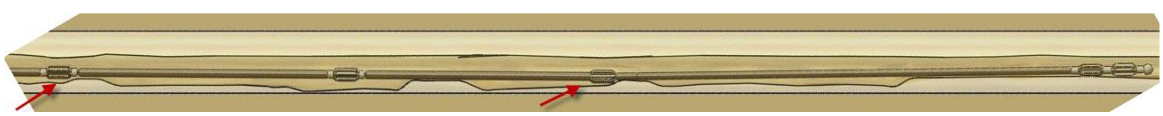

Figure 26 Two Centralizers hitting the Ledges Simultaneously

The differential sticking force can be considerably reduced by the use of centralizers. The number of centralizers needed depends on hole deviation, hole condition. The use of centralizers in soft or unconsolidated formations become very difficult, since the centralizer blades or springs will tend to embed in the formation. The number of centralizers must be sufficient to offset the lateral force and position the wireline string near the middle of the hole. The standoff distance of the used centralizers should be greater than the expected mud cake thickness inside the wellbore. Also using centralizers having small contact area shape design with the wellbore is recommended. This is by using either low-friction drag centralizers with elliptical profile, or by using roller centralizers having the contact in point.

A computer simulation model was built to facilitate a visual investigation of the conveying behavior of a downhole wireline-tool assembly, as well as to predict numerically the resultant cablehead-tension readings as an indication to its penetration performance. Different simulation studies were conducted to asses and analyze the contribution of different wireline components on the wireline overall performance in logging operation.

Figure 27 summarizes the obtained results from all simulation studies conducted by the simulator of the different wireline tool configurations. The figure shows a graphical bar representation of the Mean &Min.-Cablehead tension values of the simulation results recorded from the different studies conducted at same logging depth and same simulation period.

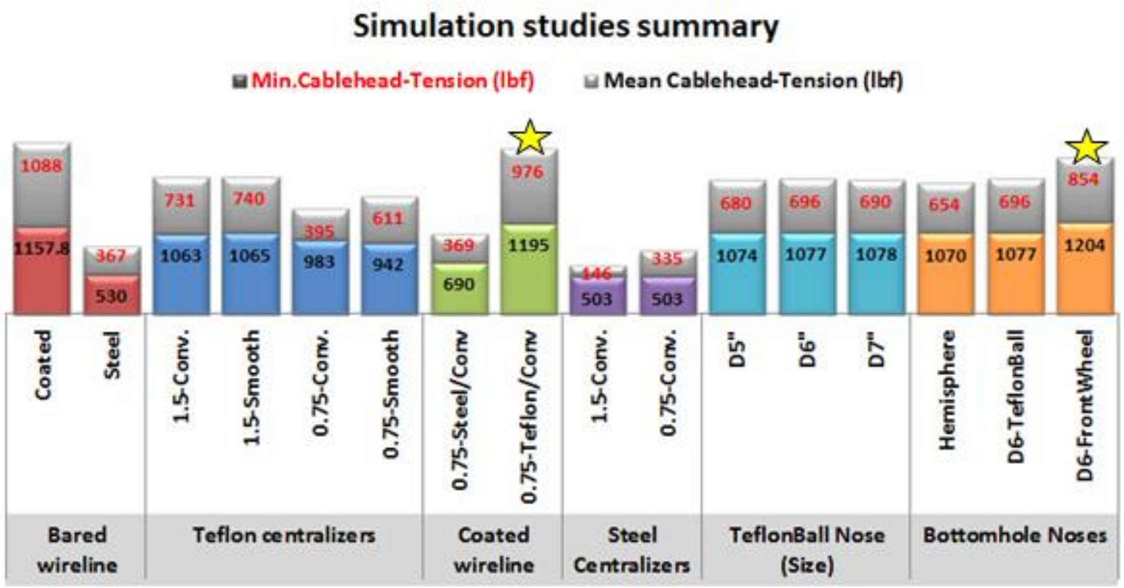

Figure 27 Summary of the Simulation Results (K4.8 ~ 5,000 FT)

According to the 'Blue section' in Figure 27, the obtained results showed that the stand-off distance factor in centralizers design has a more contribution and effect on the total wireline drag force index plot than shape factor assuming no differential sticking. Having a smooth centralizer shape design is highly recommended if overbalance or mudcake is expected.

Comparing the output results in the 'Blue section' with the one obtained in the 'Violet section' in Figure 27, the results recommend using low-friction centralizers with higher stand-offs when logging in rugose inclined wellbores.

The results obtained from Figure 21 and Figure 27 'Violet section' confirm that using conventional steel centralizers could lead the wireline string to stop in shallower depths.

The results showed, as it appears in the 'Green section' of Figure 27, that Coating the wireline tools with an efficient low-friction corrosion resistant material will definitely improve the wireline overall performance during logging and prevents tool sticking especially when pulling the wireline out of the hole after reaching extended depths. The plots showed a more flattened and continuous cablehead-tension curves with smooth wireline velocity motion.

The results also support, as it appears in the 'Orange section' of Figure 27, that by using passive bottom nose designs having degrees of freedoms (more flexibility) could considerably reduce the resistance forces acting on the wireline string, and hence improve the penetration performance.

As an overall summary, we can conclude that using wireline tools with efficient low-friction coating in combination with smooth shape 'low' centralizers, that comprises rollers or low-friction material and attached to a swivel-articulated-rolling bottom-nose tool could lead to an optimum most efficient wireline tool arrangement when logging in highly deviated rugose wellbores. However this arrangement considers being the most expensive because of the coating feature. Alternatively, uncoated wireline tools is best to be combined with smooth shape 'high' centralizers, that comprises rollers or low-friction material, and attached to a swivel-articulated-rolling bottom-nose tool as a second most optimum wireline string arrangement and again that in case of high borehole rugosity. If the borehole openhole profile has less irregularity, then 'Low' centralizers should be used.

Using 'smart' standoff-adjusting centralizers (maybe by using spring loaded rollers) could lead to a remarkable improvement in the wireline cablehead-tension reading by reducing the dips intense due to impacts. Centralizers may also be clamped to the logging cable itself to prevent key-seating and differential sticking.

The results of this work can be used in conjunction with other factors (e.g. additives for lubrication and reducing mudcake thickness) to improve wireline logging performance especially in highly deviated rugose openhole wells to overcome different challenging wellbore conditions. This may increase in accordance the percentage of the successful logging operations and hence reduce time, cost and improve data quality and increase wellbore coverage.

Table 1 Suggested Wireline-String Configuration based on Wellbore Condition

		CASED	**OPEN HOLE**			
			Vertical	Low inclination	High inclination	
					low	severe
Centralizers	Small	X	X	X	X	
	Big					X
Bottom Nose	Hemisphere	X	X			
	Teflon-Ball			X	X	
	Front-Wheel					X
Coating						X

Table 1 provides some suggestions for the recommended conveyance configurations to be used in wireline logging operations based on the investigations done and under the different wellbore conditions to achieve the highest logging penetration rate. In case of cased boreholes, with any inclination, it is suggested to use only centralizers with low friction coefficient having small stand-offs, with a normal steel hemisphere nose at the bottom of the logging tools assembly. However, if the wellbore will have an open-hole zone, the logging performance will be affected significantly on the conveyance accessories will be selected. For vertical openholes; centralizers with small stand-offs and a hemisphere steel nose are still recommended, as the small stand-off distance under the gravitational force will be sufficient to levitate the logging tools from contact the formation and prevents any impacts on the bottom nose, therefore a hemisphere steel nose is satisfactory. However, by having more borehole inclination with the vertical and more borehole rugosity, the conveyance tools should have low friction coefficients and more degrees-of-freedom (more flexible) to reduce losses due to friction and drag resistance. For example, in highly deviated openholes with severe rugosity, low friction coated logging tools with swivel front-wheel bottom nose and ‘High’ Teflon centralizers are recommended to achieve the best logging penetration rate. Reducing losses due to friction and drag will cause the wireline string to preserve its momentum to achieve higher penetration depths. Tractors, or more actuated devices, should be used in extended reach horizontal openhole wells, as the tools’ momentum will be totally vanished due to impacts, friction, and gravitational force absence.

5. PART TWO: DRILLSTRING VIBRATION DYNAMICS

In this part we will discuss the dynamic behavior of the drillstring during the drilling operation using different approaches to model and simulate its vibration modes under different operation conditions. First, problem identification will be introduced with quick survey on literatures that tackled the problem previously from one or more sides. The objective will then be defined with a proposed methodology to achieve it step-by-step.

5.1 Problem Identification

Drillstring vibration is one of the major causes of the deterioration of drilling performance by reducing the rate of penetration (ROP) and hence increasing the non-productive time (NPT). This violent downhole vibration can also impact negatively all drillstring subassemblies, including measurement instruments, mud motor, and drillbit, and put them at risk of major failure. Furthermore, these vibrations can cause an interference with the signals from measurement while-drilling (MWD) tools, as well as it can be a source for wellbore instabilities.

Drillstring vibrations can be classified into three modes: axial, torsional, and lateral. Each vibration mode has a different destructive nature, and different excitation sources. Drilling dynamics is a very complex problem, and this necessitates the investigation and analysis of the different types of drillstring vibrations, especially the most sever lateral type of vibration, and finding practical solutions to suppress or mitigate these harmful vibrations in order to increase drilling efficiency and prevent subassemblies from possible operation failure. Figure 28 shows the different vibration modes that could be induced in the drillstring during the drilling operation. The three vibration type will be discussed in details in the coming section.

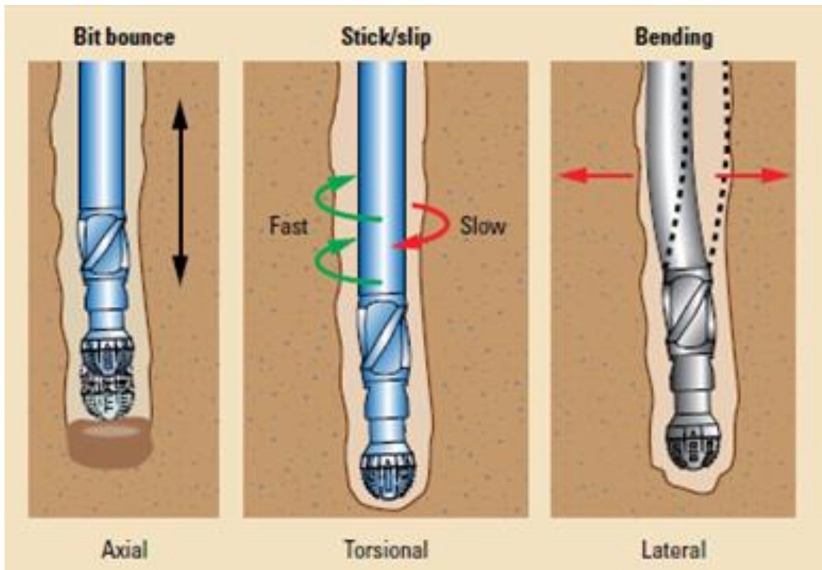

Figure 28 Drillstring Vibration Types [31]

5.2 Background and Literature Review

Drillstrings is typically consists of drillpipe, that transmits drilling fluids, drill-collars, stabilizers, tools, and drillbit. The drillstring is usually made up of hollow steel collars so that drilling fluid can be pumped thoroughly down to the drillbit. The drill collars should be in thick-walled large diameter pipes in order to provide sufficient stiffness to avoid buckling and the chance of bending vibrations. The BHA; is called on the bottom assembly of the drillstring which comprises the drill-collars, stabilizers, and the drillbit in addition to other logging tools and instruments. Stabilizers, known also as centralizers, are tools assembled along the drill collars and above drillbit used to center the BHA, and usually have a lower friction coefficient than the drill-collars. They also have a major contribution in BHA bending prevention as we will see later in the simulation analysis. The drillstring is resting with the bit on the formation surface and pulled from the top end upward with a hook at the rig. The thin drillpipe section of the drillstring is therefore constantly in tension while the thick-walled lower part is partly in compression. The tension applied on the drillpipes prevents them from buckling or bending. However, the drillpipes are subjected to torsional loads due to their lengths and thin walls. Drilling fluids are pumped down through the drillstring hollow, and then out through the drillbit nozzles to provide lubricating and cooling for the drillbit, as well as to transport the cuttings to the surface for cleaning. Figure 29 shows the main components for the drillstring assembly and how they are assembled.

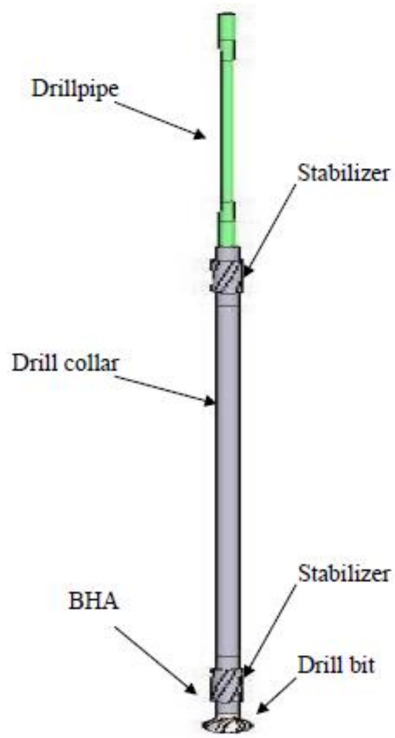

Figure 29 Drillstring Assembly [32]

While drilling, the axial reaction force on the drillbit, known as weight-on-bit (WOB), can become excessive and results in large fluctuations causing axial vibration in drillstring. This phenomenon is called bit-bounce, which can lead to deterioration in drilling rate-of-penetration (ROP) as well as damaging bit cutters and poor directional control. Torsional vibrations results from bit chatter, stick-slip interaction between drillbit and wellbore formation. Stick-slip is usually occurs while drilling in which the drillbit becomes stationary for a while "sticks" due to buildup of torque-on-bit (TOB) followed by an increasing of rotational acceleration as the bit breaks free "slips". This causes a severe form of drillstring torsional oscillation. Severe stick-slip motion can cause eventually a reversing of the bit direction. The third and most destructive type of drillstring vibration is due lateral vibrations. Lateral or bending vibration can create large shocks as the BHA impacts the wellbore wall [31].

This type of violent vibration results from the interactions between the BHA components with formation due to bend drillstring, or mass imbalance in the drillstring caused by the embedded Measurement-while-drilling (MWD) tools, drillbit unbalance, and drill collar sag. Drillbit plays an important role in coupling mechanism as it converts axial to lateral vibrations. The interaction between the BHA or drillstring contact points may, under certain circumstances, cause to what called "Backward whirl". Backward whirl, known also as 'Rolling' contact motion, is the most severe type of drillstring vibration that which results into high-frequency large-magnitude bending moment fluctuations that leads to components and connections failure such as fatigue cracking, washouts, and possible twist-offs as shown in figure 30. The increased friction results in increased torque at the contact point, which causes the BHA collar to rotate in the opposite direction of the rotation of the drillstring.

Forward whirl, known also as sliding contact motion, is another form of drillstring lateral vibration observed when the angular rotation of the BHA component is in the same direction as the whirling direction. This results in one-sided wear "Rubbing" of components in which the BHA rubs the formation along the same part of the collar as the drillstring rotates. If the formation is aggressive excessive wear will occur along the part of the collar that rubs the formation. This wear can be seen as a flat spots on one side of the collar, or as a single worn blade or stabilizer as shown below.

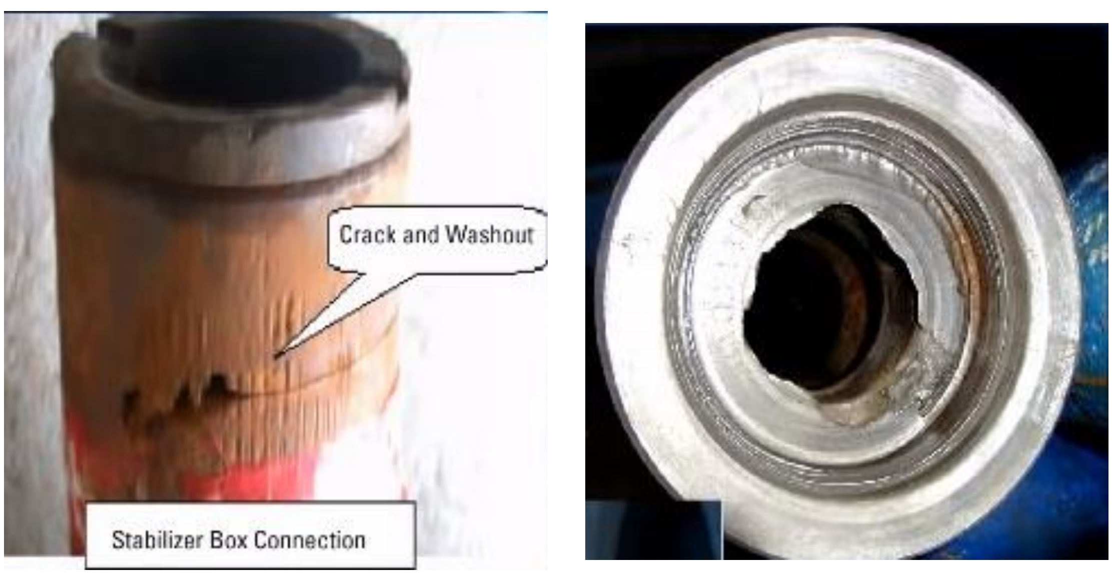

Figure 30 Drill String Components Failures due to Backward Whirl [31]

Figure 31 shows the possible failure that the drillstring components could account due to forward whirling.

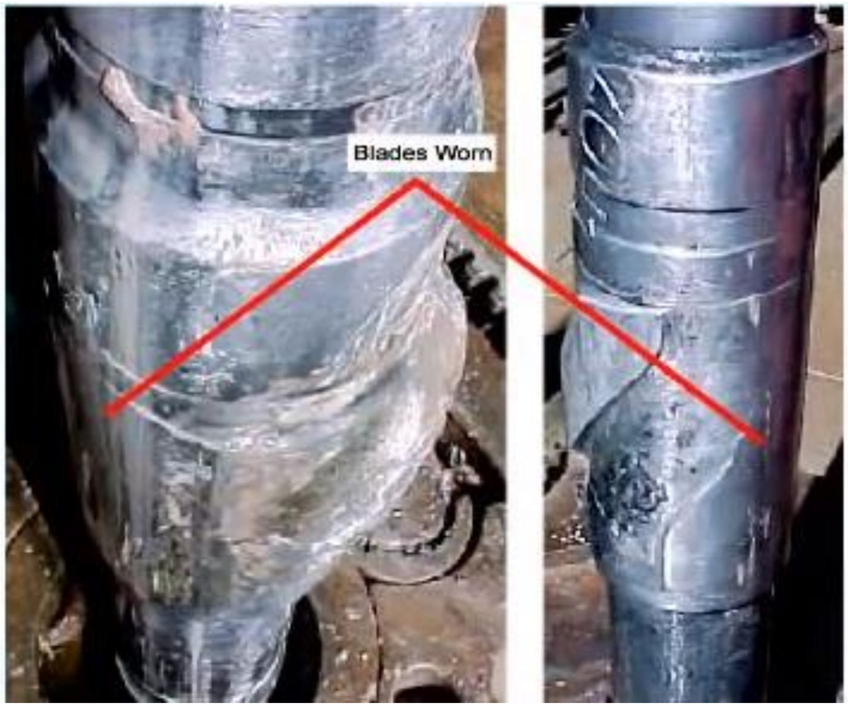

Figure 31 Drillstring Components Failure due to Forward Whirl [31]

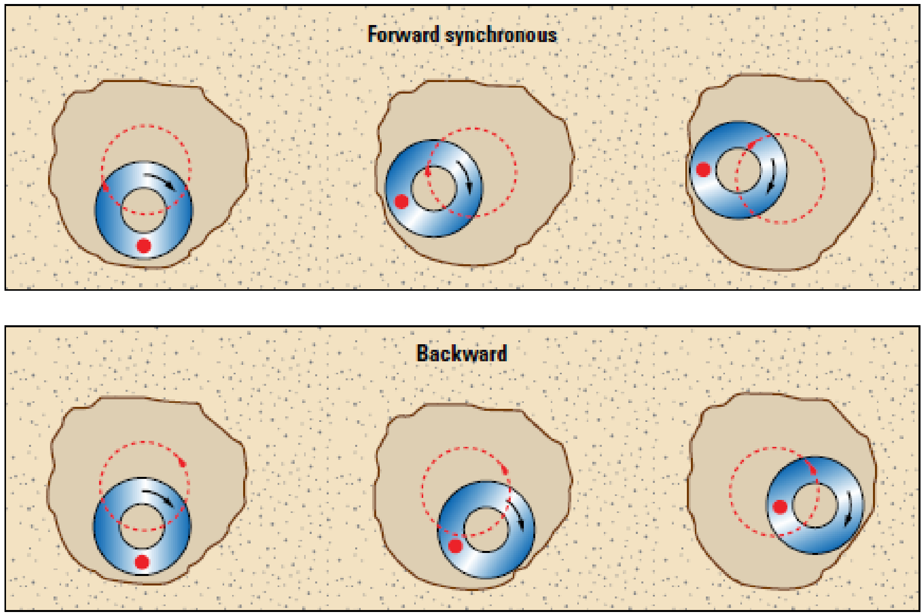

Figure 32 BHA Whirl [31]

Figure 32 describes the different between forward and backward whirling in terms of whirling directions compared to the rotation direction.

The sources of drillstring vibration during drilling can be summarized as follows:

- Bit Bounce
- Stick-Slip
- Mud Motors
- Backward Whirl
- Forward Whirl
- Hydraulic vibration

As described before, there are various potential excitation sources of drillstring vibration such as: mass imbalance, friction factor between drillstring and borehole, operational spin velocity, cutting action of the drillbit, BHA stiffness, clearance between

BHA components and borehole, Bent angle, stabilizers locations, and fluid forces around the drillstring.

Most of drillstring vibration literatures focus on simulation analysis of the torsional and axial vibrations. However there is still a big lack in studies that predicts the lateral chaotic vibrations in drillstring specifically the most severe mode “Backward whirl”.

Mongkolcheep et al [32] presented a methodology to predict lateral vibrations of drilllstrings accounting the flexibility of drill collar utilizing a modal coordinate condensed, finite element approach. The nonlinear effects of drillstring/borehole contact, friction and quadratic damping were included. A study that considered the length of time to steady state, the number and duration of linearization sub-intervals, the presence of rigid body modes and the number of finite elements and modal coordinates, was conducted on factors for improving the accuracy of Lyapunov Exponents to predict the presence of the chaotic vibration.

Feng and Zhang [33] discussed a linear system analytical model with only 2-DOF of a simple rotor and fixed stator. The paper discusses the vibration phenomena resultant from rotor rubbing inside a stator by an initial perturbation. The perturbation is an instantaneous change of the radial velocity when the rotor is rotating in its normal steady state. The studies shows the effect of formation coefficient friction and operating speed on the rotor’s dynamic rubbing behavior and the transition from forward whirling to full backward whirling.

When the rotor contacts the stator, the changes of the friction forces acting on the rotor can drastically affect the rotor dynamics. The paper assumed linear system with only two degrees-of-freedoms. So they ignored the effect of inertia and stiffness non-linearities inherent in rotor systems.

Khulief et al. [34] formulated a finite-element-model (FEM) for the drill-pipes and drill-collars of the drillstring that accounts for gyroscopic and axial-bending coupling via the gravitational force field using a Lagrangian approach in order to study the self-excited nature of stick-slip oscillations and bit-bounce. Explicit expressions of the finite element coefficient matrices were derived using a consistent mass formulation and the developed model is integrated into a computational scheme to calculate time-response of the drillstring system in the presence of stick–slip excitations.

Saeed and Palazzolo [35] proposed a novel concept for a downhole flywheel energy storage module to be embedded in a bottom-hole-assembly. The paper discussed the sizing of the embedded flywheel in the BHA. Magnetic levitation control system was designed and tuned to maintain the continuous suspension of the flywheel under the different drilling vibrations of the BHA excluding the lateral vibration modes.

Lein and Van Campen [36] presented a Stick-slip whirl interaction model as a simplification of an oil well drillstring dynamics confined in a borehole with drilling fluid. Full-scale drilling rig experiment has been conducted to validate the numerical results obtained. The model consists of a sub-model for the whirling motion and a sub-model for the stick-slip motion. The model is a simple 3-DOF model that exposes only the basic phenomena of stick-slip and whirling.

Richard, Germay, and Detournay [37] studied the self-excited stick–slip oscillations of a rotary drilling system with a drag bit, using a discrete model taking into consideration the torsional and axial vibration modes of the PDC-drillbit. Both axial and torsional vibrations of the bit, as well as the coupling between the two vibration modes through the bit-rock interaction laws are considered as well as the interface laws that account both for cutting of the rock and for frictional contact between the cutter wearflats and the rock. The evolution of the system is governed by two coupled delay differential equations, with the delay being part of the solution, and by discontinuous contact conditions. Detournay et al. [37, 38] presented also a method suggesting that the time-delay in the formation cutting of PDC bits is the vibration cause for stick-slip mode. They divided *WOB* and *TOB* into two separate processes, where the drilling action of a drag bit consists of a pure cutting process in front of each blade and a frictional process along wear flats.

Yigit and Christoforou [39] they used a simple model that captures the dynamics and coupling between the axial and torsional vibrations to simulate the effects of varying operating conditions on stick-slip and bit-bounce interactions. The authors demonstrated that the conditions at the bit/formation interface, such as bit speed and formation stiffness, are major factors that can affect the dynamic response of the model. They claim that due to the varying and the uncertain nature of these conditions, simple operational guidelines will not be sufficient to eliminate both stick-slip and bit-bounce. They also suggested parameters that could be used to represent a typical PDC bit on a hard formation. A Non-linear continuous function that represents the relation between drillbit friction torque with bit speed has been provided according experimental results.

Moreover, Yigit and Christoforou [40] have also studied the coupled torsional and bending vibrations of drillstrings subject to impact with friction.

Franca and Mahjoob [41] developed a relationship for tri-cone bits in rotary operations based on experimental results.

Patil and Teodoriu [42] presented a mathematical model of a torsional drillstring based on nonlinear differential equations which were formulated to consider drillpipes and bottom-hole-assembly separately. They represented the bit-rock interaction by a nonlinear friction force. They carried out a parametric study to analyze the influence of drilling parameters such as surface rotations per minute (RPM) and weight-on-bit (*WOB*) on torsional oscillations. They built the torsional drillstring model using MATLAB/SIMULINK interface.

5.3 Objective and Significance

The objective of the this work is to extend previous works stated in literature of simulating downhole drillstring dynamics, specifically works presented by Saeed and Palazzolo [35], and Mongkolcheep et al [32], and make it more comprehensive by including the lateral vibration dynamics. This will gives a complete identification and modeling of the drillstring dynamics, and in accordance will give a better understanding and control over its functional operation and improve the drilling performance. Knowing the potential excitation sources of the different vibration modes, will lead to better troubleshooting to mitigate vibrations of the BHA subassemblies and measuring tools. That should give more grounded answers to the crucial questions about the operation conditions that possibly causes backward whirl vibrations, possible stabilizers' configuration to reduce chance of backward whirl, and other arising questions. Vibration response predictions may assist drilling rig operators in changing a variety of controlled parameters to improve operation procedures and/or equipment.

5.4 Methodology

The objective is being achieved step-by-step as follows:

1) Initiate with a simplified mathematical based model with only two degrees-of-freedom to simulate the rotor dynamics due to friction contact between a simple rotating rotor and a fixed stator. This should give the fundamental understanding of rotor lateral vibrations (in X-Y plane) due to varying the friction coefficient between the rotor and stator as well as stator stiffness, and their effect on forward and backward whirl. Success in getting proper results from this step, by applying the right boundary conditions with logic behind presence or absence of contact, will help in achieving the targeted objective in the final system model. Literature [33] is used as reference in this step.
2) Build another simplified mathematical based model of two degrees-of-freedom (Z, φ_z) to capture the dynamics and coupling between axial and torsional vibration of a drillbit model and to simulate the effects of varying operating conditions on stick-slip and bit-bounce interactions taking into consideration the nonlinear effects of drillbit/wellbore friction torque. Literatures [36, 37, and 39] were used as references in this step.
3) Extend the system capabilities of the mathematical based model by combining (1) and (2) together to form an analytical model having a four DOF that captures the lateral vibration in addition to the axial and torsional vibration for a single rotor

mass inside a stator. The rotor here represents the drillbit inside the borehole. Literature [40] is used as a reference in this step.

4) Building a more complex and accurate mathematical model consists of three lumped masses that represents the drillstring assembly in its FULL DOF's (6-DOF for each lumped mass) based on (3). The upper mass represents the drillpipe model lumped with a stabilizer having a radius bigger that the BHA radius. This mass portion is coupled with the rotary table from top, and with the 2nd mass portion (Intermediate BHA lump mass) with an equivalent torsional & bending stiffness springs, as well as axial damping & stiffness coefficients. The second lumped mass (the intermediate BHA mass portion) is considered to not have a stabilizer component. Therefore the radius of this mass portion will be less than the upper mass portion and the lower mass portion. The lower lumped mass (the third one) is considered to sum the drill-bit model with the second portion of BHA mass. The drillbit is considered to have almost the same radius of the borehole. Literature [42] is used as a reference in this step.

5) Enhance the drillstring dynamics model using a more accurate approach, Finite-Element-Method, to simulate the drillstring vibrations. Instead of treating the BHA as three lumped masses in step (4), the BHA is meshed or discretized into a number 3D- Timoshenko beam elements and the drillpipes can be substituted by a lumped mass, torsional spring, and damper attached to the top node of the BHA. Stabilizers models can be applied and located at any of the BHA's nodes by adding the corresponding DOF's and geometry profile. Right boundary conditions and

contact logic can be applied in the same manner as in step (1) for lateral vibration, and step (2) for axial & torsional vibration such that the drillstring experiences axial, torsional, and lateral vibrations. External forces are applied at each BHA nodes including stabilizers' nodes and the bottom node for the PDC-drillbit. The model accounts the gyroscopic effect, the torsional/bending inertia coupling, and the effect of the gravitational force. This model is a more complex and will give a more accurate prediction to the rotordynamic behavior of the BHA, and the PDC-Drillbit cutting dynamics. Literatures [32] and [35] are used as references in this step.

6) Investigate the behavior of drillstring vibrations from the finite element model to obtain better understanding the effect of system parameters to the system response.
7) Conduct different simulation studies on the final finite element model to fulfill the targeting objective by obtaining the following dynamic behaviors with the corresponding analysis:
    - Forward whirling under self-excited vibration
    - Rolling whirling under self-excited vibration
    - Chaotic whirling under self-excited vibration
    - Stick-slip drilling
    - Bit bounce
8) Verify model by check cases

6. MODELLING OF DRILLSTRING DYNAMICS

In this section theoretical investigations of the drillstring dynamics will be initiated with the simple Jeffcott rotor-stator model with a relatively low degree of freedom approach to simulate the lateral and rotational vibrations. A more accurate but still simplified mathematical model of drillstring is then applied using lumped-system modelling approach to capture more vibration modes, including axial vibrations, with 6-DOF for each lumped mass. A final finite element method is introduced to model a more accurate and reliable model for the drillstring dynamics, including drillbit and centralizers, to investigate the different vibration modes that the drillstring could encounter during the drilling operation in vertical wells by giving a full analysis of the dynamic response and highlighting on the most destructive vibration mode 'Backward whirling' and the conditions that leads to it.

6.1 Rotor-Stator Modeling

Objective

As a first step, a simple 3-DOF rotor/stator mathematical based model will be presented to describe the interaction phenomenon between stick-slip and whirl motion as simple as possible. The model will qualitatively simulate the rotor dynamics due to friction contact between a simple rotating rotor and a fixed stator. This should give the fundamental understanding of rotor lateral vibrations in two-DOF model (X-Y plane) due to varying the friction coefficient between the rotor and stator as well as stator stiffness, and their effect on forward and backward whirl. The third-DOF (φ_z) is to capture the dynamics of the rotor's torsional vibration with the effects of varying operating conditions on stick-slip taking into consideration the nonlinear effects of the Stribeck friction. The rotor mass imbalance will be the self-excitation vibration source and rotor whirling. Fluid forces model will be presented to form the interaction mechanism between torsional and lateral motions.

Theoretical Background

The vibration theory for rotor-dynamic systems was first developed by Föppl in 1895 and Jeffcott in 1919 [43]. The presented 3-DOF rotor/stator model is employed based on the simplified Föppl/Jeffcott rotor system, which is often employed to evaluate more complex rotor-dynamic systems in the real world.

To have a good understanding of the various types of vibrations that undergoes the drillstring during drilling and be able to simulate them, we need first to identify the different parameters that contributes to each drillstring vibration phenomenon, and also to understand and analyze the kinematics of a simple rotating rotor inside a fixed stator and the conditions that may enforce the rotor to switch from state to state especially when whirling.

Lateral vibrations in drillstring, also called drillstring whirling, in which the center of rotation of the drillbit, or BHA-stabilizer/BHA-collar, rotates not coincident with the center of the wellbore causing the whirling motion. It is often results from bit/formation interaction, drill collar mass imbalance, and from fluid forces around drillstring. In case of contact with the borehole formation, two different modes can be obtained while whirling: Forward and Backward whirl. Forward whirling is called when either the drill collar, drillbit, or the stabilizer, has a sliding contact with borehole wall and rotates around the borehole axis in the same direction as around its own axis. However backward whirling is called when rotates clockwise on its axis while traveling counter-clockwise around the inside of the hole. The drillstring hence starts creating traction with the borehole wall and continues to rotate at very high frequency, depending on the clearance between the drillstring component that is in whirl status and the borehole, and reach frequencies 5 to 30 times the rotational speed of the drillstring. This violent vibration can cause a major failure in drillstring components if left unchecked due to a combination of high fatigue & impact loading as well can cause in over-gauged boreholes due to bit whipping & whirling. Figure 9 shows how bit whirling can results in an over-gauged borehole.

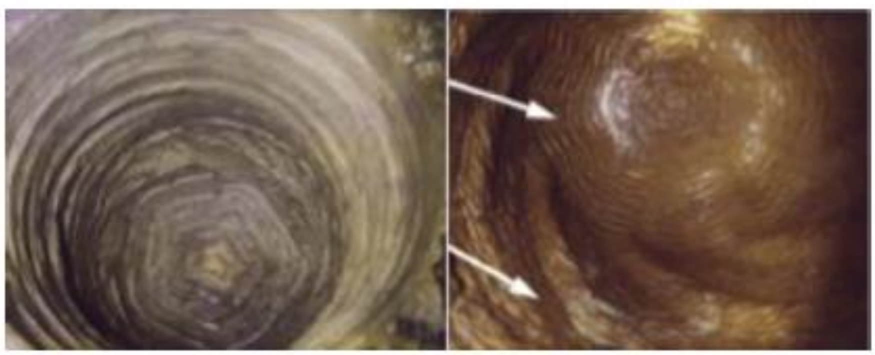

Figure 33 Resultant Over-gauged Boreholes from Whirling Bit [44]

Backward whirl is more likely to occure at lower wellbore inclinations and as the inclination increases and the drilling trajectory becomes more horizontal, the likelihood of backward whirl decreases, however it can still occur in any wellbore environments. Furthermore, sharp edges on the drillstring can bite into the rock, creating traction that can lead to backward whirl. [45]

The relative speed, V_{rel}, between the two contacting surfaces, rotor and stator, is used to determine and differentiate whether there is sliding or rolling contact, and hence forward whirling or backward whirling. When the relative speed between the stator and rotor reaches zero, perfect or pure rolling occurs.

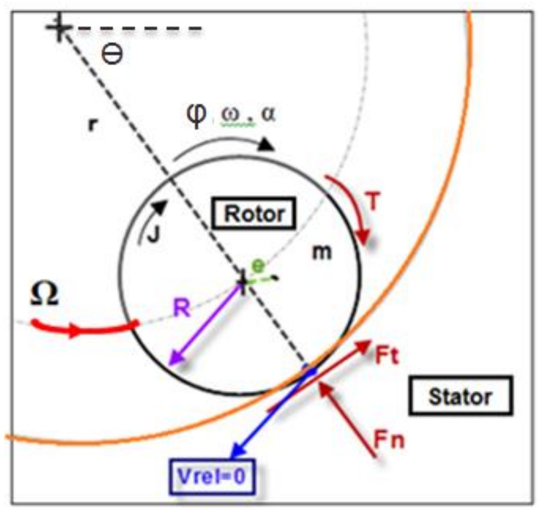

Figure 34 Rotor Stator Kinematics

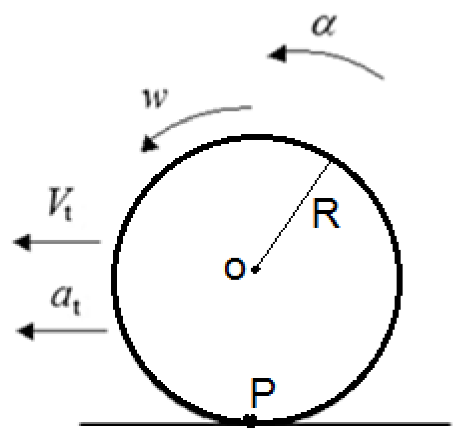

Figure 35 Rotor Rolling on a Flat Surface

To understand the conditions that govern the motion of the rotor inside a stator and predict whether sliding or rolling motion will occur, we need first to analyze the rotor/stator kinematics. From the above figures, $\boldsymbol{\alpha}$ is the angular acceleration of the rotor, $\boldsymbol{\omega}$ is the angular velocity of the rotor, $\boldsymbol{R}$ is the radius of the rotor, $\boldsymbol{r}$ is the radial displacement of the rotor from the stator geometric center, $\boldsymbol{\Omega}$ is the rotor whirling velocity, $\boldsymbol{V_t}$ is the tangential velocity of the geometric center $\boldsymbol{O}$ of the rotor with respect to ground, $\boldsymbol{a_t}$ is the translational acceleration of the geometric center $\boldsymbol{O}$ of the rotor with respect to ground, ***P*** is the contact point between rotor and stator. The rotor rolls without slipping only if there is no translational movement of the rotor at the contact point ***P***. Point ***P*** therefore must also have zero horizontal (or translational) movement, which means not sliding. In this case, 'Pure rolling' or 'rolling without sliding' occurs and the following conditions must apply:

$$V_{rel} = 0 \tag{12}$$

$$V_t = \omega.R \tag{13}$$

$$a_t = \alpha.R \tag{14}$$

Otherwise, when the relative velocity is nonzero, and the velocity $\boldsymbol{V_t}$ will not equal to $\boldsymbol{\omega.R}$ ($V_t \neq \omega.R$). The relative velocity hence is given by:

$$V_{rel} = \Omega.r + \omega.R \tag{15}$$

Referring to Figure 35, equations (12-14) are also applicable for rolling on curved surfaces. The contact point ***P*** velocity would still be zero for no slipping condition, and equations (13, 14) would still apply. The velocity $\boldsymbol{V_t}$ and acceleration $\boldsymbol{a_t}$ are parallel to the tangent to surface at contact point ***P*** and the friction force $\boldsymbol{F_t}$.

In case of "Rolling with Slipping" or "Transition": equations (12), (13), and (14) are not applicable, and the relative velocity at contact point ***P*** is not zero and hence there is no relationship between the velocity (and acceleration) of the geometric center ***O*** with the angular velocity (and angular acceleration) of the wheel.

Torsional, or rotational, vibrations are caused by the nonlinear interaction between the drillbit, or the drillstring, with the formation. This type of vibrations caused by stick-slip where the drillstring, specifically the drillbit, characterized by alternating stops then intervals of large angular velocity after. As the strength of the formation increases, more weight-on-bit (*WOB*) is required to maintain efficient rate-of-penetration (*ROP*) and depth-of-cut (DOC). Increased *WOB* in hard formations with low rotation drilling speeds will often create stick-slip, a violent reaction of building up torsional energy along the drillstring body then releasing it suddenly. During the "stick" phase, the bit stops drilling while *WOB* and *TOB* are still applied, the resulting built-up torque in the drillstring will cause the bit eventually give away or "slip" causing a high sudden increase in its rotational speed, which can reach to more than five times the top drive rotational speed. This causes the drillbit to wear out due to friction, and a remarkable decrease in rate-of-penetration (*ROP*) and increase in the non-productive-time (*NPT*) in accordance.

Stick-Slip and Whirling Modelling

A dynamic analytical model of a simplified mathematical based model with only three degrees-of-freedom (x, y, φ_z) is used to simulate the two vibration types of stick-slip and whirl. One-degree of freedom for the torsional vibration type, and the other two degrees of freedom to model the lateral vibration type. The analytical stick-slip whirl model is a simplification of a drillstring confined in a borehole wall with mud. The BHA will be modeled as a rigid disk with mass, *m*, and inertia, *J*, and having radius *R*. The disk is attached at the bottom end of a massless flexible shaft (represents the drill pipe) as indicated in Figure 36. The disk has an eccentricity, *e*, between its center of mass and its geometric center.

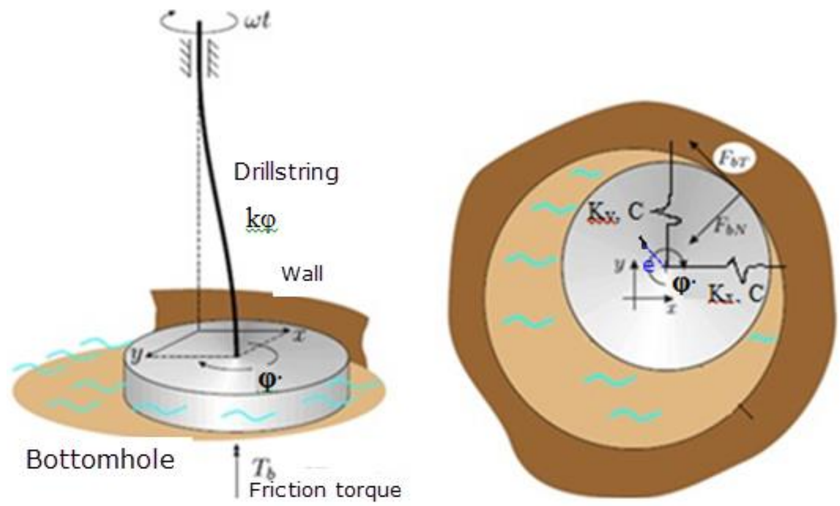

Figure 36 Analytical Model of Simple 3-DOF Rotor/Stator

The upper end of the flexible shaft is fixed in two-DOF's (X, Y) and driven with a constant rotation speed, $\boldsymbol{\omega}$, which represents the upper constant rotary table speed. The massless shaft is subjected to bending and torsion with bending (or lateral) stiffness, K, in (X, Y) and torsion stiffness, K_{φ}, about the axial axis (or axis of rotation). The displacement of the geometric center of the rigid disk occurs in the (X, Y) plane of the stationary coordinate system as shown in Figure 36. The disk rotates with an angle, φ, about its center with angular velocity $\dot{\varphi}$. The disk has a clearance, R_c, with the stator. A friction torque, T_f, acts on the disk (or the rotor) in the opposite of the rotation direction. This torque parameter will be extended later in the more complete drillstring model as Torque-On-Bit (*TOB*).

By initial exciting the rotor in the normal steady state will cause the rotor to pass through a transient vibration process. During this process the rotor may or may not contact the stator due to the rotor clearance with the stator. If the centrifugal force, F_e, resultant from the mass imbalance or eccentricity, e, is high enough, the disk will rotates in a spiral motion till it hits the stator wall. The stator will induce normal and tangential forces on the rotor when the radial displacement of the rotor becomes larger than the clearance, $r > R_c$. The normal contact force resultant from formation contact can be modeled simply as spring force having a spring stiffness k_b, which represents here the contact stiffness or formation stiffness

$$F_N = \begin{cases} k_b(r - R_c), & r > R_c \\ 0, & r \leq 0 \end{cases} \tag{16}$$

The normal contact force will induce a tangential friction force due to dry friction between rotor and the wall (stator). Here we will apply two models for the friction coefficient μ. The first assuming a constant value for the friction coefficient, and the other using an approximated smooth Stribeck function for the friction coefficient as adapted from reference [46], where the friction force is simulated as a function of relative velocity and is assumed to be the sum of Stribeck, Coulomb, and viscous components, as shown in figure 37.

$$\mu = -\frac{2}{\pi}\arctan(\varepsilon_f v_{rel})\left[\frac{\mu_s - \mu_d}{1 + \delta_f |v_{rel}|} + \mu_d\right] \tag{17}$$

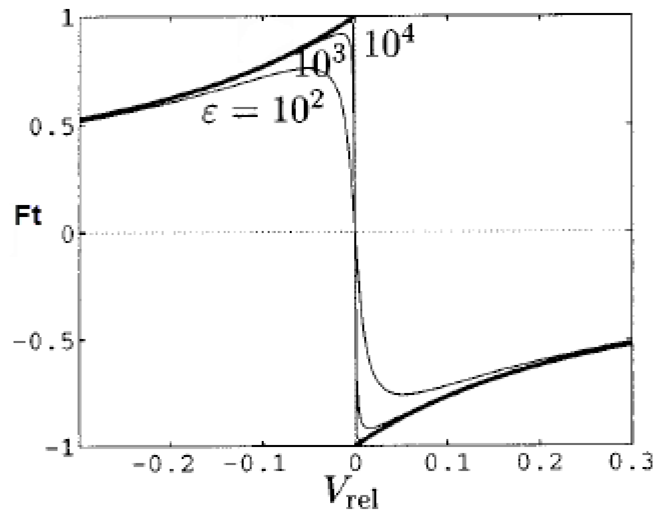

Figure 37 Friction Force Relation with Relative Velocity [46]

Where ε, determines the steepness of the approximation function and parameter δ_f is a positive number that determines the rate at which the static friction coefficient approaches by the dynamic friction coefficient with respect to relative velocity. If the relative velocity between the rotor and the stator is nonzero, the tangential friction force, F_t, could be then:

$$F_t = -\mu . sign(V_{rel}) F_N \quad , V_{rel} \neq 0 \tag{18}$$

From the relative velocity equation (15), the whirling velocity, **Ω**, equals:

$$\Omega = \dot{\alpha} = \frac{d}{dt}\left(\tan^{-1}\frac{y}{x}\right) = \frac{\dot{y}x - \dot{x}y}{r^2} \tag{19}$$

Where, $\dot{\alpha}$ or Ω is also known as the angular rate of change of the rotor geometric center position.

In case of pure rolling, as illustrated before, the relative velocity reaches zero (V_{rel}=0), and the tangential friction force must be between

$$-\mu . F_N \leq F_t \leq \mu . F_N \tag{20}$$

The tangential friction force in this case (Pure Rolling) can be determined from the kinematics analysis of the rotor when in contact with the stator. The equations of motion for a whirling rotor in polar coordinates:

$$ma_r + C\dot{r} + Kr = -F_N + F_e \tag{21}$$

$$ma_t + C\Omega r = F_t \tag{22}$$

$$J\alpha + K_\varphi(\varphi - \omega t) + C_\varphi \dot{\varphi} = -F_t R \tag{23}$$

Where $\boldsymbol{r}$ is the rotor radial displacement, $\boldsymbol{C}$ is the lateral damping value, and $\boldsymbol{C_\varphi}$ is the rotational damping coefficient due to surrounding drilling fluid (mud).

$$r = \sqrt{x^2 + y^2} \tag{24}$$

From equation (22),

$$a_t = (F_t - C.\Omega.r)/m \tag{25}$$

Then from equation (14): as $\alpha = a_t$/R, then The tangential friction force can be determined from equation (23):

$$F_t = \frac{C.\Omega.r - \left(\frac{m.R}{J}\right)\left(K_\varphi(\varphi - \omega.t) + C_\varphi.\dot{\varphi}\right)}{\left(1 + \frac{m.R^2}{J}\right)} \tag{26}$$

Hence,

$$F_t = \begin{cases} eiq.(25) \quad if \quad Ft < Ft_{max} ==> Pure\ Rolling \\ eiq.(18) \quad if \quad Ft > Ft_{max} ==> Sliding/Transition \end{cases} \tag{27}$$

The contact force can be expressed in stationary coordinate system in x and y as:

$$F_x = \frac{-F_t.y - F_N.x}{r} \tag{28}$$

$$F_y = \frac{F_t . x - F_N . y}{r} \tag{29}$$

The lateral forces due to mass unbalance that causes the lateral motion are given as:

$$F_{ex} = m. e. \dot{\varphi}^2 . \cos \varphi \tag{30}$$

$$F_{ey} = m. e. \dot{\varphi}^2 . \sin \varphi \tag{31}$$

Where, φ is the rotor rotation angle, and $\dot{\varphi}$ is the rotor angular velocity.

For simplification in this model, we will assume that the rotor disk represents a BHA collar not a drillbit so we will not consider the forces related to *WOB* and *TOB*. As the contact between rotor and stator induces the contact forces F_N and F_t, the tangential contact force F_t induces a torque on the rotor,

$$T_b = F_t . R \tag{32}$$

Equation of Motions

The equations of motion for the rotor's stick-slip model and whirl model combining the lateral and the torsional vibrations, and taking into account the lateral and rotational damping due to drilling fluids, contact forces, contact torque, and lateral forces due to mass unbalance, gives the following set of equations of motion in its general form:

$$m\ddot{x} + c\dot{x} + kx = F_x + F_{ex} \tag{33}$$

$$m\ddot{y} + c\dot{y} + ky = F_y + F_{ey} \tag{34}$$

$$J\ddot{\varphi} + c_\varphi \dot{\varphi} + k_\varphi(\varphi - \omega t) = T_b \tag{35}$$

Where (X, Y) is the position of the rotor's geometric center, and φ is the rotor's rotational angle.

From previous discussions we can summarize the following conditions for Forward and Backward whirling.

Backward Whirling with Pure Rolling

The rotor will roll without slipping over the stator only when four conditions are satisfied:

1. There is contact between rotor and stator, ($r \geq R_c$),
2. Relative velocity is zero, ($V_{rel}=\Omega\, r+ \varpi\, R=0$),
3. Tangential contact force does not exceed the maximal friction force, ($-\mu\, F_N <= F_t <= \mu\, F_N$)
4. Whirling direction is opposite to the rotor's rotational direction about its center.

The mean angular whirling velocity of the rotor in case of backward whirling is found to beclose to $-(R/r).\omega$, which implies that the contact between the rotor and the stator wall approaches that of (Rolling without slipping) where the rotor tangential velocity $\Omega r=\omega R$. Therefore we can calculate theoretically the backward whirling velocity as follows:

$$\Omega = -\left(\frac{R}{R_c}\right)\omega = -\Gamma.\omega \qquad (36)$$

Where, Γ is the precession frequency ratio (PFR) which represents the ratio of whirl frequency to rotor angular speed that is governed by the measured radius-to-clearance ratio at the contact location. Since the rotor radius, R, is much larger than the radial displacement or the clearance, R_c, the backward whirl velocity can reach to more than 30 times that of the rotor's angular velocity. Therefore dry–friction instabilities at low speeds can still produce high frequency vibrations, and that makes the backward whirling vibration mode in drillstring is the most severe and violent mode of vibration.

In simulation, as there will be a numerical difficulty for the integrator to reach a whole zero value for the relative velocity, V_{rel}, at pure-rolling condition, it is recommended to set minimum velocity value (V_{min}=0.001 m/s) so as to consider the rotor in a backward whirling condition if the relative velocity reached below this value ($V_{rel} < V_{min}$).

Forward Whirling (Pure Sliding)

The rotor will whip over the stator wall with a slipping friction behavior when three conditions are satisfied:

1. There is contact between rotor and stator, ($r \geq Rc$),
2. Relative velocity is non-zero, ($V_{rel}=\Omega\, r+ \omega\, R\neq 0$),
3. Whirling direction is the same to the rotor's rotational direction about its center

Otherwise 'Pure-rolling' or 'pure-sliding', the rotor can experience a mix of backward-whirling with some sliding (not pure rolling), or a discrete contact with the stator resultant from unstable random impacts with the stator wall.

Simulation Flowchart Logic

The flowchart below illustrates the logic behind the rotor/stator simulation program using Matlab, indicating the different modes that could encounter the rotating rotor inside the stator under the different mathematical constraints.

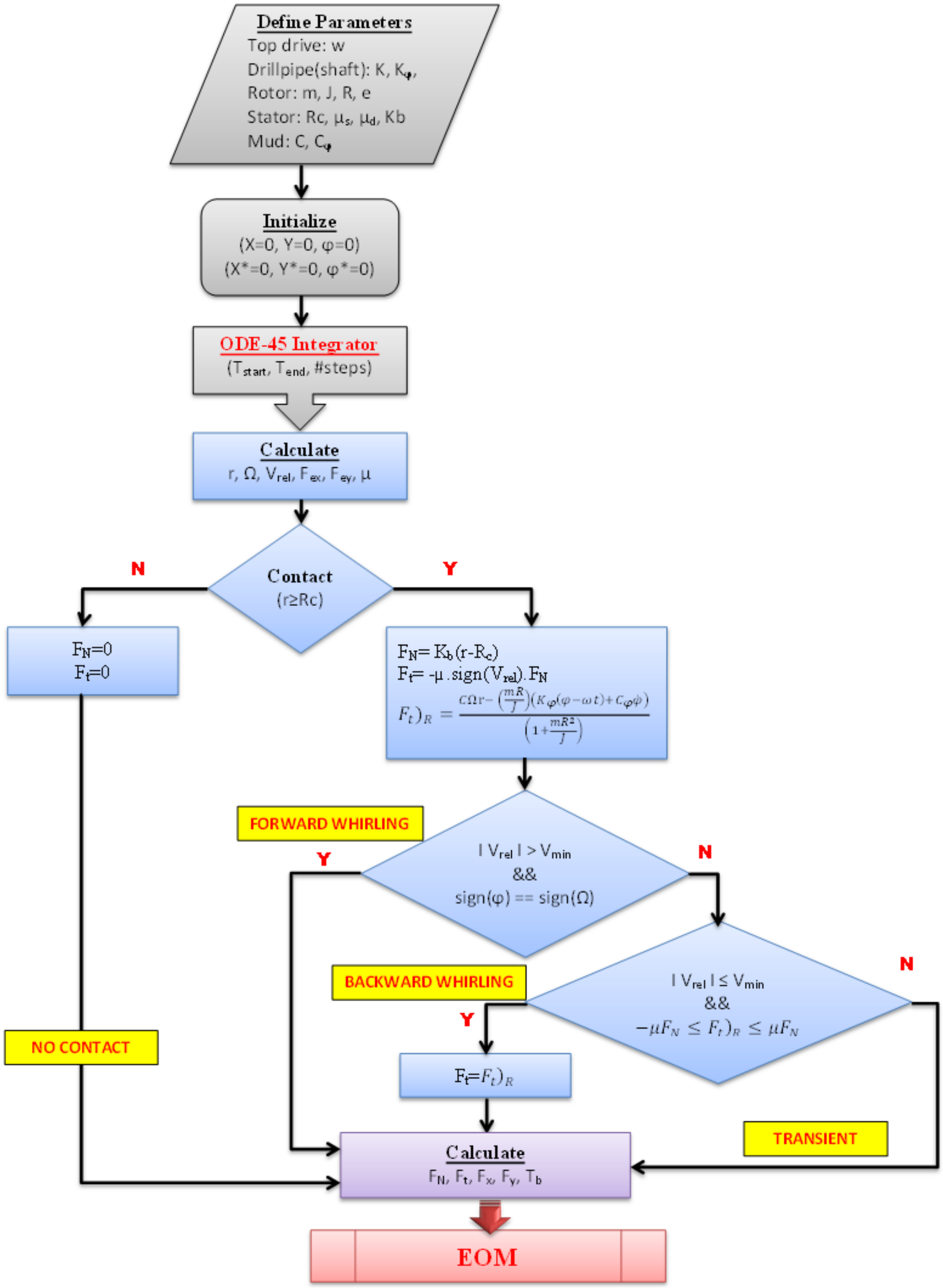

Figure 38 Simulation Flowchart Logic

Simulation Studies

Different studies have been conducted to simulate the different rotor dynamics modes before, during, and after rotor/stator contact under variable friction coefficients between the rotor and the stator, as well as under different operational speeds. Applying the equations of motion (33), (34), and (35), the differential integration solver ODE45 in Matlab is used to solve the differential equations using the 4^{th} order Runge-Kutta method. Stator stiffness is chosen to be 10^4 times that of the rotor's to understand the effect of the elastic contact between the rotor and the stator. A uniform clearance, R_c, is assumed between the rotor and the stator when the rotor is stationary. The effect of the gravity is ignored. The rotor has an eccentricity, e, between its center of mass and its geometric center. The rotor will have a different friction coefficient in each simulation run under a fixed operational speed to study the effect of varying the friction coefficient on the rotor dynamics. The rotor also will have a different operational speed in another patch of simulation runs under a fixed coefficient of friction to study and analyze the resultant dynamics. The code generally follows the same logic illustrated in the flowchart shown above in figure 38. The following parameters have been fixed in all the four simulation studies:

Table 2 Simulation Parameters for Rotor-Stator Model

Parameter	Value
Rotor radius, R	0.05 (m)
Rotor eccentricity, e	0.001 (m)
Rotor clearance, R_c	0.0025 (m)
Shaft bending stiffness, K	40 (N/m)
Shaft torsional stiffness, K_φ	0.6 (N.m/rad)
Stator stiffness, K_b	40e4 (N/m)
Rotor mass, m	1 (Kg)
Rotor inertia, J	0.0013 (Kg.m^2)
Mud lateral damping, C	1 (N/ms)
Mud torsional damping, C_φ	0.2 (N.s/rad)
Top drive angular speed, ω	12 – 16 (rad/sec)
Friction coefficient,	0 - 0.15 (-)

Following are the results obtained from the different studies conducted using the above parameters' values listed in Table 2.

Simulation Results

Rotor-Stator Contact with Synchronous Forward Whirling

For a very small coefficient of friction, the rotor starts with a short transient impact phase, due to initial perturbation from the mass imbalance excitation, followed by full rubbing with the stator wall. The full rubbing behavior is denoted with a continuous contact with the stator in a forward whirling motion having the same direction and rate as the rotor rotation about its center. Figure 39 shows the dynamic response of the rotor-stator model under self-excitation.

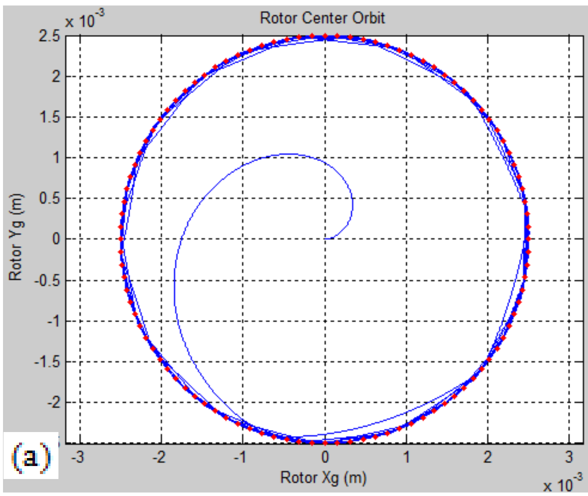

ω= 12.6491 (rad/sec)

μ= 0.001

kb/k= 10,000 (N/m)

e= 0.001 (m)

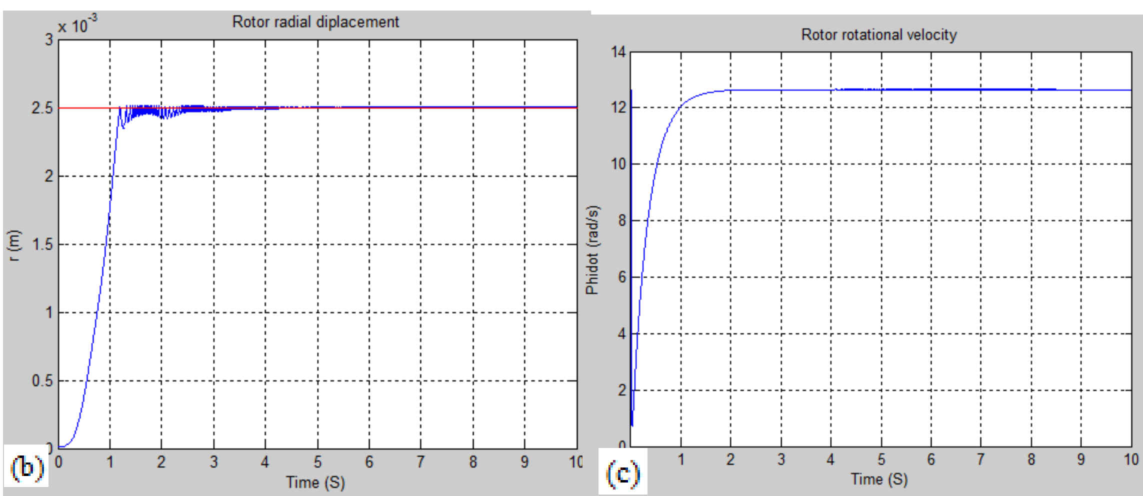

Figure 39 Rotor-Stator Contact with Synchronous Forward-Whirl

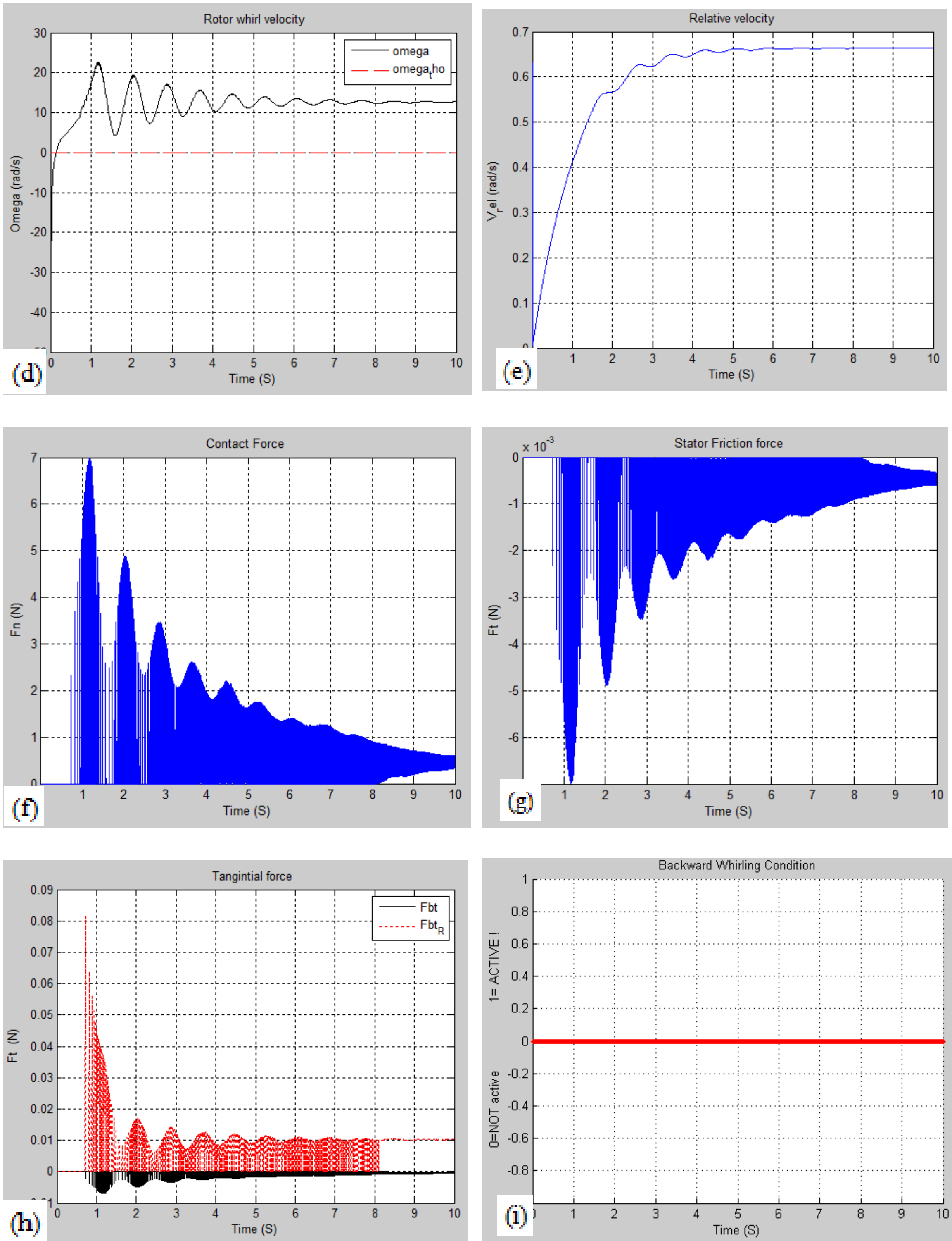

Figure 39 Continued

Panel (a) shows the orbit of the rotor geometric center in the (X, Y) plane. The doted red circle indicates the clearance boundary. Panel (b) shows the radial excursion of the rotor as a function of time, where the red line indicates the clearance boundary limit. Panel (c) the angular velocity of the rotor as a function of time. Panel (d) the rotor whirling velocity and the dashed red line indicates the theoretical whirling velocity in case of backward whirling. Panel (e) the relative velocity between the rotor and the stator at the contact point. Panel (f) shows the normal contact force on the rotor. Panel (g) the tangential friction force on the rotor. Panel (h) indicates the tangential friction force at a nonzero relative velocity condition (black line), compared to the friction force calculated at zero relative velocity (red dashed line) using equation (26). Panel (i) indicates the backward status of the rotor throughout the simulation time when all four conditions are satisfied as mentioned previously.

From the results obtained we can conclude that the friction force is not high enough to change the synchronous, or the continuous, forward full rubbing motion of the rotor into “Backward whirling” with pure dry-friction rolling motion.

Rotor-Stator Dynamic Response with Discrete Impact and Unsteady Whirl

The increase of friction coefficient changes the response nature of the rotor dynamics. The rotor makes discrete random contact with the stator. The rotor geometric center behaves with a forward whirling motion but not at a constant rate as in the previous study. A discrete rotor impact with chaotic unsteady whirling motion is resultant at an intermediate coefficient of friction.

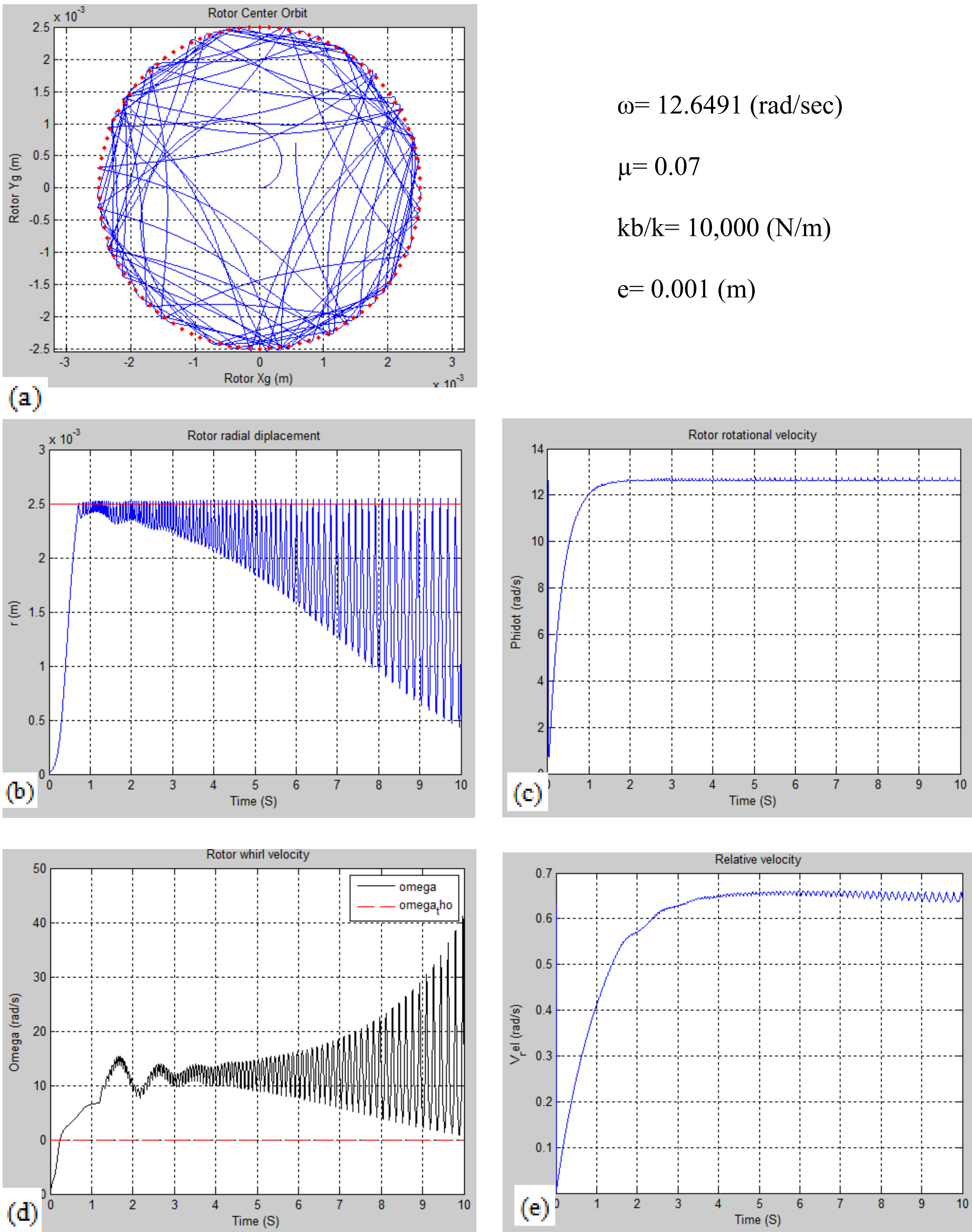

ω= 12.6491 (rad/sec)

μ= 0.07

kb/k= 10,000 (N/m)

e= 0.001 (m)

Figure 40 Rotor-Stator Dynamic Response with Discrete Impact and Unsteady Whirl

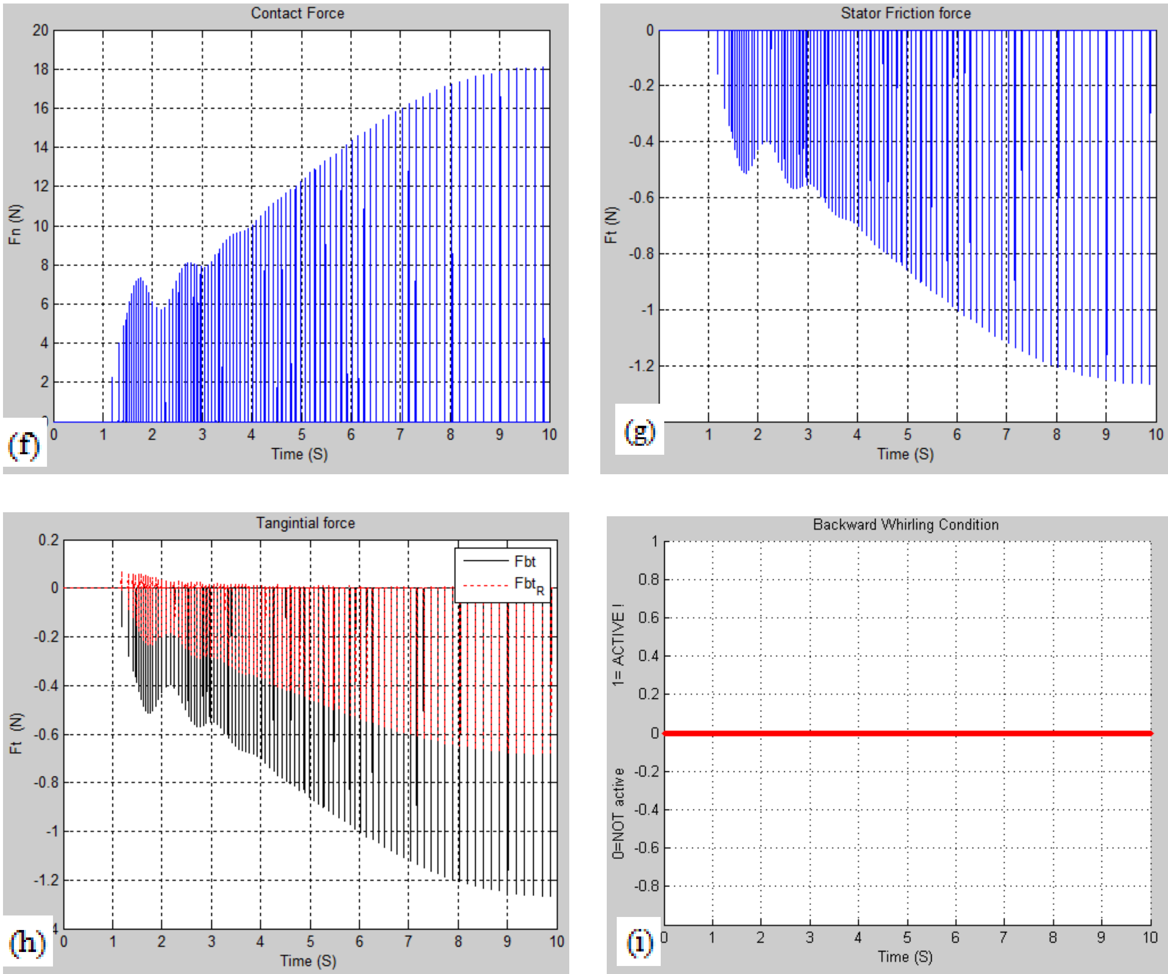

Figure 40 Continued

From the results we can conclude that the friction coefficient still not high enough to apply sufficient friction force on the rotor contact to resist the sliding motion and switch it in to rolling motion, or to a backward whirling.

Rotor-Stator Dynamic Response with a Backward Whirl

By increasing the friction coefficient, the rotor starts with a discrete impacts characterized by unsteady whirling then a backward whirl is fully developed at about 7.3 second when the relative velocity at the contact point between the rotor and stator reaches zero as shown in figure 41 (e). That leads to a very large whirling velocity, about 26 times the rotor's angular velocity, where it reaches to about 330 (rad/sec) compared to 12.6 (rad/sec) for the rotor's angular velocity as shown below in figure 41 (d). A large centrifugal force will result from the very high frequency backward whirl, which can lead to a large stator deformation as shown in the last panels (a) and (b).

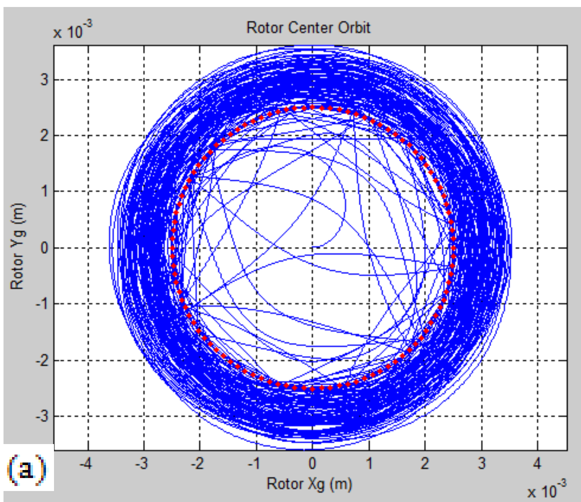

ω= 12.6491 (rad/sec)

μ= 0.15

kb/k= 10,000 (N/m)

e= 0.001 (m)

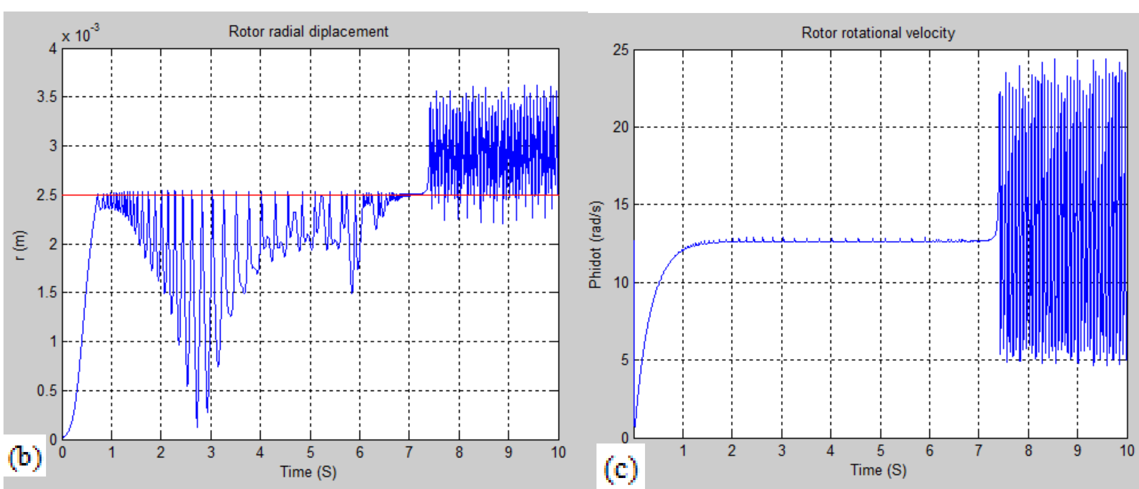

Figure 41 Rotor-Stator Dynamic Response with Backward Whirl

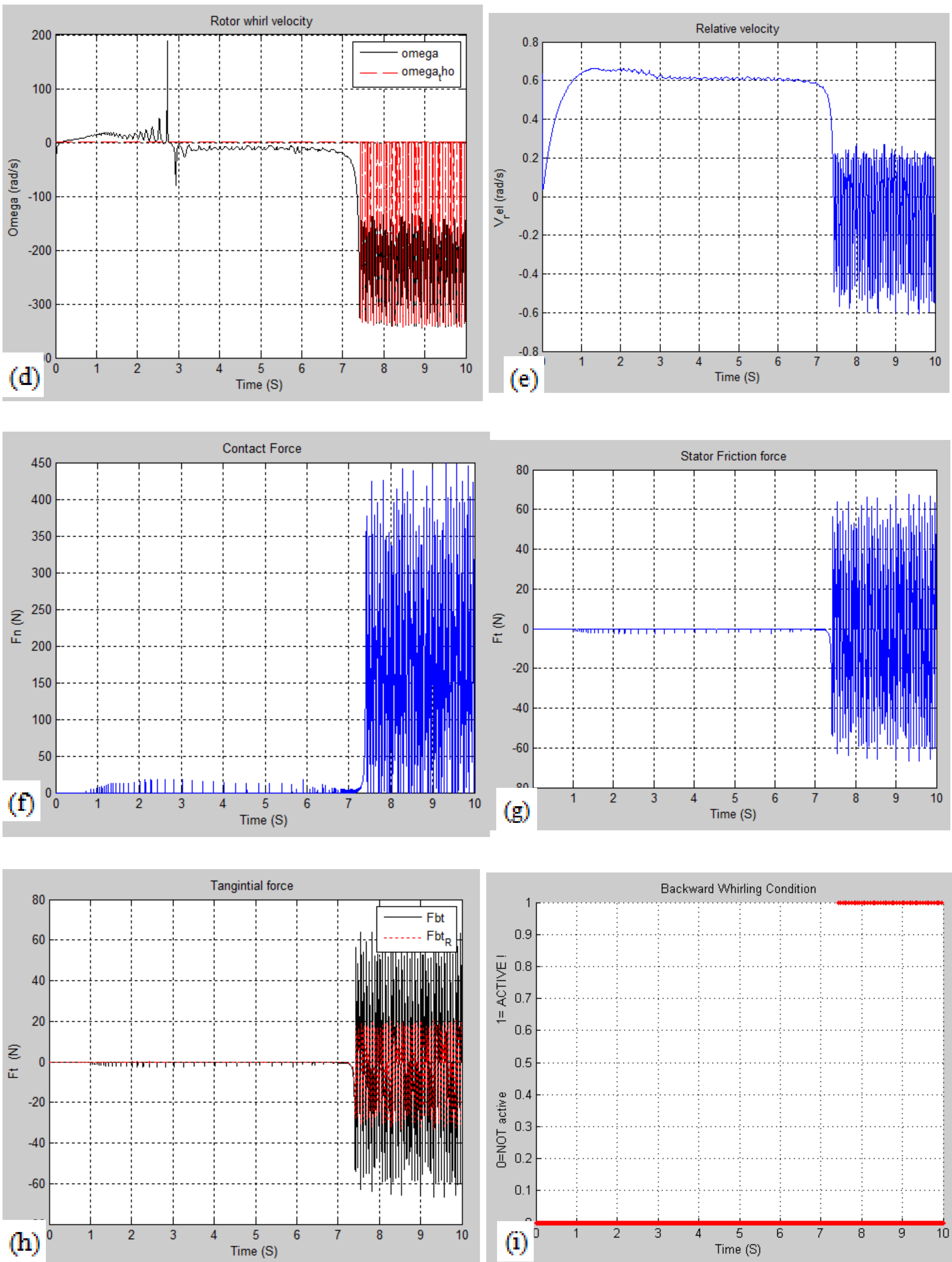

Figure 41 Continued

The increase of friction leads to an increase of the friction torque at the contact point and hence a deceleration and decrease of the rotor's angular speed occurs. As there is a constant applied torque on the top shaft, the applied torque will build up along the shaft length till it overcomes the friction torque causing a rapid acceleration in the rotor's rotation speed. This can explain the fluctuations in the rotor's angular velocity shown in panel (c) reaching double the operating rotation speed. Panel (d) shows how the theoretical backward whirl velocity calculated from equation (36) indicated by the dashed red line, is very close to the whirl velocity indicated by the black line obtained from dynamic response. Panel (h) indicates the tangential friction force at a nonzero relative velocity condition (black line), compared to the friction force calculated at zero relative velocity (red dashed line), where in case of backward whirl the Ft_R should be less than Ft as illustrated previously in equations (20) and (26). Panel (i) indicates the backward status of the rotor throughout the simulation time when all four conditions are satisfied as mentioned before. From the plot the pure rolling, or backward whirl, begins to occur at about 7.3 sec when the contact relative velocity reaches to zero, and Ft_R is less than the Ft.

Conclusion

The friction coefficient of the formation and the rotor's rotational speed can dramatically affects the rotor dynamics. Figure 42 shows how by increasing the friction coefficient between the rotor and stator, the geometric center of the rotor can change from pure sliding forward whirl to backward whirl and even to pure rolling without slipping, indicated by reaching to a zero contact relative velocity. When the rotor rubs the stator, the friction changes the forces acting on the rotor dynamics which can be drastically different.

Figure 43 shows how by increasing the spinning velocity of the rotor, the backward whirl could occur earlier. The imbalance centrifugal force, due to eccentricity, has a direct proportional relationship with ω^2 as shown in equation (30). Increasing the rotor's spinning velocity results in higher centrifugal force acting on the rotor providing an early contact with the stator with a higher contact friction force, induced form higher normal contact force, and hence a higher probability of an early backward whirl.

In addition to the coefficient of friction and rotor's rotational speed parameters, the rotor's radius to clearance ration (R/R_c) affects significantly the rotor dynamics and specifically the backward whirl velocity. The backward whirl velocity will be large if this ratio is large. Therefore, in engineering drillstring design, the clearance between the largest component radius and the borehole is an important parameter, where the ration should be minimal. The eccentricity in the drillbit, or the in the overall drillstring/BHA body length, is another very important parameter. The mass imbalance is the major cause of lateral vibration self-excitation due to the centrifugal force induced.

Rotational vibration is induced mainly from three parameters; rotation speed, coefficient of friction, and axial force or *WOB*. Operating at low spinning speeds with high friction coefficient will cause in higher friction torque applied on the rotor. This results in rotor's speed deceleration till the built-up applied torque overcomes it and releases the rotor before reaching the stop or 'Stick' status causing the 'Slip' behavior.

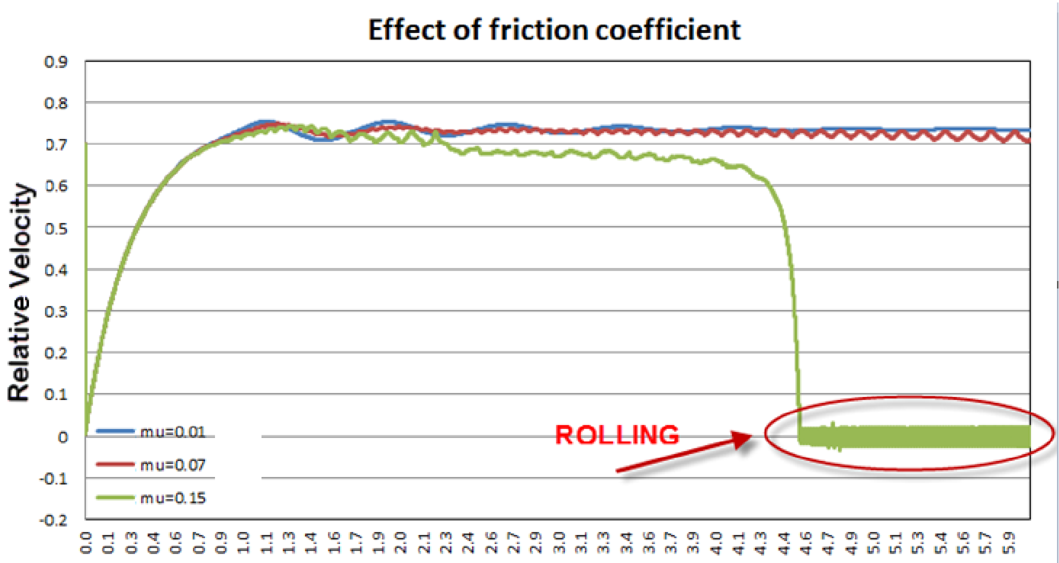

Figure 42 Effect of Friction Coefficient on the Rotor Dynamics

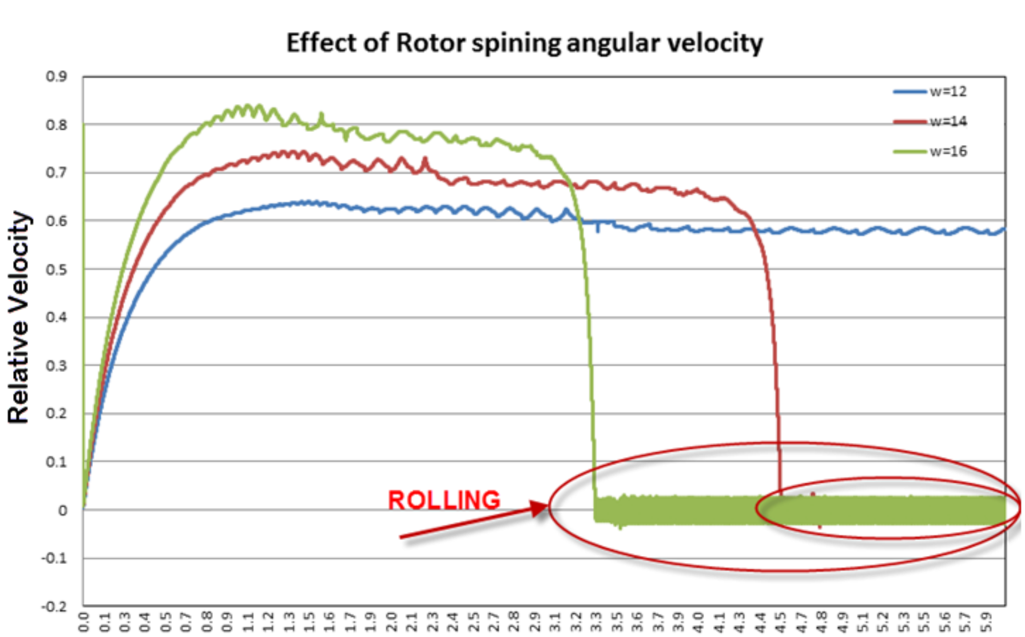

Figure 43 Effect of Rotor Rotational Angular Velocity on the Rotor Dynamics

In a more advanced system model and by taking into consideration the axial DOF, we will see how the Torque-On-Bit, which is directly proportional to *WOB*, contributes in Stick-slip vibrations. Increasing the *WOB* will result in high frictional torque on bit, which will leads eventually to a total 'Stick' and 'Slip'. Stick-slip vibrations are self-excited and caused mainly by the nonlinear frictional torque between the drillstring component and the borehole.

6.2 Drillstring Lumped System Modeling

Objective

The objective here is to build a more accurate, but still simplified, mathematical model to simulate the drillstring dynamics including drillbit consisting of three lumped masses that represents the drillstring assembly with its FULL-DOF's (6 DOF for each lumped mass). The model allows studying and analyzing the drill-pipes, BHA, stabilizers, and drillbit dynamic behaviors including axial and rotational vibrations with bit/rock interaction.

Theoretical Background

In the previous section we were able to simulate the lateral and rotational vibrations in a simple rotor-stator model with 3-DOF system model representing the drillpipes with lumped mass system. The advantages of using this lumped mass and spring method in modelling drillstring is to keep the simplicity and have a considerably faster analysis compared to the FE-Method. Another advantage is that we can simply adjust the model parameters to reproduce the nonlinear drillstring vibrations for a quick dynamic analysis of the drilling process. To be able to simulate the drillstring dynamics using the lumped mass approach, we need first to model the drillbit dynamics including the axial and torsional motion and the coupling between them. This requires modeling the nonlinear drillbit-rock interaction, and understanding the relation between the friction Torque-On-Bit (*TOB*) with the Weight-On-Bit (*WOB*) and bit diameter.

Drillbit is responsible for rock formation cutting and penetration in drillstring. There are two different kinds of bits exist: fixed cutter and roller cone. A fixed cutter bit is one where there are no moving parts, but drilling occurs due to percussion or rotation of the drill string. A Roller cone bit usually has three cone shape devices with teeth or cutters, whereas the drillstring rotates the cones rotate to drill ahead. The Polycrystalline-Diamond-Compact bit (PDC), which is a fixed cutter bit type, and the tricone Roller-cone bit, are the most generally used in drilling.

For the (PDC) drillbit type, the depth of cut per revolution per blade is given as below:

$$d_n(t) = x_{db}(t) - x_{db}(t - t_n) \tag{37}$$

Where x_{db}, is the vertical position of the drillbit, $t_n$is instantaneous time delay that the bit requires to rotate by 2π/n to its current position at time *t* obtained by solving the equation:

$$\varphi_{db}(t) - \varphi_{db}(t - t_n) = 2\pi/n \tag{38}$$

Where φ_{db}, is the drillbit angular position, and *n* is the number of blades. Hence, the combined depth of cut for the bit is given as:

$$d_c = n.d_n \tag{39}$$

The bit response depends on two important parameters; Weight-On-Bit (*WOB*), and Torque-On-Bit (*TOB*).The drilling action of a bit consists of a pure cutting process, and a frictional process. Both *WOB* and *TOB* thus should be expressed into two components:

$$WOB = W_c + W_f \tag{40}$$

$$TOB = T_c + T_f \tag{41}$$

The cutting and frictional components for both *WOB* and *TOB* are given as [15]:

$$W_c = a.\xi.\varepsilon.d_c \tag{42}$$

$$T_c = \frac{a^2}{2}.\varepsilon.d_c \tag{43}$$

$$W_f = a.l.\sigma \tag{44}$$

$$T_f = \frac{a^2}{2}.\gamma.l.\sigma.\mu \tag{45}$$

Where, a is the bit radius, ξ characterizes the inclination of the cutting force and typically $0.6 \leq \xi \leq 0.8$, $\boldsymbol{\varepsilon}$ is the intrinsic specific energy (the energy required to cut a unit volume of rock), σ is the normal stress acting across the wear flat interface, and γ characterizes the spatial orientation and distribution of the chamfers/wearflats and for a flat-bottom bit is typically $1 \leq \gamma \leq 1.3$. l is the equivalent total wear flat for the bit and is given as:

$$l = n.l_n \tag{46}$$

Where l_n , is the width of wearflat for a single blade.

The above relations of *WOB* and *TOB* are specifically to model a typical PDC drill bit with a time delay function due to the cutting action of the blades. However, in a more general and simple representation form to model the PDC, or roller-cone bits with no time delay term, the instability hence could be represented in terms of the self-excitation with the sinusoidal nature. Therefore, the *WOB* and *TOB* can be expressed as follows [39, 40]:

$$WOB = \begin{cases} K_c.(x_{db} - S), & if\ x_{db} \geq S \\ 0, & if\ x_{db} < S \end{cases} \tag{47}$$

Where K_c, is the formation contact stiffness, which can be calculated from the following equation:

$$K_c = a.n.\zeta.\varepsilon \tag{48}$$

The formation surface elevation, S, is given as:

$$S = S_0.\sin(\varphi_{db}) \tag{49}$$

The depth of cut per revolution, d_c, in this case is given as:

$$d_c = \frac{2.\pi.ROP}{\dot{\varphi_{db}}} \tag{50}$$

The average Rate-Of-Penetration, *ROP*, is a function of the applied load W_0, bit speed $\dot{\varphi_{db}}$, and the bit/rock characteristics given as [39]:

$$ROP = C_1.W_0.\sqrt{\dot{\varphi_{db}}}+C_2 \tag{51}$$

The *TOB* is function in *WOB* and cutting conditions, and is given as:

$$TOB = WOB.\left(\mu + \sqrt{\frac{d_c}{a}}\right).a \tag{52}$$

Equations, (47) and (52), describes the coupling between the axial and rotational vibrations induced by the self-excitation axial sinusoidal function from equation (49).

The Stribeck friction model is utilized according to [35, 39] to describe the nonlinear friction behavior between the bit and the formation. This behavior is modeled by a continuous function given as:

$$\mu = \mu_0 . \left(\tan^{-1} \dot{\varphi_{db}} + \frac{\alpha . \dot{\varphi_{db}}}{1 + \beta . \dot{\varphi_{db}}^{2\gamma}} + \nu . \dot{\varphi_{db}} \right) \tag{53}$$

Where μ_0, α, β, γ, and ν are the parameters of the friction model, which characterize the friction behavior as shown in figure 20. These parameters depend on the type of formation and of drillbit used. The negative slope at very low speeds causes the instability in the rotational motion and the bit may reaches to speeds up to three times the operation speed (desired speed). This results in self-sustained stick-slip oscillations. Increasing bit speed will result in a more stable system.

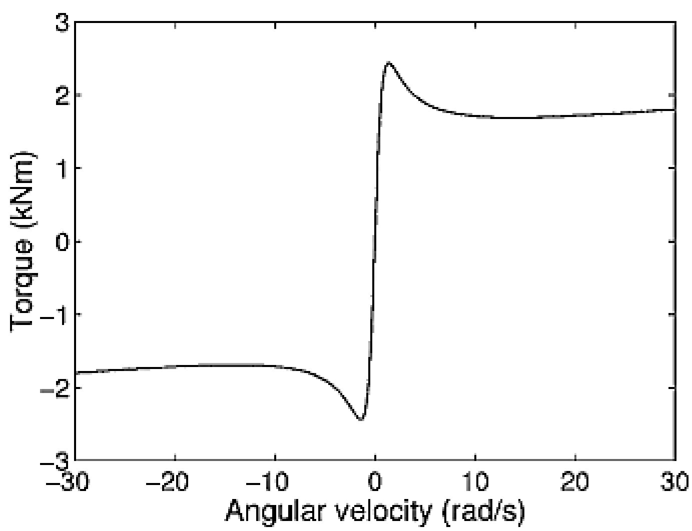

Figure 44 Friction Behavior of the Drillbit and Rock Formation [39]

At normal drilling operation with steady-state condition, the axial penetration velocity of the drillbit is equal to the *ROP*, and drillbit should have the same rotational velocity as the top drive speed applied at the surface. This implies that the *WOB* is equal to the applied load, W_0, on the drillstring at the surface, and the *TOB* is equal to the driving torque T_d. If the *TOB* is higher than the top driving torque T_d, the drillbit decelerates and could reach to zero spinning which known as 'sticking'. As the built-up torsional torque potential energy overcomes the applied *TOB*, the drillbit is suddenly released causing it to accelerate to even three times the top drive speed. This behavior is known as 'slipping'. This Stick-slip cycle will usually repeat again and again as long as the same conditions are applied and the operation left unchecked. Bit-Bounce; is an axial vibration behavior occurs when the normal reaction force from the formation, or *WOB*, is greater than the top applied load, W_0, which results in drillbit loss of contact with the bottom formation forcing the BHA upwards with negative axial displacement and velocity, till the top applied load, W_0, and the total weight of drillstring and mud weight force the BHA downwards again to contact with the bottom formation.

Lumped System Modeling

The model describing the drillstring is obtained by assuming that the drillstring is divided into three lumped masses (with inertias) connected one to each other by lateral, axial, and torsional stiffness, as well as axial, and lateral damping. Viscous torsional damping is applied on the whole drillstring assembly that represents the drilling fluid damping effect.

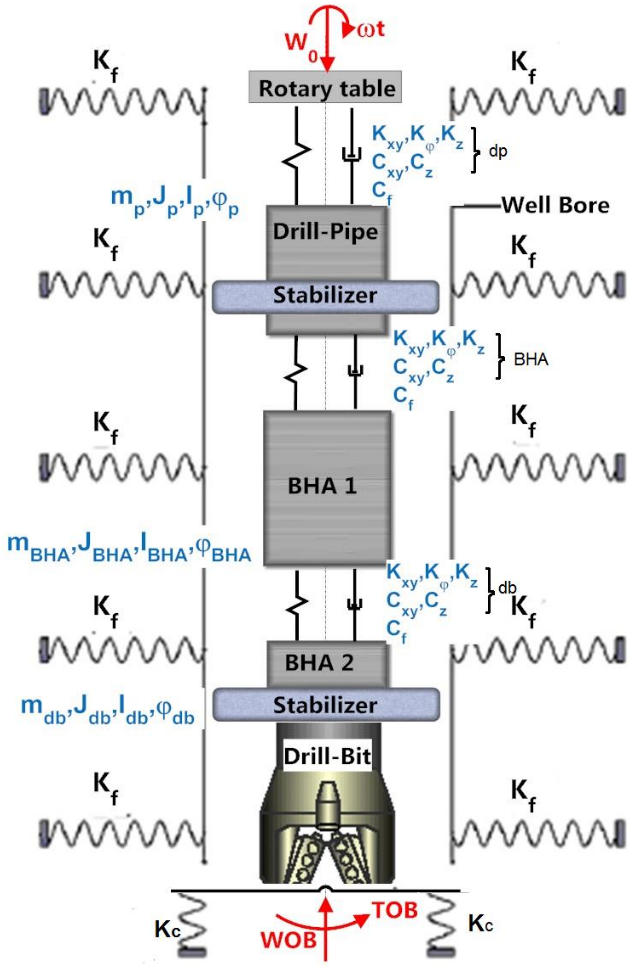

Figure 45 Drillstring Lumped System Model

Figure 45 describes the simplified drillstring assembly in its full DOFs. The model consists of four elements:

1) A massless top-rotary system with applied axial load from top W_0, and constant rotational speed ω. The massless rotary system is fixed in 4-DOFs except the axial and rotational direction about the Z-axis.

2) The drillpipes with lumped mass m_{dp} and inertias J_{dp} and $I_{dp.}$ The lumped mass model has 6-DOFs (X, Y, Z, φ_x, φ_y, φ_z) and coupled with the rotary table from the top with axial, lateral, and torsional stiffness, as well as with axial, and lateral torsional damping. A stabilizer, with a radius bigger than the BHA radius, is attached to the drillpipes lumped mass.

3) The intermediate lumped mass represents the first half of the BHA-drill collars. This model has mass m_{BHA} and inertias J_{BHA} and $I_{BHA.}$ The lumped mass model has 6-DOFs (X, Y, Z, φ_x, φ_y, φ_z) and coupled with the drillpipes lumped mass model from top with axial, lateral, and torsional stiffness, as well as with axial, and lateral torsional damping.

4) The bottom lumped mass is considered to sum the drillbit model with the second half of the BHA-drill collars. A second stabilizer is attached to the lumped mass model having a radius equal to the drillbit. A very small clearance is considered between the stabilizers and the borehole. This mass portion will have 6-DOFs as well.

The Stribeck nonlinear friction model described in equation (17) is applied on both stabilizers in case of contact, as well as to the intermediate BHA lumped mass model. The Stribeck friction model that describes the nonlinear friction behavior between the bit and the formation (equation 53) is considered at the bit. *WOB*, and *TOB* are applied at the bit when in contact with formation. A ground viscous torsional damping, C_f, is applied on the whole drillstring assembly that represents the rotational damping due drilling fluid (mud).

The equations below describe the equation of motion of the drillstring assembly in its complete DOFs.

EOM-Drillpipes lumped mass

$$m_{dp}\ddot{X}_{dp} + C_{dp}(\dot{X}_{dp}) + C_{BHA}(\dot{X}_{dp} - \dot{X}_{BHA}) + K_{dp}(X_{dp}) + K_{BHA}(X_{dp} - X_{BHA}) = F_{x\_dp} \tag{54}$$

$$m_{dp}\ddot{Y}_{dp} + C_{dp}(\dot{Y}_{dp}) + C_{BHA}(\dot{Y}_{dp} - \dot{Y}_{BHA}) + K_{dp}(Y_{st}) + K_{BHA}(Y_{dp} - Y_{BHA}) = F_{y\_dp} \tag{55}$$

$$m_{dp}\ddot{Z}_{dp} + C_{z\_dp}(\dot{Z}_{dp}) + C_{z\_BHA}(\dot{Z}_{dp} - \dot{Z}_{BHA}) + K_{z\_dp}(Z_{dp}) + K_{z\_BHA}(Z_{dp} - Z_{BHA}) = W_0 + F_{z\_dp} \tag{56}$$

$$J_{dp}\ddot{\varphi_{z\_dp}} + C_f(\dot{\varphi_{z\_dp}}) + K_{\varphi z\_dp}(\varphi_{z\_dp} - \omega t) + K_{\varphi z\_BHA}(\varphi_{z\_dp} - \varphi_{z\_BHA}) = -T_{z\_dp} \tag{57}$$

$$I_{dp}\ddot{\varphi_{x\_dp}} + C_f(\dot{\varphi}_{X-dp}) + K_{\varphi x\_dp}(\varphi_{x\_dp}) + K_{\varphi x\_BHA}(\varphi_{x\_dp} - \varphi_{x\_BHA}) = -T_{x\_dp} \tag{58}$$

$$I_{dp}\ddot{\varphi_{y\_dp}} + C_f(\dot{\varphi}_{y\_dp}) + K_{\varphi y\_dp}(\varphi_{y\_dp}) + K_{\varphi y\_BHA}(\varphi_{y\_dp} - \varphi_{y\_BHA}) = -T_{y\_dp} \tag{59}$$

EOM-BHA lumped mass

$$m_{BHA}\ddot{X}_{BHA} + C_{BHA}(\dot{X}_{BHA} - \dot{X}_{dp}) + C_{BHA}(\dot{X}_{BHA} - \dot{X}_{db}) + K_{BHA}(X_{BHA} - X_{dp}) + K_{BHA}(X_{BHA} - X_{db}) = F_{x\_BHA} + F_{ex} \tag{60}$$

$$m_{BHA}\ddot{Y}_{BHA} + C_{BHA}(\dot{Y}_{BHA} - \dot{Y}_{dp}) + C_{BHA}(\dot{Y}_{BHA} - \dot{Y}_{db}) + K_{BHA}(Y_{BHA} - Y_{dp}) + K_{BHA}(Y_{BHA} - Y_{db}) = F_{y\_BHA} + F_{ey} \tag{61}$$

$$m_{BHA}\ddot{Z}_{BHA} + C_{z\_BHA}(\dot{Z}_{BHA} - \dot{Z}_{dp}) + C_{z\_BHA}(\dot{Z}_{BHA} - \dot{Z}_{db}) + K_{z\_BHA}(Z_{BHA} - Z_{dp}) + K_{z\_BHA}(Z_{BHA} - Z_{db}) = +F_z \tag{62}$$

$$(J_{BHA} + J_e)\ddot{\varphi_{z\_BHA}} + C_f(\dot{\varphi_{z\_BHA}}) + K_{\varphi z\_BHA}(\varphi_{z\_BHA} - \varphi_{z\_dp}) + K_{\varphi z\_BHA}(\varphi_{z\_BHA} - \varphi_{db}) = -T_{z\_BHA} \tag{63}$$

$$I_{BHA}\ddot{\varphi_{X\_BHA}} + C_f\left(\dot{\varphi}_{X\_BHA}\right) + K_{\varphi x-BHA}\left(\varphi_{X\_BHA} - \varphi_{X\_db}\right) + K_{\varphi x\_BHA}(\varphi_{X-BHA} - \varphi_{X-db}) = -T_{x\_BHA} \tag{64}$$

$$I_{BHA}\ddot{\varphi_{y\_BHA}} + C_f\left(\dot{\varphi}_{y\_BHA}\right) + K_{\varphi y\_BHA}\left(\varphi_{y\_BHA} - \varphi_{y\_db}\right) + K_{\varphi y\_BHA}\left(\varphi_{y\_BHA} - \varphi_{y\_db}\right) = -T_{y\_BHA} \tag{65}$$

EOM-Drillbit Lumped Mass

$$m_{BHA}\ddot{X}_{db} + C_{BHA}\left(\dot{X}_{db} - \dot{X}_{BHA}\right) + K_{BHA}(X_{db} - X_{BHA}) = F_{x\_db} - WOB_x \tag{66}$$

$$m_{BHA}\ddot{Y}_{db} + C_{BHA}\left(\dot{Y}_{db} - \dot{Y}_{BHA}\right) + K_{BHA}(Y_{db} - Y_{BHA}) = F_{y\_db} - WOB_y \tag{67}$$

$$m_{BHA}\ddot{Z}_{db} + C_{z\_BHA}\left(\dot{Z}_{db} - \dot{Z}_{BHA}\right) + K_{z\_BHA}(Z_{db} - Z_{BHA}) = F_{z\_db} - WOB_z \tag{68}$$

$$J_{db}\ddot{\varphi_{z\_db}} + C_f(\dot{\varphi_{z\_db}}) + K_{\varphi z\_BHA}\left(\varphi_{z\_db} - \varphi_{z\_BHA}\right) = -TOB - T_{z\_db} \tag{69}$$

$$I_{db}\ddot{\varphi_{x\_db}} + C_f\left(\dot{\varphi}_{x\_db}\right) + K_{\varphi x\_BHA}\left(\varphi_{x\_db} - \varphi_{x\_BHA}\right) = -T_{x\_db} \tag{70}$$

$$I_{db}\ddot{\varphi_{y\_db}} + C_f\left(\dot{\varphi}_{y\_db}\right) + K_{\varphi y\_BHA}\left(\varphi_{y\_db} - \varphi_{y\_BHA}\right) = -T_{y\_db} \tag{71}$$

For the upper lumped mass that represents the Drillpipes mass with stabilizer, the contact forces can be expressed or analyzed in the Cartesian stationary system (X, Y, Z) as:

$$F_{x\_dp} = [-F_{N\_db}.\left(X_{dp}\right) - F_{t\_dp}.\left(Y_{dp}\right)]/r_{dp} \tag{72}$$

$$F_{y\_dp} = \left[-F_{N\_db}.\left(Y_{dp}\right) + F_{t\_dp}.\left(X_{dp}\right)\right]/r_{dp} \tag{73}$$

$$F_{z\_dp} = -sign\left(\dot{Z}_{dp}\right).\mu_0.F_{N\_dp} \tag{74}$$

Hence, the toques applied due to contact forces in X, Y, Z axes:

$$T_{x\_dp} = sign(\dot{\varphi_{x\_dp}}).\mu_0.F_{N\_dp}.R_{st}.\frac{\left|Y_{dp}\right|}{r_{dp}} \tag{75}$$

$$T_{y\_dp} = sign(\dot{\varphi_{y\_dp}}).\mu_0.F_{N\_dp}.R_{st}.\frac{|X_{dp}|}{r_{dp}} \tag{76}$$

$$T_{z\_dp} = sign(\dot{\varphi_{z\_dp}}).F_{t\_dp}.R_{st} \tag{77}$$

For the intermediate lumped mass that represents the first portion of the BHA-Drill collars, the contact forces can be expressed or analyzed in the Cartesian stationary system (X, Y, Z) as:

$$F_{x\_BHA} = [-F_{N\_BHA}.(X_{BHA}) - F_{t\_BHA}.(Y_{BHA})]/r_{BHA} \tag{78}$$

$$F_{y\_BHA} = [-F_{N\_BHA}.(Y_{BHA}) + F_{t\_BHA}.(X_{BHA})]/r_{BHA} \tag{79}$$

$$F_{z\_BHA} = -sign(\dot{Z}_{BHA}).\mu_0.F_{N\_BHA} \tag{80}$$

Hence, the toques applied due to contact forces in X,Y,Z axes:

$$T_{x\_BHA} = sign(\dot{\varphi_{x\_BHA}}).\mu_0.F_{N\_BHA}.R_{BHA}.\frac{|Y_{BHA}|}{r_{BHA}} \tag{81}$$

$$T_{y\_BHA} = sign(\dot{\varphi_{y\_BHA}}).\mu_0.F_{N\_BHA}.R_{BHA}.\frac{|X_{BHA}|}{r_{BHA}} \tag{82}$$

$$T_{z\_BHA} = sign(\dot{\varphi_{z\_BHA}}).F_{t\_BHA}.R_{BHA} \tag{83}$$

The eccentricity force induced due to mass imbalance can be expressed in X, Y coordinates as:

$$F_{ex} = F_e \, . \cos\varphi_{z\_BHA} \tag{84}$$

$$F_{ey} = F_e . \sin\varphi_{z\_BHA} \tag{85}$$

Where;

$$F_e = e.m_{BHA}.\dot{\varphi_{z\_BHA}}^2 \tag{86}$$

For lower lumped mass that represents the second portion of the BHA-Drill collars in addition to the drillbit and stabilizer, the contact forces can be expressed or analyzed in the Cartesian stationary system (X, Y, Z) as:

$$F_{x\_db} = [-F_{N\_db}.(X_{db}) - F_{t\_db}.(Y_{db})]/r_{BHA} \tag{87}$$

$$F_{y\_db} = [-F_{N\_db}.(Y_{db}) + F_{t\_db}.(X_{db})]/r_{db} \tag{88}$$

$$F_{z\_db} = -sign(\dot{Z}_{db}).\mu_0.F_{N\_db} \tag{89}$$

Hence, the toques applied due to contact forces in X,Y,Z axes:

$$T_{x\_db} = sign(\dot{\varphi}_{x\_db}).\mu_0.F_{N\_db}.a.\frac{|Y_{db}|}{r_{db}} \tag{90}$$

$$T_{y\_db} = sign(\dot{\varphi}_{y\_db}).\mu_0.F_{N\_db}.a.\frac{|X_{db}|}{r_{db}} \tag{91}$$

$$T_{z\_db} = sign(\dot{\varphi}_{z\_db}).F_{t\_db}.a \tag{92}$$

Where, a, is the drillbit radius.

Most of the drill collar weight is supported by the drillpipe and a fraction of it is applied on the bit (applied *WOB*). Under static conditions this applied force W_0 is the difference between the total weight and the hook load. *WOB* is the weight on bit, which is the axial force applied at the bit under dynamic conditions, and in our case here is given as:

$$\mathrm{WOB}_Z = \begin{cases} K_c(z-s) & \text{if } z \geq s \\ 0 & \text{if } z < s \end{cases} \tag{93}$$

Where K_c is the formation contact stiffness and S is the formation surface elevation given as:

$$S = S_0 \,.\, \sin(\varphi_{z\_db}) \tag{94}$$

If there is a drillbit tilt angle, α, there will be lateral forces components for the *WOB* in X,Y direction acts on the drillbit as well:

$$WOB_x = WOB_z \,.\, \tan\alpha \,.\, \cos\varphi_{z\_db} \tag{95}$$

$$WOB_y = WOB_z \,.\, \tan\alpha . \sin\varphi_{z\_db} \tag{96}$$

The toque on bit, *TOB*, is related to the *WOB* and cutting conditions and is given as:

$$TOB = WOB_Z \left(\mu_{(\dot{\varphi_{z\_db}})} + \sqrt{\frac{d_c}{a}} \right) a \tag{97}$$

Where d_c is the depth of cut per revolution, and $\mu_{(\dot{\varphi_{z\_db}})}$ is the Stribeck nonlinear friction function of the drillbit rotation speed and are given as:

$$\mu_{(\dot{\varphi_{z\_db}})} = \mu_0 \left(\tan^{-1} \dot{\varphi_{z\_db}} + \frac{2\dot{\varphi}_{z\_db}}{1 + \dot{\varphi_{z\_db}}^2} + 0.01\dot{\varphi_{z\_db}} \right) \tag{98}$$

$$d_c = \frac{2.\pi.ROP}{\dot{\varphi_{z\_db}}} \tag{99}$$

The rate of penetration, *ROP*, here will be a function of applied weight on bit W_0, and the bit speed, and rock/bit characteristics given as:

$$ROP = C_1 . W_0 . \sqrt{\dot{\varphi_{z\_db}}} + C_2 \tag{100}$$

Table 3 contains the simulation parameters for the different drillstring components that correspond to a real system design.

Table 3 Simulation Parameters for Drillstring Lumped-System Model

Drillpipe Parameters	**Value**	**BHA Collar Parameters (One Segment)**	**Value**
Length, L_{dp}	5700 m	Length	180/2 m
OD	5 in	OD	6.75 in
ID	3/8 in	ID	4 in
Cross section area, A_c	0.0126 m^2	Cross section area, A_c	0.015 m^2
Nominal wt., M_{dp}	$5.6363 x 10^5$ Kg	Nominal wt., M_{BHA}	$1.30583 x 10^4$ Kg
Inertia (z), J_{dp}	$1.1427 x 10^3$ $Kg.m^2$	Inertia (z), J_{BHA}	52.5467 $Kg.m^2$
Inertia (x,y), I_{dp}	$1.9075 x 10^{11}$ $Kg.m^2$	Inertia (x,y),, I_{BHA}	$8.9396 x 10^5 Kg.m^2$
Radial stiffness, K_x/K_y	$2.4720 x 10^8$ N/m	Radial stiffness, K_x/K_y	$1.4699 x 10^9$ N/m
Axial stiffness, K_z	$2.21 x 10^6$ N/m	Axial stiffness, K_z	$1.6644 x 10^8$ N/m
Radial Damping, C_x/C_y	100 Nms/rad	Radial Damping, C_x/C_y	200 Nms/rad
Axial Damping, C_z	100 Nms/rad	Axial Damping, C_z	1000 Nms/rad
Rotational stiffness,$K_{\varphi x,y}$	$10 x 10^5$ Nm/rad	Rotational stiffness,$K_{\varphi x,y}$	$20 x 10^4$ Nm/rad
Torsional stiffness, $K_{\varphi z}$	$10 x 10^4$ Nm/rad	Torsional stiffness, $K_{\varphi z}$	$50 x 10^4$ Nm/rad
Stabilizer Parameters	**Value**	Eccentricity, e	0.135 m
OD	7 in	Eccentricity Inertia, J_e	$M_{BHA}.e^2$
Drillbit Parameters	**Value**	**Material Parameters**	**Value**
OD	7 in	Young modulus, E	$200 x 10^9$ N/m^2
Radius, a	3.5 in	Steel density, ρ	7850 Kg/m^3
Bit bent angle, α	0*Pi/180	Shear Modulus, G	(3/8)*E

Table 3 Continued

Other	**Value**	Poisson ratio, υ	0.3
Applied Static load, W_0	50×10^3 N	**Formation Parameters**	**Value**
Rotary table RPM,	140	Formation stiffness, K_c	67×10^5 N/m
Min. relative velocity, V_{min}	0.001 m/s	Borehole radius, R_h	(7.4/2) in
		Friction Coefficient, μ_0	0.3
		Mud radial damping, C_f	200 Nms/rad
		Mud axial damping, C_{fz}	10 Nms/rad

The stiffnesses of the drillpipe as well as the BHA collar are modeled as beam elements having 6-DOF. All stiffnesses are calculated accordingly and using the below stiffness matrix for 3D beam element:

$$\mathbf{K}_p = \begin{pmatrix} \frac{EA}{l} & 0 & 0 & 0 & 0 & 0 & -\frac{EA}{l} & 0 & 0 & 0 & 0 & 0 \\ & \frac{12EI_z}{l^3} & 0 & 0 & 0 & \frac{6EI_z}{l^2} & 0 & -\frac{12EI_z}{l^2} & 0 & 0 & 0 & \frac{6EI}{l^2} \\ & & \frac{12EI_y}{l^3} & 0 & -\frac{6EI_y}{l^2} & 0 & 0 & 0 & -\frac{12EI_y}{l^3} & 0 & -\frac{6EI_y}{l^2} & 0 \\ & & & \frac{GJ}{l} & 0 & 0 & 0 & 0 & 0 & -\frac{GJ}{l} & 0 & 0 \\ & & & & \frac{4EI_y}{l} & 0 & 0 & 0 & \frac{6EI_y}{l^2} & 0 & \frac{2EI_y}{l} & 0 \\ & & & & & \frac{4EI_z}{l} & 0 & -\frac{6EI_z}{l^2} & 0 & 0 & 0 & \frac{2EI_z}{l} \\ & & & & & & \frac{EA}{l} & 0 & 0 & 0 & 0 & 0 \\ & & & & & & & \frac{12EI_z}{l^3} & 0 & 0 & 0 & -\frac{6EI_z}{l^2} \\ & sym. & & & & & & & \frac{12EI_y}{l^3} & 0 & \frac{6EI_y}{l^2} & 0 \\ & & & & & & & & & \frac{GJ}{l} & 0 & 0 \\ & & & & & & & & & & \frac{4EI_y}{l} & 0 \\ & & & & & & & & & & & \frac{4EI_z}{l} \end{pmatrix} \quad (101)$$

Simulation Results

In this section we will present the results obtained from one of the simulation studies done on the drillstring lumped system model. The vibrations are initially self-induced due to imbalance mass eccentricity in the intermediate lumped mass model. Boundary conditions, represented in the top drive constant speed $\boldsymbol{\omega}$, dynamic friction coefficient μ_0, eccentricity value e, and applied static load W_0, were applied. Stiffness and damping parameters for the three lumped masses were slightly tuned by try and error to provide the required dynamic response.

Figure 46 shows simulation results obtained from the lumped system model of the drillstring. Panel (a) shows the 2D plane C.G. orbit of the upper stabilizer inside the borehole. Panel (b) shows the 2D orbit of the BHA C.G. inside the borehole. As the BHA collar has a smaller diameter than the stabilizer and drillbit, the clearance hence is bigger. Panel (c) shows the 3D pathline of the drillbit inside the borehole indicating the drilling direction, while panel (d) shows the projection 2D plane orbit of the drillbit. The centrifugal force due to mass imbalance is induced in the intermediate BHA C.G. lump mas, which in accordance affects the dynamic behavior of the upper and lower lump masses. The whirling motion induced in the three lump masses appears to be unstable causing an unstable drilling operation and hence reduction in the rate of penetration. Panel (e) shows the rotation velocities of the three lumped masses. Once there is lateral contact with the borehole formation and friction torque is applied, more oscillations begin to appear which leads to higher torsional vibrations. Panel (f) shows the relative velocities between the lump masses and formation. The relative velocities measurement gives the first indication if pure rolling is going to happen once a zero value is reached. Panel (g) shows the whirling velocities of the mass bodies. Panels (h) and (i) show *WOB* and *TOB* respectively. The plots show bit-bounce results from axial drillstring vibrations. Axial vibrations reduce the rate of penetration of drilling due to fluctuations in *WOB*. Bit-Bounce are caused when there is a temporary lift-off of the drillbit from the formation and the *WOB* and *TOB* readings reach zero. Panels (j) and (k) show the normal contact forces on the three masses, and the friction contact force respectively. When there is more continuous contact with the formation, in case of forward whirling or backward whirling, continuous readings are obtained with higher magnitudes.

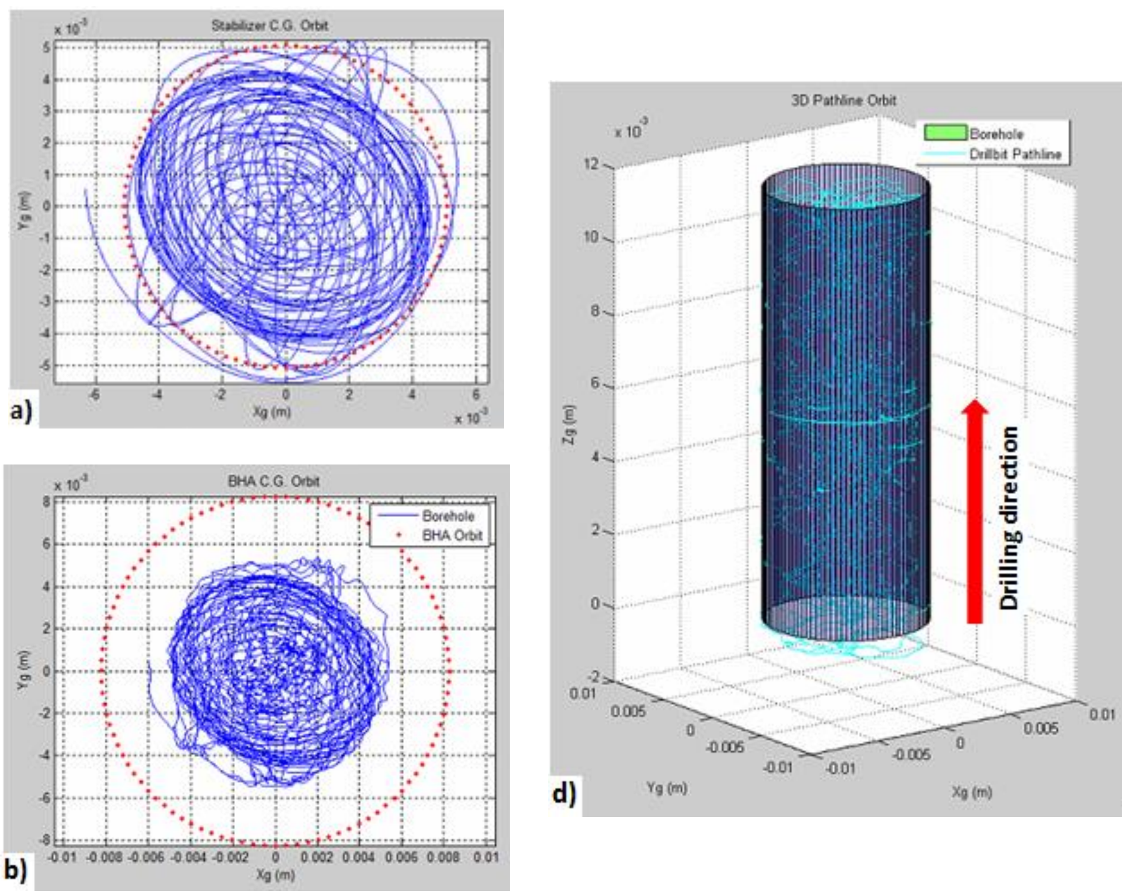

Figure 46 Simulation Results of Lumped-System Drillstring

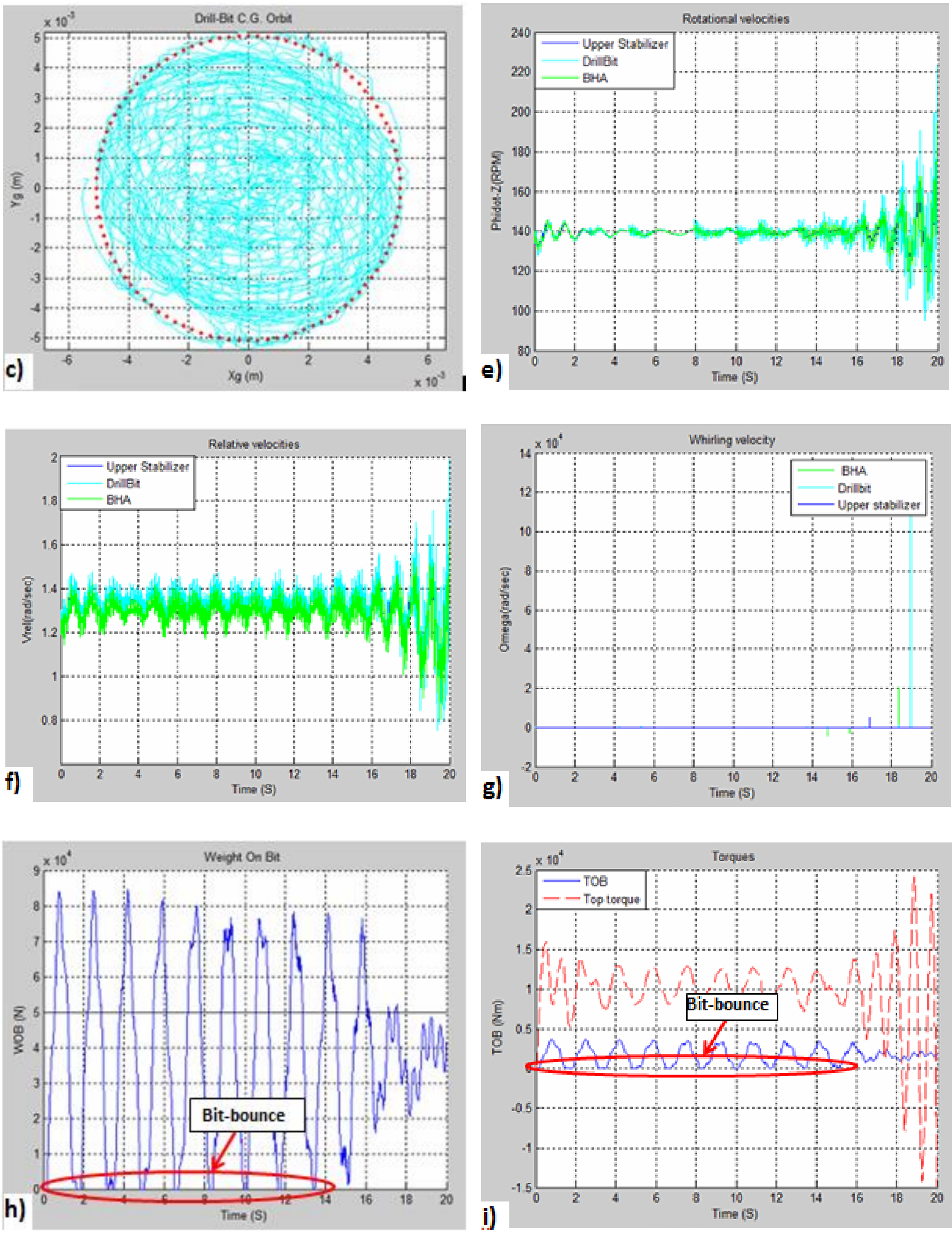

Figure 46 Continued

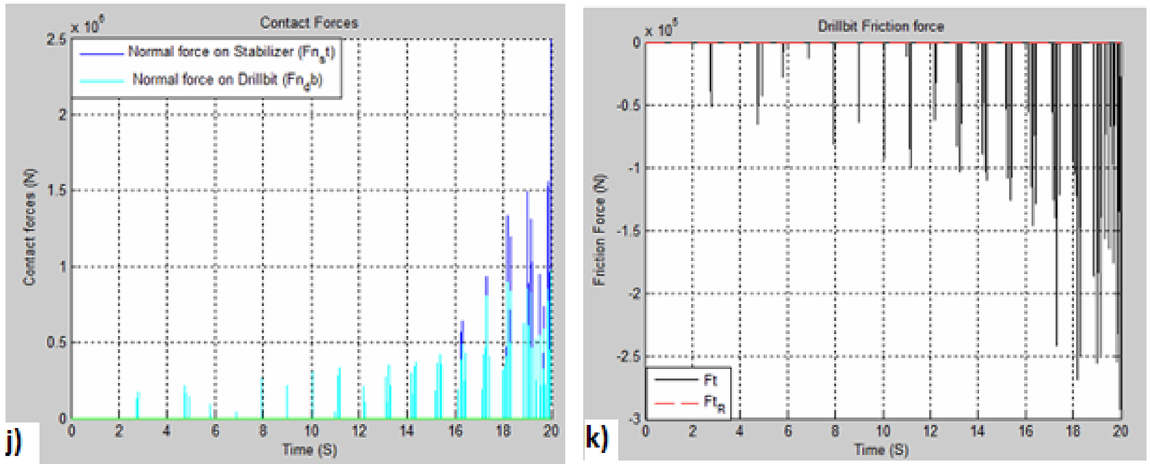

Figure 46 Continued

Conclusion

Lumped system modelling is a very useful method in order to have a better understanding of the equation of motions and better sense of how applied forces and boundary conditions could affect the system dynamics, as well as how each mass dynamic behavior affects others due to the interaction of stiffnesses. Another advantage in using this method is to have a relatively fast numerical calculation. However this method is not accurate as the system is discrete and lumped into a limited number of masses instead of one continuous mass. The stiffness parameters that couple the lump masses together might need extensive tuning by try and error so as to give a close system behavior as in real.

6.3 Drillstring Finite Element Modeling

In this section, Finite-Element-Method is used to enhance the drillstring dynamics model using a more accurate approach. Instead of treating the BHA as three lumped masses as discussed in the previous section, the BHA will be meshed or discretized into a number of 3D-Cylindrical Timoshenko beam elements, where each node will have 6-

DOF. The drillpipes can be substituted by a lumped mass, axial & torsional springs, and damper attached to the top node of the BHA, as they are generally much lighter than the BHA and have a negligible contribution on the drillstring dynamics. Stabilizers models will be applied and located at any of the BHA's nodes by adding the corresponding DOF's and geometry profile. Right boundary conditions and contact logic can be applied in the same manner as in the previous two sections for lateral vibration, and axial & torsional vibrations such that the drillstring experiences axial, torsional, and lateral vibrations. External forces are applied at each BHA nodes including stabilizers' nodes and the bottom node for the PDC-drillbit. The model accounts the gyroscopic effect, the torsional/bending inertia coupling, and the effect of the gravitational force. This model is a more complex and will give a more accurate prediction to the rotordynamic behavior of the BHA, and the PDC-Drillbit cutting dynamics. Reference [35] is used as a major reference in this step, as the work will be extended to account the Backward whirl.

Different simulation studies will be conducted to investigate the drillstring different vibration modes from the finite element model to obtain better understanding of the effect of system parameters on system response.

Objective

To simulate more accurately the dynamics of the drillstring while drilling by building a 3D Finite-Element-Model using cylindrical Timoshenko beam element to describe the axial, lateral, and rotational vibration modes with the nonlinear bit/rock interaction. Gyroscopic effects will also be included. Following are the different dynamic vibration behaviors that will be investigated with detailed analysis:

- Forward whirling, under self-excited vibration
- Backward whirling with pure-rolling, under self-excited vibration
- Chaotic and random whirling vibration
- Stick-slip drilling
- Bit bounce

Theoretical Background

The Timoshenko finite element model takes into account the shear deformation and rotational inertia effects, unlike Euler-Bernoulli beam theory that assumes the plane across sections remain plane and normal to the longitudinal axis after bending which results in zero transverse shear strain. Timoshenko beam theory assumes that the rotation of a transverse normal plane about the longitudinal axis, Θ_3, is not equal to $-dv/dx_1$, therefore the transverse shear strain is not zero [47]. Figure 47 shows the kinematics of the Timoshenko beam theory in comparison to the Euler- Bernoulli beam theory.

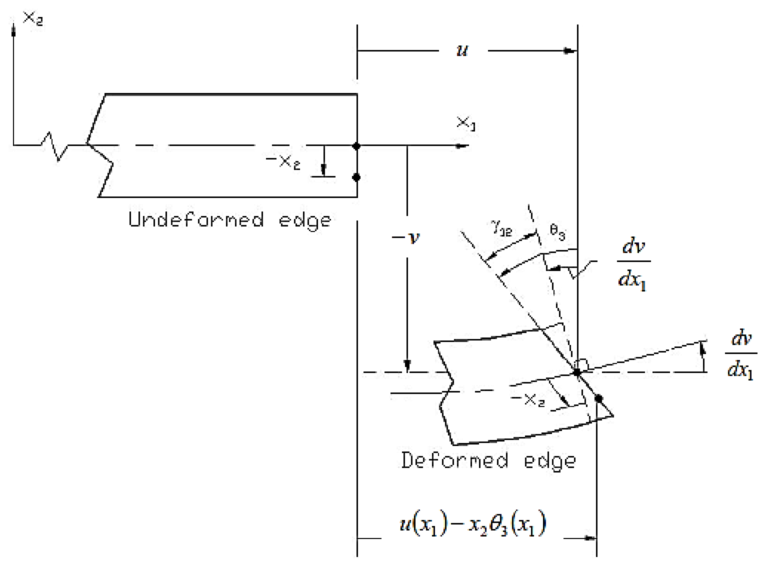

Figure 47 Deformation in Timoshenko Beam versus Euler-Bernoulli Beam [47]

The BHA- drill collars in the drillstring will be discretized using a number of hollow cylindrical Timoshenko beam elements. Each element consists of two nodes at its ends. Each nodes has six DOF consisting three translations (u, v, w) in the (x, y, z) and three rotations about the three axis (Θ_1, Θ_2, Θ_3)). Figure 48 describes the translation and rotation in a 3D beam element.

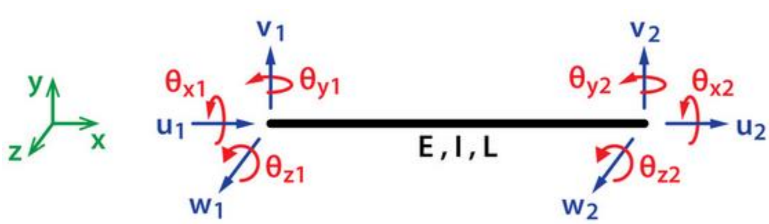

Figure 48 Translation and Rotation in 3D Beam Element

Mongkolcheep [48] discussed in details the generation of the shape function matrix $[N]$ of the 3D finite element, and the correspondent translation deformations, rotations and torsional deformations based on the shape function matrix. Calculating the elastic strain energy of the axial, torsional, shear and bending deformations is used to formulate the element stiffness matrices. Equation (102) shows the formulated element stiffness matrix of a 3D 2-node Timoshenko beam element based on the total elastic body strain energy

$$\mathbf{K}^e = \begin{bmatrix} R^a & 0 & 0 & 0 & 0 & 0 & -R^a & 0 & 0 & 0 & 0 & 0 \\ 0 & 12R^b_{z3} & 0 & 0 & 0 & 6R^b_{z2} & 0 & -12R^b_{z3} & 0 & 0 & 0 & 6R^b_{z2} \\ 0 & 0 & 12R^b_{y3} & 0 & -6R^b_{y2} & 0 & 0 & 0 & -12R^b_{y3} & 0 & -6R^b_{y2} & 0 \\ 0 & 0 & 0 & R^t & 0 & 0 & 0 & 0 & 0 & -R^t & 0 & 0 \\ 0 & 0 & -6R^b_{y2} & 0 & 4R^b_y & 0 & 0 & 0 & 6R^b_{y2} & 0 & 2R^b_y & 0 \\ 0 & 6R^b_{z2} & 0 & 0 & 0 & 4R^b_z & 0 & -6R^b_{z2} & 0 & 0 & 0 & 2R^b_z \\ -R^a & 0 & 0 & 0 & 0 & 0 & R^a & 0 & 0 & 0 & 0 & 0 \\ 0 & -12R^b_{z3} & 0 & 0 & 0 & -6R^b_{z2} & 0 & 12R^b_{z3} & 0 & 0 & 0 & -6R^b_{z2} \\ 0 & 0 & -12R^b_{y3} & 0 & 6R^b_{y2} & 0 & 0 & 0 & 12R^b_{y3} & 0 & 6R^b_{y2} & 0 \\ 0 & 0 & 0 & -R^t & 0 & 0 & 0 & 0 & 0 & R^t & 0 & 0 \\ 0 & 0 & -6R^b_{y2} & 0 & 2R^b_y & 0 & 0 & 0 & 6R^b_{y2} & 0 & 4R^b_y & 0 \\ 0 & 6R^b_{z2} & 0 & 0 & 0 & 2R^b_z & 0 & -6R^b_{z2} & 0 & 0 & 0 & 4R^b_z \end{bmatrix} \quad (102)$$

Where $[\mathrm{K_e}] = [\mathrm{K_A}] + [\mathrm{K_T}] + [\mathrm{K_S}] + [\mathrm{K_B}] + [\mathrm{K_G}]$ is the element stiffness matrix given by the axial stiffness matrix $[\mathrm{K_A}]$, the torsional stiffness matrix $[\mathrm{K_T}]$, the shear stiffness matrix $[\mathrm{K_S}]$, the bending stiffness matrix $[\mathrm{K_B}]$, and the stress stiffening matrix $[\mathrm{K_G}]$. The entries of the element stiffness matrix in equation (102) are presented in details in reference [49] and in the appendix.

Finite-Element-Modeling

The model consists of the BHA, drillbit, two stabilizers, and drillpipes model. A typical 200m BHA is meshed into six 3D-Timoshenko hollow cylindrical beam elements to represent the heavy drill collars in the drillstring. Each element consists of 2-nodes with added axial and torsional stiffness. The assembled Global Mass, Stiffness, Damping, as well as Gyroscopic Matrices have been successfully generated and verified. The drillpipes are substituted by a single lumped mass, torsional spring, as well as torsional and axial damper, and attached to the top node of the BHA. Each to its correspondent node's DOF. The static load, W_0, is applied axially on the top node. The top drive torque (motor torque) with a constant driving rotation speed is applied as well on the BHA top node. The PDC-Drillbit model and its characteristics have been applied on the BHA bottom node with the associate *WOB*, and *TOB* when the drillbit is penetrating the rock formation and by taking into consideration the time delay term. Two rigid massless stabilizers are considered at two location along the BHA; one at the top node, and the other at the last node before the bottom. The stabilizers have the same radius as the drillbit. The borehole is modeled as formation with spring stiffness K_f from the radial direction, and K_c from the bottom. A clearance R_c is left between the borehole and the stabilizers. An imbalance centrifugal force is induced at the second stabilizer node at the bottom. The contact forces between the stabilizers and wellbore occur when the lateral displacement of the stabilizer becomes larger than the clearance R_c. Lateral and torsional damping are applied on the BHA due to drilling fluid (mud) viscosity. Two choices are given in the code to implement any mass body (e.g. flywheel) under dynamics investigation inside the BHA collars. Choices are either the node above the drillbit location at the bottom of the BHA-Assembly, or at the BHA's C.G. location. This will give the advantage for any future work to extend the code capability to study the effect of the induced drillstring vibrations on a possible implemented flywheel inside the BHA collars.

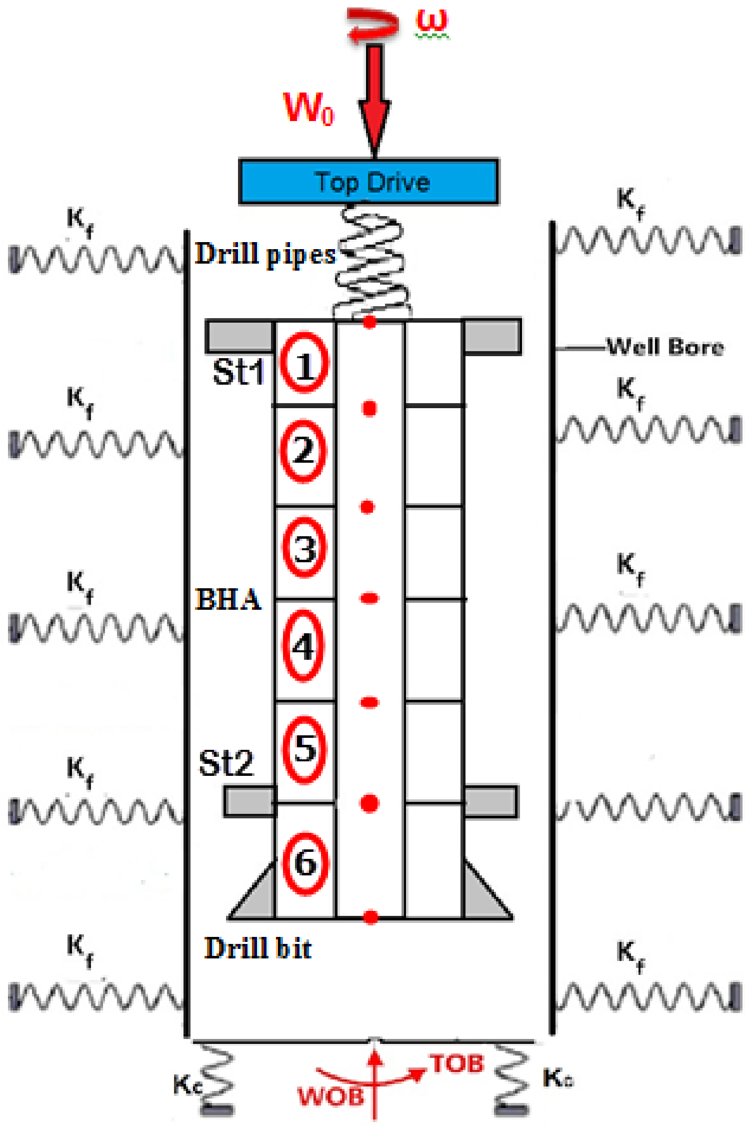

Figure 49 FEM of the BHA

Figure 49 describes the FEM of the BHA indicating the position of the drillbit, drillpipes, and stabilizers correspondent to the BHA elements nodes as well as the applied loads. The table below (Table 4) shows the parameters with the values used in the FEM-Drillstring simulation studies.

Table 4 Simulation parameters for Drillstring FEM

Drillpipe Parameters	**Value**	**BHA Collar Parameters**	**Value**
Length	110 m	Length	200m
OD	5 in	OD	6.75 in
ID	3/8 in	ID	variable in
Cross section area, A_c	0.0126 m^2	Eccentricity, e	0.003 m
Nominal wt., M_{dp}	1.0877×10^4 Kg	**Stabilizers Parameters**	**Value**
Inertia about Z, J_{dp}	22.0528 $Kg.m^2$	OD	8.5 in
Axial Damping, C_z	15×10^3 Nms/rad	**Formation Parameters**	**Value**
Torsional Damping, $C_{\varphi z}$	500 Nm/rad	Borehole diameter	9.5 in
Torsional stiffness, $K_{\varphi z}$	600 Nm/rad	Formation Stiffness, K_f	variable N/m
Drillbit Parameters	**Value**	Formation contact damping, C_f	1000Nms/rad
OD	8.5 in	Mud axial damping, Cr_f	10 Nms/rad
Radius, a	4.25 in	Mud torsional damping, $C_{\varphi f}$	2000 Nm/rad
Bit tilting angle, α	0*Pi/180	Friction coefficient, μ_0	variable
Number of blades, n	8	**Other**	**Value**
Material Parameters	**Value**	Applied Static load, W_0	variable
Young modulus, E	200×10^9 N/m^2	Rotary table RPM, ω	variable
Steel density, ρ	7850 Kg/m^3		
Shear Modulus, G	(3/8)*E		
Poisson ratio, υ	0.3		

Simulation Results

The main objective of the simulation studies conducted is to examine the drillstring dynamic response under influence of the operation parameters and examine the interaction or coupling between torsional and axial vibrations, rather than predicting quantitatively a real drilling dynamics using a particular drillbit type.

Although the drillstring might be perfectly symmetric, assuming perfect symmetric drillbit and any other implemented instruments including mud motor, the drillstring can still encounter the different types of vibrations. Formation stiffness, as well as the stiffness of the drill-collars itself, play a major role in initiating one mode of vibration that could lead to the other two modes of vibrations. For example, drilling in hard formations (high *WOB*) with low rotation speeds could initiate first the bit stick-slip vibration mode due to the non-linear Stribeck friction function that causes instability in torsional motion at low speeds. Accordingly, and due to the direct proportional between the *TOB* and the *WOB* expressed in equation (97), axial vibrations will be then imitated. Another example, in case of hard formations and weak (non-stiff) drill-collars and high applied static load, that could cause drillstring to bend or to buckle which will lead in accordance to lateral or whirling motion.

The studies below summarize the different vibration modes that could encounter the drillstring during the drilling operation.

Chaotic lateral vibration with Bit-bounce

Drilling under low upper static applied load will lead to low *WOB*, which under normal to high rotational speed will eliminate the stick-slip behavior but can cause on the other hand bit-bounce. Mass Imbalance (or eccentricity) under normal to high rotational speeds will induce whirling motion in the drillstring. If the formation has a low coefficient of friction, forward whirling will occur. However, if the formation has a slightly higher coefficient of friction, a chaotic unstable whirling behavior will occur till the friction force at the point of contact is high enough that encourages the body to roll.

Table 5 shows the parameters values used in this simulation study that induced the chaotic lateral drillstring vibrations with bit-bounce behavior.

Table 5 Simulation Parameters for Chaotic Drillstring Vibrations

Parameter	**Value**
Rotary Table Speed, ω	100 (rpm)
Upper static applied load, W_0	50e3(N)
Coulomb dry friction coefficient, μ_0	0.07
Radial formation contact stiffness, K_f	2e8 (N/m)
Eccentricity, e	0.003 (m)
Applied eccentricity node	Node #6
BHA inner diameter, *ID*	4(in)

Panel (a) shows the axial penetration displacement of the drillbit by time. The plot shows increasing axial fluctuating (vibration) as the rotation speed of the drillbit increases to catch the upper applied rotary table speed. That causes decrease in *ROP* and depth of cut. Panel (b) shows the 3D path-line orbit of the drillbit function of time. As the drillbit is increasing its rotation speed from zero to the operating top drive speed, higher *ROP* and DOC are achieved. As axial vibration increases ROP and the achieved DOC is decreased accordingly. Panel (c), (d), (e), and (f) show the 2D lateral vibration of the upper stabilizer, BHA-CG, bottom stabilizer, and drillbit respectively. The red doted circle indicates the clearance boundary between the component CG and the borehole. The BHA collar has the biggest clearance with the borehole, as it has the smallest diameter compared to the stabilizers and the drillbit. The bottom stabilizer has the most sever lateral vibrations induced, as the eccentricity is applied at its node. The upper stabilizer is about 167m far from the bottom stabilizer, and that is why it has the least whirling motion induced. A chaotic lateral vibration is induced that causes the bottom stabilizer to have discrete impacts with unsteady whirl at intermediate coefficient of friction with the formation (μ_0=0.07). Panel (g) shows the rotational velocities of the BHA components, where the drillbit has the most severe rotation speed variation due to friction with the bottom formation while cutting, as well as the torsional stiffness of the BHA and drill pipes. Panel (h) shows the relative velocities of the different BHA components. The relative velocity might reach to zero value, but still other conditions are still not satisfied to achieve the pure rolling status. That appears in panel (i) as the whirling velocity doesn't indicate high whirling frequency with a negative value. Panels (j), and (k) show the *WOB* and *TOB* respectively. The zero values of the *WOB* and *TOB* indicate bit-bounce as the drillbit lose contact with the bottom formation and hence now weight is applied on the bit as well torque. Panel (l) shows the normal contact force applied on the bottom stabilizer due to radial impacts with the borehole formation.

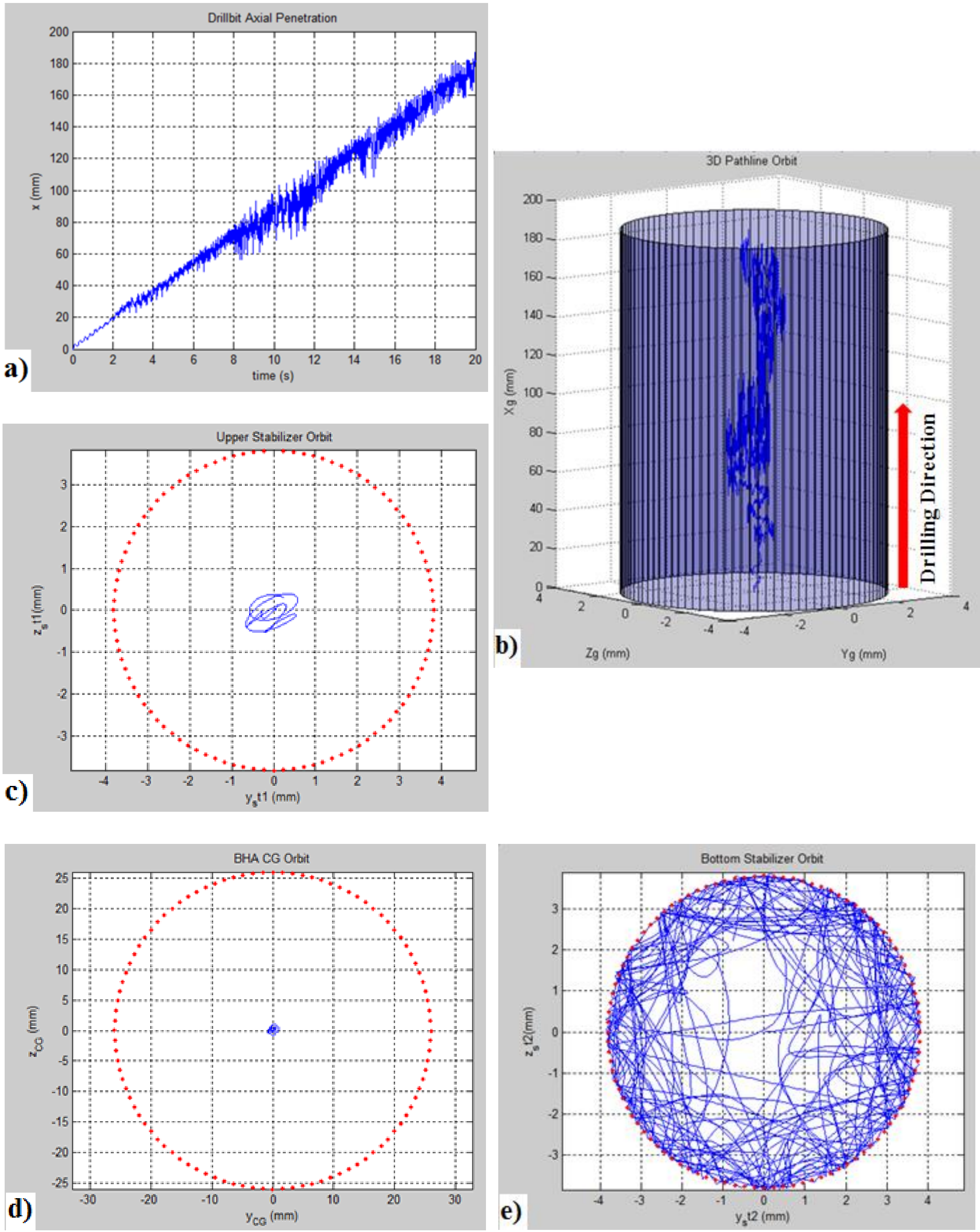

Figure 50 Simulation Results of Chaotic Vibration Behavior with Bit-Bounce

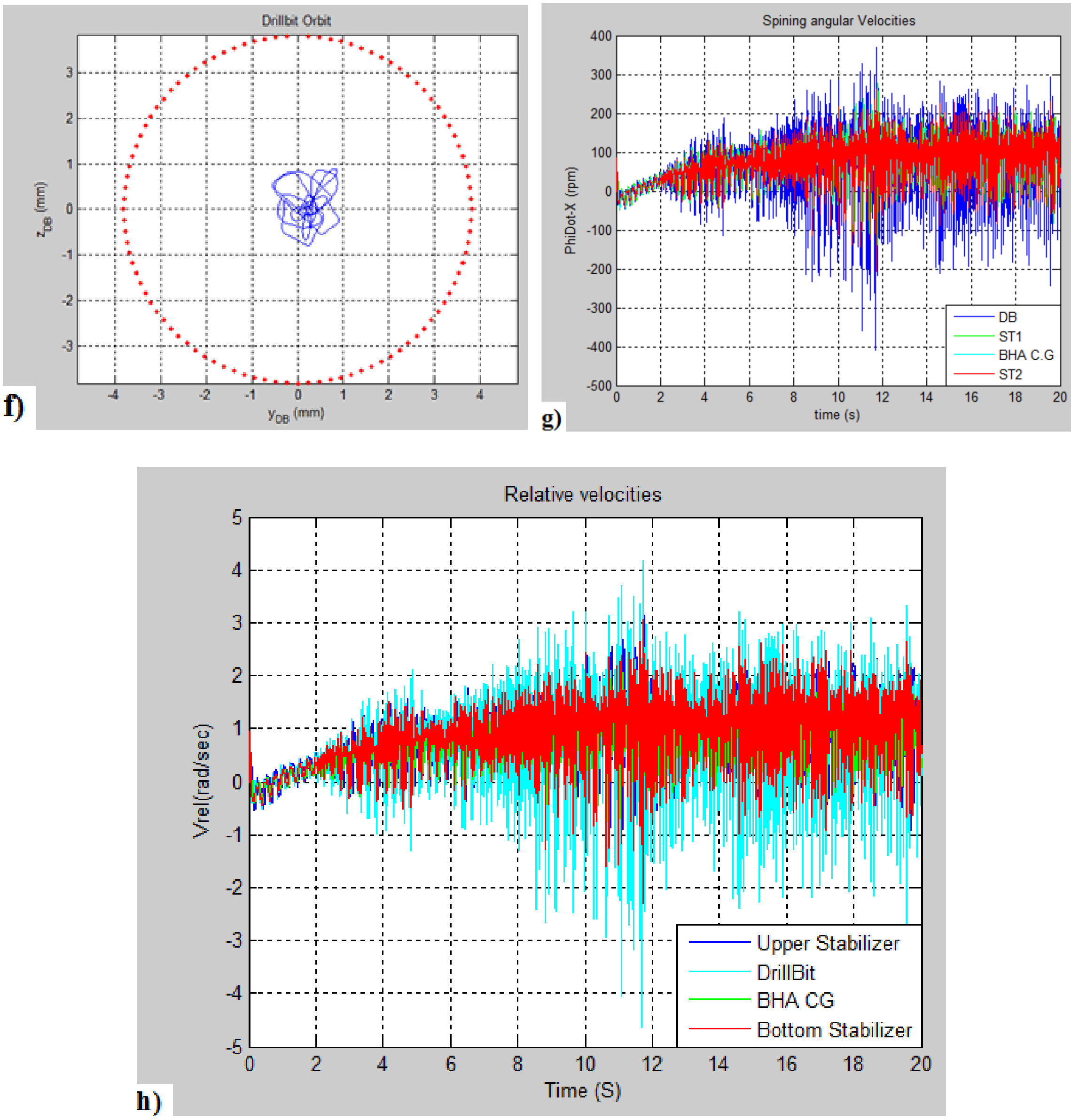

Figure 50 Continued

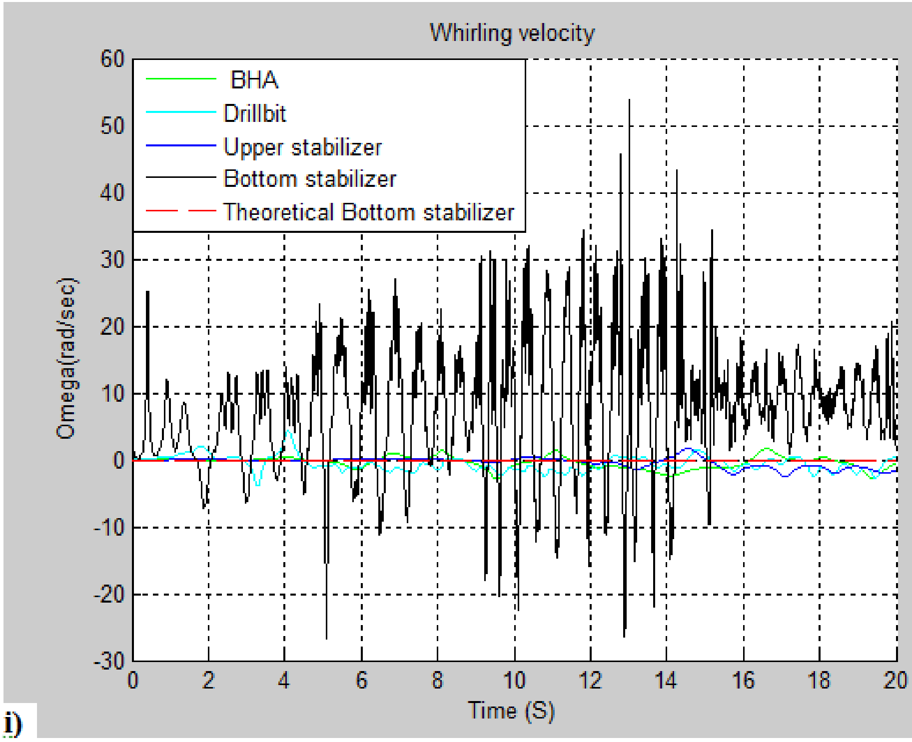

i)

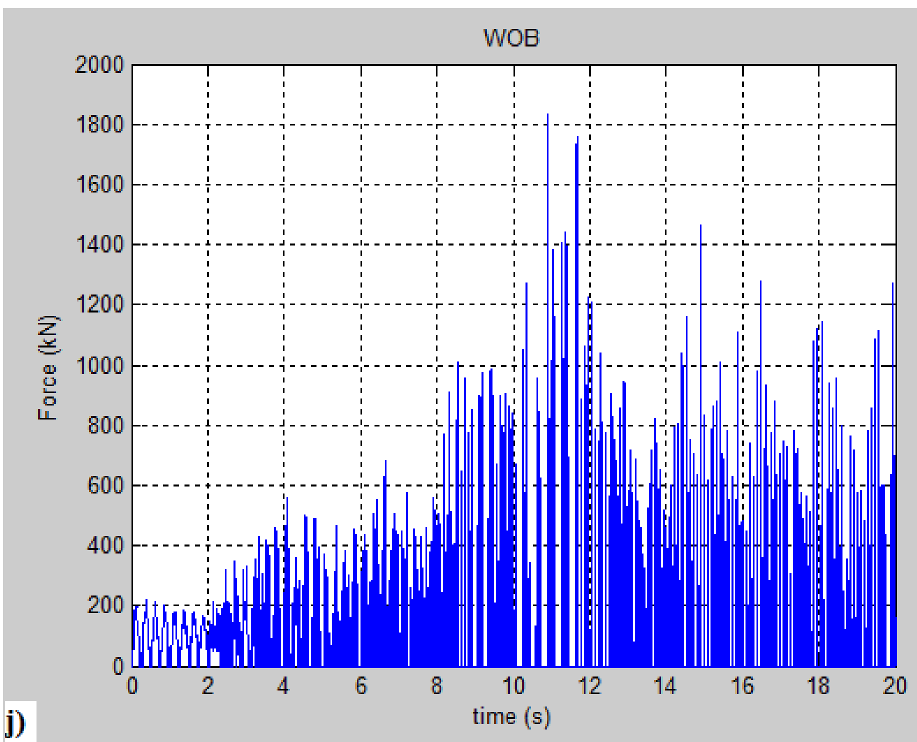

j)

Figure 50 Continued

k)

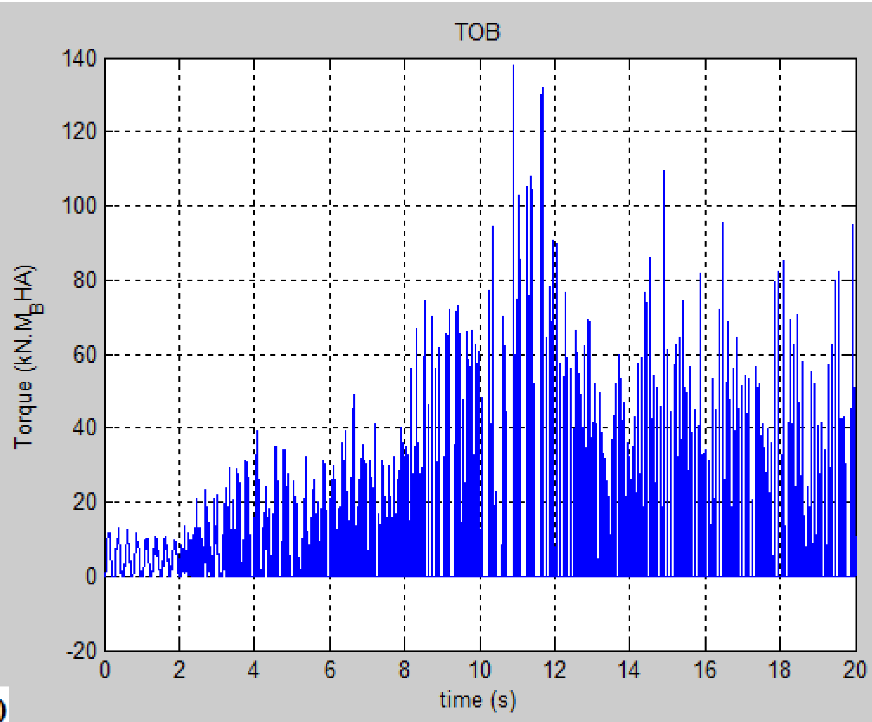

l)

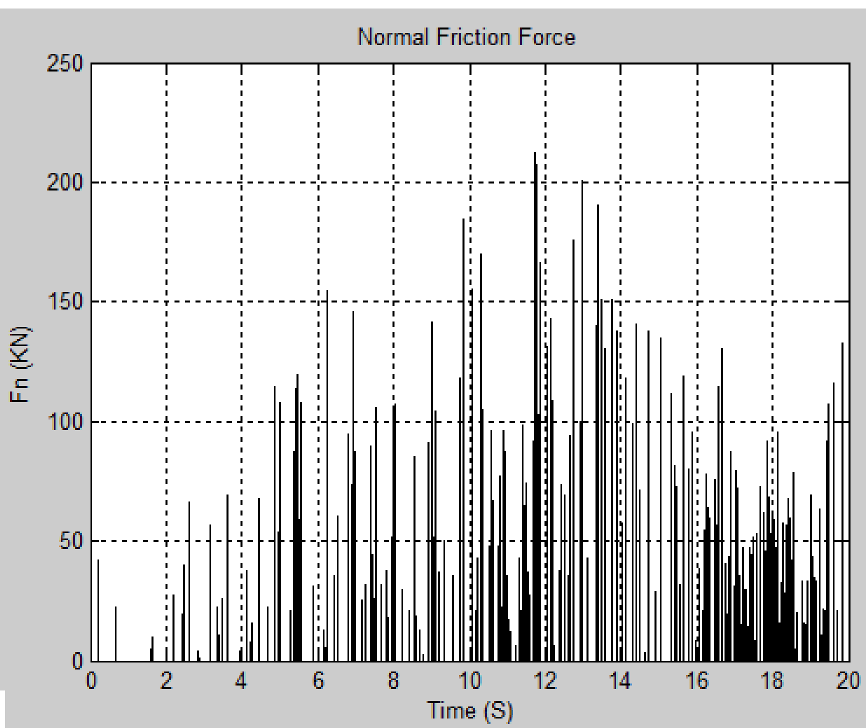

Figure 50 Continued

Backward Whirling with Pure Rolling Motion

Five major parameters can lead to backward whirling with pure rolling; to have a weak (or non-stiff) drillstring, assembly imbalance, low *WOB*, high rotational speed, and high friction coefficient with the formation. Table 6 shows the input parameters values that were used to achieve the backward whirling with pure rolling. The stiffness of the BHA has been reduced by decreasing the drill-collars wall thickness by 0.25" compared to the previous study. Rotary table drive speed has been increased from 100 rpm to 120 rpm. Formation friction coefficient increased from 0.07 to 0.2. Low *WOB* can be achieved, according to equations, either by having weak formation stiffness or be reducing the applied top static load W_0.

Table 6 Simulation Parameters for Drillstring with Pure Rolling Motion

Parameter	**Value**
Rotary Table Speed, ω	120 (rpm)
Upper static applied load, W_0	50e3(N)
Coulomb dry friction coefficient, μ_0	0.2
Radial formation contact stiffness, K_f	2e8 (N/m)
Eccentricity, e	0.003 (m)
Applied eccentricity node	Node #6
BHA inner diameter, *ID*	4.5(in)

Panel (a) in figure 51 shows the axial penetration achieved by the drillbit as a function of time. The high frequency oscillation in the plot at certain time periods with magnitudes below the mean value indicates bit-bounce, and as indicated in panel (c) where the drillbit has a negative axial penetration velocity. Plot (a) also indicates reduction in rate of penetration at certain time periods due to lateral motion instead of axial or vertical motion. This could be concluded more clearly from panel (b), where at certain depths the drillbit motion is switched to lateral motion rather than vertical motion. This could be due to forward or backward whirling. Three measurements could indicate whether the body is in forward whirling mode or in backward, and whether it is mixed or fully (purely) developed. These measurements are the relative velocity, the whirling velocity or whirling frequency, and whirling direction. As the eccentricity is applied at node #6 at the bottom stabilizer location, we should suspect first that the whirling is occurring at this location. If the whirling is too severe with a really weak BHA stiffness, whirling behavior could be extended to other BHA component that has lower clearance with the borehole (e.g. drillbit or upper stabilizer). To affirm what components exactly that might experience whirling behavior we should inspect the lateral vibration of each component body or the plane orbit of the components' C.G. Panels (d), (e), (f), and (g) show the 2D C.G. orbit of the upper stabilizer, BHA, bottom stabilizer, and drillbit. The results show only a whirling behavior in the bottom stabilizer as suspected, while other components barely have contact with borehole formation.

Panel (h) indicates high oscillations in the drillbit and bottom stabilizer rotation velocities resultant from formation contact friction that causes applied friction torques on the rotating body. The plot shows that the drillstring is taking almost 50 seconds to reach the full operation set drive speed 120 rpm. Panel (i) indicates the relative velocity measurement of each BHA component. The plot indicates a sudden drop in the relative velocity of the bottom stabilizer reaching zero value with high oscillations around it. This is a first indication that backward whirling is happing here, but probably mixed with sliding motion as the tangential velocity vector ($\Omega_{whirl}.r$) is bigger than ($\varphi.R$) (refer to figures 34 & 35).

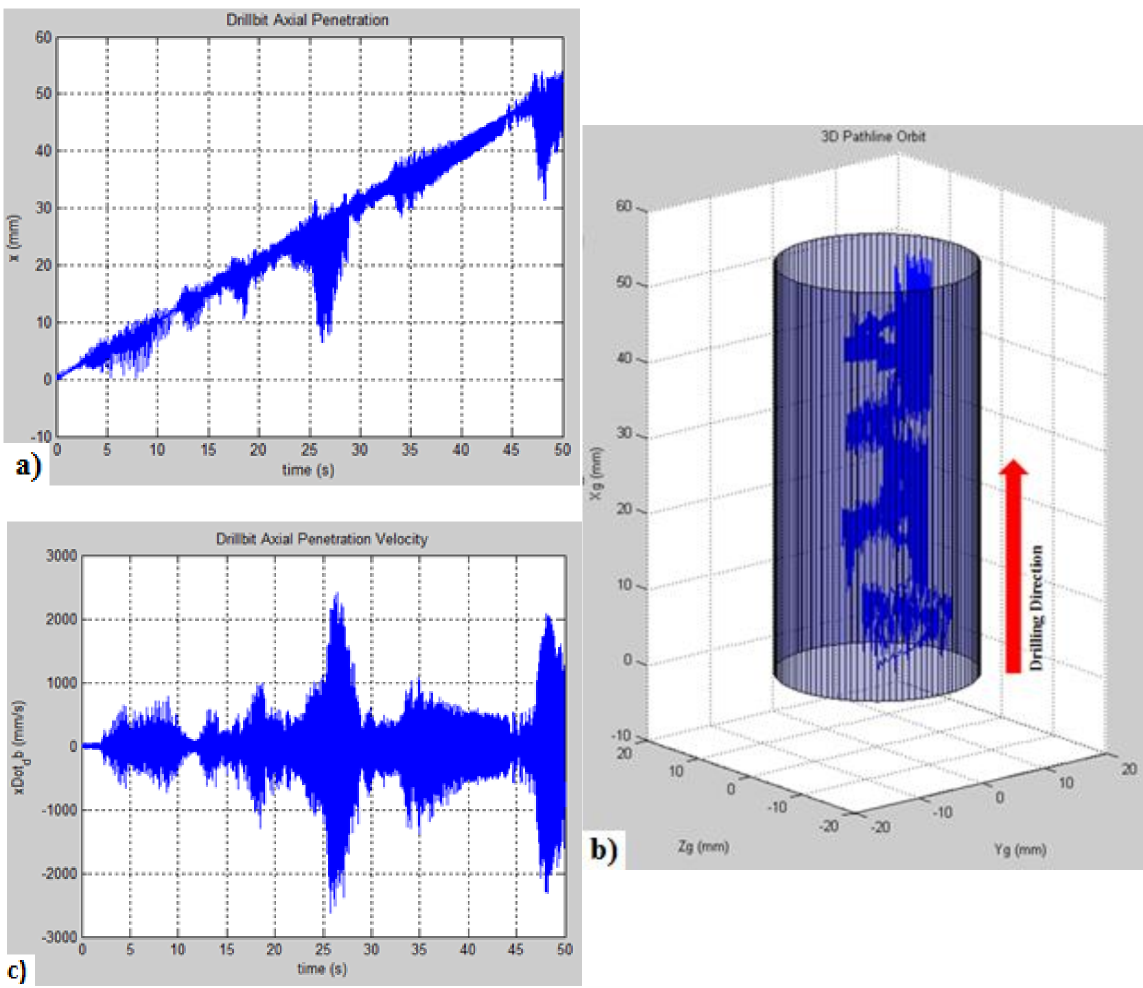

Figure 51 Simulation Results of Backward Whirling with Pure Rolling Motion

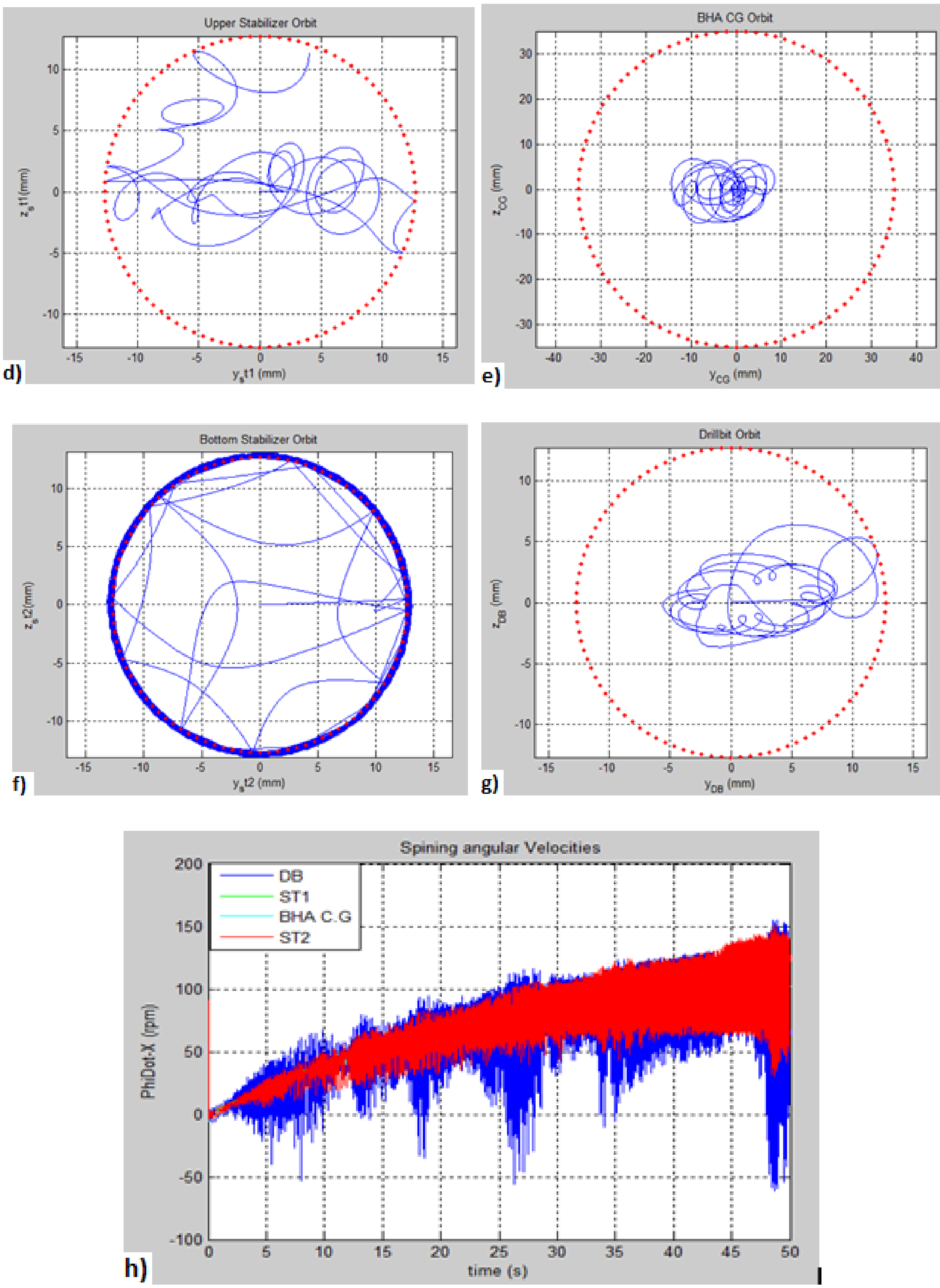

Figure 51 Continued

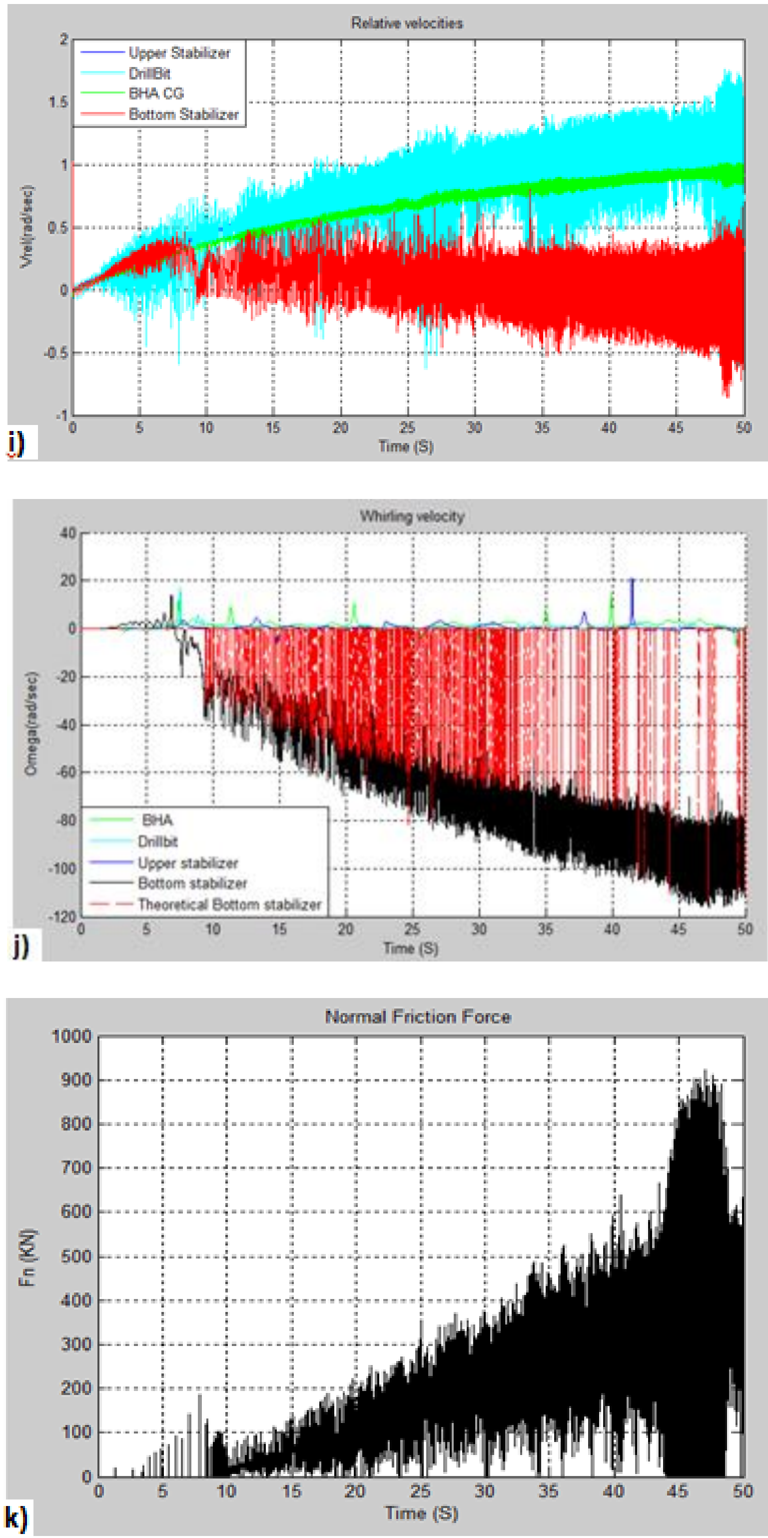

Figure 51 Continued

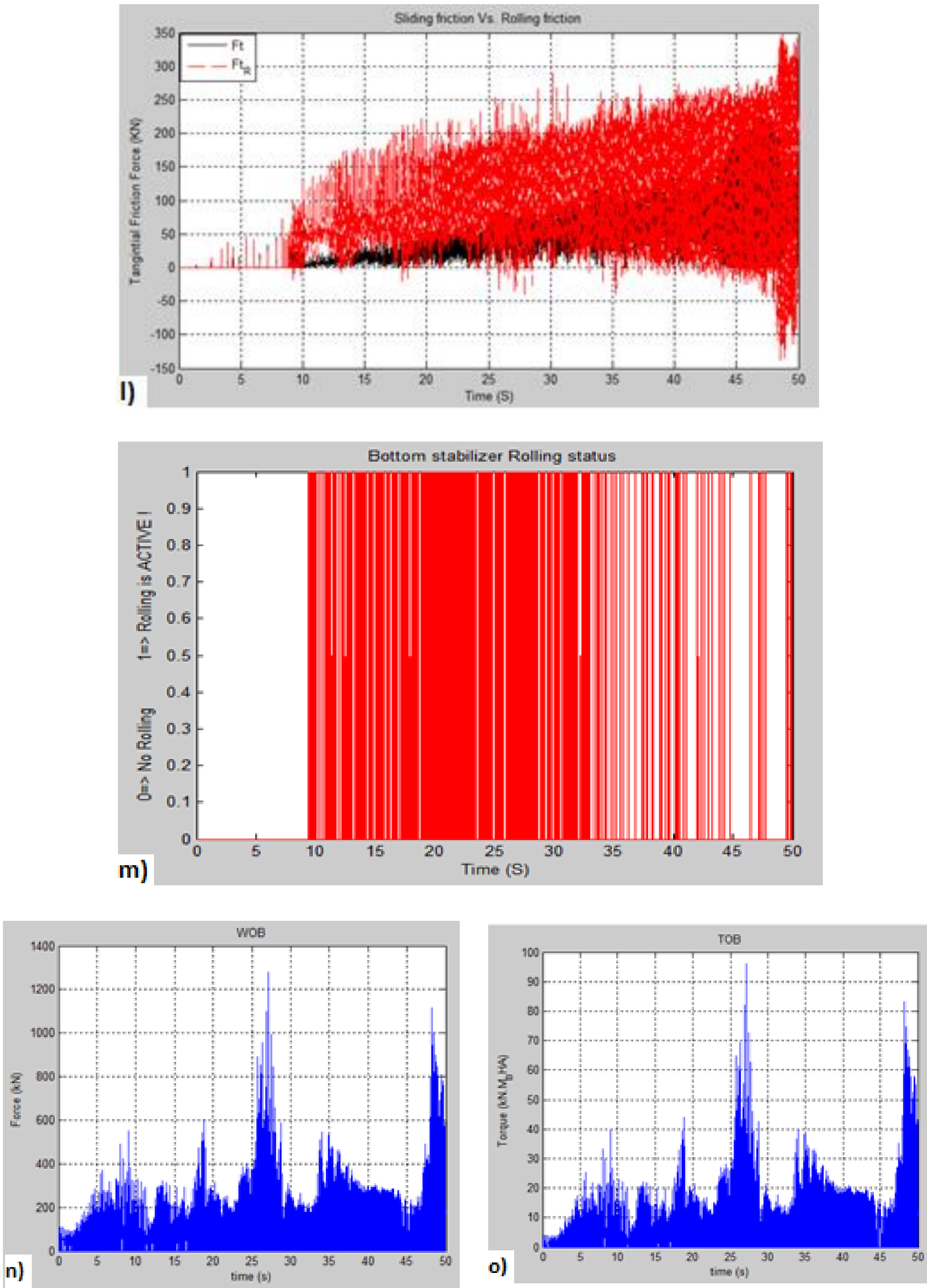

Figure 51 Continued

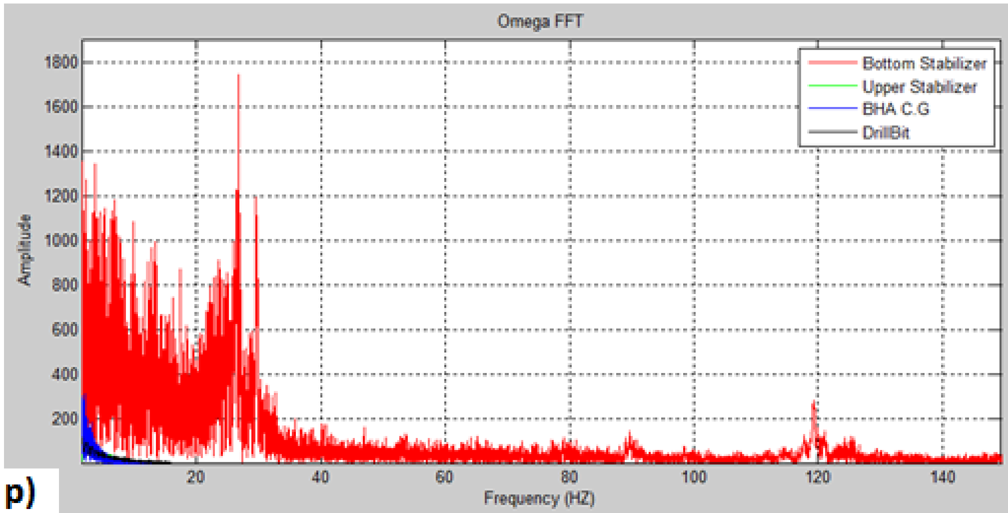

Figure 51 Continued

Panel (j) shows the whirling velocities, Ω_{whirl}, of the BHA components. A second indication for backward whirling is the negative jump in the whirling velocity reading of the bottom stabilizer reaching high frequency values as the rotation velocity increase. Other whirling velocity readings for the drillbit, upper stabilizer, and BHA-C.G indicate forward whirling with positive sign direction and low stable magnitudes. The red dashed lines indicates the theoretical, or the calculated, whirling velocity of the bottom stabilizer according to equation (36), as well the conditions described in simulation flowchart (figure 38). From equation, the value of the backward whirl velocity depends on the component rotation velocity, and the radial displacement of the component C.G. (or simply the clearance between the body and borehole). The smaller clearance we have, the higher whirling frequency is obtained. This value could reaches more than 30 to 60 times that of rotation velocity φ, which is totally destructive vibration behavior to the drillstring assembly. Panel (k) shows the normal contact force applied on the bottom stabilizer due to radial impacts with the borehole formation. Panel (l) shows the tangential friction force applied on the bottom stabilizer due to contact with formation, and the corresponding calculated tangential friction force if pure rolling occurs (red dashed line). The calculated value is used to indicate whether the bottom stabilizer will switch from mixed or forward whirling to pure rolling status (rolling without slipping) or not, where the tangential contact force should not exceed the maximal friction force and be bounded between $-\mu F_N \leq F_t \leq \mu F_N$. Panel (m) indicates the pure rolling status of the bottom stabilizer if all mentioned conditions are satisfied and according to the simulation logic presented in figure 38. The figure shows a discontinuous pure rolling behavior of the bottom stabilizer associated with interval sliding motion in-between. Panels (n) and (o) show the *WOB* and *TOB* respectively. The zero values of the *WOB* and *TOB* indicate bit-bounce as the drillbit lose contact with the bottom formation and hence now weight is applied on the bit as well torque.

Conclusion

Modeling using finite element method, and more specifically using Timoshenko beam element theory, gives a more accurate and trustful results than using the lumped system method. This method doesn't require intervention to tune the element stiffness parameters as needed when using lumped system method.

Drillbit cutting dynamics has a coupling between axial and torsional modes expressed in the relationship between the *WOB* and *TOB*. The non-linear Stribeck friction function between the drillbit and formation can initiate a self-excited torsional vibration mode on the drillbit at lower values of top drive spin speeds and in accordance to an axial vibration mode which can be characterized by bit bouncing and a total stick-slip. Increasing the top drive spin speed should mitigate the instability effect of the non-linear Stribeck friction and leads to a more stable cutting process and rate of penetration. Reducing the applied *WOB* could help alleviate torsional vibrations by reducing the *TOB*, however lower *WOB* will negatively affect the drilling efficiency by having a lower rate of penetration as well as can lead to bit bounce.

Drillstring stiffness is one of the major factors that lead to lateral vibrations even if the drillstring is perfectly symmetric and has no eccentricity or mass imbalance. Drilling in hard formation under high static applied load could cause the BHA to buckle and bend which under the rotation velocity leads to BHA whirling.

Formation friction coefficient as well as rotation speed are responsible in characterizing the type of whirling motion induced, whether forward or backward whirling. Five major parameters can lead to backward whirling with pure rolling; to have a weak (or non-stiff) drillstring, assembly imbalance, low *WOB*, high rotational speed, and high friction coefficient with the formation. The calculated tangential friction force, at zero contact relative velocity, in case of pure rolling should not exceed the maximal friction force ($\mu.F_N$) otherwise the body will switch to a non-pure rolling motion status.

The clearance between the borehole and the BHA components, especially the installed stabilizers, plays a major role in identifying the severity of the whirling frequency in case of pure rolling.

Axial, torsional, and lateral vibrations lead to reduction in rate of penetration and in accordance increasing the non-productive time, despite the destructive nature on the drillstring assembly.

Checking and determining drillstring mass unbalance magnitude and angular position before the drilling operation could help in determining the optimal positions to install the stabilizers and ways to suppress the vibrations.

7. DRILLSTRING VIBRATION DYNAMICS CONCLUSIONS

The following conclusions are based upon the studies conducted to simulate the drillstring dynamics using different methods, and from the results obtained.

- There are various potential excitation sources of drillstring vibration such as: mass imbalance, friction factor between drillstring and borehole, operational spin velocity, cutting action of the drillbit, BHA stiffness, clearance between BHA components and borehole, bent angle, stabilizers locations, and fluid forces around the drillstring.
- The friction coefficient of the formation and the top drive angular speed can drastically affect the rotor dynamics. Increasing the friction coefficient can change rotation behavior from forward whirl with pure sliding to backward whirl and even to pure rolling without slipping. The non-linear Stribeck friction function causes instability in the rotation motion at low angular velocities which can leads to drillbit stick-slip torsional vibration.
- Stick-slip vibration behavior is induced generally at low drilling operational speeds and high applied *WOB* (high formation stiffness).
- There is a coupling between the torsional and axial vibrations of the drillstring dynamics. Drillbit is the major cause of this coupling expressed in the direct relationship between the *TOB* and the *WOB*.
- Drillbit with bent angle is a major source in self-exciting the three types of vibration in the drillstring while drilling, as the lateral component of the *WOB* causes a coupling between the axial and the lateral modes of vibration and hence

torsional. The coupling between the three vibration modes is first addressed by Saeed and Palazzolo [35], and is implemented in the codes presented here as a feature used in the simulation investigations.

- Lateral vibrations are the most destructive type of vibration and are generally induced due to drillstring bending from the imbalance of the assembly or weak BHA stiffness, and at high angular velocities. The interaction between a BHA component (e.g. stabilizer, drillbit) and the borehole formation determined by the friction coefficient value leads either to forward whirl, chaotic discrete lateral vibration, or in certain circumstances to backward whirl.
- Backward whirl is an undesired vibration mode since it can lead to a pure rolling contact motion behavior that causes destructive reverse bending vibration mode with high frequency whirling motion. This results in high rates of BHA component and connection fatigue, as well as in an over gauged borehole due to high frequency rubbing.
- Five major parameters can lead to backward whirling with pure rolling; to have a weak (or non-stiff) drill-collars, assembly imbalance, low WOB, high rotational speed, and high side friction coefficient with the formation.
- The clearance between the borehole and the BHA components, especially the installed stabilizers, plays a major role in identifying the severity of the whirling frequency in case of pure rolling.
- A Novel model has been described for investigating the drillstring dynamics while drilling, using Timoshenko finite-element-modelling including the most

destructive mode of vibration "Backward whirling with pure rolling". This gives a more accurate examination of the drillstring dynamic response under the influence of the operation parameters, more than any other models addressed before in literature.

- Some features are added to the code to give a wider range of input conditions such as; non-linear Stribeck friction, drilling mud damping effect, drillbit bent angle, locations for implemented mass bodies inside the BHA collars (e.g. flywheel), node selection for applied eccentricity, and node selection for attached stabilizers.

REFERENCES

[1] Coleman, S., *Stuck Pipe Prevention Book*. Shyne Coleman, EBook, 2012.

[2] Abdul-Ameer, M. R., *An empirical correlation to estimate solid stresses for differentially stuck pipes*, Journal of Engineering, 2005. 11(4): p.787.

[3] Bowes, C.; Procter, R., *Drillers stuck pipe handbook*, guidelines & drillers handbook credits, 1997. Schlumberger, Ballater.

[4] Paiaman, A.M., *Using nanoparticles to decrease differential pipe sticking and its feasibility in Iranian Oil fields*, Oil and Gas Business, 2008.

[5] Guzman, J. M.; Khalil, M. E., *Stuck-Pipe Prevention Solutions in Deep Gas Drilling; New Approaches*, SPE Saudi Arabia Section Technical Symposium and Exhibition, 8-11 April 2012, Al-Khobar, Saudi Arabia, SPE-160875-MS.

[6] Sheiretov, Todor K., *System and method for unsticking a tool stuck in a wellbore*. US Patent No. 20070227736. Washington, DC: U.S. Patent and Trademark Office. 2007.

[7] Oilfield Glossary. Schlumberger,www.glossary.oilfield.slb.com/Display.cfm?Term=washout. 15 October 2011.

[8] Oilfield Glossary. Schlumberger, www.glossary.oilfield.slb.com/Display.cfm?Term=keyseat, October 2011.

[9] Wheater, G., *Wirelien Stand-off*, UK Patent No. GB 2450918 B. UK Intellectual Property Office. 2011.

[10] Schlumberger. *Schlumberger Wireline Deployment*. 2011.

[11] Wheater et al., *Low friction Wirelien Stand-off*. US Patent No. 2012/0031609 A1. Washington, DC: U.S. Patent and Trademark Office. 2012.

[12] Gorski, L., *Pipe Sticking Mechanism Categories*. www.scribd.com/doc/57635318/Pipe-Sticking-Mechanism-Categories. 2011.

[13] Thomas et al., *Method and apparatus for well bore hole-finding with simultaneous borehole or formation sensing*. US Patent No. 6,002,257. Washington, DC: U.S. Patent and Trademark Office. 2009.

[14] IODP United States Implementing Organization (IODP-USIO), *Downhole logging tools – Hole finder*. iodp.ldeo.columbia.edu/TOOLS_LABS/OTHER/hole_finder.html. December 2011.

[15] Wireline-Engineering Ltd. *Wireline conveyance products - Roller Bogie Hole Finder*. www.wireline-engineering.com/technology2.cfm?tech_ID=12. November 2011.

[16] Maidla, E. E., Wojtanowicz, A. K., *Laboratory Study of Borehole Friction Factor with a Dynamic-Filtration Apparatus*, SPE Drilling Engineering, 1990. 5(3): p.247-255. SPE-18558-PA.

[17] Behenna, R., CTES, L.P., *Intervention modeling reduces costs*, E&P Magazine, 2006. Feb.2012 <www.epmag.com/EP-Magazine/archive/Intervention-modeling-reduces-costs_5652>.

[18] Slotboom, O.F., *Simplified estimation of helically steel armored cable elongation, diameter reduction, and rotation*, OCEANS '95. MTS/IEEE. Challenges of Our Changing Global Environment. Conference Proceedings. , vol.1, no., p.126-137 vol.1, 9-12 Oct 1995

[19] M. Machado et al., *Dynamic Response of Multibody Systems with 3D Contact-Impact Events: Influence of the Contact Force Model*, EUROMECH Colloquium 524, Multibody System Modelling, Control and Simulation for Engineering Design. 2012.

[20] Chang, K., *Motion Simulation and Mechanism Design with COSMOSMotion-User Manual*, COSMOSMotion, 2011.

[21] *Introduction to Well Logging (Logging Procedures),* Web log post. Petroleum, Crude Oil. N.p., Nov. 2008. Web. June 2012. <http://petroleumcrudeoil.blogspot.com/>.

[22] Zhuk, Y., *Coating extends downhole tool life*, E&P Magazine. 2006. Feb.2012 <www.epmag.com/EP-Magazine/archive/Coating-extends-downhole-tool-life_6280>.

[23] McCormick, J. E.; Le, J.; Evans, C., *Coating Optimized For Abrasion And Fatigue Resistance For Use In Extreme Well Geometries*, SPE/IADC Drilling Conference and Exhibition, 1-3 March 2011, Amsterdam, The Netherlands .p:1-9. SPE-139769-MS.

[24] Thornton, T. J. O., *Downhole tools*, US Patent No. 7,918,274 B2. Washington, DC: U.S. Patent and Trademark Office. 2011.

[25] Saenger, R.; Desroches, J.; Quisel, N., *Durability of Downhole Tools*, US Patent No. 2011/0061945 A1. Washington, DC: U.S. Patent and Trademark Office. 2011.

[26] Al-zahrani, M. S., *System, method, and apparatus for survey tool having roller knuckle joints for use in highly deviated horizontal wells*, US Patent No. 7188671. Washington, DC: U.S. Patent and Trademark Office. 2007.

[27] Wheater, G., *Articulated wireline hole finder*, UK Patent No. GB 2483227. UK Intellectual Property Office. 2012.

[28] Moore, B. N., *Wellbore tractor with fluid conduit sheath*, US Patent No. 20080047715. Washington, DC: U.S. Patent and Trademark Office. 2008.

[29] Newman, K. R.; Haver, N. A.; Speller, D. J., *Wellbore tractor and method of moving an item through a wellbore*, US Patent No. 5794703. Washington, DC: U.S. Patent and Trademark Office. 1998.

[30] Brian, S.; Kristine, H., *The Development of Wireline-Tractor Technology*, SPE-Tech 101 Series. 2009.

[31] "*Drillstring Vibrations and Vibration modeling*," Schlumberger, www.slb.com/drillinggop, 2010, (accessed January 2014).

[32] K. Mongkolcheep et al, *A Modal Approach for Chaotic Vibrations of a Drillstring*, Proceedings of the ASME IDETC/CIE 2009, San Diego, California, USA.

[33] Feng, Z.C.; Zhang, X., *Rubbing phenomena in rotor-stator contact, Chaos, Solutions and Fractals*, 14 (2002), p. 257-267.

[34] Khulief et al., *Vibration Analysis of Drillstrings with Self-Excited Stick–Slip Oscillations*, Journal of Sound and Vibration 299. 2007, p. 540–558.

[35] Saeed, A.; Palazzolo, A.; Ahmed, S., *A Novel magnetically-levitated flywheel energy storage alternative to lithium-ion battery packs for oilfield service*, ASME 2012 International Mechanical Engineering Conference & Exposition IMECE, Houston, Texas, USA, 2012.

[36] Leine, R.I.; D. H. van Campen, *Stick-slip whirl interaction in drillstring dynamics*, Journal of Vibration and Acoustics, ASME, Vol. 124, April 2002, p. 209-220.

[37] Richard, T.; Germay, C.; and Detournay, E., *Self-Excited Stick–Slip Oscillations of Drill Bits*, C.R. Mecanique 332, 2004, p. 619–626.

[38] Detournay E.; and Defourny, P., *A Phenomenological Model for the Drilling Action of Drag Bits*, International Journal of Rock Mechanics and Mining Sciences & Geomechanics Abstracts, 1992, 29 (1), p. 13-23.

[39] Yigit & Christoforou, *Stick-Slip and Bit-Bounce Interaction in Oil-Well Drillstrings*, Journal of Energy Resources Technology, Vol. 128, December 2006, p. 268-274.

[40] Yigit & Christoforou, *Coupled Torsional and Bending Vibrations of Drillstring Subject to Impact with Friction*, Journal of Sound and Vibration, 1998, Vol 215, No, p. 167-181.

[41] Franca, L.F.P., *Drilling Action of Roller-Cone Bits: Modeling and Experimental Validation*, Journal of Energy Resources Technology, 2010. 132: p. 1-9.

[42] Patil, P.; Teodoriu, C., *Model development of torsional drillstring and investigating parametrically the stick-slips influencing factors*, Journal of Energy Resources Technology, ASME, Vol. 135, March 2013.

[43] Nelson, F.C., *Rotor Dynamics without Equations*, International Journal of COMADEM, 10(3) July 2007, P. 2–10.

[44] Roberts T. S., *Development of a new concept of steerable pdc bit for directional drilling*. In IADC/SPE Drilling Conference, 1998, number IADC/SPE 39307, 141-151, Dallas, Texas, U.S.A. Society of Petroleum Engineers.

[45] Stroud, d.; Pagett, j.; and Minett-Smith, D., *Real-Time Whirl Detector Improves RSS Reliability, Drilling Efficiency*, Weatherford International Ltd. 2011.

[46] N. Vlajic et al, *Rotor torsion vibrations in the presence of continuous stator contact,* ASME 2012 International Mechanical Engineering Congress & Exposition IMECE2012, November 9-15, 2012, Houston, Texas, USA.

[47] Reddy, J.N., *An Introduction to the Finite Element Method*, McGraw-Hill Higher Education, 2006. New York.

[48] Mongkolcheep, K., *A lyapunov exponent approach for identifying chaotic behavior in a finite element based drillstring vibration model*, Master's thesis, Texas A&M University, Aug 2009.

[49] Luo, Y., *An Efficient 3D Timoshenko Beam Element with Consistent Shape Functions*, Adv. Theor. Appl. Mech., Vol. 1, 2008, no. 3, p. 95–106.

APPENDIX A

Entries of the element stiffness matrix of a 3D Timoshenko beam element with 2-nodes according to reference [26]. The other not listed entries are zeroes.

$$k_{1,1} = k_{7,7} = -k_{1,7} = \frac{EA}{L}$$

$$k_{2,2} = -k_{2,8} = \frac{12kGA\,EI_y(12EI_y + kGAL^2)}{L(12EI_y - kGAL^2)^2}$$

$$k_{2,6} = k_{2,12} = \frac{6kGA\,EI_y(12EI_y + kGAL^2)}{(12EI_y - kGAL^2)^2}$$

$$k_{3,3} = k_{3,9} = \frac{12kGA\,EI_z(12EI_z + kGAL^2)}{L(12EI_z - kGAL^2)^2}$$

$$k_{3,5} = k_{3,11} = -\frac{6kGA\,EI_z(12EI_z + kGAL^2)}{(12EI_z - kGAL^2)^2}$$

$$k_{4,4} = k_{7,7} = -k_{4,10} = \frac{G(I_y + I_z)}{L}$$

$$k_{5,5} = \frac{4EI_z[(kGA)^2L^4 + 3kGAL^2\,EI_z + 36(EI_z)^2]}{L(12EI_z - kGAL^2)^2}$$

$$k_{5,9} = \frac{6kGA\,EI_z(12EI_z + kGAL^2)}{(12EI_z - kGAL^2)^2}$$

$$k_{5,11} = -\frac{2EI_z[72(EI_z)^2 - (kGA)^2L^4 - 30kGAL^2\,EI_z]}{L(12EI_z - kGAL^2)^2}$$

$$k_{6,6} = \frac{4EI_y[(kGA)^2L^4 + 3kGAL^2\,EI_y + 36(EI_y)^2]}{L(12EI_y - kGAL^2)^2}$$

$$k_{6,8} = -\frac{6kGA\,EI_y(12EI_y + kGAL^2)}{(12EI_y - kGAL^2)^2}$$

$$k_{6,12} = -\frac{2EI_y[-(kGA)^2L^4 - 30kGAL^2\,EI_y + 72(EI_y)^2]}{L(12EI_y - kGAL^2)^2}$$

$$k_{8,8} = \frac{12kGA\,EI_y(12EI_y + kGAL^2)}{L(12EI_y - kGAL^2)^2}$$

$$k_{9,11} = \frac{6kGA\,EI_z(12EI_z + kGAL^2)}{(12EI_z - kGAL^2)^2}$$

$$k_{11,11} = \frac{4EI_z[(kGA)^2L^4 + 3kGAL^2\,EI_z + 36(EI_z)^2]}{L(12EI_z - kGAL^2)^2}$$

$$k_{12,12} = \frac{4EI_y[(kGA)^2L^4 + 3kGAL^2\,EI_y + 36(EI_y)^2]}{L(12EI_y - kGAL^2)^2}$$

APPENDIX B

MATLAB CODES

Lumped_RotorStator.m

```
% % Omar Abdelzaher
% Rotor-Stator 3-DOF lateral/rotational model using lumped mass method
% Created September 10, 2013
% Updated April 10, 2014

%%
clc
clear all
close all
global m K K_phi C Cphi Jc w Phidot Phi Fe V_rel theta Jt Vmin Je omega Kb
global mu0 mud mus e R Rh Rc   wn   r Fbn Fbt  Fx ma mf B1 B2 D

%% [1]% INPUT SYSTEM PARAMETERS  %%%%%%%%%%%%%%%%%%%%%%%%%%%%%%%%%%%%%%%%%
%%%%%%%%%%%%%%%%%%%%%%%%%%%%%%%%%%%%%%%%%%%%%%%%%%%%%%%%%%%%%%%%%%%%%%%%%%%%
Vmin=0.001;            % Set the Minimum relative velocity
Kb=400000;             % Borehole Contact Stiffness
% mu0=0.12;            % Borehole Contact Friction
mud=0.07;              % Borehole dynamic Contact Friction
% mus=1.1*mud;         % Borehole static Contact Friction
ma=1;                  % Rotor mass
e= 0.001;              % eccentricity of rotor's center mass
R= 0.05;               % Rotor radius
% Rh=0.503;            % Borehole radius
% Rc=Rh-R;             % Rotor-Borehole Clearance according to (Rh)
Rc=0.0025;             % Rotor-Borehole Clearance
K=40;                  % Rotor radial stiffness
%zeta= 0.3;            % Damping ratio
%C=zeta*2*sqrt(ma*K);  % Rotor damping coefficient calculated
C=1;                   % Rotor lateral damping coefficient
Cphi=0.2;              % Rotor torsional coefficient
%wn=sqrt(K/ma);        % Rotor natural freq
w=12.6491;             % Top Drive Spin Speed (rad/s)
Jc= 0.5*ma*R^2;        % Rotor's moment inertia at center
Je=ma*e^2;             % Moment Inertia at unbalance mass
Jt= Jc+Je;             % Total rotation moment of inertia
K_phi=0.6;             % Torsional stiffness of rotor

% % Input Fluid Mud Parameters

% If presence of Mud
%%%%%%%%%%%%%%%%%%%
% D=0.1;                 % fluid friction coefficient
% B1=0.1;                % constant 1
% B2=0.0;                % constant 2
% mf=0.5;                % fluid mass

% No Mud
%%%%%%%%%%%%%%%
D=0;                     % fluid friction coefficient
B1=0;                    % constant 1
B2=0;                    % constant 2
mf=0;                    % fluid mass

% % Calculate total system mass
m=ma+mf;                 % Total sys mass


%% [2]% SIMULATION TIME   %%%%%%%%%%%%%%%%%%%%%%%%%%%%%%%%%%%%%%%%%%%%%%%%%
```

```
%%%%%%%%%%%%%%%%%%%%%%%%%%%%%%%%%%%%%%%%%%%%%%%%%%%%%%%%%%%%%%%%%%%%%%%%%%%%
tstart=0;                                    % Start Simulation Time
tend=10;                                     % End Simulation Time
n=300000;                                    % Number of steps
maxstep=0.01;                                % Maximum Simulation Step (Output Data)

tspan=linspace(tstart,tend,n);               %(fixed step size=tend/n)
% tspan= [tstart tend];                      %(variable step size)

% Define the initial conditions making sure to use the right ordering
initial_x=   [0.000001 0 ];                  % X(0)=0 , X'(0)=0
initial_y=   [0.00001  0 ];                  % Y(0)=0 , Y'(0)=0
initial_phi= [0        w ];                  % Phi(0)=0 , Phi'(0)=0
initials= [initial_x initial_y initial_phi ];

% % ODE - INTEGRATION
options = odeset('AbsTol',1e-6,'RelTol',1e-5,'initialStep',0.01,'MaxStep',maxstep);
tic

% Ode- Integrator Type Selection
[t,x]=ode45(@Lumped_RotorStator_sub,tspan,initials,options); % more STIFF Integrator
% [t,x]=ode23s(@Lumped_RotorStator_sub,tspan,initials,options);
% [t,x]=ode15s(@Lumped_RotorStator_sub,tspan,initials,options);
toc


%% [3]% Defining  Output variables:
%%%%%%%%%%%%%%%%%%%%%%%%%%%%%%%%%%%%%%%%%%%%%%%%%%%%%%%%%%%%%%%%%%%%%%%%%%%%
X=x(:,1);                      % Rotor X-Displacement
Xdot=x(:,2);                   % Rotor X-Velocity
Y=x(:,3);                      % Rotor Y-Displacement
Ydot=x(:,4);                   % Rotor Y-Velocity
Phi=x(:,5);                    % Rotor rotational angle
Phidot=x(:,6);                 % Rotor rotational angular velocity

r=sqrt(X.^2+Y.^2);              % radial displacement of rotor's center
theta= atan (Y./X);             % radial angle of rotor's center
omega= (X.*Ydot-Y.*Xdot)./r.^2;% whirl velocity
V_rel=Phidot.*R+omega.*r;       % Relative velovity
Fbn= Kb.*(r-Rc);                % contact force
Fbn(Fbn<0)=0;                   % set zero for any negative value in Fbn
Fbt= -mud.*sign(V_rel).*Fbn;    % friction force
omega_theo= zeros (size(X));    % Initiate Theoritical whirling velocity (Omega)
for i= 1 : size(X)
if Fbn(i)==0       % No fromation radial contact
    Fbt_R(i)=0;
else
    % Calculate the theoritical rotor friction force at Pure-Rolling status
    % (Zero relative velocity)
Fbt_R(i)= ((m.*K_phi.*R./Jt).*(w.*t(i)-Phi(i))+ C.*omega(i).*r(i)-
Cphi.*m.*R.*Phidot(i)/Jt)./(1+ (m.*R.^2)./Jt);
end
end

% Apply Stribeck Friction between Rotor and Formation
% mu= - (2./pi).*atan(10.^4.*V_rel).*( ((mus-mud)./(1+10.^3.*abs(V_rel)))+mud);
% Fbt= mu.*Fbn;

% % Check whirling Status - FLAGS !
% Initializing Flags
NC= zeros (size(X));    % NO-CONTACT
SL= zeros (size(X));    % SLIDING  (Forward Whirling)
RL= zeros (size(X));    % Pure- Rolling with No Sliding (Backward Whirling) !!
TR= zeros (size(X));    % TRANSITION (Mixed)

 for i= 1: size(X)
     if Fbn(i)==0      % No Rotor/Formation Contact
```

```
        NC(i)=1;
     elseif Fbn(i)~=0  % There is Rotor/Formation Contact
         if abs(V_rel(i))>Vmin && sign(Phidot(i))== sign(omega(i))
             SL(i)=1;  % SLIDING  (Forward Whirling)
     elseif abs(V_rel(i))<=Vmin && abs(Fbt_R(i))<=abs(Fbt(i))
         RL(i)=1;      % Pure- Rolling with No Sliding (Backward Whirling) !!
         omega_theo(i)= -(R./r(i)).*Phidot(i);
     else TR(i)=1;     % TRANSITION (Mixed)
         end
     end
 end
%
Total_Fc= sqrt(Fbn.^2 + Fbt.^2);   % Magnitude of total contact force

%% [4]% Plotting Output Data  %%%%%%%%%%%%%%%%%%%%%%%%%%%%%%%%%%%%%%%%%%%%%
%%%%%%%%%%%%%%%%%%%%%%%%%%%%%%%%%%%%%%%%%%%%%%%%%%%%%%%%%%%%%%%%%%%%%%%%%%%%

% Plotting- Rotor x,y position
figure (1)
plot (X,Y);
hold on
Radius=Rc;
[cx,cy,z] = cylinder(Radius,100);
axis equal
plot(cx(1,:),cy(1,:),'r.');
grid
title('Rotor Center Orbit');
xlabel('Rotor Xg (m)');
ylabel(' Rotor Yg (m)' );

% Plotting- Rotor whirling velocity
figure (2)
plot (t,omega,'k');
hold on
grid
plot (t, omega_theo,'--r');
title(' Rotor whirl velocity');
xlabel('Time (S)');
ylabel('Omega (rad/s)' );
legend ('omega','omega_tho');

% Plotting- Rotor contact force
figure (3)
plot (t,Fbn);
grid
title('Contact Force ');
xlabel('Time (S)');
ylabel(' Fn (N)' );

% Plotting- Rotor friction force
figure (4)
plot (t,Fbt);
grid
title('Stator Friction force');
xlabel('Time (S)');
ylabel(' Ft (N)' );

% Plotting- Rotor relative velocity
figure (5)
plot (t,V_rel);
grid
title('Relative velocity');
xlabel('Time (S)');
ylabel(' V_rel (rad/s) ' );

% Plotting- Rotor rotational velocity
figure (6)
```

```
plot (t,Phidot);
grid
title('Rotor rotational velocity');
xlabel('Time (S)');
ylabel(' Phidot (rad/s) ' );

% Plotting- Rotor radial displacement
figure (7)
plot (t,r);
grid
title('Rotor radial diplacement');
xlabel('Time (S)');
ylabel(' r (m) ' );
hold on
plot (t,Rc,'--r');
hold off

% Plotting- Rotor Total contact force
% figure (8)
% plot (t,Total_Fc);
% grid
% title('Total Contact force (magnitude) ');
% xlabel('Time (S)');
% ylabel(' F contact (N)' );

% Plotting- Rotor friction force Vs. Theor pure-rolling friction force
figure (9)
plot (t,Fbt,'k');
grid
hold on
plot (t,Fbt_R,':r');
title('Tangintial force ');
xlabel('Time (S)');
ylabel(' Ft  (N)' );
legend ('Fbt','Fbt_R');

%Plotting- Rotor motion Status
figure (10)
% plot (t, NC, '-k');
hold on
grid on
% plot (t, SL, '-B');
plot (t, RL, '.R');
% plot (t, TR, '-G');
title ( 'Backward Whirling Condition');
xlabel('Time (S)');
ylabel('0=NOT active                  1= ACTIVE !' );
% legend ('No Contact','Sliding', 'ROLLING !!','Transition');
```

Lumped_RotorStator_sub.m

```
%% Omar Abdelzaher
% Rotor-Stator 3-DOF lateral/rotasional model using lumped mass method
% Created September 10, 2013
% Updated April 10, 2014

%% call intigration function
%%%%%%%%%%%%%%%%%%%%%%%%%%%%%%%%%%%%%%%%%%%%%%%%%%%%%%%%%%%%%%%%%%%%%%%%%%%%
function xdot= Lumped_RotorStator_sub(t,x)
global m K K_phi r C Jt mu0 Vmin  e B1 B2 R Cphi Rc mu mus mud V_rel omega
global D w eta1 eta2 ma mf Fe Fe_x Fe_y Fb_x Fb_y Fbn Fbt Kb  Tb

% State Variables
% x= [ x xdot y ydot phi phidot]
% x= zeros(6,1);
```

```
% xdot=zeros(6,1);
% x=x(1);
% xdot=x(2);
% y=x(3);
% ydot=x(4);
% phi=x(5);
% phidot=x(6);

%% Caculating variables
r= sqrt(x(1)^2+x(3)^2);                        % Rotor radial desplacement
eta1=B1*r^2;                                   % Fluid nonlinear function 1
eta2=B2*r^2;                                   % Fluid nonlinear function 2
omega= (x(1)*x(4)-x(3)*x(2))/r^2;              % Rotor whirl velocity
V_rel= x(6)*R+omega*r;                         % rotor Relative velocity
Fe=e*ma*(x(6)^2);                              % centrifugal  force
Fe_x=Fe*cos(x(5));                             % eccentricity- centrifugal force in X-dir
Fe_y=Fe*sin(x(5));                             % eccentricity- centrifugal force in Y-dir

%% Logic for rotor motion status
if r<=Rc        % If (NO CONTACT)
    Fbn=0;                     % No Contact force
    Fbt=0;                     % No friction force
%      disp('-- NO CONTACT ---------------------');
else      % If (THERE IS CONTACT)
Fbn= Kb*(r-Rc);                % Calculate Normal Contact force
Fbt= -mud*sign(V_rel)*Fbn;     % Calculate friction force
% Calculate theoritical friction force incase of Pure-Rolling (Vrel=0)
Fbt_R= ((m*K_phi*R/Jt)*(w*t-x(5))+ C*omega*r - Cphi*m*R*x(6)/Jt)/(1+ (m*R^2)/Jt);
   if abs(V_rel)>Vmin && sign(x(6))== sign(omega)
%     disp('---------  SLiding ----------------');
   elseif  abs(V_rel)<=Vmin && -(mud*Fbn)<=Fbt_R <=(mud*Fbn)
           Fbt=Fbt_R;
%     disp('--------------- Pure Rolling -----');
   else
%        disp('------------------ TRANSITION -----');
   end
end
%% Calculate applied forces on Rotor
Fb_x=(-Fbt*x(3)-Fbn*x(1))/r;                   % Contact force in X-dir
Fb_y=(Fbt*x(1)-Fbn*x(3))/r;                    % Contact force in Y-dir
Tb=Fbt*R;                                      % Friction Torque on Rotor

%% EOM's %%%%%%%%%%%%%%%%%%%%%%%%%%%%%%%%%%%%%%%%%%%%%%%%%%%%%%%%%%%%%%%
%%%%%%%%%%%%%%%%%%%%%%%%%%%%%%%%%%%%%%%%%%%%%%%%%%%%%%%%%%%%%%%%%%%%%%%%%%%
% % (X-axis)
xdot_1= x(2);
xdot_2= ( -C*x(2)- K*x(1)+ Fe_x +Fb_x )/m;           % Incase of No Mud fluid
% xdot_2= -((C+D+eta2)/m)*x(2)-((x(6)*mf)/m)*x(3)-((K-((x(6)^2)/4)*mf+eta1)/m)*x(1)-
(((x(6)/2)*D+(w/2)*eta2)/m)*x(3)+(Fe_x)/m +Fb_x/m;
% % (Y-axis)
xdot_3= x(4);
xdot_4= ( Fe_y + Fb_y - C*x(4) - K*x(3) )/m ;        % Incase of No Mud fluid
% xdot_4= (Fe_y)/m + Fb_y/m -((C+D+eta2)/m)*x(4)-(-x(6)*mf)*x(2)-((K+eta1-
((x(6)^2)/4)*mf)/m)*x(3)- (((-x(6)/2)*D-(x(6)/2)*eta2)/m)*x(1) ;
% % (Z-axis)
xdot_5= x(6);
xdot_6= (-K_phi*(x(5)-w*t)- Cphi*x(6)-Tb)/Jt;


xdot= [ xdot_1; xdot_2; xdot_3; xdot_4; xdot_5; xdot_6];
t
end
```

Lumped_Drillstring.m

```
% % Omar Abdelzaher
% Drillstring Lumped-System-Model using Three lumped masses with 6-DOF
% Created December 15, 2014
% Updated April 24, 2014

%%
clc
clear all
close all
%dbstop if naninf

%% Difine Global Variables
global Tx_db Ty_db  Tz_db X_0 mu_s WOB landa f Rh w Vmin w_fl W0 M_st J_st
global Je I_st M_BHA M_fl J_BHA I_BHA M_db J_db I_db e q S0 b C1 C2 alpha
global r_st r_fl R_st Rc_st  omega_st Vrel_st mu_st mu  Kf Kc  Fn_st Ft_st
global Kxy_BHA Kxy_dp  Kxy_fl Kz_dp Kz_BHA Kz_fl KphiZ_dp KphiZ_BHA KphiXY_BHA
global KphiXY_dp Cxy_dp Cxy_BHA Cxy_fl Cz_dp Cz_BHA Cz_fl Cf J_m  Rm Km Lm
global r_BHA R_BHA Rc_BHA omega_BHA Vrel_BHA mu_BHA Fn_BHA Ft_BHA n J_rt
global r_db a Rc_db omega_db Vrel_db mu_db S Fn_db Ft_db Cf_z WOB_z TOB

%% [1]% INPUT SYSTEM PARAMETERS  %%%%%%%%%%%%%%%%%%%%%%%%%%%%%%%%%%%%%%%%%%
%%%%%%%%%%%%%%%%%%%%%%%%%%%%%%%%%%%%%%%%%%%%%%%%%%%%%%%%%%%%%%%%%%%%%%%%%%%%

% A)STEEL material properties
%%%%%%%%%%%%%%%%%%%%%%%%%%%%%%%%%%
E= 200e9;                              % Modulus of Elasticity Pa
nu= 0.4;                               % Poisson's Ratio
mass_rho = 7850;                       %  Density kg/m^3
G= (3/8)*E;                            % Calculate Element Shear Moduli  . (lb/in^2)
%Mass=mass_rho*Ac*L;                   % Mass of element

% B)Rotary Table parameters
%%%%%%%%%%%%%%%%%%%%%%%%%%%%%%%%%%
rpm= 140;                              % rotary speed of rotary table (RPM)
w= rpm*2*pi/60;                        % rotary speed of rotary table (rad/s)
n=7.2 ;
Rm=0.01  ;                             % armature resistance (Ohm)
Lm=0.005;                              % armature inductance (H)
J_rt=930;                              % Rotary table inertia (Kg.m2)
J_m=23;                                % Motor inertia (Kg.m2)
Km= 6;                                 % Motor constant

% C)loads parameters
%%%%%%%%%%%%%%%%%%%%%%%%%%%%%%%%%%
W0=50e3;                               % upper applied Static load 100 KN
Vmin=0.001;

% D)Formation parameters
%%%%%%%%%%%%%%%%%%%%%%%%%%%%%%%%%%
Rh=(7.4/2)*0.0254;                     % Borehole radius
Kf=2e10;                               % lateral formation Contact Stiffness // for
bit bounce result try softer formation stiffness let Kb=50000000
Kc=67e5;                               % axial formation Contact Stiffness
mu=0.3;                                % formation Contact Friction
% mu_s=mu+0.1;
b=1;                                   % Formation surface function constant
S0=0.001;                              % Formation elevation amplitude = 1mm
C1=  1.35e-8;                          % Penetration Constant
C2= -1.9e-4;                           % Penetration Constant 2

% E)Drilling fluids parameters
%%%%%%%%%%%%%%%%%%%%%%%%%%%%%%%%%%
Cf= 2e2;                               % Drilling fluid  torsional Damping
Cf_z=10e0;                             % Drilling fluid  Axial Damping
```

```
% F)Drillpipe parameters
%%%%%%%%%%%%%%%%%%%%%%%%%%%%%%%%%%
L_dp=5700;                             % Drill-pipe length
OD_dp=(5)*0.0254;                      % Drill-pipe OD
ID_dp=(3/8)*0.0254;                    % Drill-pipe ID
Ac_dp = pi/4*(OD_dp.^2 - ID_dp.^2);    % Drill-pipe cross section area
M_dp=mass_rho*Ac_dp*L_dp;              % Drill-pipe total mass
J_dp=(M_dp/8)*(OD_dp^2+ID_dp^2);       % Drill-pipe moment of Inertia about Z
I_dp=(1/(12*8))*M_dp*(3*(OD_dp^2+ID_dp^2)+L_dp^2);
% Kz_dp= 10e7;
Kz_dp=(5)*(Ac_dp*E)/L_dp;              % Axial drillpipe stiffness in Z
% Kxy_dp= Kf/1000  ;
Kxy_dp=(0.1)*(12*E*I_dp/L_dp^3)/1000;  % Equivalent Drill-pipe Bending stiffness in
x,y
%KphiXY_dp=4*E*I_dp/L_dp;
KphiXY_dp=10e5;                        % Equivalent Drill-pipe Torsional stiffness
about X,Y
%KphiZ_dp=G*J_dp/L_dp;
KphiZ_dp=1e5;                          % Equivalent Drill-pipe Torsional stiffness
about Z
Cxy_dp=10e1;                           % Equivalent lateral Drill-pipe damping
coefficient in x,y
Cz_dp=1e2;                             % Axial Drill-pipe damping

% G)Stabilizer parameters
%%%%%%%%%%%%%%%%%%%%%%%%%%%%%%%%%%
R_st= (7/2)*0.0254;                    % Stabilizer radius
Rc_st=Rh-R_st;                         % Stabilizer clearance
M_st= M_dp;
J_st= J_dp;
I_st= I_dp;

% H)Flywheel parameters
%%%%%%%%%%%%%%%%%%%%%%%%%%%%%%%%%%
% N_fl=3000;                          % flywheel (rpm)
N_fl=1;                               % flywheel (rpm)
w_fl=N_fl*2*pi/60;                    % flywheel angular speed (rad/sec)
% R_fl=0.0730;                        % R_BHA-0.5*0.0254;
R_fl=0.001;                           % R_BHA-0.5*0.0254;
H=2;                                  % Flywheel length
% M_fl=132;                           % flywheel mass
M_fl=1;                               % flywheel mass
% q=5e-6;                             % Flywheel eccentricity
q=0;                                  % NO Flywheel eccentricity
J_fl=0.5*(M_fl*R_fl^2)+M_fl*q^2;      % Flywheel Inertia moment about Z
I_fl=(1/12)*M_fl*(3*R_fl^2+H^2);      % Flywheel Inertia moment about X,Y
Kxy_fl=(0.001)*12*E*I_fl/H^3;         % MB Radial stiffness in x,y
Kz_fl=M_fl*w_fl^2;                    % MB axial Stiffness between Flywheel/BHA spring
% Cxy_fl= 2e2;
Cxy_fl= 0.001;                        % Damping radial
% Cz_fl= 10 ;
Cz_fl= 0.001 ;                        % Damping axial

% I)BHA Drill-Collar parameters
%%%%%%%%%%%%%%%%%%%%%%%%%%%%%%%%%%
L_BHA=180/2;                          % BHA  length/segment  ((we have TWO segments))
e= 0.135 ;                            % eccentricity of rotor's center mass
OD_BHA = (6.75)*0.0254;               % Outer Diameters  (m)
R_BHA= OD_BHA/2;                      % BHA drill-collar radfius
Rc_BHA=Rh-R_BHA;                      % BHA drillcollar/Borehole Clearance
ID_BHA = (4)*0.0254 ;                 % BHA drill-collar Inner Diameters  (m)
Ac_BHA = pi/4*(OD_BHA.^2 - ID_BHA.^2);% BHA drill-collar Cross Sectional Area (m^2)
M_BHA=mass_rho*Ac_BHA*L_BHA;          % Mass BHA/ segment
J_BHA=((M_BHA+M_fl)/8)*(OD_BHA^2+ID_BHA^2);% Total rotation moment of inertia
Je=M_BHA*e^2;
I_BHA=(1/(12*8))*M_BHA*(3*(OD_BHA^2+ID_BHA^2)+L_BHA^2);
Kz_BHA=(5)*((Ac_BHA*E)/L_BHA);        % Equivalent BHA axial stiffness
```

```
Kxy_BHA=(0.5)*(12*E*I_BHA/L_BHA^3)/1000;% BHA radial stiffness in x,y
KphiZ_BHA= 5e5;                      % Equivalent BHA Torsional stiffness about Z
KphiXY_BHA= KphiXY_dp*2 ;            % Equivalent BHA Bending stiffness about X,Y
Cxy_BHA= Cxy_dp*2;                   % Equivalent lateral BHA damping coefficient in
x,y
Cz_BHA= Cz_dp*10;                    % Axial BHA drill-collar damping

% J)Drillbit
%%%%%%%%%%%%%%%%%%%%%%%%%%%%%%%%%%
OD_db= (7)*0.0254;                   % DRILLBIT Diameter
a=OD_db/2;                           % Tricone Drillbit- radius
Rc_db=Rh-a;                          % Rotor-Borehole Clearance
M_db=M_BHA;                          % Drillbit assembly total mass
J_db=J_BHA;                          % Total rotation moment of inertia about Z
I_db= I_BHA;                         % Total rotation moment of inertia about X,Y
alpha=0*pi/180;                      % Drillbit bent/tilt angle
X_0=0.001;                           % Drillbit parameter 1
f=0.005;                             % Drillbit parameter 2
landa= 0.9;                          % Drillbit parameter 3

%% [2]% SIMULATION TIME   %%%%%%%%%%%%%%%%%%%%%%%%%%%%%%%%%%%%%%%%%%%%%%%%%
%%%%%%%%%%%%%%%%%%%%%%%%%%%%%%%%%%%%%%%%%%%%%%%%%%%%%%%%%%%%%%%%%%%%%%%%%%%

to=0;                                % Start Simulation Time
tfinal=20;                           % Final Simulation Time
% Nsamples=5001;                     % Number of steps
maxstep=0.01;                        % Max. step size
% dt=tfinal/(Nsamples-1);
% tsim=[to:dt:tfinal];               % fixed step
tsim= [to tfinal];                   %(variable step size)

% define the initial conditions making sure to use the right ordering
X0= 0.00001;                         % Initial X-location
Y0= 0.00001;                         % Initial Y-location
Z0= -0.001;                          % Initial Z-location

% Stabilizer (1)
X0_st=     [X0     0 ];              % X(0)=X0   , X'(0)=0
Y0_st=     [Y0     0 ];              % Y(0)=Y0   , Y'(0)=0
Z0_st=     [Z0     0 ];              % z(0)=Z0   , z'(0)=0
PhiZ0_st=  [0      w ];              % Phi_z(0)=0, Phi'(0)=w
PhiX0_st=  [0      0 ];              % Phi_x(0)=0, Phi_x'(0)=0
PhiY0_st=  [0      0 ];              % Phi_y(0)=0, Phi_y'(0)=0

initialize_st= [ X0_st Y0_st Z0_st PhiZ0_st PhiX0_st PhiY0_st];

% BHA Drill-collars
X0_BHA=     [X0     0 ];             % X(0)=X0   , X'(0)=0
Y0_BHA=     [Y0     0 ];             % Y(0)=Y0   , Y'(0)=0
Z0_BHA=     [Z0     0 ];             % z(0)=Z0   , z'(0)=0
PhiZ0_BHA=  [0      w ];             % Phi_z(0)=0, Phi'(0)=w
PhiX0_BHA=  [0      0 ];             % Phi_x(0)=0, Phi_x'(0)=0
PhiY0_BHA=  [0      0 ];             % Phi_y(0)=0, Phi_y'(0)=0

initialize_BHA= [ X0_BHA Y0_BHA Z0_BHA PhiZ0_BHA PhiX0_BHA PhiY0_BHA];

% Flywheel
X0_fl=     [X0     0 ];              % X(0)=X0   , X'(0)=0
Y0_fl=     [Y0     0 ];              % Y(0)=Y0   , Y'(0)=0
Z0_fl=     [Z0     0 ];              % z(0)=Z0   , z'(0)=0

initialize_fl= [ X0_fl Y0_fl Z0_fl];

% Drillbit + Stabilizer (2)
X0_db=     [X0     0 ];              % X(0)=X0   , X'(0)=0
Y0_db=     [Y0     0 ];              % Y(0)=0 , Y'(0)=0
Z0_db=     [Z0     0 ];              % z(0)=0 , z'(0)=0
```

```
PhiZ0_db=  [0      w ];               % Phi_z(0)=0, Phi'(0)=w
PhiX0_db=  [0      0 ];               % Phi_x(0)=0, Phi_x'(0)=0
PhiY0_db=  [0      0 ];               % Phi_y(0)=0, Phi_y'(0)=0

initialize_db= [ X0_db Y0_db Z0_db PhiZ0_db PhiX0_db PhiY0_db];

% Motor + Rotary Table
I0_m=  0.001;                        % Drive motor Inertia
Phi0_rt=   [0       w];              % Rotary table fixed angular speed

initialize_rt= [I0_m  Phi0_rt];

% Initialization Matrix
initials= [initialize_st initialize_BHA initialize_fl initialize_db initialize_rt];

% % ODE - INTEGRATION
options = odeset('AbsTol',1e-6,'RelTol',1e-5,'initialStep',0.0001,'MaxStep',maxstep);
tic

% Ode- Integrator Type Selection
[t,x]=ode45(@Lumped_Drillstring_sub,tsim,initials, options);
% [t,x]=ode23s (@Lumped_Drillstring_sub,tsim,initials, options);
% [t,x]=ode15s (@Lumped_Drillstring_sub,tsim,initials, options);
% [t,x]=ode113 (@Lumped_Drillstring_sub,tsim,initials, options);
toc

%% [3]% Defining  Output variables:
%%%%%%%%%%%%%%%%%%%%%%%%%%%%%%%%%%%%%%%%%%%%%%%%%%%%%%%%%%%%%%%%%%%%%%%%%%%%%%

% Stabilizer (1)
X_st=x(:,1);
Xdot_st=x(:,2);
Y_st=x(:,3);
Ydot_st=x(:,4);
Z_st=x(:,5);
Zdot_st=x(:,6);
PhiZ_st=x(:,7);
PhiZdot_st=x(:,8);
PhiX_st=x(:,9);
PhiXdot_st=x(:,10);
PhiY_st=x(:,11);
PhiYdot_st=x(:,12);

%  BHA
X_BHA=x(:,13);
Xdot_BHA=x(:,14);
Y_BHA=x(:,15);
Ydot_BHA=x(:,16);
Z_BHA=x(:,17);
Zdot_BHA=x(:,18);
PhiZ_BHA=x(:,19);
PhiZdot_BHA=x(:,20);
PhiX_BHA=x(:,21);
PhiXdot_BHA=x(:,22);
PhiY_BHA=x(:,23);
PhiYdot_BHA=x(:,24);

% Flywheel
X_fl=x(:,25);
Xdot_fl=x(:,26);
Y_fl=x(:,27);
Ydot_fl=x(:,28);
Z_fl=x(:,29);
Zdot_fl=x(:,30);

% Drillbit
X_db=x(:,31);
```

```
Xdot_db=x(:,32);
Y_db=x(:,33);
Ydot_db=x(:,34);
Z_db=x(:,35);
Zdot_db=x(:,36);
PhiZ_db=x(:,37);
PhiZdot_db=x(:,38);
PhiX_db=x(:,39);
PhiXdot_db=x(:,40);
PhiY_db=x(:,41);
PhiYdot_db=x(:,42);

% Motor dynamics + Rotary table
I_m= x(:,43);
Phi_rt= x(:,44);
Phidot_rt=x(:,45);

%% [4]% Output variables calculation  %%%%%%%%%%%%%%%%%%%%%%%%%%%%%%%%%%%%%
%%%%%%%%%%%%%%%%%%%%%%%%%%%%%%%%%%%%%%%%%%%%%%%%%%%%%%%%%%%%%%%%%%%%%%%%%%%%

% Radial diplacements
r_st= sqrt(X_st.^2+Y_st.^2);                            % radial desplacement of Upper
stabilizer's mass center
r_BHA=sqrt(X_BHA.^2+Y_BHA.^2);                          % radial desplacement of
intermediate BHA's mass center
r_db= sqrt(X_db.^2+Y_db.^2);                            % radial desplacement of
Drillbit's mass center
r_fl= sqrt(X_fl.^2+Y_fl.^2);                            % radial desplacement of
Flywheel's mass center

% Whirling velocities
omega_st=  (X_st.*Ydot_st-Y_st.*Xdot_st)./r_st.^2;      % whirl velocity for upper
stabilizer mass
omega_BHA= (X_BHA.*Ydot_BHA-Y_BHA.*Xdot_BHA)./r_BHA.^2; % whirl velocity for
intermediate BHA mass
omega_db=  (X_db.*Ydot_db-Y_db.*Xdot_db)./r_db.^2;      % whirl velocity for Drillbit
mass

% Relative velocities
Vrel_st= PhiZdot_st.*R_st+omega_st.*r_st;               % relative velocity for upper
stabilizer mass
Vrel_BHA=PhiZdot_BHA.*R_BHA+omega_BHA.*r_BHA;           % relative velocity for
intermediate BHA mass
Vrel_db= PhiZdot_db.*a+omega_db.*r_db;                  % relative velocity for bottom
drillbit mass

% friction coefficients
mu_st=  mu;                                             % applied friction on upper
stabilizer mass
mu_BHA= mu;                                             % applied friction on
intermediate BHA mass
mu_db=  mu.*(tanh(PhiZdot_db)+(2.*PhiZdot_db)./(1+PhiZdot_db.^2)+(0.01).*PhiZdot_db);
% applied Stribeck friction on drillbit mass

% Contact forces
Fn_st= Kf.*(r_st-Rc_st);                                % contact force on upper
stabilizer mass
Fn_st(Fn_st<0)=0;                                       % set zero for any negative
value in
Ft_st= -mu_st.*sign(Vrel_st).*Fn_st;                    % friction force on upper
stabilizer mass

Fn_BHA= Kf.*(r_BHA-Rc_BHA);                             % contact force on
intermediate BHA mass
Fn_BHA(Fn_BHA<0)=0;                                     % set zero for any negative
value in
```

```
Ft_BHA= -mu_BHA.*sign(Vrel_BHA).*Fn_BHA;                % friction force on
intermediate BHA mass

Fn_db= Kf.*(r_db-Rc_db);                                % contact force on drillbit
mass
Fn_db(Fn_db<0)=0;                                       % set zero for any negative
value in
Ft_db= -mu.*sign(Vrel_db).*Fn_db;                       % friction force on drillbit
mass

% WOB
% Approach 1
S= S0.*sin(b.*PhiZ_db);                                 % formation surface elevation
WOB=Kc.*(Z_db-S);                                       % Weight on bit
WOB(WOB<0)=0;                                           % set zero if bit-bounce or no
formation contact
WOB_z=cos(alpha).*WOB;                                  % Axial WOB in Z-dirc dueto
bit angle
WOB_x=sin(alpha).*WOB.*cos(PhiZ_db);                    % Lateral WOB in X-dirc dueto
bit angle
WOB_y=sin(alpha).*WOB.*sin(PhiZ_db);                    % Lateral WOB in Y-dirc dueto
bit angle
ROP=C1.*W0.*sqrt(PhiZdot_db)+C2;                        % average rate of penetration
dc= (2.*pi.*ROP)./PhiZdot_db;                           % depth of cut
TOB=WOB.*a.*(mu_db+sqrt(dc./a));                        % Torque on bit

% % Check Drillbit pure-rolling status
FtR_db= zeros (size(Vrel_db));                          % Initialize Drillbit
theoritical applied friction force incase of pure-rolling (Vrel=0)
Rolling_db= zeros (size(Vrel_db));                      % Initialize Pure-Rolling Flag
!
for i = 1: size(Vrel_db)
    if Fn_db(i)~=0 && abs(Vrel_db(i))<=Vmin             % first logic condition check
for Backward whirling
     % Calculating theoritical applied friction force incase of pure-rolling
     FtR_db(i)=  (Cxy_BHA.*omega_db(i).*r_db(i)-
(M_db.*a./J_db).*(KphiZ_BHA.*(PhiZ_db(i)-PhiZ_BHA(i))+
Cf.*M_db.*a.*PhiZdot_db(i)))./(1+ (M_db.*a.^2)./J_db);
    if  -(mu.*Fn_db(i))<= FtR_db(i) <=(mu.*Fn_db(i))    % Second logic condition check
for Pure-Rolling
    Rolling_db (i)=1;                                   % If yes ===> Flag !
    else
    FtR_db(i)=0;                                        % If No
    end
    else
    end
end


% Approach 2   Ref.Parimal Patil (Model Development of Torsional
% drillstring and Investigating..)
% S= S0.*sin(b.*PhiZ_db);
% % WOB= W0+Kc.*X_0.*(1-sin(2.*pi.*f.*t));              % Vertical WOB in Z-dirc duto
bit inclination
% WOB=Kc.*X_0.*(1-sin(2.*pi.*f.*t));
% WOB(WOB<0)=0;
% WOB_z=cos(alpha).*WOB;
% WOB_x=sin(alpha).*WOB.*cos(PhiZ_db);                  % Lateral WOB in X-dirc duto
bit inclination
% WOB_y=sin(alpha).*WOB.*sin(PhiZ_db);
% TOB=50.*PhiZdot_db+a.*WOB.*(mu+(mu_s-mu).*e.^(-landa.*abs(PhiZdot_db)));


% Calculate applied torques
Td= KphiZ_dp.*(Phi_rt-PhiZ_st);
```

```
Tx_db= mu.*Fn_db.*a.*(abs(Y_db)./r_db);                  % Applied torque on drillbit
about X-axis
Ty_db= mu.*Fn_db.*a.*(abs(X_db)./r_db);                  % Applied torque on drillbit
about Y-axis
Tz_db= Ft_db.*a;                                          % Applied torque on drillbit
about Z-axis


% Convert obtained Angular velocities from (Rad/sec) to (RPM)
PhiZdot_st_RPM= (PhiZdot_st.*60)./(2.*pi);
PhiZdot_BHA_RPM=(PhiZdot_BHA.*60)./(2.*pi);
PhiZdot_db_RPM= (PhiZdot_db.*60)./(2.*pi);


%% [5]% Plotting Output Data  %%%%%%%%%%%%%%%%%%%%%%%%%%%%%%%%%%%%%%%%%%%%%
%%%%%%%%%%%%%%%%%%%%%%%%%%%%%%%%%%%%%%%%%%%%%%%%%%%%%%%%%%%%%%%%%%%%%%%%%%%

% Plotting- upper stabilizer x,y position
figure (1)
plot (X_st,Y_st,'b');
hold on
grid
Radius_st=Rc_st;
[cx_st,cy_st,z_st] = cylinder(Radius_st,100);
axis equal
plot(cx_st(1,:),cy_st(1,:),'r.');
title('Stabilizer C.G. Orbit');
xlabel(' Xg (m)');
ylabel(' Yg (m)' );

% Plotting- intermediate BHA mass x,y position
figure (2)
plot (X_BHA,Y_BHA,'b');
hold on
% plot (X_fl,Y_fl,'k--');   % plot the inside flywheel x,y position
grid
Radius_BHA=Rc_BHA;
[cx_BHA,cy_BHA,z_BHA] = cylinder(Radius_BHA,100);
plot(cx_BHA(1,:),cy_BHA(1,:),'r.');
axis equal
title('BHA C.G. Orbit');
xlabel(' Xg (m)');
ylabel(' Yg (m)' );
legend('Borehole','BHA Orbit');

% Plotting- Drillbit  x,y position
figure (3)
% subplot(1,3,3);
plot (X_db,Y_db,'c');
hold on
grid
Radius_DB=Rc_db;
[cx_DB,cy_DB,z_DB] = cylinder(Radius_DB,100);
axis equal
plot(cx_DB(1,:),cy_DB(1,:),'r.');
title('Drill-Bit C.G. Orbit');
xlabel(' Xg (m)');
ylabel(' Yg (m)' );

% Plotting- Drillbit  3D pathline inside the borehole
figure (4)
hold on
grid
NN=100;
[X,Y,Z] = cylinder(Rc_db,NN);
Z(2,:)= min(Z_db);
Z(2,:)= max(Z_db);
```

```
h2 = surf(X,Y,Z);
set(h2,'FaceAlpha',0.3)
% plot3(Xdb,Ydb,Z_db,'c');
% plot3(Xst,Yst,Z_st,'b');
% plot3(Xbha,Ybha,Z_BHA,'g');
plot3(X_db,Y_db,Z_db,'c');
% plot3(X_st,Y_st,Z_st,'b');
% plot3(X_BHA,Y_BHA,Z_BHA,'g');
xlabel(' Xg (m)');
ylabel(' Yg (m)' );
zlabel(' Zg (m)' );
title('3D Pathline Orbit');
legend('Borehole','Drillbit Pathline');
view([-37.5 30])
hold off

% Plotting- the Three masses axial displacements
figure (5)
hold on
grid
plot (t,Z_st,'b');
plot (t,Z_BHA,'g');
plot (t,Z_db,'c');
title('Axial diplacement');
xlabel(' Time (S)');
ylabel(' Z (m)' );
legend('Stabilizer (1)','BHA ','Drillbit ');

% Plotting- the upper stabilizer mass radial displacement
figure (6)
plot (t,r_st,'b');
hold on
grid
plot(t,Rc_st,'r');
title('Upper Stabilizer Radial Displacement');
xlabel(' Time (S)');
ylabel(' r (m)' );
legend('Borehole','Stabilizer (1)');
axis square

% Plotting- the upper stabilizer mass radial displacement
figure (7)
plot (t,r_BHA,'g');
hold on
grid
% plot (t,r_fl,'k--');    % Plot flywheel radial displacement
plot(t,Rc_BHA,'r');
title('BHA Radial Displacement');
xlabel(' Time (S)');
ylabel(' r (m)' );
% legend('Borehole','BHA','Flywheel');
legend('Borehole','BHA');
axis square


% Plotting- the drillbit radial displacement
figure (8)
plot (t,r_db,'c');
hold on
grid
plot(t,Rc_db,'r');
title('Drillbit Radial Displacement');
xlabel(' Time (S)');
ylabel(' r (m)' );
legend('Borehole','Drillbit');
axis square
```

```
% Plotting- the drillstring components rotational angles in degrees
figure (9)
hold on
grid
plot (t,PhiZ_st*180/pi, 'b');
plot (t,PhiZ_BHA*180/pi,'g');
plot (t,PhiZ_db*180/pi, 'c');
title(' Rotation angles aroun Z-dir ');
xlabel('Time (S)');
ylabel(' Phi-Z (Degrees)' );
legend('Stabilizer (1)','BHA','Drillbit');
hold off

% Plotting- Drillbit WOB and Applied static load
figure (10)
hold on
grid
plot (t,WOB_z);
plot (t,W0,'k-');
title('Weight On Bit ');
xlabel('Time (S)');
ylabel(' WOB (N)' );

% Plotting- Drillbit TOB and Applied top drive torque
figure (11)
hold on
grid
plot (t,TOB);
plot (t,Td,'r--');
title('Torques ');
xlabel('Time (S)');
ylabel(' TOB (Nm)' );
legend('TOB','Top torque');

% Plotting- Applied contact forces on drillstring components
figure (12)
hold on
grid
plot (t,Fn_st,'b');
%plot (t,Fx_st,'g-');
plot (t,Fn_db,'c');
%plot (t,Fx_db,'g');
plot (t,Fn_BHA,'g');
title('Contact Forces');
xlabel('Time (S)');
ylabel(' Contact forces (N)' );
legend('Normal force on Stabilizer (Fn_st)',' Normal force on Drillbit (Fn_db)');

% Plotting- drillstring components angular velocities in RPM
figure (13)
hold on
grid
plot (t,PhiZdot_st_RPM,'b');
plot (t,PhiZdot_db_RPM,'c');
plot (t,PhiZdot_BHA_RPM,'g');
title(' Rotational velocities');
xlabel('Time (S)');
ylabel(' Phidot-Z(RPM)' );
legend('Upper Stabilizer','DrillBit','BHA');

% Plotting- drillstring components relative velocities
figure (14)
hold on
grid
plot (t,Vrel_st,'b');
plot (t,Vrel_db,'c');
plot (t,Vrel_BHA,'g');
```

```
title('Relative velocities');
xlabel('Time (S)');
ylabel(' Vrel(rad/sec)' );
legend('Upper Stabilizer','DrillBit','BHA');

% Plotting- drillstring components whirling velocities
figure (15)
hold on
grid
plot (t,omega_BHA,'g');
plot (t,omega_db,'c');
plot (t,omega_st,'b');
title('Whirling velocity');
xlabel('Time (S)');
ylabel(' Omega(rad/sec)' );
legend(' BHA','Drillbit','Upper stabilizer');

% Plotting- Drillbit rolling status
figure (16)
plot (t, Rolling_db, 'r');
title('Drillbit Rolling status');
xlabel('Time (S)');
ylabel(' 0 ==> Not Active     1 ==> Rolling CTIVE !!' );

% Plotting- Drillbit friction force Vs. theoritical calculated friction force incase
of pure-rolling (vrel=0)
figure (17)
plot (t,Ft_db, 'k')
hold on
grid on
plot (t,FtR_db, 'r--')
title('Drillbit Friction force');
xlabel('Time (S)');
ylabel(' Friction Force (N)' );
legend('Ft ','Ft_R');

% Plotting- Drilling depth
figure (18)
hold on
grid
plot (t,Z_db);
title('Drilling depth)');
xlabel('Time (S)');
ylabel(' Depth (m)' );
```

Lumped_Drillstring_sub.m

```
% % Omar Abdelzaher
% Drillstring Lumped-System-Model using Three lumped masses with 6-DOF
% Created December 15, 2014
% Updated April 24, 2014

%% call intigration function
%%%%%%%%%%%%%%%%%%%%%%%%%%%%%%%%%%%%%%%%%%%%%%%%%%%%%%%%%%%%%%%%%%%%%%%%%%%%
function xdot= Lumped_Drillstring_sub(t,x)

global w Vmin w_fl W0 M_st J_st I_st M_BHA M_fl J_BHA Je I_BHA M_db J_db
global I_db e q S S0 dc ROP TOB WOB_x WOB_y WOB_z b C1 C2 alpha Rm Km Lm
global r_st WOB R_st Rc_st  omega_st Vrel_st mu_st mu  Kf Kc Tm J_rt J_m Vc
global Fn_st Ft_st Fx_st Fy_st Fz_st Kxy_BHA Kxy_dp Kxy_fl Kz_dp Kz_BHA
global Kz_fl KphiZ_dp KphiZ_BHA KphiXY_BHA KphiXY_dp Cz_BHA Cz_fl Cf
global r_BHA  R_BHA Rc_BHA omega_BHA Vrel_BHA mu_BHA Fn_BHA Ft_BHA Fx_BHA
global Fy_BHA Fz_BHA Fe Fe_x Fe_y Fq Fq_x Fq_y Cxy_dp Cxy_BHA Cxy_fl Cz_dp
global r_db  a Rc_db omega_db Vrel_db mu_db Fn_db Ft_db Fx_db Fy_db Fz_db
global Tx_st Ty_st Tz_st Tx_BHA Ty_BHA Tz_BHA Tx_db Ty_db Tz_db r_fl n Cf_z
```

```
%% % State Variables

%%%%%%%% Stabilizer 1
% X_st= x(1);
% Xdot_st= x(2);
% Y_st= x(3);
% Ydot_st=x(4);
% Z_st=x(5);
% Zdot_st=x(6)
% PhiZ_st=x(7);
% PhiZdot_st=x(8);
% PhiX_st=x(9);
% PhiXdot_st=x(10);
% PhiY_st=x(11);
% PhiYdot_st=x(12);

%%%%%%%% BHA DOF's
% X_BHA=x(13);
% Xdot_BHA=x(14);
% Y_BHA=x(15);
% Ydot_BHA=x(16);
% Z_BHA=x(17);
% Zdot_BHA=x(18)
% PhiZ_BHA=x(19);
% PhiZdot_BHA=x(20);
% PhiX_BHA=x(21);
% PhiXdot_BHA=x(22);
% PhiY_BHA=x(23);
% PhiYdot_BHA=x(24);

%%%%%%%% Flywheel
% X_fl= x(25)
% Xdot_fl= x(26);
% Y_fl= x(27);
% Ydot_fl=x(28);
% Z_fl=x(29);
% Zdot_fl=x(30);

%%%%%%%%% DrillBit + Stabilizer 2
% X_bit= x(31);
% Xdot_bit= x(32);
% Y_bit= x(33);
% Ydot_bit=x(34);
% Z_bit=x(35);
% Zdot_bit=x(36);
% PhiZ_bit=x(37);
% PhiZdot_bit=x(38);
% PhiX_bit=x(39);
% PhiXdot_bit=x(40);
% PhiY_bit=x(41);
% PhiYdot_bit=x(42);

%% Caculating variables  %%%%%%%%%%%%%%%%%%%%%%%%%%%%%%%%%%%%%%%%%%%%%%%%%
%%%%%%%%%%%%%%%%%%%%%%%%%%%%%%%%%%%%%%%%%%%%%%%%%%%%%%%%%%%%%%%%%%%%%%%%%%

%%%  A)Rotary Table + Motor
%%%%%%%%%%%%%%%%%%%%%%%%%%%%%
Tm=Km*x(43);                                            % Motor Torque
Vc=Km*n*w;                                              % Motor voltage

%%%  B)STABILIZER (1)
%%%%%%%%%%%%%%%%%%%%%%%%%%%%%
r_st= sqrt(x(1)^2+x(3)^2);                              % upper stabilizer mass radial
displacement
omega_st= (x(4)*x(1)-x(2)*x(3))/r_st^2;                 % upper stabilizer mass whirl
velocity
```

```
Vrel_st=x(8)*R_st+omega_st*r_st;                    % upper stabilizer mass Relative
velocity
mu_st=mu;                                           % applied friction coefficient

% Logic for uppaer stabilizer mass motion status
if r_st<Rc_st   % If No contact
    Fn_st=0;                                        % No Normal Contact force
    Ft_st=0;                                        % No Friction contact force
    %      disp('-- NO CONTACT ----------------------');
else Fn_st= Kf*(r_st-Rc_st);                        % Normal Contact force
     Ft_st= -mu_st*sign(Vrel_st)*Fn_st;             % Friction contact force
     % Calculate theoritical friction contact force incase of pure-rolling(Vrel=0)
     FtR_st=  (Cxy_dp*omega_st*r_st -(M_st*R_st/J_st)*(KphiZ_dp*(x(7)-
x(44))+KphiZ_BHA*(x(7)-x(19))+ Cf*M_st*R_st*x(8)))/(1+ (M_st*R_st^2)/J_st);
   if abs(Vrel_st)>Vmin && sign(x(8))== sign(omega_st) % Check for Forward whirling
%     disp('---------  SLiding ----------------');
   elseif  abs(Vrel_st)<=Vmin && -(mu_st*Fn_st)<=FtR_st <=(mu_st*Fn_st) % Check for
pure-rolling (Backward whirling)
           Ft_st=FtR_st;                            % iF YES !
%     disp('--------------- Pure Rolling -----');
   else
%        disp('------------------ TRANSITION -----');
   end
end

% Calculate applied loads
Fx_st= (-Ft_st*x(3) - Fn_st*x(1))/r_st;            % Applied force in X-dir
Fy_st= (Ft_st*x(1) - Fn_st*x(3))/r_st;             % Applied force in Y-dir
Fz_st= -sign(x(6))*mu*Fn_st;                       % Applied force in Z-dir
Tx_st= -sign(x(10))*mu*Fn_st*R_st*(abs(x(3))/r_st);% Applied friction Torque about X-
dir
Ty_st= -sign(x(12))*mu*Fn_st*R_st*(abs(x(1))/r_st);% Applied friction Torque about Y-
dir
Tz_st= -sign(x(8))*Ft_st*R_st;                     % Applied friction Torque about Z-
dir


%%%  C)BHA intermediate mass
%%%%%%%%%%%%%%%%%%%%%%%%%%%%%
r_BHA= sqrt(x(13)^2+x(15)^2);                      % Intermediate BHA mass radial
displacement
omega_BHA= (x(16)*x(13)-x(14)*x(15))/r_BHA^2;      % Intermediate BHA mass whirl
velocity
Vrel_BHA=x(20)*R_BHA + omega_BHA*r_BHA;            % Intermediate BHA mass Relative
velocity
mu_BHA= mu;                                        % applied friction coefficient

% Logic for Intermediate BHA mass motion status
if r_BHA<Rc_BHA   % If No contact
    Fn_BHA=0;                                      % No Normal Contact force
    Ft_BHA=0;                                      % No Friction contact force
%      disp('-- NO CONTACT ----------------------');
else Fn_BHA= Kf*(r_BHA-Rc_BHA);                    % Normal Contact force
     Ft_BHA= -mu_BHA*sign(Vrel_BHA)*Fn_BHA;        % Tangential friction Contact force
     % Calculate theoritical friction contact force incase of pure-rolling(Vrel=0)
     FtR_BHA=  (Cxy_BHA*omega_BHA*r_BHA -(M_BHA*R_BHA/(J_BHA+Je))*(KphiZ_BHA*(x(19)-
x(7))+KphiZ_BHA*(x(19)-x(37))+ Cf*M_BHA*R_BHA*x(20)))/(1+ (M_BHA*R_BHA^2)/(J_BHA+Je));
   if abs(Vrel_BHA)>Vmin && sign(x(20))== sign(omega_BHA) % Check for Forward whirling
%     disp('---------  SLiding ----------------');
   elseif  abs(Vrel_BHA)<=Vmin && -(mu_BHA*Fn_BHA)<=FtR_BHA <=(mu_BHA*Fn_BHA)  % Check
for pure-rolling (Backward whirling)
           Ft_BHA=FtR_BHA;                         % iF YES !
%     disp('--------------- Pure Rolling -----');
   else
%        disp('------------------ TRANSITION -----');
   end
end
```

```
% Calculate applied loads
Fx_BHA= (-Ft_BHA*x(15)- Fn_BHA*x(13))/r_BHA;            % Applied force in X-dir
Fy_BHA= (Ft_BHA*x(13) - Fn_BHA*x(15))/r_BHA;            % Applied force in Y-dir
Fz_BHA= -sign(x(18))*mu*Fn_BHA;                         % Applied force in Z-dir
Tx_BHA= -sign(x(22))*mu*Fn_BHA*R_BHA*(abs(x(15))/r_BHA);% Applied friction Torque
about X-dir
Ty_BHA= -sign(x(24))*mu*Fn_BHA*R_BHA*(abs(x(13))/r_BHA);% Applied friction Torque
about Y-dir
Tz_BHA= -sign(x(20))*Ft_BHA*R_BHA;                      % Applied friction Torque
about Z-dir

% Calculate centrifugal force dueto eccentricity (Mass imbalance)
Fe=e*M_BHA*x(20)^2;                                     % Total centrifugal force
Fe_x= Fe*cos(x(19));                                    % centrifugal force in X-dir
Fe_y= Fe*sin(x(19));                                    % centrifugal force in Y-dir


%%%  D)FLYWHEEL
%%%%%%%%%%%%%%%%%%%%%%%%%%%%%
r_fl= sqrt(x(25)^2+x(27)^2);                            % Flywheel mass radial
displacement
Fq=q*M_fl*w_fl^2;                                       % Flywheel mass Total
centrifugal force dueto mass imbalance
Fq_x= Fq*cos(w_fl*t);                                   % Flywheel mass centrifugal
force in X-dir dueto mass imbalance
Fq_y= Fq*sin(w_fl*t);                                   % Flywheel mass centrifugal
force in Y-dir dueto mass imbalance

%%%  E)DRILL-BIT + STABILIZER (2)
%%%%%%%%%%%%%%%%%%%%%%%%%%%%%
r_db= sqrt(x(31)^2+x(33)^2);                            % drillbit mass radial
desplacement
omega_db= (x(34)*x(31)-x(32)*x(33))/r_db^2;             % drillbit mass whirl velocity
Vrel_db= x(38)*a+omega_db*r_db;                         % drillbit mass Relative
velocity
mu_db= mu*(tanh(x(38))+(2*x(38))/(1+(x(38)^2))+0.01*x(38));% Drillbit/formation
Stribeck friction

% Logic for Drillbit mass motion status
if r_db<Rc_db   % If No contact
    Fn_db=0;                                            % No Normal Contact force
    Ft_db=0;                                            % No friction Contact force
    %      disp('-- NO CONTACT ---------------------');
else Fn_db= Kf*(r_db-Rc_db);                            % Normal Contact force
     Ft_db= -mu*sign(Vrel_db)*Fn_db;                    % tangential friction Contact
force
     % Calculate theoritical friction contact force incase of pure-rolling(Vrel=0)
     FtR_db=  (Cxy_BHA*omega_db*r_db -(M_db*a/J_db)*(KphiZ_BHA*(x(37)-x(19))+
Cf*M_db*a*x(38)))/(1+ (M_db*a^2)/J_db);
   if abs(Vrel_db)>Vmin && sign(x(38))== sign(omega_db) % Check for Forward whirling
%     disp('---------  SLiding ----------------');
   elseif  abs(Vrel_db)<=Vmin && -(mu*Fn_db)<=FtR_db <=(mu*Fn_db) % Check for Backward
whirling with Pure-rolling
           Ft_BHA=FtR_db;                               % If YES !
   disp('--------------- Pure Rolling -----');
   else
%        disp('------------------ TRANSITION -----');
   end
end

% Calculate applied loads
Fx_db= (-Ft_db*x(33)- Fn_db*x(31))/r_db;                % Applied force in X-dir
Fy_db= ( Ft_db*x(31)- Fn_db*x(33))/r_db;                % Applied force in Y-dir
Fz_db= - sign(x(36))*mu*Fn_db;                          % Applied force in Z-dir
Tx_db= - sign(x(40))*mu*Fn_db*a*(abs(x(33))/r_db);      % Applied friction Torque
about X-dir
```

```
Ty_db= - sign(x(42))*mu*Fn_db*a*(abs(x(31))/r_db);      % Applied friction Torque
about Y-dir
Tz_db= - sign(x(38))*Ft_db*a;                            % Applied friction Torque
about Z-dir

% % Check if Bit-Bounce or No drilling
S= S0*sin(b*x(37));
if x(35)< S    % If No drillbit/formation contact
   WOB=0;                                                % set No WOB
%         disp('-- No Drilling ---------------------');
else WOB=Kc*(x(35)-S);                                   % axial WOB in Z-dirc duto bit
inclination
%         disp('--------------- Drilling -----------');
end

% Calculate applied loads
WOB_z= cos(alpha)*WOB;                                   % Axial WOB in Z-dirc duto bit
angle
WOB_x= sin(alpha)*WOB*cos(x(37));                        % Lateral WOB in X-dirc duto
bit angle
WOB_y= sin(alpha)*WOB*sin(x(37));                        % Lateral WOB in y-dirc duto
bit angle
ROP=C1*W0*sqrt(x(38))+C2;                                % rate of penetration
dc= (2*pi*ROP)/x(38);                                    % Depth of cut
TOB= sign(x(38))*WOB*a*(mu_db+sqrt(dc/a));               % Torque ON BIT



%% EOM's %%%%%%%%%%%%%%%%%%%%%%%%%%%%%%%%%%%%%%%%%%%%%%%%%%%%%%%%%%%%%%%%%
%%%%%%%%%%%%%%%%%%%%%%%%%%%%%%%%%%%%%%%%%%%%%%%%%%%%%%%%%%%%%%%%%%%%%%%%%%

%%% EOM's UPPER STABILIZER MASS %%%%%%%%%%%%%%%%%%%%%%%%%%%%%%%%%%%%%%%%%%
%X
xdot_1= x(2);
xdot_2= ( -Kxy_dp*x(1)-Kxy_BHA*(x(1)-x(13))-Cxy_dp*x(2)-Cxy_BHA*(x(2)-x(14))+ Fx_st )/
M_st;
%Y
xdot_3= x(4);
xdot_4= ( -Kxy_dp*x(3)-Kxy_BHA*(x(3)-x(15))-Cxy_dp*x(4)-Cxy_BHA*(x(4)-x(16))+Fy_st )/
M_st;
%Z
xdot_5= x(6);
xdot_6= ( -Kz_dp*x(5)-Kz_BHA*(x(5)-x(17))-Cz_dp*x(6)-Cz_BHA*(x(6)-x(18))+W0+Fz_st )/
M_st ;
%PhiZ
xdot_7= x(8);
xdot_8= ( -KphiZ_dp*(x(7)-x(44))-KphiZ_BHA*(x(7)-x(19))- Cf*x(8)+ Tz_st)/J_st;
%PhiX
xdot_9= x(10);
xdot_10= (-KphiXY_dp*x(9)-KphiXY_BHA*(x(9)-x(21))- Cf_z*x(10)+ Tx_st )/I_st;
%PhiY
xdot_11= x(12);
xdot_12= (-KphiXY_dp*x(11)-KphiXY_BHA*(x(11)-x(23))- Cf_z*x(12)+ Ty_st)/I_st;

%%% EOM's INTERMEDIATE MASS %%%%%%%%%%%%%%%%%%%%%%%%%%%%%%%%%%%%%%%%%%%%%
%X
xdot_13= x(14);
xdot_14= ( -Kxy_BHA*(x(13)-x(1))-Kxy_BHA*(x(13)-x(31))-Kxy_fl*(x(13)-x(25))-
Cxy_BHA*(x(14)-x(2))-Cxy_BHA*(x(14)-x(32))-Cxy_fl*(x(14)-x(26))+ Fx_BHA+ Fe_x )/M_BHA;
%Y
xdot_15= x(16);
xdot_16= ( -Kxy_BHA*(x(15)-x(3))-Kxy_BHA*(x(15)-x(33))-Kxy_fl*(x(15)-x(27))-
Cxy_BHA*(x(16)-x(4))-Cxy_BHA*(x(16)-x(34))-Cxy_fl*(x(16)-x(28))+Fy_BHA+Fe_y)/M_BHA;
%Z
xdot_17= x(18);
xdot_18= ( -Kz_BHA*(x(17)-x(5))-Kz_BHA*(x(17)-x(35))-Kz_fl*(x(17)-x(29))-
Cz_BHA*(x(18)-x(6))-Cz_BHA*(x(18)-x(36))-Cz_fl*(x(18)-x(30)) +Fz_BHA )/M_BHA ;
```

```
%PhiZ
xdot_19= x(20);
xdot_20= ( -KphiZ_BHA*(x(19)-x(7))-KphiZ_BHA*(x(19)-x(37))-Cf*x(20)+ Tz_BHA
)/(J_BHA+Je);
%PhiX
xdot_21= x(22);
xdot_22= (-KphiXY_BHA*(x(21)-x(9))-KphiXY_BHA*(x(21)-x(39))-Cf_z*x(22)+Tx_BHA )/I_BHA;
%PhiY
xdot_23= x(24);
xdot_24= (-KphiXY_BHA*(x(23)-x(11))-KphiXY_BHA*(x(23)-x(41))-Cf_z*x(24)+Ty_BHA
)/I_BHA;

%%% EOM's FLYWHEEL MASS %%%%%%%%%%%%%%%%%%%%%%%%%%%%%%%%%%%%%%%%%%%%%%%%%%%
%X
xdot_25= x(26);
xdot_26= ( -Kxy_fl*(x(25)-x(13))-Cxy_fl*(x(26)-x(14))+ Fq_x )/M_fl;
%Y
xdot_27= x(28);
xdot_28= ( -Kxy_fl*(x(27)-x(15))-Cxy_fl*(x(28)-x(16))+Fq_y)/M_fl;
%Z
xdot_29= x(30);
xdot_30= ( -Kz_fl*(x(29)-x(17))-Cz_fl*(x(30)-x(18)))/M_fl ;

%%% EOM's DRILLBIT MASS %%%%%%%%%%%%%%%%%%%%%%%%%%%%%%%%%%%%%%%%%%%%%%%%%%%
%X
xdot_31= x(32);
xdot_32= ( -Kxy_BHA*(x(31)-x(13))-Cxy_BHA*(x(32)-x(14))+ Fx_db -WOB_x)/M_db;
%Y
xdot_33= x(34);
xdot_34= ( -Kxy_BHA*(x(33)-x(15))-Cxy_BHA*(x(34)-x(16))+Fy_db -WOB_y)/M_db;
%Z
xdot_35= x(36);
xdot_36= ( -Kz_BHA*(x(35)-x(17))-Cz_BHA*(x(36)-x(18))+Fz_db -WOB_z)/M_db ;
%PhiZ
xdot_37= x(38);
xdot_38= ( -KphiZ_BHA*(x(37)-x(19))-Cf*x(38) -TOB +Tz_db)/J_db;
%PhiX
xdot_39= x(40);
xdot_40= ( -KphiXY_BHA*(x(39)-x(21))-Cf_z*x(40)+Tx_db )/I_db;
%PhiY
xdot_41= x(42);
xdot_42= ( -KphiXY_BHA*(x(41)-x(23))-Cf_z*x(42)+Ty_db )/I_db;

%%% EOM MOTOR DYNAMICS %%%%%%%%%%%%%%%%%%%%%%%%%%%%%%%%%%%%%%%%%%%%%%%%%%%
xdot_43= (-Rm*x(43)-Km*n*x(45)+Vc)/Lm;

%%% EOM's ROTARY TABLE %%%%%%%%%%%%%%%%%%%%%%%%%%%%%%%%%%%%%%%%%%%%%%%%%%%
xdot_44= x(45);
xdot_45= (-KphiZ_dp*(x(44)-x(7))+n*Tm)/(J_rt+(n^2)*J_m);


%%
xdot= [xdot_1; xdot_2; xdot_3; xdot_4; xdot_5; xdot_6 ;xdot_7; xdot_8; xdot_9;
xdot_10; xdot_11; xdot_12; xdot_13; xdot_14; xdot_15; xdot_16; xdot_17; xdot_18;
xdot_19; xdot_20; xdot_21; xdot_22; xdot_23; xdot_24; xdot_25; xdot_26; xdot_27;
xdot_28; xdot_29; xdot_30; xdot_31; xdot_32; xdot_33; xdot_34; xdot_35; xdot_36;
xdot_37; xdot_38; xdot_39; xdot_40; xdot_41; xdot_42; xdot_43; xdot_44; xdot_45];
t
end
```

FEM_BHA.m

```
% % Omar Abdelzaher
% Finite Element Method for BHA (Discretizing )
% creating BHA global mass Matrix [M], stiffness matrix [K], and Dmaping MATRIX [C].
% Created December 15, 2014
```

```
% Updated April 24, 2014
% Reference: PhD. Ahmed Saeed's Codes

%%
clear all; close all; clc;

%% [1]% SECTION 1: INPUT SYSTEM PARAMETERS  %%%%%%%%%%%%%%%%%%%%%%%%%%%%%%%
%%%%%%%%%%%%%%%%%%%%%%%%%%%%%%%%%%%%%%%%%%%%%%%%%%%%%%%%%%%%%%%%%%%%%%%%%%%%%%

% BHA Sizing  %%%%%%%%%%%%%%%%%%%%%%%%%%%%%%%%%%%%%%%%%%%%%%%%%%%%%%%%%%%%%
BHA_L=200;                                  % Total BHA length in m
noe=6;                                      % # of elements desired  %m: 4 to 6
E= 210e9*ones(1,noe);                       % Modulus of Elasticity Pa
nu= 0.3*ones(1,noe);                        % Poisson's Ratio
d1 = 8e-6; d2 = 8;                          % d1, d2: dampening ratio (D = d1*K +
d2*M)
rho = 7850*ones(1,noe);                     % Density kg/m^3  %m:7859 to 8500
BHA_OD = (6.75)*0.0254*ones(1,noe);         % Outer Diameters  (m) (inch to 0.0254
meter)
BHA_ID = (4.5) *0.0254*ones(1,noe) ;        % Inner Diameters  (m)   ==> (ID=3")
default
Node_z_coord = [0: BHA_L/noe :BHA_L];       % Get The Z coordinate for each element
NumberNodes = size(Node_z_coord,2);         % Get Total Number of Nodes

for i=1:1:NumberNodes-1
 element_length(1,i) =   Node_z_coord(1,i+1) - Node_z_coord(1,i); % Get element length
end

% Axial and Torsional Restraint Stiffneses Attached Between Node 1 and Ground
KZ = 1.0;
KTHETA = 1.0;

%% %%%%%%%%%%% (OPTIONAL SECTION) %%%%%%%%%%%%%%%%%%%%%%%%%%%%%%%%%%%%%%%%%%
% % If added mass Inerta @ nodes //  unbalance mass // lumbed mass
% %  Added Inertias.  Enter any disc, etc. inertias not accounted for with the
stiffness or mass diameter distributions
% %  (Define the following row vectors. Leave vectors blank [] if no added inertias
exist)

% node_added_inertia = [0 0];               % List all node numbers where added
inertias will be attached  %m: [1 2] to [2 4]
% Mass_added= [0 0];                        % kg
% IP_added= [0 0];                          % kg.m^2
% IT_added= [0 0];                          % kg.m^2
% mass_rho = 7850*ones(1,noe);              % Density kg/m^3
% mass_ID = 0*0.0254*ones(1,noe);
% mass_OD = 0*0.0254*ones(1,noe);
%%%%%%%%%%%%%%%%%%%%%%%%%%%%%%%%%%%%%%%%%%%%%%%%%%%%%%%%%%%%%%%%%%%%%%%%%%%%%%


%% [2]% ANALYSIS SECTION 2:  DETERMINE THE K, M, G AND C MATRICES FOR THE BHA MODEL
%%%%%%%%%%%%%%%%%%%%%%%%%%%%%%%%%%%%%%%%%%%%%%%%%%%%%%%%%%%%%%%%%%%%%%%%%%%%%%%%%%%%%%

LenTot=0 ;                                 % Total length

% Nodes coordinate in X
x1(1,1)=0;
NEL = size(element_length,2);
for i=1:1:NEL
LenTot = LenTot+element_length(1,i);
x1(1,i+1) = LenTot;
end

Number_Nodes = size(x1,2);                 % Number of Nodes
Number_Elem = Number_Nodes-1 ;             % Number of Elements

% Integer parameters for arrays
```

```
Nnode = Number_Nodes;                          % No. of Nodes
Nd = 6*Nnode;                                  % No. of Global-Free system degrees of
freedom
% Nnpd = Nd;                                   % No. of non-prescribed degrees of freedom
Ne = Number_Elem;                              % No. of elements

% Nodes coordinates in Y, Z
x2 = zeros(1,Number_Nodes) ;
x3 = zeros(1,Number_Nodes) ;

% Nodal Connectivities (Ref.E12.14.1(a)) , Element Types and Orientation Angle
% BEAMS
for ee = 1:1:Number_Elem
   ICON(ee,1) = ee ;
   ICON(ee,2) = ee+1 ;
end

%%%%%%%%%%%%%%%%%%%%%%%%%%%%%%%%%%%%%%%%%%%%%%%%%%%%%%%%%%%%%%%%%%%%%%%%%%%%
%%%%%%%%%%%%% (OPTIONAL SECTION) %%%%%%%%%%%%%%%%%%%%%%%%%%%%%%%%%%%%%%%%%%
% Plotting BHA Finite-Element geometry
irotor_geom=0;       % 1==> Plot, 0==> Don't Plot

if irotor_geom==1
% MODEL CHECK PLOT
for i =1:1:Number_Elem
   x1plt = [x1(ICON(i,1))  x1(ICON(i,2)) ] ;
   x2plt = [x2(ICON(i,1))  x2(ICON(i,2)) ] ;
   x3plt = [x3(ICON(i,1))  x3(ICON(i,2)) ] ;
   figure(1)
   plot3(x1plt,x2plt,x3plt,'k-*')
   if i==1
   xlabel('z position  (m)');
   ylabel('x position  (m)');
   zlabel('y position  (m)');
   title('Shaft Model Geometry Verification Plot');
   %msg=sprintf('Plot Record = %s',PlotRecord);
   %text(5,0,-2,msg);
   end
   view(45,45);
   grid on
   zoom on
   hold on
end
end   % if irotor_geom==1

% Plotting BHA Finite-Element profile  ( OPTIONAL)
irotor_profile=0;   % 1==> Plot, 0==> Don't Plot

if irotor_profile==1
for i=1:1:NEL
    figure(2)
    subplot(2,1,1)
    for j=1:1:4
        if j==1
            xplot=[x1(1,i+1), x1(1,i)];
            yplot=[BHA_OD(1,i)/2,BHA_OD(1,i)/2];
        elseif j==2
            xplot=[x1(1,i), x1(1,i)];
            yplot=[BHA_OD(1,i)/2,-BHA_OD(1,i)/2];
        elseif j==3
            xplot=[x1(1,i), x1(1,i+1)];
            yplot=[-BHA_OD(1,i)/2,-BHA_OD(1,i)/2];
        elseif j==4
            xplot=[x1(1,i+1), x1(1,i+1)];
            yplot=[-BHA_OD(1,i)/2,BHA_OD(1,i)/2];
        end
```

```
        plot(xplot,yplot,'k-')
        hold on
    end

    for j=1:1:4
        if j==1
            xplot=[x1(1,i+1), x1(1,i)];
            yplot=[BHA_ID(1,i)/2,BHA_ID(1,i)/2];
        elseif j==2
            xplot=[x1(1,i), x1(1,i)];
            yplot=[BHA_ID(1,i)/2,-BHA_ID(1,i)/2];
        elseif j==3
            xplot=[x1(1,i), x1(1,i+1)];
            yplot=[-BHA_ID(1,i)/2,-BHA_ID(1,i)/2];
        elseif j==4
            xplot=[x1(1,i+1), x1(1,i+1)];
            yplot=[-BHA_ID(1,i)/2,BHA_ID(1,i)/2];
        end
        if BHA_ID(1,i)~=0
        plot(xplot,yplot,'k--')
        hold on
        end
    end
    if i==1
        title('Stiffness Inner and Outer Diameter Profile Plot of Rotor Model')
        xlabel('X-axis');
        ylabel('Y-axis');

    end
end
end   % if irotor_profile==1
%%%%%%%%%%%%%%%%%%%%%%%%%%%%%%%%%%%%%%%%%%%%%%%%%%%%%%%%%%%%%%%%%%%%%%%%%%%
%%%%%%%%%%%%%%%%%%%%%%%%%%%%%%%%%%%%%%%%%%%%%%%%%%%%%%%%%%%%%%%%%%%%%%%%%%%


% BHA Cross Sectional Area according to element type . (in^2)
A_BHA = pi/4*(BHA_OD.*BHA_OD - BHA_ID.*BHA_ID);
%Area Moment of Inertia Ix3tilda according to element type.(in^4),(Ref.12.3.24 )
Ix3_BHA= pi/64*(BHA_OD.*BHA_OD.*BHA_OD.*BHA_OD - ...
            BHA_ID.*BHA_ID.*BHA_ID.*BHA_ID);
% BHA Area Moment of Inertia Ix2tilda according to element type.(in^4),(Ref.12.3.24 )
Ix2_BHA=Ix3_BHA;
% BHA Torsion Constant according to element type. (in^4)  (Ref.12.3.24 )
Jp_BHA= Ix2_BHA+Ix3_BHA ;
% Calculate Element Shear Moduli  . (lb/in^2)
G= 1/2*E./(  ones(1,Ne) +  nu) ;
% Calculate Shear Form Factors .
ksh = 6*(ones(1,Ne) + nu)./(7*ones(1,Ne) + 6*nu);

% Form the Element Inertias
L_element = x1(1,2:Nnode) - x1(1,1:Nnode-1);
M_element_stiff = pi/4*rho.*L_element.*( BHA_OD.*BHA_OD - BHA_ID.*BHA_ID);
M_element = M_element_stiff ;
Ip_element = 1/8*M_element_stiff.*(  BHA_OD.*BHA_OD + BHA_ID.*BHA_ID );
It_element = 1/12*M_element_stiff.*( 3/4*( BHA_OD.*BHA_OD + BHA_ID.*BHA_ID )+...
                                         L_element.*L_element );

% Form the Nodal Lumped Inertias
M_node  =zeros(1,Nnode);
Ip_node =zeros(1,Nnode);
It_node =zeros(1,Nnode);

for e=1:1:Ne
    M_node(1,e)   = M_node(1,e)   + M_element(1,e)/2;
    M_node(1,e+1) = M_node(1,e+1) + M_element(1,e)/2;

    Ip_node(1,e)   = Ip_node(1,e)   + Ip_element(1,e)/2;
```

```
    Ip_node(1,e+1) = Ip_node(1,e+1) + Ip_element(1,e)/2;

    It_node(1,e)   = It_node(1,e)   + It_element(1,e)/2;
    It_node(1,e+1) = It_node(1,e+1) + It_element(1,e)/2;
end

%% [3]% SECTION 3:  DETERMINE THE K, M, G AND C MATRICES FOR THE BHA MODEL
%%%%%%%%%%%%%%%%%%%%%%%%%%%%%%%%%%%%%%%%%%%%%%%%%%%%%%%%%%%%%%%%%%%%%%%%%%%%%%

% Form the Global Mass Matrix [Mc]
% ===================================
Mc = zeros(Nd,Nd);

for i=1:1:Nnode
   Mc( 6*(i-1)+1,6*(i-1)+1 ) = Mc( 6*(i-1)+1,6*(i-1)+1 ) + M_node(1,i);
   Mc( 6*(i-1)+2,6*(i-1)+2 ) = Mc( 6*(i-1)+2,6*(i-1)+2 ) + M_node(1,i);
   Mc( 6*(i-1)+3,6*(i-1)+3 ) = Mc( 6*(i-1)+3,6*(i-1)+3 ) + M_node(1,i);

   Mc( 6*(i-1)+4,6*(i-1)+4 ) = Mc( 6*(i-1)+4,6*(i-1)+4 ) + Ip_node(1,i);
   Mc( 6*(i-1)+5,6*(i-1)+5 ) = Mc( 6*(i-1)+5,6*(i-1)+5 ) + It_node(1,i);
   Mc( 6*(i-1)+6,6*(i-1)+6 ) = Mc( 6*(i-1)+6,6*(i-1)+6 ) + It_node(1,i);
end

% Determine the DOF connectivity array ICONDOF
for e=1:1:Ne
   for j =1:1:2
      for k=1:1:6
         l=6*(j-1) + k ;
         ICONDOF(e,l) = 6*(ICON(e,j)-1) + k ;
      end
   end
end

% Form the Global Stiffness Matrix [Kc]
% ======================================

Kc=zeros(Nd,Nd)  ;

% First form the beam element contributions
for e=1:1:Ne

   del1 = x1(ICON(e,2)) - x1(ICON(e,1)) ;
   del2 = x2(ICON(e,2)) - x2(ICON(e,1)) ;
   del3 = x3(ICON(e,2)) - x3(ICON(e,1)) ;
   L = sqrt( del1^2 + del2^2 + del3^2) ;


% Form the element stiffness matrix in element coordinates
%Ref. (12.9.6) for the following variables

PHI12 = 12*E(1,e)*Ix3_BHA(1,e)/ksh(1,e)/A_BHA(1,e)/G(1,e)/L^2 ;
PHI13 = 12*E(1,e)*Ix2_BHA(1,e)/ksh(1,e)/A_BHA(1,e)/G(1,e)/L^2 ;
BETA_a_12 = E(1,e)*Ix3_BHA(1,e)/(1+PHI12) ;
BETA_a_13 = E(1,e)*Ix2_BHA(1,e)/(1+PHI13) ;
BETA_b_12 = (4+PHI12)*BETA_a_12 ;
BETA_b_13 = (4+PHI13)*BETA_a_13 ;
BETA_c_12 = (2-PHI12)*BETA_a_12 ;
BETA_c_13 = (2-PHI13)*BETA_a_13 ;

% REF. TABLE 12.9.1 for all Ketilda definitions
Ketilda = zeros(12,12) ;

Ketilda(1,1) = E(1,e)*A_BHA(1,e)/L ;
Ketilda(7,7) = Ketilda(1,1) ;
Ketilda(7,1) = -Ketilda(1,1) ;

Ketilda(4,4) = G(1,e)*Jp_BHA(1,e)/L ;
```

```
Ketilda(10,10) = Ketilda(4,4) ;
Ketilda(10,4) = -Ketilda(4,4) ;

Ketilda(2,2) = 12*BETA_a_12/L^3 ;
Ketilda(8,8) = Ketilda(2,2) ;
Ketilda(8,2) = - Ketilda(2,2) ;

Ketilda(6,2) = 6*BETA_a_12/L^2 ;
Ketilda(8,6) = -Ketilda(6,2) ;
Ketilda(12,2) = Ketilda(6,2) ;
Ketilda(12,8) = - Ketilda(6,2) ;

Ketilda(6,6) = BETA_b_12/L ;
Ketilda(12,12) = Ketilda(6,6) ;

Ketilda(12,6) = BETA_c_12/L ;

Ketilda(3,3) = 12*BETA_a_13/L^3 ;
Ketilda(9,9) = Ketilda(3,3) ;
Ketilda(9,3) = - Ketilda(3,3) ;

Ketilda(5,3) = -6*BETA_a_13/L^2 ;
Ketilda(9,5) = -Ketilda(5,3) ;
Ketilda(11,3) = Ketilda(5,3) ;
Ketilda(11,9) = - Ketilda(5,3) ;

Ketilda(5,5) = BETA_b_13/L ;
Ketilda(11,11) = Ketilda(5,5) ;

Ketilda(11,5) = BETA_c_13/L ;

     for i = 1:1:12    % Symmetry
        for j = i:1:12
           Ketilda(i,j) = Ketilda(j,i) ;
        end
     end

% Form the element stiffness matrix in global coordinates (Ref.12.3.10 and 12.12.4)
Ke = Ketilda ;

% Assemble Global Condensed Matrices
for m=1:1:12
   for n =1:1:12
      g_e_m = ICONDOF(e,m) ;
      g_e_n = ICONDOF(e,n) ;
            Kc(g_e_m,g_e_n) = Kc(g_e_m,g_e_n) + Ke(m,n) ;
   end
end


end  %  "e" loop

% Assemble the axial and torsional restraint stiffnesses at Node 1 into the Kc matrix
Kc(1,1) = Kc(1,1) + KZ ;
Kc(4,4) = Kc(4,4) + KTHETA;


% Form the Global Damping Matrix [Cc]
% ====================================
Cc = zeros(Nd,Nd);

%% [4]% SECTION 4:  Form System State variables  matricies
%%%%%%%%%%%%%%%%%%%%%%%%%%%%%%%%%%%%%%%%%%%%%%%%%%%%%%%%%%%%%%%%%%%%%%%%%%%%%%

N = 2*Nd;
% Form State-space system Matrix
AS = zeros(N,N);
```

```
AS(1:Nd,Nd+1:2*Nd) = eye(Nd);
AS(Nd+1:2*Nd,1:Nd) = -inv(Mc)*Kc;
% Form Input system Matrix
BS = zeros(2*Nd,Nd);
BS(Nd+1:2*Nd,1:Nd) = inv(Mc);

% gForce = zeros(Nd,1);

% Form the Gyroscopic Matrix  [Gyro]
% ====================================
rpm= 110;                    % Typically should be range from 80 rpm to 130 rpm
omega= rpm*pi/30;
Gyro= zeros(Nd,Nd);
for i=1:1:Nnode
  Gyro(6*(i-1)+5,6*(i-1)+6)= omega*Mc(6*(i-1)+4,6*(i-1)+4);
  Gyro(6*(i-1)+6,6*(i-1)+5)= -omega*Mc(6*(i-1)+4,6*(i-1)+4);
end



% % updating the State/system Matrix due to Geroscopic
AS(Nd+1:2*Nd,Nd+1:2*Nd) = -inv(Mc)*( Gyro+Cc ) ;

%%
% irpm=1;
% System_eigenvalues(irpm,1:N)=eig(AS);  % un-time scale the eigenvalues
% real_eigen= real(System_eigenvalues(irpm,1:N));
% imag_eigen= imag(System_eigenvalues(irpm,1:N));
%
% [sort_imag_eigen(irpm,1:N),Iorder(irpm,1:N)]=  sort(imag_eigen);
% for i=1:1:N
%    sort_real_eigen(irpm,i) =  real_eigen(1,Iorder(irpm,i));
% end

%% [5]% SECTION 5:  Eigenvalues & Mode Shapes
%%%%%%%%%%%%%%%%%%%%%%%%%%%%%%%%%%%%%%%%%%%%%%%%%%%%%%%%%%%%%%%%%%%%%%%%%%%%
[eigvector_mat,Eigen] = eig(AS);
damp(AS);
EV = diag(Eigen);

% % boundary condition
% Kc(1:6,:)=[]; Kc(:,1:6)=[];
% Mc(1:6,:)=[]; Mc(:,1:6)=[];
% dampening matrix
DS = d1*Kc + d2*Mc ;
% global output vectors
CS=zeros(1,6*N);
% CS(1,N*6-3)=1; % output: beam tip, +z

% ========== second order --> first order ==========
% FS = eye(6*N);
% ES = [F zeros(6*N,6*N); zeros(6*N,6*N) Mc];
% sys = dss(AS,BS,CS,ES);

% Determing Nateral frequencies with ordering
omega_nf=sqrt(EV);
natfreq=omega_nf/2/pi;
[natfreq_ordered,Iorder] = sort(natfreq);

% %
% printeig(1:N,2)=real(EV);
% printeig(1:N,3)=imag(EV);
% printeig(1:N,1)= (1:1:N)';
% % Sorting Eigenvalues
% sorted_eigvectors=eigvector_mat;
% sorted_eig=printeig;
% sorted_eig(:,3)=abs(sorted_eig(:,3))*30/pi;
```

```
%
% for i=1:N
%     if abs(sorted_eig(i,2))<=1e-4
%         sorted_eig(i,2)=0;
%     end
% end
%
% for i=1:1:N-1
%     for j=i+1:1:N
%         if sorted_eig(j,3)<=sorted_eig(i,3)
%             zwap3=sorted_eig(i,3);
%             sorted_eig(i,3)=sorted_eig(j,3);
%             sorted_eig(j,3)=zwap3;
%
%             zwap2=sorted_eig(i,2);
%             sorted_eig(i,2)=sorted_eig(j,2);
%             sorted_eig(j,2)=zwap2;
%
%             zwap1=sorted_eig(i,1);
%             sorted_eig(i,1)=sorted_eig(j,1);
%             sorted_eig(j,1)=zwap1;
%
%             zwap0=EV(i,1);
%             EV(i,1)=EV(j,1);
%             EV(j,1)=zwap0;
%
%             zwap=sorted_eigvectors(:,i);
%             sorted_eigvectors(:,i)=sorted_eigvectors(:,j);
%             sorted_eigvectors(:,j)=zwap;
%         end
%     end
% end
%
% disp('-----------------------------------------------')
% disp('------Sorted DNF & Damping Ratios--------------')
% disp('---------Mode #-------Real-----Imag (CPM)-------Zeta (%)')
% damp_ratio=-real(EV)./abs(EV)*100;
% [sorted_eig damp_ratio];


%% [6]% SECTION 6:  Storing Global BHA Matrices
%%%%%%%%%%%%%%%%%%%%%%%%%%%%%%%%%%%%%%%%%%%%%%%%%%%%%%%%%%%%%%%%%%%%%%%%%%%%
MBHA=Mc;
KBHA=Kc;
CBHA=Cc;
save ('MBHA.mat', 'MBHA');
save ('KBHA.mat', 'KBHA');
save ('CBHA.mat', 'CBHA');
```

FEM_Drillstring.m

```
% % Omar Abdelzaher
% Drillstring Finite-Element-Model using Timoshenko Beam Element method
% Drillstring Dynamics Analysis ( Forward & Backward whirling, Bit-Bounce,Stick-Slip)
% Stick Slip Via Time Delay (Detournay et al.) - PDC Drillbit
% Created January 15, 2014
% Updated April 20, 2014

%%
clear all; close all; clc;
```

```
%% Difine Global Variables
global Wo A0 M_BHA B0 mus Vmin Ctf  R_BHA cDB  e psi cBH cST  R_st kT_dp w
global Kf eta gma a eps sgma l mu0 n xi phii xtni phitni tni tn0 bounce x
global Cf Cr ROLLINGst2 SLIDINGst2 phi loci dt tsim d casex NNODE r_st1
global omega_st1 Vrel_st1 Fn_st1 Ft_st1 r_CG omega_BHA Vrel_BHA Fn_CG Ft_CG
global r_st2 omega_st2 Vrel_st2 Fn_st2 Ftst2_R rdb omega_db Vrel_db WOB TOB

%% [1]% INPUT SYSTEM PARAMETERS  %%%%%%%%%%%%%%%%%%%%%%%%%%%%%%%%%%%%%%%%%%
%%%%%%%%%%%%%%%%%%%%%%%%%%%%%%%%%%%%%%%%%%%%%%%%%%%%%%%%%%%%%%%%%%%%%%%%%%%%

% A)Formations parameters
% ===================================
Vmin=0.001;
mu0=0.2;% Mean Friction Coefficient ***************************************
mus=1.2*mu0;
Kf=2e9;                            % Formation Contact Stiffness
Cf=1000;                           % Formation Contact damping
Ctf=2000;                          % adding tortional damping constant ofr drilling
mud
Rh=(9.5/2)*0.0254;                 % Borehole radius
eta=0.7;                           % Bit-formation interaction factor
gma=1.2;                           % Bit-formation interaction factor
eps=13.3e6*3*3;                    % Rock Intrinsic Specific Energy
sgma=9.33e6*3*3;                   % Rock Cutting Stress
Cr= 10;                            % Adding fluid radial damping to BHA

% B)FEM-BHA parameters
% ===================================
load 'MBHA' ;                      % Load [M],[C],[K] for BHA-FEM ((From FEM_BHA.m))
load 'KBHA' ;
load 'CBHA' ;

noe=6;                             % No of elements used in ((FEM_BHA.m))
e= 0.003;% eccentricity of BHA's center mass ******************************
OD_BHA= (6.75)*0.0254;             % BHA Drill-collars Outer Diameters  (m)
ID_BHA= (4.5)*0.0254 ;             % BHA Drill-collars Inner Diameters  (m)==> Default
3"
L_BHA=200;                         % BHA total length used in ((FEM_BHA.m))
rho=7850;                          % BHA steel density
M_BHA=pi/4*rho*L_BHA*( OD_BHA^2 - ID_BHA^2);  % BHA Effective Mass (use for mass
unbalance)==>> SHOULD CORRESPOND TO KBHA CBHA MBHA OF THE FEM_Drillstring.m
R_BHA= OD_BHA/2;                   % BHA Drill-collars radius
cBH= Rh-R_BHA;                     % Borehole-BHA Clearance


% C) Applied static load at the Top of the Rig
% ====================================
Wo=50e3; % Applied Load (Nfft) ********************************************


% D) Drillpipe parameters
% ====================================
mass_rho = 7850;                   % Density kg/M_BHA^3
L_dp=110;                          % Drill-pipe length (M_BHA)
OD_dp=(5)*0.0254;                  % Drill-pipe OD
ID_dp=(3/8)*0.0254;                % Drill-pipe ID
Ac_dp = pi/4*(OD_dp.^2 - ID_dp.^2);% Drill-pipe cross section area
M_dp=mass_rho*Ac_dp*L_dp;          % Drill-pipe mass on top of BHA
J_dp=(M_dp/8)*(OD_dp^2+ID_dp^2);   % Drill-pipe Moment of Inertia
kT_dp=600;                         % Equivalent Torsional Stiffness-to-ground
cT_dp=500;                         % Equivalent Torsional damping-to-ground
cb_dp=(0.5)*30e3;                  % Equivalent Axial damping-to-ground

% E) DrillBit Parameters
% ====================================
n=8;                               % Number of PDC Blades
```

```
OD_db= (8.5)*0.0254;                 % DRILLBIT OD
a=OD_db/2;                           % PDC Drillbit- radius
cDB=Rh-a;                            % Drillbit/borehole clearance
l=5e-3;                              % Wearflat length
psi=0*pi/180;                        % WOB Vertical Inclination wrt to the BHA
((DrillBit bent angle))

% F) Rotary Table parameters
% ===================================
rpm= 120; % Top Drive Spin (RPM) ******************************************
w= rpm*2*pi/60;                      % (wd)Top Drive Spin rotary table Speed(rad/s)
tn0=1*pi/n/w;                        % time required for the bit to rotate by 2Pi/n to
its current position at time t

% G) ADDING FLYWHEEL
% ===================================
N_fl=3000;                         % flywheel (rpm)
w_fl=N_fl*2*pi/60;                 % flywheel angular speed (rad/sec)
q=5e-6;                            % Flywheel eccentricity
E_fw = 30456846*6894.76;           % Flywheel Young Modulus of Elasticity in Pa
rho_fw= 7850;                      % Flywheel Density in kg/m3
nu_fw = 0.3;                       % Flywheel Poisson's Ratio
EW_desired = 1.0e3*3600;           % Desired Energy to be stored in Flywheel in W.s OR J
ID_fw =124.3662e-3;                % Flywheel Inner Diameter (M_BHA)
OD_fw =177.1357e-3;                % Flywheel Outer Diameter (M_BHA)
max_rpm =2.9146e+04;               % Flywheel Maximum Speed (RPM)
E_Whr =7.5761;                     % Flywheel Energy Density (W.hr/kg)
L_fw =1.3456;                      % Flywheel Length (M_BHA)
M_fw =131.9935;                    % Flywheel Mass (kg)
Jp_fw=(0.5*M_fw*((ID_fw/2)^2+(OD_fw/2)^2))+M_fw*q^2;% Flywheel Inertia (kgm^2)
zeta=0.3;                          % damping ration
% FW Axial (X-axis)
kb_fw=M_fw*(w_fl)^2;               % FW Axial Stiffness
cf_fw=2*(zeta)*(w_fl)*(M_fw);      % FW Axial Damping
% FW Torsional  (X-axis)
kTb_fw=1*60;                       % FW Torsional Stiffness
cTb_fw=1*500;                      % FW Torsional Damping
% FW Lateral/Radial (Y/Z-axis)
kr_fw=1*M_fw*(zeta)^2;             % FW Lateral Stiffness
cr_fw=0.1*2*(w_fl)*(zeta)*M_fw;    % FW Lateral Damping

% H) ADDING STABILIZERS
% ===================================
% Stabilizers
R_st=(8.5/2)*0.0254;               % Stabilizer radius
cST=Rh-R_st;                       % Stabilizer/Borehole clearance
klat_st=0*5000;                    % Stabilizer Stiffness
clat_st=0*600;                     % Stabilizer Damping


%% [2]% AASEMBLING MATICES %%%%%%%%%%%%%%%%%%%%%%%%%%%%%%%%%%%%%%%%%%%%%%%%%
%%%%%%%%%%%%%%%%%%%%%%%%%%%%%%%%%%%%%%%%%%%%%%%%%%%%%%%%%%%%%%%%%%%%%%%%%%%%%

NNODE=size(MBHA,2);                % Get Total number of DOF's for the loaded BHA only

% % Get the CG node index for the  BHA
node_un=ceil(NNODE/noe/2);
loc_unx=6*(node_un-1)+1;
loc_uny=6*(node_un-1)+2;
loc_unz=6*(node_un-1)+3;
loc_unphi=6*(node_un-1)+4;

% % Constructing SYSTEM MATRICES

% Adding 4 DOF's ot the BHA - 4 DOF's for added Flywheel (x,y,z, Phix)
MC=zeros(NNODE+4,NNODE+4);
CC=zeros(NNODE+4,NNODE+4);
```

```
KC=zeros(NNODE+4,NNODE+4);

% Adding the BHA matrices to the global
MC(1:NNODE,1:NNODE)=MBHA;
CC(1:NNODE,1:NNODE)=CBHA;
KC(1:NNODE,1:NNODE)=KBHA;

% Adding equivelant top drillpipe weight, Tortional stiffness, damping
MC(1,1)=MC(1,1)+M_dp;
KC(4,4)=KC(4,4)+kT_dp;
CC(4,4)=CC(4,4)+cT_dp;
CC(1,1)=CC(1,1)+cb_dp;

% Adding drilling fluid radial damping constant to BHA in (Y)
for i=1:NNODE/6
    CC(i+(1+5*(i-1)),i+(1+5*(i-1)))=CC(i+(1+5*(i-1)),i+(1+5*(i-1)))+Cr;
end

% Adding drilling fluid radial damping constant to BHA in (Z)
for i=1:NNODE/6
    CC(i+(2+5*(i-1)),i+(2+5*(i-1)))=CC(i+(2+5*(i-1)),i+(2+5*(i-1)))+Cr;
end

% Adding drilling fluid tortional damping constant to BHA  (PhiX)
for i=1:NNODE/6
    CC(i+(3+5*(i-1)),i+(3+5*(i-1)))=CC(i+(3+5*(i-1)),i+(3+5*(i-1)))+Ctf;
end

% % ADDING FLYWHEEL INSIDE THE BHA- DRILL COLLARS
% ======================================================

% % OPTION (1) Either Placing the FW  Near Drillbit

% MC(NNODE+1,NNODE+1)=M_fw;
% MC(NNODE+2,NNODE+2)=Jp_fw;  %% ?!! ======= CHEK HERE PLZ from the original file !!
% MC(NNODE+3,NNODE+3)=M_fw;
% MC(NNODE+4,NNODE+4)=M_fw;
% % Add FW axial stiffness (X-dir)
% KC(NNODE-5,NNODE-5)=KC(NNODE-5,NNODE-5)+kb_fw;
% KC(NNODE+1,NNODE+1)=kb_fw;
% KC(NNODE-5,NNODE+1)=-kb_fw;
% KC(NNODE+1,NNODE-5)=-kb_fw;
% % Add FW Tortional stiffness (PhiX-dir)
% KC(NNODE-2,NNODE-2)=KC(NNODE-2,NNODE-2)+kTb_fw;
% KC(NNODE+2,NNODE+2)=kTb_fw;
% KC(NNODE-2,NNODE+2)=-kTb_fw;
% KC(NNODE+2,NNODE-2)=-kTb_fw;
% % Add FW Radial/Lateral stiffnesses (Y-dir)
% KC(NNODE-4,NNODE-4)=KC(NNODE-4,NNODE-4)+kr_fw;
% KC(NNODE+3,NNODE+3)=kr_fw;
% KC(NNODE-4,NNODE+3)=-kr_fw;
% KC(NNODE+3,NNODE-4)=-kr_fw;
% % Add FW Radial/Lateral stiffnesses (Z-dir)
% KC(NNODE-3,NNODE-3)=KC(NNODE-3,NNODE-3)+kr_fw;
% KC(NNODE+4,NNODE+4)=kr_fw;
% KC(NNODE-3,NNODE+4)=-kr_fw;
% KC(NNODE+4,NNODE-3)=-kr_fw;
%
% % Add FW axial damping (X-dir)
% CC(NNODE-5,NNODE-5)=CC(NNODE-5,NNODE-5)+cf_fw+cb_dp;
% CC(NNODE+1,NNODE+1)=cf_fw;
% CC(NNODE-5,NNODE+1)=-cf_fw;
% CC(NNODE+1,NNODE-5)=-cf_fw;
% % Add FW axial Tortional damping (PhiX-dir)
% CC(NNODE-2,NNODE-2)=CC(NNODE-2,NNODE-2)+cTb_fw;
% CC(NNODE+2,NNODE+2)=cTb_fw;
% CC(NNODE-2,NNODE+2)=-cTb_fw;
```

```
% CC(NNODE+2,NNODE-2)=-cTb_fw;
% % Add FW Radial/Lateral damping (Y-dir)
% CC(NNODE-4,NNODE-4)=CC(NNODE-4,NNODE-4)+cr_fw;
% CC(NNODE+3,NNODE+3)=cr_fw;
% CC(NNODE-4,NNODE+3)=-cr_fw;
% CC(NNODE+3,NNODE-4)=-cr_fw;
% % Add FW axial damping (Z-dir)
% CC(NNODE-3,NNODE-3)=CC(NNODE-3,NNODE-3)+cr_fw;
% CC(NNODE+4,NNODE+4)=cr_fw;
% CC(NNODE-3,NNODE+4)=-cr_fw;
% CC(NNODE+4,NNODE-3)=-cr_fw;


% % OPTION (2)  Placing the FW Near CG

MC(NNODE+1,NNODE+1)=M_fw;
MC(NNODE+2,NNODE+2)=Jp_fw;  %% ?!! ======= CHEK HERE PLZ from the original file !!
MC(NNODE+3,NNODE+3)=M_fw;
MC(NNODE+4,NNODE+4)=M_fw;
% Add FW axial stiffness (X-dir)
KC(loc_unx,loc_unx)=KC(loc_unx,loc_unx)+kb_fw;
KC(NNODE+1,NNODE+1)=kb_fw;
KC(loc_unx,NNODE+1)=-kb_fw;
KC(NNODE+1,loc_unx)=-kb_fw;
% Add FW Tortional stiffness (PhiX-dir)
KC(loc_unphi,loc_unphi)=KC(loc_unphi,loc_unphi)+kTb_fw;
KC(NNODE+2,NNODE+2)=kTb_fw;
KC(loc_unphi,NNODE+2)=-kTb_fw;
KC(NNODE+2,loc_unphi)=-kTb_fw;
% Add FW Radial/Lateral stiffnesses (Y-dir)
KC(loc_uny,loc_uny)=KC(loc_uny,loc_uny)+kr_fw;
KC(NNODE+3,NNODE+3)=kr_fw;
KC(loc_uny,NNODE+3)=-kr_fw;
KC(NNODE+3,loc_uny)=-kr_fw;
% Add FW Radial/Lateral stiffnesses (Z-dir)
KC(loc_unz,loc_unz)=KC(loc_unz,loc_unz)+kr_fw;
KC(NNODE+4,NNODE+4)=kr_fw;
KC(loc_unz,NNODE+4)=-kr_fw;
KC(NNODE+4,loc_unz)=-kr_fw;
% Add FW axial damping (X-dir)
CC(loc_unx,loc_unx)=CC(loc_unx,loc_unx)+cf_fw;
CC(NNODE+1,NNODE+1)=cf_fw;
CC(loc_unx,NNODE+1)=-cf_fw;
CC(NNODE+1,loc_unx)=-cf_fw;
% Add FW axial Tortional damping (PhiX-dir)
CC(loc_unphi,loc_unphi)=CC(loc_unphi,loc_unphi)+cTb_fw;
CC(NNODE+2,NNODE+2)=cTb_fw;
CC(loc_unphi,NNODE+2)=-cTb_fw;
CC(NNODE+2,loc_unphi)=-cTb_fw;
% Add FW Radial/Lateral damping (Y-dir)
CC(loc_uny,loc_uny)=CC(loc_uny,loc_uny)+cr_fw;
CC(NNODE+3,NNODE+3)=cr_fw;
CC(loc_uny,NNODE+3)=-cr_fw;
CC(NNODE+3,loc_uny)=-cr_fw;
% Add FW Radial/Lateral damping (Z-dir)
CC(loc_unz,loc_unz)=CC(loc_unz,loc_unz)+cr_fw;
CC(NNODE+4,NNODE+4)=cr_fw;
CC(loc_unz,NNODE+4)=-cr_fw;
CC(NNODE+4,loc_unz)=-cr_fw;

% % Adding Stabilizers to the BHA model
% =================================================

% OPTION (1) Adding first stabilizer at BHA's CG location

% % Lateral (Y-Dir)
% KC(loc_uny,loc_uny)=KC(loc_uny,loc_uny)+klat_st;
```

```
% CC(loc_uny,loc_uny)=CC(loc_uny,loc_uny)+clat_st;
% % Lateral (Z-Dir)
% KC(loc_unz,loc_unz)=KC(loc_unz,loc_unz)+klat_st;
% CC(loc_unz,loc_unz)=CC(loc_unz,loc_unz)+clat_st;

% OPTION (2) Adding Second stabilizer at Top of the BHA
% Lateral (Y-Dir)
KC(2,2)=KC(2,2)+klat_st;
CC(2,2)=CC(2,2)+clat_st;
% Lateral (Z-Dir)
KC(3,3)=KC(3,3)+klat_st;
CC(3,3)=CC(3,3)+clat_st;

% OPTION (3) Adding Third stabilizer at the bottom
% Lateral (Y-Dir)
KC(NNODE-4,NNODE-4)=KC(NNODE-4,NNODE-4)+klat_st;
CC(NNODE-4,NNODE-4)=CC(NNODE-4,NNODE-4)+clat_st;
% Lateral (Z-Dir)
KC(NNODE-3,NNODE-3)=KC(NNODE-3,NNODE-3)+klat_st;
CC(NNODE-3,NNODE-3)=CC(NNODE-3,NNODE-3)+clat_st;

%% [3]% FORMING STATE-SPACE %%%%%%%%%%%%%%%%%%%%%%%%%%%%%%%%%%%%%%%%%%%%%%%%
%%%%%%%%%%%%%%%%%%%%%%%%%%%%%%%%%%%%%%%%%%%%%%%%%%%%%%%%%%%%%%%%%%%%%%%%%%%%

A0=zeros(2*NNODE+8,2*NNODE+8);
A0(1:NNODE+4,NNODE+4+1:2*NNODE+8)=eye(NNODE+4);
A0(NNODE+4+1:2*NNODE+8,1:NNODE+4)=-inv(MC)*KC;
A0(NNODE+4+1:2*NNODE+8,NNODE+4+1:2*NNODE+8)=-inv(MC)*CC;

B0=zeros(2*NNODE+8,NNODE+4);
B0(NNODE+4+1:2*NNODE+8,:)=inv(MC);


%% [4]% SIMULATION TIME  %%%%%%%%%%%%%%%%%%%%%%%%%%%%%%%%%%%%%%%%%%%%%%%%%%%
%%%%%%%%%%%%%%%%%%%%%%%%%%%%%%%%%%%%%%%%%%%%%%%%%%%%%%%%%%%%%%%%%%%%%%%%%%%%

to=0;                            % Start Simulation Time
tfinal=50;                       % Final Simulation Time
maxstep=0.0025;                  % Max. step size
Nsamples=(tfinal/maxstep)+1;     % Get Number of steps
dt=tfinal/(Nsamples-1);
tsim=[to:dt:tfinal];             % Integration with fixed step

% Initializing system state space..
% ================================
tp=0;
tk=0;

% initializing DRILLBIT Outputs variables (Node #7)
% =====================================
x=zeros(Nsamples,1);             % Drillbit axial penetration in X-dir
xDot_db=zeros(Nsamples,1);       % Drillbit axial velocity in  X-dir
y_db=zeros(Nsamples,1);          % Drillbit Lateral position in Y-dir
z_db=zeros(Nsamples,1);          % Drillbit Lateral position in Z-dir
yDot_db=zeros(Nsamples,1);       % Drillbit Lateral velocity in Y-dir
zDot_db=zeros(Nsamples,1);       % Drillbit Lateral velocity in Z-dir
phi=zeros(Nsamples,1);           % Drillbit axial rotation angle X-dir
PhiXDot_db=zeros(Nsamples,1);    % Drillbit axial rotation velocity Phi-X
rDB=zeros(Nsamples,1);           % Drillbit radial displacement
omegaDB=zeros(Nsamples,1);       % Drillbit whirling velocity
VrelDB=zeros(Nsamples,1);        % Drillbit relative velocity
wob=zeros(Nsamples,1);           % Drillbit WOB
tob=zeros(Nsamples,1);           % Drillbit TOB

% initializing Flywheel Outputs variables  (Node #8)
% =====================================
x_fw=zeros(Nsamples,1);          % FW axial motion  X-dir
```

```
xDot_fw=zeros(Nsamples,1);          % FW axial velocity  X-dir
PhiX_fw=zeros(Nsamples,1);          % FW axial rotation angle X-dir
PhiXDot_fw=zeros(Nsamples,1);       % FW axial rotation velocity Phi-X-dir
y_fw=zeros(Nsamples,1);             % FW lateral motion  Y-dir
yDot_fw=zeros(Nsamples,1);          % FW lateral velocity  Y-dir
z_fw=zeros(Nsamples,1);             % FW lateral motion  Z-dir
zDot_fw=zeros(Nsamples,1);          % FW lateral velocity  Z-dir

% initializing STABILIZER 1 Outputs variables  (Node #1)
% =======================================
y_st1=zeros(Nsamples,1);            % ST1 lateral motion  Y-dir
z_st1=zeros(Nsamples,1);            % ST1 lateral motion  Z-dir
%r_st1= zeros(Nsamples,1);           % ST1 radial displacement
rst1=zeros(Nsamples,1);             % ST1 radial displacement
omegast1=zeros(Nsamples,1);         % ST1 whirling velocity
Vrelst1=zeros(Nsamples,1);          % ST1 relative velocity
Fnst1=zeros(Nsamples,1);            % ST1 normal contact force
Ftst1=zeros(Nsamples,1);            % ST1 friction force

% initializing BHA CG outputs variables (Node #4)
% =======================================
yG=zeros(Nsamples,1);               % C.G. Lateral position in Y-dir
zG=zeros(Nsamples,1);               % C.G. Lateral position in Z-dir
yDot_G=zeros(Nsamples,1);           % C.G. Lateral velocity in Y-dir
zDot_G=zeros(Nsamples,1);           % C.G. Lateral velocity in Z-dir
PhiX_G=zeros(Nsamples,1);           % C.G. rotation angle about X-dir
PhiXDot_G=zeros(Nsamples,1);        % C.G. rotation velocity about X-dir
rCG=zeros(Nsamples,1);              % C.G. radial displacement
omegaBHA=zeros(Nsamples,1);         % C.G. whirling velocity
VrelBHA=zeros(Nsamples,1);          % C.G. relative velocity

% initializing BHA outputs variables at (Node #5)
% =======================================
y_5=zeros(Nsamples,1);              % BHA-N5 Lateral position in Y-dir
z_5=zeros(Nsamples,1);              % BHA-N5 Lateral position in Z-dir
r_5=zeros(Nsamples,1);              % BHA-N5 radial displacement

% initializing STABILIZER 2 Outputs at (Node #6)
% =======================================
y_st2=zeros(Nsamples,1);            % ST2 lateral motion  Y-dir
z_st2=zeros(Nsamples,1);            % ST2 lateral motion  z-dir
rst2=zeros(Nsamples,1);             % ST2 radial displacement
omegast2=zeros(Nsamples,1);         % ST2 whirling velocity
Vrelst2=zeros(Nsamples,1);          % ST2 relative velocity
Fnst2=zeros(Nsamples,1);            % ST2 normal contact force
Ftst2=zeros(Nsamples,1);            % ST2 friction force
Ftst2R=zeros(Nsamples,1);           % ST2 calculated friction force incase of pure-
rolling
ROLLING_st2=zeros(Nsamples,1);      % ST2 Pure-Rolling FLAG !
SLIDING_st2=zeros(Nsamples,1);      % ST2 Sliding FLAG !


Wf=a*l*sgma;                        % fractional componont of WOB
v0=(Wo-Wf)*w/2/pi/a/eta/eps;        % Penetration rate
d0=2*pi*v0/w;

% Initializing the State matricies for ode
% =======================================
z0=zeros(NNODE+4,1); dz0=zeros(NNODE+4,1);

for i=1:1:NNODE/6
    dz0(6*(i-1)+1,1)=v0;            % apply initiAL axial  velcoity of V0 to all nodes
    dz0(6*(i-1)+4,1)=w;             % apply Initial axial rotation velocity of w to all
nodes
end

xtn=zeros(Nsamples,1);
```

```
phitn=zeros(Nsamples,1);
dd=zeros(Nsamples,1);
tn=zeros(Nsamples,1);
tni=tn0;
tn(1,1)=tni;

% initializing condition flags
% =====================================
bounce=0;
casex=zeros(Nsamples,1);


%% [5]% ODE-Integrating ... %%%%%%%%%%%%%%%%%%%%%%%%%%%%%%%%%%%%%
%%%%%%%%%%%%%%%%%%%%%%%%%%%%%%%%%%%%%%%%%%%%%%%%%%%%%%%%%%%%%%%%%%%%%%%%%%%
tic

for i=1:Nsamples-1

    tii=tsim(1,i)
    tfi=tsim(1,i+1);

    loci=i;
    xi=x(i,1);
    phii=phi(i,1);
 options = odeset('AbsTol',1e-4,'RelTol',1e-3);
%     [tr zi]=ode45('FINAL_FEM_sub',[tii tfi],[z0;dz0]);
[tr zi]=ode45('FEM_Drillstring_sub',[tii tfi],[z0;dz0], options);
%     [tr zi]=ode23s('FEM_Drillstring_sub',[tii tfi],[z0;dz0]);
%     [tr zi]=ode23('FEM_Drillstring_sub',[tii tfi],[z0;dz0]);
%     [tr zi]=ode15s('FEM_Drillstring_sub',[tii tfi],[z0;dz0]);
%     [tr zi]=ode113('FEM_Drillstring_sub',[tii tfi],[z0;dz0]);
    ni=size(zi,1);
    z0=zi(ni,1:NNODE+4)';
    dz0=zi(ni,NNODE+4+1:2*NNODE+8)';

    xtn(i+1,1)=xtni;
    phitn(i+1,1)=phitni;
    tn(i+1,1)=tni;
    dd(i+1,1)=d;                         % Depth of cut

% Outputs for DB (Node# 7)
% ===========================================
    x(i+1,1)=z0(NNODE-5,1);              % axial penetration   X
    y_db(i+1,1)=z0(NNODE-4,1);           % lateral position    Y
    z_db(i+1,1)=z0(NNODE-3,1);           % lateral position    Z
    phi(i+1,1)=z0(NNODE-2,1);            % axial rotation angle  Phi-x
    xDot_db(i+1,1)=dz0(NNODE-5,1);       % axial velocity   Xdot
    yDot_db(i+1,1)=dz0(NNODE-4,1);       % Lateral velocity   Ydot
    zDot_db(i+1,1)=dz0(NNODE-3,1);       % Lateral velocity   Zdot
    PhiXDot_db(i+1,1)=dz0(NNODE-2,1);    % axial angular velocity PhiDot-X
    rDB(i+1,1)=rdb;                      % radial displacement
    omegaDB(i+1,1)= omega_db;            % Whirling velocity
    VrelDB(i+1,1)=Vrel_db;               % Relative velocity
    wob(i+1,1)= WOB;                     % WOB
    tob(i+1,1)= TOB;                     % TOB

% Outputs for FW at it's second Node (Node# 8)
% ===========================================
    x_fw(i+1,1)=z0(NNODE+1,1);           % Axial diplazement  X
    xDot_fw(i+1,1)=dz0(NNODE+1,1);       % Axial velocity  X
    PhiX_fw(i+1,1)=z0(NNODE+2,1);        % rotation angle about  X
    PhiXDot_fw(i+1,1)=dz0(NNODE+2,1);    % rotation velocity about  X
    y_fw(i+1,1)=z0(NNODE+3,1);           % Lateral diplacement  Y
    yDot_fw(i+1,1)=dz0(NNODE+3,1);       % Lateral velocity  Y
    z_fw(i+1,1)=z0(NNODE+4,1);           % Lateral diplacement  z
    zDot_fw(i+1,1)=dz0(NNODE+4,1);       % Lateral velocity  z
```

```
% Outputs for BHA C.G. (Node# 4)
% ============================================
    yG(i+1,1)=z0(loc_uny,1);                    % Lateral diplacement  Y
    zG(i+1,1)=z0(loc_unz,1);                    % Lateral diplacement  z
    yDot_G(i+1,1)=dz0(loc_uny,1);               % Lateral velocity  Y
    zDot_G(i+1,1)=dz0(loc_unz,1);               % Lateral velocity  z
    PhiX_G(i+1,1)=z0(6*(node_un-1)+4,1);        % rotation angle about  X
    PhiXDot_G(i+1,1)=dz0(6*(node_un-1)+4,1);% rotation velocity about  X
    rCG(i+1,1)=r_CG;                            % radial displacement
    omegaBHA(i+1,1)=omega_BHA;                  % Whirling velocity
    VrelBHA(i+1,1)=Vrel_BHA;                    % Relative velocity
    FnBHA(i+1,1)=Fn_CG;                         % Contact force
    FtBHA(i+1,1)= Ft_CG;                        % friction force

% Outputs for STABILIZER 1 (Node# 1)
% ============================================
    y_st1(i+1,1)=z0(6*(1-1)+2,1);               % Lateral diplacement  Y
    z_st1(i+1,1)=z0(6*(1-1)+3,1);               % Lateral diplacement  z
    yDot_st1(i+1,1)=dz0(6*(1-1)+2,1);           % Lateral velocity  Y
    zDot_st1(i+1,1)=dz0(6*(1-1)+3,1);           % Lateral velocity  z
    PhiX_st1(i+1,1)=z0(6*(1-1)+4,1);            % rotation angle about  X
    PhiXDot_st1(i+1,1)=dz0(6*(1-1)+4,1);        % rotation velocity about  X
    rst1(i+1,1)=r_st1;                          % radial displacement
    omegast1(i+1,1)= omega_st1;                 % Whirling velocity
    Vrelst1(i+1,1)=Vrel_st1;                    % Relative velocity
    Fnst1(i+1,1)=Fn_st1;                        % Contact force
    Ftst1(i+1,1)=Ft_st1;                        % friction force

% Outputs for (Node# 5)
% ============================================
    y_5(i+1,1)=z0(6*(5-1)+2,1);                 % Lateral diplacement  Y
    z_5(i+1,1)=z0(6*(5-1)+3,1);                 % Lateral diplacement  z
    yDot_5(i+1,1)=dz0(6*(5-1)+2,1);             % Lateral velocity  Y
    zDot_5(i+1,1)=dz0(6*(5-1)+3,1);             % Lateral velocity  z
    PhiX_5(i+1,1)=z0(6*(5-1)+4,1);              % rotation angle about  X
    PhiXDot_5(i+1,1)=dz0(6*(5-1)+4,1);          % rotation velocity about  X

% Outputs for STABILIZER 2 (Node# 6)
% ============================================
    y_st2(i+1,1)=z0(6*(6-1)+2,1);               % Lateral diplacement  Y
    z_st2(i+1,1)=z0(6*(6-1)+3,1);               % Lateral diplacement  z
    yDot_st2(i+1,1)=dz0(6*(6-1)+2,1);           % Lateral velocity  Y
    zDot_st2(i+1,1)=dz0(6*(6-1)+3,1);           % Lateral velocity  z
    PhiX_st2(i+1,1)=z0(6*(6-1)+4,1);            % rotation angle about  X
    PhiXDot_st2(i+1,1)=dz0(6*(6-1)+4,1);        % rotation velocity about  X
    rst2(i+1,1)=r_st2;                          % radial displacement
    omegast2(i+1,1)= omega_st2;                 % Whirling velocity
    Vrelst2(i+1,1)=Vrel_st2;                    % Relative velocity
    Fnst2(i+1,1)=Fn_st2;                        % Contact force
    Ftst2(i+1,1)=  mus.*Fn_st2;                 % friction force
    Ftst2R(i+1,1)= Ftst2_R;                     % calculated friction force incase of
Pure-rolling
    ROLLING_st2(i+1,1)=ROLLINGst2;              % Pure-Rolling FLAG !
    SLIDING_st2(i+1,1)=SLIDINGst2;              % Sliding FLAG !
end

toc

% Theoritical whirling velocity at Stabilizer-2 when Backward whirling
omega_Theo_ST2= zeros(size(Fnst2));
for j= 1: size(Fnst2)
    if Fnst2(j)~=0 && (-mus*Fnst2(j))<= Ftst2R(j)<=(mus*Fnst2(j)) &&
abs(Vrelst2(j))<Vmin
       omega_Theo_ST2(j)= -(R_st/cST)*PhiXDot_st2(j);
    else
    end
end
```

```
% % FFT
% =================================
m=length(omegast2);
Nfft= pow2(nextpow2(m));
Fs= Nsamples/tfinal;                    % sample frequency (Hz)
f= (0:Nfft/2-1)* (Fs/Nfft);             % Frequency vector
% f= (0:Nfft-1)* (Fs/Nfft);             % Frequency range  % Fs/Nfft=frequency
increment

% ST1
FFT_Omega_ST1= fft(omegast1./(2*pi),Nfft);
FFT_Omega_ST1= abs(FFT_Omega_ST1);
FFT_Omega_ST1 = FFT_Omega_ST1(1:Nfft/2); % FFT is symmetric, throw away second half
FFT_Y_ST1= abs(fft(y_st1,Nfft));
FFT_Z_ST1= abs(fft(z_st1,Nfft));
FFT_Y_ST1 = FFT_Y_ST1(1:Nfft/2);
FFT_Z_ST1 = FFT_Z_ST1(1:Nfft/2);

% ST2
FFT_Omega_ST2= fft(omegast2./(2*pi),Nfft);
FFT_Omega_ST2= abs(FFT_Omega_ST2);
FFT_Omega_ST2 = FFT_Omega_ST2(1:Nfft/2); % FFT is symmetric, throw away second half
% FFT_Omega_ST2=FFT_Omega_ST2.*conj(FFT_Omega_ST2)/Nfft;
FFT_Y_ST2= abs(fft(y_st2,Nfft));
FFT_Z_ST2= abs(fft(z_st2,Nfft));
FFT_Y_ST2 = FFT_Y_ST2(1:Nfft/2);
FFT_Z_ST2 = FFT_Z_ST2(1:Nfft/2);

% BHA
FFT_Omega_BHA= fft(omegaBHA./(2*pi),Nfft);
FFT_Omega_BHA= abs(FFT_Omega_BHA);
FFT_Omega_BHA = FFT_Omega_BHA(1:Nfft/2);

% db
FFT_Omega_db= fft(omegaDB./(2*pi),Nfft);
FFT_Omega_db= abs(FFT_Omega_db);
FFT_Omega_db = FFT_Omega_db(1:Nfft/2);
FFT_X_db= abs(fft((x+v0*tsim'),Nfft));
FFT_X_db = FFT_X_db(1:Nfft/2);

%% [6]% Plotting Output Data  %%%%%%%%%%%%%%%%%%%%%%%%%%%%%%%%%%%%%%%%%%%%%%
%%%%%%%%%%%%%%%%%%%%%%%%%%%%%%%%%%%%%%%%%%%%%%%%%%%%%%%%%%%%%%%%%%%%%%%%%%%%

% Plotting- Drillbit axial penetration
figure(1)
plot(tsim,(x+v0*tsim')*1000)
xlabel('time (s)')
ylabel('x (mm)')
title('Drillbit Axial Penetration');
grid on

% Plotting- Drillbit 3D-pathline inside Borehole
figure (2)
hold on
grid
NN=100;
[X,Y,Z] = cylinder(cDB*1000,NN);
Z(2,:)= min((x+v0*tsim')*1000);
Z(2,:)= max((x+v0*tsim')*1000);
h2 = surf(X,Y,Z);
set(h2,'FaceAlpha',0.3)
plot3(y_db*1000,z_db*1000,(x+v0*tsim')*1000,'b');
xlabel(' Yg (mm)');
ylabel(' Zg (mm)' );
zlabel(' Xg (mm)' );
```

```
title('3D Pathline Orbit');
% legend('Borehole','Drillbit Pathline');
view([-37.5 30])

% Plotting- Drillbit Axial Penetration Velocity
figure(3)
plot(tsim,(v0+xDot_db)*1000)
xlabel('time (s)')
ylabel('xDot_db (mm/s)')
title('Drillbit Axial Penetration Velocity');
grid on

% Plotting- Drillbit Rotation Angle in Degrees
figure(4)
plot(tsim,phi*180/pi)
xlabel('time (s)')
ylabel('phi (deg)')
title('Drillbit Rotation Angle');
grid on

% Plotting- Spining angular Velocities
figure(5)
plot(tsim,PhiXDot_db*30/pi,'b')
hold on
plot(tsim,PhiXDot_st1*30/pi,'g-')
plot(tsim,PhiXDot_G*30/pi,'c')
plot(tsim,PhiXDot_st2*30/pi,'r-')
xlabel('time (s)')
ylabel('PhiDot-X (rpm)')
title(' Spining angular Velocities')
legend ('DB', 'ST1','BHA C.G' ,'ST2');
grid on

% Plotting- FW Axial Displacement
% figure(6)
% plot(tsim,x_fw*1000)
% xlabel('time (s)')
% ylabel('x_f_w (mm)')
% title('FW Axial Displacement')
% grid on


% Plotting- FW-BHA Axial Clearance
% figure(7)
% plot(tsim,abs(x_fw-x)*1000)
% xlabel('time (s)')
% ylabel('dx (mm)')
% title('FW-BHA Axial Clearance')
% grid on

% Plotting- WOB
figure(8)
plot(tsim,wob/1000)
xlabel('time (s)')
ylabel('Force (kN)')
title('WOB')
grid on

% Plotting- Depth Of Cut
figure(9)
plot(tsim,dd*1000)
xlabel('time (s)')
ylabel('Depth of Cut (mm)')
grid on

% Plotting- TOB
figure(10)
```

```
plot(tsim,tob/1000)
xlabel('time (s)')
ylabel('Torque (kN.M_BHA)')
title('TOB')
grid on

% Plotting- Drillbit 2D-Orbit
figure(11)
plot(y_db*1000,z_db*1000);
hold on
Radius_db=cDB*1000;
[cx_db,cy_db,z_db] = cylinder(Radius_db,100);
plot(cx_db(1,:),cy_db(1,:),'r.');
xlabel('y_D_B (mm)')
ylabel('z_D_B (mm)')
title('Drillbit Orbit');
axis square
axis equal
grid on;

% Plotting- BHA CG 2D-Orbit
figure(12)
plot(yG*1000,zG*1000);
hold on
Radius_cg=cBH*1000;
[cx_cg,cy_cg,z_cg] = cylinder(Radius_cg,100);
plot(cx_cg(1,:),cy_cg(1,:),'r.');
xlabel('y_C_G (mm)')
ylabel('z_C_G (mm)')
title('BHA CG Orbit');
axis square
axis equal
grid on;

% Plotting- Upper Stabilizer 2D-Orbit
figure(13)
plot(y_st1*1000,z_st1*1000);
hold on
Radius_st=cST*1000;
[cx_st,cy_st,z_st] = cylinder(Radius_st,100);
plot(cx_st(1,:),cy_st(1,:),'r.');
xlabel('y_st1 (mm)')
ylabel('z_st1(mm)')
title(' Upper Stabilizer Orbit');
axis square
axis equal
grid on;

% Plotting- Bottom Stabilizer 2D-Orbit
figure(14)
plot(y_st2*1000,z_st2*1000);
hold on
grid on;
Radius_st=cST*1000;
[cx_st,cy_st,z_st] = cylinder(Radius_st,100);
plot(cx_st(1,:),cy_st(1,:),'r.');
xlabel('y_st2 (mm)')
ylabel('z_st2(mm)')
title('Bottom Stabilizer Orbit');
axis square
axis equal

% Plotting- Relative velocities
figure (15)
plot (tsim,Vrelst1,'b-');
hold on
plot (tsim,VrelDB,'c');
```

```
plot (tsim,VrelBHA,'g-');
plot (tsim,Vrelst2,'r');
title('Relative velocities');
xlabel('Time (S)');
ylabel(' Vrel(rad/sec)' );
legend('Upper Stabilizer','DrillBit','BHA CG','Bottom Stabilizer');
grid on

% Plotting- Whirling velocities
figure (16)
hold on
plot (tsim,omegaBHA,'g-');
plot (tsim,omegaDB,'c');
plot (tsim,omegast1,'b-');
plot (tsim,omegast2,'k');
plot (tsim,omega_Theo_ST2,'r--');
title('Whirling velocity');
xlabel('Time (S)');
ylabel(' Omega(rad/sec)' );
legend(' BHA','Drillbit','Upper stabilizer','Bottom stabilizer','Theoretical Bottom
stabilizer');
grid on

% Plotting- BHA CG. Radial Displacement
figure (17)
plot (tsim,rCG,'b');
hold on
grid on
plot(tsim,cBH,'r');
title('BHA CG. Radial Displacement');
xlabel(' Time (S)');
ylabel(' r (mm)' );
legend('Borehole','BHA CG radial');
axis square

% Plotting- Bottom Stabilizer Tangintial Friction Force
figure (18)
plot (tsim, Ftst2/1000,'k');
hold on
grid on
plot(tsim,Ftst2R/1000,'r--');
title('Sliding friction Vs. Rolling friction');
xlabel(' Time (S)');
ylabel(' Tangintial Friction Force (KN) ' );
legend('Ft','Ft_R');

% Plotting- Bottom Stabilizer Normal contact Force
figure (19)
plot (tsim, Fnst2/1000,'k');
hold on
grid on
title('Normal Friction Force');
xlabel(' Time (S)');
ylabel(' Fn (KN) ' );
% legend('Ft','Ft_R');

% Plotting- Bottom Stabilizer Pure-Rolling Status
figure (20)
plot (tsim,ROLLING_st2,'r');
title('Bottom stabilizer Rolling status');
xlabel(' Time (S)');
ylabel(' 0=> No Rolling           1=> Rolling is ACTIVE ! ' );

% Plotting- FFT whirling frequencies
figure (21)
plot(f,FFT_Omega_ST2,'r');
% plot(f,power,'r');
```

```
hold on
grid on
plot(f,FFT_Omega_ST1,'g');
plot(f,FFT_Omega_BHA,'b');
plot(f,FFT_Omega_db,'k');
title ('Omega FFT');
xlabel(' Frequency (HZ) ');
ylabel(' Amplitude' );
legend('Bottom Stabilizer','Upper Stabilizer','BHA C.G','DrillBit');

% Plotting- FFT Bottom Stabilizer radial frequencies
figure (22)
plot(f,FFT_Y_ST2,'b');
hold on
grid on
plot(f,FFT_Z_ST2,'k');
% plot(f,FFT_Y_ST1,'--g');
% plot(f,FFT_Z_ST1,'--c');
title ('Radial displacement(Y/Z FFT)-Bottom Stabilizer');
xlabel(' Frequency ');
ylabel(' Amplitude' );
legend('FFT_Y_ST2','FFT_Z_ST2');

% Plotting- FFT Drillbit axial frequencies
figure (23)
plot(f,FFT_X_db,'r');
grid on
title ('axial penetration FFT - Drillbit');
xlabel(' Frequency ');
ylabel(' Amplitude' );
legend('FFT_X_DB');

% Plotting- FFT Upper Stabilizer radial frequencies
figure (24)
plot(f,FFT_Y_ST1,'b');
hold on
grid on
plot(f,FFT_Z_ST1,'k');
title ('Radial displacement(Y/Z FFT)-Upper Stabilizer');
xlabel(' Frequency ');
ylabel(' Amplitude' );
legend('FFT_Y_ST1','FFT_Z_ST1');
```

FEM_Drillstring_sub.m

```
% % Omar Abdelzaher
% Drillstring Finite-Element-Model using Timoshenko Beam Element method
% Drillstring Dynamics Analysis ( Forward & Backward whirling, Bit-Bounce,Stick-Slip)
% Stick Slip Via Time Delay (Detournay et al.) - PDC Drillbit
% Created January 15, 2014
% Updated April 20, 2014

%% call intigration function
%%%%%%%%%%%%%%%%%%%%%%%%%%%%%%%%%%%%%%%%%%%%%%%%%%%%%%%%%%%%%%%%%%%%%%%%%%%%
function zdot=FEM_Drillstring_sub(t,z)

global Wo A0 B0 kT_dp Kf e w M_BHA cDB cST Mdb_NODE Jdb_NODE Kphi_NODE Vmin
global Ctf R_BHA R_st eta mus psi cBH gma a eps sgma l mu0 n xtni phitni tni
global tn0 bounce x phi loci tsim d casex NNODE Mst2_NODE Jst2_NODE
global Kphist2_NODE Cf Cr ROLLINGst2 SLIDINGst2 r_st1 omega_st1 Vrel_st1
global Fn_st1 Ft_st1 r_CG omega_BHA Vrel_BHA Fn_CG Ft_CG r_st2 omega_st2
global Vrel_st2 Fn_st2 Ft_st2 Ftst2_R rdb omega_db  Vrel_db WOB TOB
```

```
%% PDC Cutting Dynamics & Obtaining Time History
%%%%%%%%%%%%%%%%%%%%%%%%%%%%%%%%%%%%%%%%%%%%%%%%%%%%%%%%%%%%%%%%%%%%%%%%%%%

% Determining tni, xtni, phitni

phi(loci+1,1)=z(NNODE-2);    % Phi-X
phitni=z(NNODE-2)-2*pi/n;

if phitni<0   % First step time delay
    phitni=0;
    tni=tn0;
    xtni=0;
    casex(loci,1)=-1;
else          % In case not first step after getting previous time history
   j=loci;
   for jj=j:-1:2
        if phitni==phi(jj,1)
            tni=t-tsim(1,jj);
            xtni=x(jj,1);
            casex(loci,1)=2;
            break;
        elseif phitni==phi(jj-1,1)
            tni=t-tsim(1,jj-1);
            xtni=x(jj-1,1);
            casex(loci,1)=3;
            break;
        elseif phitni>phi(jj-1,1) && phitni<phi(jj,1)
            tni=t-(tsim(1,jj)+tsim(1,jj-1))/2;
            xtni=(x(jj,1)+x(jj-1,1))/2;
            casex(loci,1)=4;
            break;
        elseif jj<=1
            tni=tn0;
            xtni=0;
            casex(loci,1)=5;
        end
   end
end

%% Caculating variables  %%%%%%%%%%%%%%%%%%%%%%%%%%%%%%%%%%%%%%%%%%%%%%%%%
%%%%%%%%%%%%%%%%%%%%%%%%%%%%%%%%%%%%%%%%%%%%%%%%%%%%%%%%%%%%%%%%%%%%%%%%%%

%%%%%%%%%%%%%%%%%%  Node 2
% ========================================
node_2=2;
x_2=6*(node_2-1)+1;
 xDot_2= x_2+NNODE+4;
y_2=6*(node_2-1)+2;
 yDot_2= y_2+NNODE+4;
z_2=6*(node_2-1)+3;
 zDot_2= z_2+NNODE+4;
PhiX_2= 6*(node_2-1)+4;
 PhiXDot_2= PhiX_2+NNODE+4;
PhiY_2= 6*(node_2-1)+5;
 PhiYDot_2= PhiY_2+NNODE+4;
PhiZ_2= 6*(node_2-1)+6;
 PhiZDot_2= PhiZ_2+NNODE+4;

%%%%%%%%%%%%%%%%%% STABILIZER ONE (Node# 1)
% ========================================
node_st1=1;                   % First Node at Top
x_st1=6*(node_st1-1)+1;
 xDot_st1=x_st1+NNODE+4;
y_st1=6*(node_st1-1)+2;
 yDot_st1=y_st1+NNODE+4;
z_st1=6*(node_st1-1)+3;
```

```
 zDot_st1=z_st1+NNODE+4;
PhiX_st1= 6*(node_st1-1)+4;
 PhiXDot_st1= PhiX_st1+NNODE+4;
PhiY_st1= 6*(node_st1-1)+5;
 PhiYDot_st1= PhiY_st1+NNODE+4;
PhiZ_st1= 6*(node_st1-1)+6;
 PhiZDot_st1= PhiZ_st1+NNODE+4;

r_st1= sqrt(((z(y_st1)^2)+1e-7)+z(z_st1)^2);
rDot_st1=(z(y_st1)*z(yDot_st1)+z(z_st1)*z(zDot_st1))/r_st1;
theta_st1= atan2(z(z_st1),z(y_st1));
omega_st1= (z(zDot_st1)*z(y_st1)- z(yDot_st1)*z(z_st1))/r_st1^2;  % Rotor whirl
velocity
Vrel_st1= z(PhiXDot_st1)*R_st + omega_st1*r_st1;

Fe_st1=(0)*M_BHA*e*z(PhiXDot_st1)^2;      % change to PhiDot-X @ C.G.
Fey_st1=1*Fe_st1*cos(z(PhiX_st1));          % Phi-x @ C.g
Fez_st1=1*Fe_st1*sin(z(PhiX_st1));          % Phi-x @ C.g
Fe_st1_t=Fez_st1*cos(theta_st1)-Fey_st1*sin(theta_st1);

Mst1_NODE= 1.6781e3;      % at Nodde 1   Y,Z (2,3)
Jst1_NODE= 8.9063;        % at Nodde 1   PhiX  (4)
Kphist1_NODE= 1.6555e5;   % at Nodde 1   (4)
ROLLINGst1=0;
SLIDINGst1=0;
Ftst1_R=0;

if r_st1>=cST   % THERE IS CONTACT
    Fn_st1= 1*Kf*(r_st1-cST)+ Cf*(rDot_st1);                              % Normal
Contact force
%      disp('--  Stabilizer (1) side CONTACT -----------');
    mu_st1= -(2/pi)*atan(10^4*Vrel_st1)*(((mus-mu0)/(1+10^2*abs(Vrel_st1)))+mu0);
    Ft_st1= mu_st1*Fn_st1;                  % tangential friction Contact force
    Ftst1_R=  (((((Mst1_NODE*R_st)/Jst1_NODE)*(-Kphist1_NODE*(z(PhiX_st1)-z(PhiX_2))-
Ctf*z(PhiXDot_st1)))+ Cr*omega_st1*r_st1)/(1+(Mst1_NODE*R_st*R_st/Jst1_NODE)))-
Fe_st1_t;
%     disp('--  ST1 side CONTACT -----------');
    if abs(Vrel_st1)>=Vmin && sign(z(PhiXDot_st1))== sign(omega_st1)
        SLIDINGst1=1;
%     disp('----- ST1 Pure SLiding ----------------');
    elseif (-mus*Fn_st1)<= Ftst1_R <=(mus*Fn_st1) && abs(Vrel_st1)<Vmin
       Ft_st1=Ftst1_R;
       ROLLINGst1=1;
%     disp('----------- ST1 Pure Rolling -----');
    else
%        disp('---------------- ST1 TRANSITION -----');
    end
else    % NO CONTACT
    Fn_st1=0;
    Ft_st1=0;
    Ftst1_R=0;
   % disp('------ ST1 nO side CONTACT -----------');
end

% z/r=sin(theta_st1)
% y/r=cos(theta_st1)

% Ft_st1= -mu0*sign(Vrel_st1)*Fn_st1;                    % tangential friction
Contact force
Fy_st1= -Ft_st1*sin(theta_st1)- Fn_st1*cos(theta_st1) + Fey_st1;   % Contact force in
X-dir
Fz_st1=  Ft_st1*cos(theta_st1)- Fn_st1*sin(theta_st1) + Fez_st1;   % Contact force in
Y-dir
Fx_st1= -sign(z(xDot_st1))*mu0*Fn_st1;                  % axial friction force

Ty_st1= -sign(z(PhiYDot_st1))*mu0*Fn_st1*R_st*abs(sin(theta_st1));
Tz_st1= -sign(z(PhiZDot_st1))*mu0*Fn_st1*R_st*abs(cos(theta_st1));
```

```
Tx_st1= -sign(z(PhiXDot_st1))*Ft_st1*R_st;

%%%%%%%%%%%%%%%%%%  (Node# 5)
% ========================================
node_5=5;  % The node before the last one at the bottom
x_5=6*(node_5-1)+1;
 xDot_5= x_5+NNODE+4;
y_5=6*(node_5-1)+2;
 yDot_5= y_5+NNODE+4;
z_5=6*(node_5-1)+3;
 zDot_5= z_5+NNODE+4;
PhiX_5= 6*(node_5-1)+4;
 PhiXDot_5= PhiX_5+NNODE+4;
PhiY_5= 6*(node_5-1)+5;
 PhiYDot_5= PhiY_5+NNODE+4;
PhiZ_5= 6*(node_5-1)+6;
 PhiZDot_5= PhiZ_5+NNODE+4;


%%%%%%%%%%%%%%%%%% STABILIZER TWO (Node# 6)
% ========================================
node_st2=6;  % The node before the last one at the bottom
x_st2=6*(node_st2-1)+1;
 xDot_st2= x_st2+NNODE+4;
y_st2=6*(node_st2-1)+2;
 yDot_st2= y_st2+NNODE+4;
z_st2=6*(node_st2-1)+3;
 zDot_st2= z_st2+NNODE+4;
PhiX_st2= 6*(node_st2-1)+4;
 PhiXDot_st2= PhiX_st2+NNODE+4;
PhiY_st2= 6*(node_st2-1)+5;
 PhiYDot_st2= PhiY_st2+NNODE+4;
PhiZ_st2= 6*(node_st2-1)+6;
 PhiZDot_st2= PhiZ_st2+NNODE+4;

r_st2= sqrt(((z(y_st2)^2)+1e-7)+z(z_st2)^2);
rDot_st2=(z(y_st2)*z(yDot_st2)+z(z_st2)*z(zDot_st2))/r_st2;
theta_st2=atan2(z(z_st2),z(y_st2));
omega_st2= (z(zDot_st2)*z(y_st2)- z(yDot_st2)*z(z_st2))/r_st2^2;  % Rotor whirl
velocity
Vrel_st2=z(PhiXDot_st2)*R_st + omega_st2*r_st2;

Mst2_NODE= 3.3561e3;      % at Nodde 6   Y,Z (32,33)
Jst2_NODE= 17.8126;        % at Nodde 6   PhiX  (34)
Kphist2_NODE= 3.289e5;   % at Nodde 6   (34)
ROLLINGst2=0;
SLIDINGst2=0;
Ftst2_R=0;

Fe_st2=(1)*M_BHA*e*z(PhiXDot_st2)^2;      % change to PhiDot-X @ C.G.
Fey_st2=1*Fe_st2*cos(z(PhiX_st2));          % Phi-x @ C.g
Fez_st2=1*Fe_st2*sin(z(PhiX_st2));          % Phi-x @ C.g
Fe_st2_t=Fez_st2*cos(theta_st2)-Fey_st2*sin(theta_st2);

node_db=7;
PhiX_db=6*(node_db-1)+4;           % CG-PhiX
% There is stabilizer
if r_st2>=cST   % THERE IS CONTACT
    Fn_st2= Kf*(r_st2-cST)+ Cf*(rDot_st2);                         % Normal Contact
force
    mu_st2= -(2/pi)*atan(10^4*Vrel_st2)*(((mus-mu0)/(1+10^2*abs(Vrel_st2)))+mu0);
    Ft_st2= mu_st2*Fn_st2;                 % tangential friction Contact force
    Ftst2_R=  (((((Mst2_NODE*R_st)/Jst2_NODE)*(-Kphist2_NODE*(z(PhiX_st2)-z(PhiX_db))-
Kphist2_NODE*(z(PhiX_st2)-z(PhiX_5))-Ctf*z(PhiXDot_st2)))+
Cr*omega_st2*r_st2)/(1+(Mst2_NODE*R_st*R_st/Jst2_NODE)))-Fe_st2_t;
%     disp('--  ST2 side CONTACT -----------');
    if abs(Vrel_st2)>=Vmin && sign(z(PhiXDot_st2))== sign(omega_st2)
```

```
        SLIDINGst2=1;
%     disp('----- ST2 Pure SLiding ----------------');
    elseif (-mus*Fn_st2)<= Ftst2_R <=(mus*Fn_st2) && abs(Vrel_st2)<Vmin
       Ft_st2=Ftst2_R;
       ROLLINGst2=1;
%     disp('----------- ST2 Pure Rolling -----');
    else
%        disp('---------------- ST2 TRANSITION -----');
    end
else    % NO CONTACT
    Fn_st2=0;
    Ft_st2=0;
    Ftst2_R=0;
   % disp('------ ST2 nO side CONTACT -----------');
end

% % NOO is stabilizer
% if r_st2>=cBH   % THERE IS CONTACT
%     Fn_st2= Kf*(r_st2-cBH);                          % Normal Contact force
%     disp('--  Stabilizer (2) side CONTACT -----------');
% else Fn_st2=0;
%    disp('------ NO Stabilizer (2) side CONTACT -----------');
% end

% z/r=sin(theta_st2)
% y/r=cos(theta_st2)

Fy_st2= -Ft_st2*sin(theta_st2) - Fn_st2*cos(theta_st2)+ Fey_st2;   % Contact force in
X-dir
Fz_st2=  Ft_st2*cos(theta_st2) - Fn_st2*sin(theta_st2)+ Fez_st2;   % Contact force in
Y-dir
Fx_st2= -sign(z(xDot_st2))*mu0*Fn_st2;                             % axial friction
force

% There is stabilizer
Ty_st2= -sign(z(PhiYDot_st2))*mu0*Fn_st2*R_st*abs(sin(theta_st2));
Tz_st2= -sign(z(PhiZDot_st2))*mu0*Fn_st2*R_st*abs(cos(theta_st2));
Tx_st2= -sign(z(PhiXDot_st2))*Ft_st2*R_st;

% % No stabilizer
% Ty_st2= -sign(z(PhiYDot_st2))*mu0*Fn_st2*R_BHA*abs(sin(theta_st2));
% Tz_st2= -sign(z(PhiZDot_st2))*mu0*Fn_st2*R_BHA*abs(cos(theta_st2));
% Tx_st2= -sign(z(PhiXDot_st2))*Ft_st2*R_BHA;

%%%%%%%%%%%%%%%%%% BHA-CG. (Node# 4)
% ========================================
node_CG=ceil(NNODE/6/2);
x_CG=6*(node_CG-1)+1;              % CG-Y
 xDot_CG=x_CG+NNODE+4;
y_CG=6*(node_CG-1)+2;              % CG-Y
 yDot_CG=y_CG+NNODE+4;
z_CG=6*(node_CG-1)+3;              % CG-Z
 zDot_CG=z_CG+NNODE+4;
PhiX_CG=6*(node_CG-1)+4;           % CG-PhiX
 PhiXDot_CG=PhiX_CG+NNODE+4;
PhiY_CG=6*(node_CG-1)+5;           % CG-PhiY
 PhiYDot_CG=PhiY_CG+NNODE+4;
PhiZ_CG=6*(node_CG-1)+6;           % CG-PhiZ
 PhiZDot_CG=PhiZ_CG+NNODE+4;

r_CG=      sqrt(((z(y_CG)^2)+1e-7)+z(z_CG)^2);
rDot_CG=    (z(y_CG)*z(yDot_CG)+z(z_CG)*z(zDot_CG))/r_CG;
theta_BHA= atan2(z(z_CG),z(y_CG));
omega_BHA= (z(y_CG)*z(zDot_CG) - z(z_CG)*z(yDot_CG))/r_CG^2;
Vrel_BHA=  z(PhiXDot_CG)*R_BHA + omega_BHA*r_CG;

 % Adding Mass Unbalance Forces @ C.G.
```

```
Fe=(0)*M_BHA*e*z(PhiXDot_CG)^2;      % change to PhiDot-X @ C.G.
Fey=1*Fe*cos(z(PhiX_CG));           % Phi-x @ C.g
Fez=1*Fe*sin(z(PhiX_CG));           % Phi-x @ C.g
Fe_CG_t=Fez*cos(theta_BHA)-Fey*sin(theta_BHA);

Mcg_NODE= Mst2_NODE;      % at Nodde 4   Y,Z (20,21)
Jcg_NODE= Jst2_NODE;        % at Nodde 4   PhiX  (22)
Kphicg_NODE= Kphist2_NODE;   % at Nodde 4   (22)
ROLLINGcg=0;
SLIDINGcg=0;
FtCG_R=0;

if r_CG>=cBH   % THERE IS CONTACT
    Fn_CG= 1*Kf*(r_CG-cBH)+ Cf*(rDot_CG);     % Normal contact force
    mu_CG= -(2/pi)*atan(10^4*Vrel_BHA)*(((mus-mu0)/(1+10^2*abs(Vrel_BHA)))+mu0);
    Ft_CG= mu_CG*Fn_CG;                  % tangential friction Contact force
    FtCG_R=  (((((Mcg_NODE*R_BHA)/Jcg_NODE)*(-Kphicg_NODE*(z(PhiX_CG)-z(PhiX_5))-
Kphicg_NODE*(z(PhiX_CG)-z(PhiX_st2))-Ctf*z(PhiXDot_CG)))+
Cr*omega_BHA*r_CG)/(1+(Mcg_NODE*R_BHA*R_BHA/Jcg_NODE)))-Fe_CG_t;
  %  disp('-- BHA Center side CONTACT -----------');
    if abs(Vrel_BHA)>=Vmin && sign(z(PhiXDot_CG))== sign(omega_BHA)
        SLIDINGcg=1;
%     disp('----- BHA Center Pure SLiding ----------------');
    elseif (-mus*Fn_CG)<= FtCG_R <=(mus*Fn_CG) && abs(Vrel_BHA)<Vmin
       Ft_CG=FtCG_R;
       ROLLINGcg=1;
%     disp('----------- BHA Center Pure Rolling -----');
    else
%        disp('---------------- BHA Center TRANSITION -----');
    end
else    % NO CONTACT
    Fn_CG=0;
    Ft_CG=0;
    FtCG_R=0;
   % disp('------ BHA Center nO side CONTACT -----------');
end
% z/r=sin(theta_BHA)
% y/r=cos(theta_BHA)

% Ft_CG= - mu0*Fn_CG*sign(Vrel_BHA);

Fy_BHA= Fey + (-Ft_CG*sin(theta_BHA)- Fn_CG*cos(theta_BHA));   % Contact force in X-
dir
Fz_BHA= Fez + ( Ft_CG*cos(theta_BHA)- Fn_CG*sin(theta_BHA));    % Contact force in Y-
dir
Fx_BHA= -sign(z(xDot_CG))*mu0*Fn_CG;                  % axial friction force

Ty_BHA= -sign(z(PhiYDot_CG))*mu0*Fn_CG*R_BHA *abs(sin(theta_BHA));
Tz_BHA= -sign(z(PhiZDot_CG))*mu0*Fn_CG*R_BHA *abs(cos(theta_BHA));
Tx_BHA= -sign(z(PhiXDot_CG))*Ft_CG*R_BHA ;

%%%%%%%%%%%%%%%%% DRILLBIT (Node# 7)
% ========================================
node_db=7;
x_db=6*(node_db-1)+1;
 xDot_db=x_db+NNODE+4;
y_db=6*(node_db-1)+2;             % CG-Y
 yDot_db=y_db+NNODE+4;
z_db=6*(node_db-1)+3;             % CG-Z
 zDot_db=z_db+NNODE+4;
PhiX_db=6*(node_db-1)+4;          % CG-PhiX
 PhiXDot_db=PhiX_db+NNODE+4;

rdb=sqrt(((z(y_db)^2)+1e-7)+z(z_db)^2);
rDot_db=(z(y_db)*z(yDot_db)+z(z_db)*z(zDot_db))/rdb;
theta_db=atan2(z(z_db),z(y_db));
omega_db=(z(y_db)*z(zDot_db)-z(z_db)*z(yDot_db))/rdb^2;
```

```
Vrel_db= z(PhiXDot_db)*a + omega_db*rdb;

% Stribeck frection for DB
muf=tanh(z(PhiXDot_db))+2*z(PhiXDot_db)/(1+1*z(PhiXDot_db)*z(PhiXDot_db))+0.01*z(PhiXD
ot_db);
mu_db=muf*mu0;

dn=(z(x_db)-xtni);  % Depth of cut per revolution per blade
d=n*dn;                 % Depth of cut for all blades
% & axial vibration
if d<=0
    bounce=1;
elseif z(x_db)<0 && xtni<0
    bounce=1;
else
    bounce=0;
end

if bounce==1   % No DB cutting or friction torques or frictions
    Tf=0;
    Tc=0;
    Wf=0;
    Wc=0;
   % disp('-- BIT BOUNCE !! ----');
elseif bounce==0;
    Tf=a*a/2*gma*mu_db*l*sgma;     % Friction component for TOB
    Tc=a*a/2*eps*d;                % Cutting component for TOB
    Wf=a*l*sgma;                   % Friction component for WOB
    Wc=a*eta*eps*d;                % Cutting component for WOB
   % disp('--------------- DRILLING  :)) --');
end

% Inclined Reaction Force from WOB
WOB=Wc+Wf;
TOB=Tc+Tf;
WOB_y=1*WOB*sin(psi)*cos(z(NNODE-2));
WOB_z=1*WOB*sin(psi)*sin(z(NNODE-2));

WOB_t= WOB_z*cos(theta_db)-WOB_y*sin(theta_db);

Fe=(0)*M_BHA*e*z(PhiXDot_db)^2;      % change to PhiDot-X @ C.G.
Fey_db=1*Fe*cos(z(PhiX_db));          % Phi-x @ C.g
Fez_db=1*Fe*sin(z(PhiX_db));          % Phi-x @ C.g

Fe_t=Fez_db*cos(theta_db)-Fey_db*sin(theta_db);

Mdb_NODE= 1.6781e3;   % Y,Z (38,39)
Jdb_NODE= 8.9063;    % PhiX (40)
Kphi_NODE= 1.6495e5;  % PhiX (40)

% % Lateral and radial vibrations
if rdb>=cDB    % There is contact
    Fn_db=1*Kf*(rdb-cBH)+Cf*(rDot_db);
    mu= -(2/pi)*atan(10^4*Vrel_db)*(((mus-mu0)/(1+10^2*abs(Vrel_db)))+mu0);
    Ft_db= mu*Fn_db;
    Ft_R=  (((Mdb_NODE*a)/Jdb_NODE)*(-Kphi_NODE*(z(PhiX_db)-z(PhiX_st2))-TOB-
Ctf*PhiXDot_db)-WOB_t+Cr*omega_db*rdb)/(1+(Mdb_NODE*a*a/Jdb_NODE))-Fe_t;
    if abs(Vrel_db)>=Vmin && sign(z(PhiXDot_db))== sign(omega_db)
%     disp('----- Pure SLiding ----------------');
    elseif (-mus*Fn_db)<= Ft_R <=(mus*Fn_db) && abs(Vrel_db)<Vmin
       Ft_db=Ft_R;
%     disp('----------- Pure Rolling -----');
    else
%        disp('---------------- TRANSITION -----');
    end
else    % NO CONTACT
    Fn_db=0;
```

```
    Ft_db=0;
%     disp('-- NO CONTACT ---------------------');
end

    FnY_db= -Fn_db*cos(theta_db);  % Norma(radial) force from polar to cartisian
    FnZ_db= -Fn_db*sin(theta_db);  % Tangential force from polar to cartisian
%  Ft_db= mu0*Fn_db*sign(Vrel_db);
    FtY_db=  Ft_db*sin(theta_db);  % Radial force
    FtZ_db= -Ft_db*cos(theta_db); % Tangential force

Fy_db= WOB_y + FnY_db + FtY_db +Fey_db;
Fz_db= WOB_z + FnZ_db + FtZ_db +Fez_db;

Tb=Ft_db*a;                                   % Friction Torque on Rotor
% Tb=0;

%% Nodal Assignment of Forces Vector

F=zeros(NNODE+4,1);

% @ BHA Top node @ ST1
F(1,1)= Wo + Fx_st1;
F(2,1)= Fy_st1;
F(3,1)= Fz_st1;
F(4,1)= kT_dp*w*t + Tx_st1;
F(5,1)= Ty_st1;
F(6,1)= Tz_st1;

% @ BHA C.G.
F(x_CG,1)= Fx_BHA;
F(y_CG,1)= Fy_BHA;
F(z_CG,1)= Fz_BHA;
F(PhiX_CG,1)= Tx_BHA;
F(PhiY_CG,1)= Ty_BHA;
F(PhiZ_CG,1)= Tz_BHA;

% @ Node before last one @ ST2
F(x_st2,1)= Fx_st2;
F(y_st2,1)= Fy_st2;
F(z_st2,1)= Fz_st2;
F(PhiX_st2,1)= Tx_st2;
F(PhiY_st2,1)= Ty_st2;
F(PhiZ_st2,1)= Tz_st2;

% @ BHA Bottom Node @ DB
F(NNODE-2,1)= -TOB +Tb;
F(NNODE-3,1)= Fz_db;
F(NNODE-4,1)= Fy_db;
F(NNODE-5,1)= -WOB;

zdot=A0*z+B0*F;
```